Understanding and Improving Bolt Patterns in Wind Turbine Blade Roots

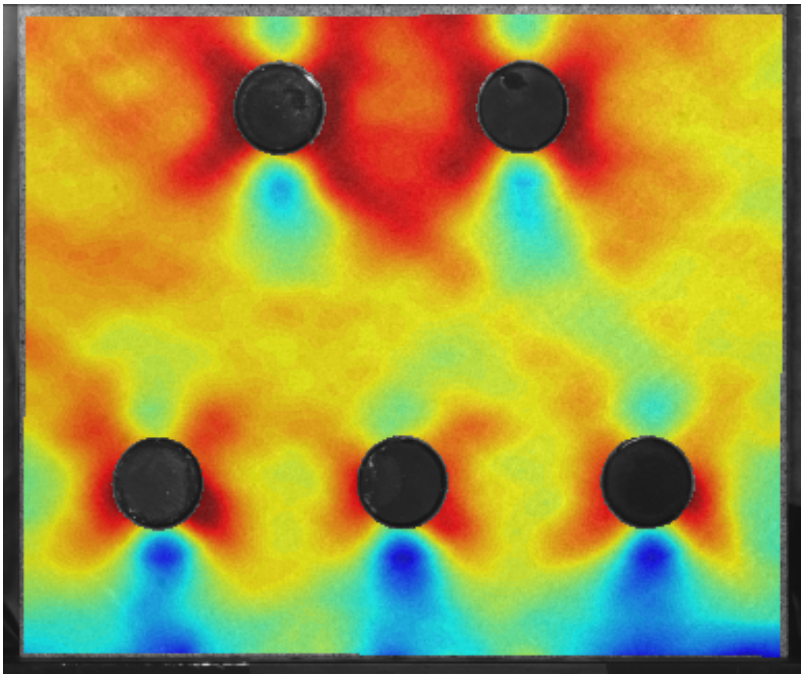

by

Cole Pernitsky

to obtain the degree of Master of Science
at the Delft University of Technology
to be defended publicly on Monday July 5, 2021 at 3:00 PM.

Student Number:	5021448	
Project Duration:	September 28, 2020 - July 5, 2021	
Thesis Committee:	Dr. ir. J.J.E. Teuwen,	TU Delft, Supervisor
	Dr. ir. R. De Breuker,	TU Delft, Chair
	Dr. ir. C. Bisagni,	TU Delft, Examiner
	Dr. ir. L.O. Bernhammer,	SGRE, Supervisor
	W. Feng,	SGRE, Daily Supervisor

This thesis is confidential and cannot be made public until 5 July 2024.

TU Delft

Abstract

As the global push to develop renewable energy sources continues, the wind industry has seen a large growth in the installation of offshore turbines. New turbines are becoming larger, but as their blades grow in length, manufacturers are being presented with unique structural challenges. The blade root is a key part of the blade and turbine in terms of cost, weight, and structural performance. One of the key reasons for this is its immense size, so there is considerable interest in increasing the load capacity of the blade root, without further increasing its size. This thesis was designed and carried out to investigate one avenue for increasing the root capacity: staggered T-Bolt patterns.

Typically wind turbine blades are connected to the hub of the turbine with either T-Bolts or adhesive inserts in a single ring around the circumference of the blade. These connections must withstand high inplane loads from the external moments applied to the blade during service, and their design involves complex trade-offs between factors such as pretension, stress concentration, and packing density. Double-row staggered bolt patterns have been identified as a method of reducing stress concentrations in the root laminate, and this study continued investigation along this path to fully explore the geometric parameters in these staggered bolt patterns.

Starting from existing literature and industry knowledge, an investigation was conceived comprising of primarily, a numerical investigation via finite element studies and secondarily, an experimental campaign to validate the model used. Starting with the numerical modelling, the critical regions and parameters of the root joint were identified. From this the key characteristics of beneficial and detrimental stagger patterns were distinguished and understood. Within the region of beneficial stagger patterns, the effects of the key axial, lateral, and radial spacing patterns on the strain response were studied. Using the axial strain as a metric for load capacity, the optimal stagger configurations were then identified.

Several different configurations, both baseline and optimal, were then manufactured for testing at the lab-scale. Static tensile tests were performed to compare the strain predictions to the actual performance of these T-Bolt designs. The test apparatus incorporated on-center and off-center loads in an attempt to imitate real blade behaviour. While the off-center load method did not properly imitate this behaviour, the experiments were successful in verifying the parameter specific trends of staggered roots. The results of the tests and simulations showed distinct size effects that prevent their results from predicting strain reductions for a full blade, but the relative performance of different specimens identified the characteristics of optimal stagger configurations.

Ultimately it was found that for maximum strain reduction, bolt patterns should first maximize their axial spacing and then incorporate a small amount of radial offset. In addition to providing a lab-scale demonstration of improved bolt patterns, the test campaign serves as a first step towards the creation of a root subcomponent test. Free edges were found not to inhibit the performance of the test specimens, while other concerns such as alignment and load offset were found to be critical in replicating full-scale blade behaviour. From this project it was clear that a full-scale subcomponent test is a feasible and valuable next step in improving wind turbine blade roots.

Acknowledgements

As this project draws to a close, I would like to thank everyone who has helped this opportunity possible. In a year that has been challenging to say the least, it has without doubt taken a village to see this through, and I am very grateful to each and every member thereof. In particular I would like to thank ...

... Julie Teuwen, my supervisor at TU Delft, for her help in no small of number of things, including: introducing me to the wind industry, connecting me with this opportunity, and providing continued support and advice throughout this thesis project and my time as a Masters student. Thank you for making this an enjoyable and memorable experience.

... Wang Feng, for his endless knowledge on all things root and all things ANSYS. Thank you for your help, because without you this project would not have been possible.

... Lars Bernhammer, for bringing this project into existence and for all his keen feedback. Your drive and support were much appreciated throughout the project.

... the whole of the SGRE team for their flexibility, warm welcome, and friendly environment that is truly a pleasure to be a part of.

... my family for their support, not only in ferrying me across the Atlantic, but for their advice, support, and encouragement through this project and my entire academic career.

... Julia for her support and friendship through out this period. Through thick and thin, this would not have been possible without you.

... my flatmates Amanda, Clément, Elsa, and Karoline, for providing some distraction at the end of the day and a wonderful place to call home in Aalborg.

... these four walls of my “home office”. In an unprecedented year, I have accomplished more within two meters of my bed than I ever thought possible. I am very grateful to everyone who helped keep projects like this going despite the challenging situation.

My sincerest gratitude,

Cole Pernitsky

Aalborg, Denmark
July 5, 2021

Contents

Abstract i

List of Figures v

List of Tables viii

Nomenclature ix

1 Introduction 1

2 Literature Review 4
2.1 Blade Overview . . . 4
2.1.1 Design . . . 5
2.1.2 Loading and Certification . . . 7
2.1.3 Fatigue Loading . . . 8
2.1.4 Load Profiles . . . 9
2.2 Failure Criteria . . . 10
2.2.1 Two-Dimensional Criteria . . . 10
2.2.2 Three-Dimensional Criteria . . . 11
2.2.3 Additional Concerns: Holes and Delaminations . . . 12
2.3 Bolted Joints . . . 14
2.3.1 Failure Modes . . . 14
2.3.2 Analysis Methods . . . 16
2.3.3 CZM and XFEM . . . 18
2.3.4 Multi-bolt Joints and Hole Interactions . . . 18
2.3.5 Additional Design Considerations . . . 20
2.4 Applied Root Design . . . 21
2.4.1 Key Design Focuses . . . 21
2.4.2 Subcomponent Testing . . . 22
2.4.3 Research Questions . . . 24

3 Methodology 25
3.1 Project Scope . . . 25
3.2 Investigation Structure . . . 27
3.2.1 Numerical Modelling . . . 27
3.2.2 Physical Testing . . . 30
3.3 Simplified Submodel . . . 32
3.3.1 Geometry . . . 32
3.3.2 Discretization . . . 35
3.3.3 Boundary Conditions and Loads . . . 39
3.3.4 Model vs Full Blade Discrepancies . . . 41

4 Numerical Modelling 43
4.1 General Model Behaviour . . . 43
4.1.1 Determining Critical Stress Component . . . 43
4.1.2 Critical Regions in the Laminate . . . 46
4.1.3 Influence of Load Path on Strain Response . . . 48
4.1.4 Beneficial and Detrimental Stagger Patterns . . . 51

4.2 Parameter Specific Behaviour . . . 53
4.2.1 Axial and Lateral Spacing . . . 54
4.2.2 Lateral Edge Spacing . . . 55
4.2.3 Axial Edge Spacing . . . 56
4.2.4 Stagger Options . . . 57
4.2.5 Radial Offset . . . 58
4.3 Optimization Modelling . . . 60
4.4 Summary of Main Findings . . . 62

5 Experimental Testing 65
5.1 Overview . . . 65
5.2 Center Loaded Tests . . . 68
5.3 Parameter Based Response . . . 71
5.3.1 Lateral Spacing . . . 71
5.3.2 Axial Spacing . . . 73
5.3.3 Radial Offset . . . 74
5.4 Experimental Limitations . . . 75
5.5 Fatigue Tests . . . 76
5.6 Summary of Main Findings . . . 78

6 Conclusions 80

7 Recommendations 83

Bibliography 85

Appendices 92
A Static Strain Maps . . . 92

List of Figures

1.1 Net electricity generation proportions in the EU in 2018, reproduced from [1]. 1

2.1 Schematic showing the components of a turbine (left) and the regions of a blade (right), adapted from Schubel and Crossley [16]. 4
2.2 Schematic diagram of the major components of a turbine blade manufactured with the butterfly method adapted from Mishnaevsky et al. [12]. 5
2.3 Typical types of blade root joints with key parts labeled, adapted from Peeters et al. [15]. 6
2.4 Standard blade coordinates as given by DNV GL [25]. 8
2.5 Failure stress as a function of hole size for OHT specimens, adapted from Kassapoglou [50]. 12
2.6 Stress as a function of radial distance from hole edge, r, with average and point characteristic distances a_0, d_0. 13
2.7 Failure modes for pin loaded joints from Pisano and Fuschi [58]. 14
2.8 Schematic of pin loaded joint with key geometric parameters. 15
2.9 Comparison between the characteristic curve proposed by Chang et al. [64] (left) and the improved curve proposed by Zhang et al. [59] (right). Graphics from Zhang et al. [59]. 17
2.10 Normalized stresses by component as a function of angle around the edge a pin loaded hole, found by [85]. 19
2.11 Stress concentration factor as a function of position around a hole for various triaxial layups. 20
2.12 Left: end view of a blade root with various root segment widths. Right: root cross section showing a design using T-Bolts (top) and inserts (bottom). 22

3.1 Flattened representation of a staggered root design, looking down at the outer surface of the root and showing key parameters. 26
3.2 Specimen design space with key dimensions and terminologies shown as defined in Table 3.1. Note, only half the specimen is shown because it is symmetric about the midplane ($z = L/2$). 27
3.3 Stagger configurations with baseline and maximum axial spacings shown on a real root segment with equivalent lab-scale dimensions. 29
3.4 CAD model of test setup with components labeled. 30
3.5 Side view of CAD model with complete test setup comparing on-center and off-center loading configurations. 31
3.6 Visualization of the cycle numbers at which the strains were sampled during fatigue testing. 32
3.7 Schematic showing region of specimens painted with DIC speckle pattern and the placement of SGs on the specimen. Note the image has been rotated for display purposes. . 32
3.8 Comparison of reduced symmetry models and 5-bolt submodel showing their respective boundary conditions. The root laminate is shown in light grey, hub in dark grey, and T-Bolt bushings shown in teal. 33
3.9 Formation of 5-bolt submodel geometry as an extracted and reflected section of a full blade root. 34
3.10 End-view (hub to tip) of the difference in geometry, specifically in the out-of-plane height, between a flat specimen and a curved section of a full root. 34
3.11 Full FE model used for simulations shown without BCs. Elements are coloured by type: beam elements are red, tetrahedral solid elements are purple, and hexahedral solid elements are cyan. 35
3.12 Numerical discretization of a single T-Bolt, showing element type by colour. 36
3.13 Process flow for creating the laminate volumes of the 5-bolt submodel. 37
3.14 Process flow for meshing the laminate volumes of the 5-bolt submodel. 38

3.15 Convergence study results showing maximum strains and node count in the cylindrical region around the bushings (region with critical stress concentrations). 39
3.16 Normalized axial strain profiles through laminate thickness at the inside of the second bushing ($\theta = 90°$) used for strain matching between models. 40
3.17 Annotated screenshot from ANSYS showing BCs and loads applied to the 5-bolt submodel. Note, pretension loads are shown in x-direction (due to local coordinate systems) but they are applied in the z-direction. 41

4.1 Left: flattened representation of the inner ring of nodes around the bushing, where the nodes shown in red were excluded due to element distortion indicated by high aspect ratios. Right: diagram showing how θ and y are defined locally for each bushing (1 to 5) in the model, and how the model is symmetric in the yz plane. 44
4.2 Stress response by component around each bushing (B1-B3) as a function of angular position (θ) for the baseline root geometry. Each stress component is shown at a constant through thickness position (y) as given in Table 4.1. This location corresponds to the maximum stress magnitudes, thereby representing the critical y position in the laminate. 45
4.3 Stress response by component around each bushing (B1-B3) as a function of vertical position (y) for the baseline root geometry. Each stress component is shown at a constant angular position (θ) as given in Table 4.1. This location corresponds to the maximum stress magnitudes, thereby representing the critical θ location around the bushing. . . . 46
4.4 Comparison of max strains at five different locations within the model for a variety of stagger geometries. Each of the 5 groups has an array of 24 strain values organized into 3 rows each with 8 columns. Each row and colour represents a d_L spacing while each column represents a d_A spacing. Note the B1R region group title is omitted to define the d_A spacings. 47
4.5 Max strains at different locations within the laminate compared to show: a) the difference in first and second row strain response through a comparison of B2R to B3L with and without axial spacing, and b) the influence of edge effects in the B1L region by contrasting the difference between the strains at B1L and B1R with to the similarity of them at B1R and B3L. 48
4.6 Sketch showing load paths through the submodel when an external load is applied to the endplate and pretension is applied to the shaftbolts. The corresponding load in each shaftbolt is also shown to show how the load path changes when contact is lost between the laminate and the endplate (otherwise known as gap opening). 49
4.7 Axial strain at multiple locations through the thickness of the laminate adjacent to B2R and B3L as a function of applied external load. The height at which the strain is extracted ranges from the inner surface $y/t = 0$ to the outer surface $y/t = 1$ according to the colour gradient. 50
4.8 Annotated comparison of max strain in the 5-bolt specimen for different lateral and axial spacing configurations, with two example configurations shown on the right. Surface plot produced using code from [105]. 51
4.9 Normalized axial and shear strain fields compared under different axial spacings. The plots show the strain values moving radially outward from $\theta = 90°$ and $-90°$ of B3L and B4R respectively, as shown by the region highlighted in yellow on the right-hand sketch. 52
4.10 Key spacing parameters overlaid onto a screenshot of the 5 bolt submodel used for simulations. 53
4.11 Overall max strain in model as a function of lateral (left) and axial (right) spacing shown in two dimensions to isolate normalized strain trends. Two dimensional interpolations were performed using code from [105]. 54
4.12 Maximum strains adjacent to the outer bushing as a function of lateral edge distance for different configurations. 55

4.13 Maximum axial strain as a function of axial edge distance. Results are displayed at three locations (from top to bottom: B2R, B1L, and B3L) and colours are used to distinguish four different spacing geometries: combinations of small and large lateral spacings ($d_L = 25$ mm or $d_L = 26$ mm) with small and large radial offsets ($d_R = 0.0$ mm or $d_R = 1.0$ mm). All geometries used an axial spacing of $d_A = 42.9$ mm. 56
4.14 Front view sketches of the different options for the positioning of the shaftbolts through the thickness of the laminate. 58
4.15 Comparison of strain profiles through the thickness of the laminate at the B2R location for different radial offset distances. All configurations have $d_L = 26$ mm and $d_A = 60$ mm 59
4.16 Overall max strain in model as a function of radial (x-axis) and axial (y-axis) spacing for $d_L = 25$ mm shown as a surface plot. Two dimensional interpolations were performed using code from [105]. 59
4.17 Maximum axial strain in the B2R region for different radial offsets as a function of axial spacing for $d_L = 23.7$ mm. 60
4.18 Maximum axial strain in the B2R region for different radial offsets as a function of axial spacing. Results are separated by lateral spacing where a) contains data from $d_L = 25.0$ mm and b) from $d_L = 26.0$ mm. Each of the plots also highlights the configurations used for physical testing with red circles. 61
4.19 Maximum axial strain in the B3 region for different radial offsets and lateral spacings as a function of axial spacing. 62
4.20 Overview of suggested root design process for minimizing axial strain including a sketched graph showing the impact of axial spacing and radial offsets on the maximum strain in the laminate. 64

5.1 Overview of the differences between test specimens: specimen number (1-5) identifying the axial and lateral spacings and specimen letter (A-C) identifying the measured radial offset and load method. 66
5.2 Test machine load vs displacement data for all static specimens, with a zoomed in region on the right highlighting the differences in displacement at the target load of 260 kN. The three labelled trends on the left correspond to the two specimens (1B and 1C) that exhibited nut failure and specimen 5A which was loaded past the yield point. 66
5.3 Axial displacement plots of the back surface of specimen 1A using the unloaded state as a reference (left) compared to the pretension state (right). Above the displacement fields, the load values of each state are defined. 67
5.4 Locations across the laminate at which strain values were extracted from the DIC analysis for comparison between the experimental results and numerical predictions. 68
5.5 Comparison between predicted and measured axial strains for the front (top) and back (bottom) surfaces of specimen 1A. The predictions from ANSYS are shown on the left, while the measured DIC strains are on the right. All strain values were calculated from the pretension state. 70
5.6 Measured strain maps showing the influence of increasing d_L from 25 mm to 26 mm between specimens 1C and 4B (top) and 2C to 5A (bottom) using the unloaded state as a reference. 72
5.7 Measured strain maps showing the influence of increasing d_A from 43 mm to 80 mm (top) and from 62 mm to 80 mm (bottom) using the pretension state as a reference. . . 73
5.8 Measured strain maps showing the influence of changing the radial offset from $d_R = -0.3$ mm for 1B (left) to $d_R = 0.9$ mm for 1C (right) using the pretension state as a reference. 74
5.9 Change in axial strain at each location over the duration of the fatigue tests. At each location, strain was calculated as the difference between the strain at the current cycle and the initial cycle divided by the initial strain. Only the locations on the left half of the specimen are shown due to symmetry. 77
5.10 Axial strains from the second row over the duration of the fatigue tests normalized by the strain at that location from the static test specimen with the same geometry. For 1F (left) this is specimen 1A, and for 2F (right) this is 3A. 77

List of Tables

3.1 Parameter definitions used to define specimen geometry as shown in Figure 3.2. 28
3.2 Specimen descriptions with load method and hole pattern dimensions for the 12 specimens tested. 31
3.3 ANSYS element types and corresponding material definitions used for each component in the 5-bolt submodel. 36

4.1 Vertical (y) and angular (θ) locations in cylindrical coordinates of the planes containing the maximum stresses around each bushing. Locations are grouped by stress component and given for bushings 1 through 3 (bushings 3 through 5 are symmetric and their inclusion is redundant). The local coordinate systems used are defined in Figure 4.1. . 45
4.2 Maximum strain gradients calculated at six points: low, medium, and high axial spacings (d_A) in combination with low and high lateral spacings (d_L) . The spacing values and normalized axial strain at each location are also provided for context. 52
4.3 Summary of optimal strain values and associated strain reductions found from the numerical model for different stagger configurations with their associated dimensions. All strain values are the overall maximum in the laminate, and the strain reductions are calculated from a configuration with no staggering ($d_L = 23.7$ mm and $d_A, d_R = 0$ mm). Only one lateral spacing is shown here, because d_L is typically fixed by external factors and is preferred to be as low as possible. 64

5.1 Second row strains for center load specimens on the front and back surfaces. Note all strains are given in [µm/m], and the error values are calculated using the ANSYS predictions as the reference. 70
5.2 Strain gauge results (SG) compared to the strains from DIC and the numerical model for the center loaded specimens at the row two net-section and inside edge of bushing two. 71
5.3 Percent change in strains from specimen 1C to 4B (left) and 2C to 5A (right) for both measured (DIC) and predicted (ANSYS) values as a result of increased lateral spacing. Strains were calculated from the unloaded state on the front surface. 72
5.4 Percent change in strains from specimen 1B to 2B (left) and 3A to 2C (right) for both measured (DIC) and predicted (ANSYS) values as a result of increased axial spacing. Strains were calculated from the pretension state on the front surface. 74
5.5 Percent change in strains from specimen 1B to 2B (left) and 3A to 2C (right) for both measured (DIC) and predicted (ANSYS) values as a result of offsetting the shaftbolts from the laminate centerline. Strains were calculated from the pretension state on the front surface. 75

Nomenclature

Acronym	Definition
2D	Two-dimensional
3D	Three-dimensional
B#	Bushing number # (example: B4 is bushing 4)
B#L	Laminate adjacent to bushing number # on the left side
B#R	Laminate adjacent to bushing number # on the right side
BC	Boundary Condition
BCD	Bolt Circle Diameter
BEM	Boundary Element Method
BJSFM	Bolted Joint Stress Field Model
CFD	Computation Fluid Dynamics
CFRP	Carbon Fibre Reinforced Polymer
CLD	Constant Life Diagram
CLPT	Classical Laminated Plate Theory
CZE	Cohesive Zone Element
CZM	Cohesive Zone Modelling
deg	Degrees, also denoted as °
DIC	Digital Image Correlation
DNV GL	Det Norske Veritas Germanischer Lloyd
EU	European Union
FE	Finite Element
FEA	Finite Element Analysis
FEM	Finite Element Method
FRP	Fibre Reinforced Polymer
FS	Full-scale
GFRP	Glass Fibre Reinforced Polymer
IFF	Inter-fibre Failure
IR	Inner Ring of nodes or elements around a bushing
LEFM	Linear Elastic Fracture Mechanics
LS	Lab-scale
OHT	Open Hole Tension
OR	Outer Ring of nodes or elements around a bushing
PET	Polyethylene terephthalate
PreT	Pretension
R#	Bushing Row # (either R1 or R2 for the first or second row of bushings)
RTM	Resin Transfer Moulding
SCF	Stress Concentration Factor
SCT	Subcomponent Test
SG	Strain Gauge
SGRE	Siemens Gamesa Renewable Energy
w.r.t.	with respect to
XFEM	Extended Finite Element Method

Symbol	Definition	Units
α	Shear characteristic distance factor	-
γ	Shear strain	μm/m
γ_{xy}, γ_{xz}, ...	Shear strain in the xy, xz, ... direction	μm/m
γ_m	Partial safety factor	-
γ_{m0}, γ_{m1}, ...	Baseline factor, partial factor 1, ...	-
δ	Displacement	mm
$\delta_{laminate}$, δ_{bolt}	Displacement in laminate or bolt	mm
ϵ	Strain	μm/m
ϵ_x, ϵ_y, ϵ_z	Strain in the x, y, or z direction	μm/m
$\epsilon_{x,T}^{ult}$, $\epsilon_{x,C}^{ult}$	Ultimate failure strain in compression (C) or tension (T)	μm/m
ϵ_z^*	Normalized axial strain (z direction)	-
θ	Angular position	°
κ	Curvature	1/m
κ_x, κ_y, ...	Curvature in the x, y, ... direction	1/m
σ	Stress	MPa
σ_x,σ_y, ...	Stress in the x, y, ... direction	MPa
σ_T^{ult}	Ultimate failure stress under tension loading	MPa
$\overline{\sigma}$	Average stress	MPa
σ^*	Normalized stress	-
τ	Shear stress	MPa
τ_{xy}, τ_{xz}, ...	Shear stress in the xy, xz, ... direction	MPa
a	Crack (hole) size	mm
A	Laminate membrane stiffness matrix	N/mm
A_{11}, A_{12}, ...	11, 12, ... component of the A matrix	N/mm
A_{xc}	Cross-sectional area	mm^2
a_0	Characteristic distance for the average stress method	mm
B	Laminate membrane-bending stiffness matrix	N m/m
B_{11}, B_{12}, ...	11, 12, ... component of the B matrix	N m/m
D	Laminate bending stiffness matrix	N m
D_{11}, D_{12}, ...	11, 12, ... component of the D matrix	N m
d	Diameter	mm
d_b	Bushing diameter	mm
d_{sh}	Shaftbolt hole diameter	mm
d_{sb}	Shaftbolt diameter	mm
d_0	Characteristic distance for the point stress method	mm
d_{0C}, d_{0T}	Characteristic distance in compression (C) or tension (T)	mm
d_A	Axial spacing	mm
d_{Ae}	Axial edge distance	mm
d_L	Lateral spacing	mm
d_{Le}	Lateral edge distance	mm
d_R	Radial offset	mm
e	Failure index	-
E	Stiffness	N/mm^2
E_{11}, E_{12}, ...	Stiffness in the 11, 12, ... direction	N/mm^2
F	Force	kN
F_{bolt}	Force in the shaftbolt	kN
F_{ext}	Applied external force	kN
$F_{laminate}$	Force in the laminate	kN
$F_{separation}$	Applied force at separation	kN
G_c	Fracture toughness	N/mm
G_{Ic}, G_{IIc}, G_{IIIc}	Mode I, II, III fracture toughness	N/mm

Symbol	Definition	Units
k_t	Stress concentration factor	-
L	Length	mm
M	Moment	
M_{XB}, M_{YB}, M_{ZB}	Blade moment in the X, Y, or Z direction	N m
M_x, M_y, M_{xy}	Moment per unit width in the x, y, or xy direction	N m/m
N	Line Load (load per unit width)	N/mm
N_x, N_y, N_{xy}	Line load components in the x, y, and xy directions	N/mm
n	Number	-
P	Pressure	MPa
P_0	Average pressure	MPa
$P(y)$	Pressure as a function of y	MPa
P_0	Average pressure	MPa
r	Radius	mm
r_c	Characteristic curve radius	mm
R	R Ratio (for fatigue loading)	-
R_{OL}	Overload Ratio	-
S_c	Shear strength	MPa
t	Thickness	mm
w	Width	mm
X_C, X_T	Axial strength in compression (C) or tension (T)	MPa
Y_C, Y_T	Transverse strength in compression (C) or tension (T)	MPa
z_{off}	Offset in z-direction	mm
U	Displacement in ANSYS	mm
UX, UY, UZ	ANSYS displacement in the x, y, and z directions	mm
℄	Centerline	-

1

Introduction

Countries are increasingly turning to renewable energy for power generation. The motivations for developing renewable energy sources are well understood and undeniable. They include greenhouse gas emissions, their effects on climate change, and the finite nature of fossil fuels to name a few. As the world works to economically rebuild in the wake of the coronavirus pandemic, focus on developing a sustainable future has further intensified, with European Commission President Ursula von der Leyen describing the newly ratified European Union (EU) budget as “a recovery lead by the green and digital transition.” [1]. For an indication of what this implies, the EU plans to cut emissions by 80-95% before 2050 through the increased use of renewable energy sources [2].

As of 2018, the most common renewable energy sources in the EU are (in order) hydro, wind, and solar, as shown in Figure 1.1. Clearly, wind energy is one of the key avenues to renewable power generation. In fact, it is one of the fastest growing sources of renewable energy [3]. One of the reasons for this is its low cost. In the early 2000s wind power was already as cheap as 0.05 USD/kWh, a number that has since decreased to under 0.02 USD/kWh [4]. This, and other factors, have created a fast growing industry. After first emerging in the 1990s, the wind industry’s annual, worldwide, power generation grew at rates in excess of 30% into the 2000s [5]. Over the last 20 years this growth has continued, taking the industry from an installed capacity of 121 MW worldwide in 2008, to 651 GW in 2019, where over 60 GW were installed in 2019 alone [6, 7].

As the industry has grown, turbine technology has also continued to advance. Enabled by modern

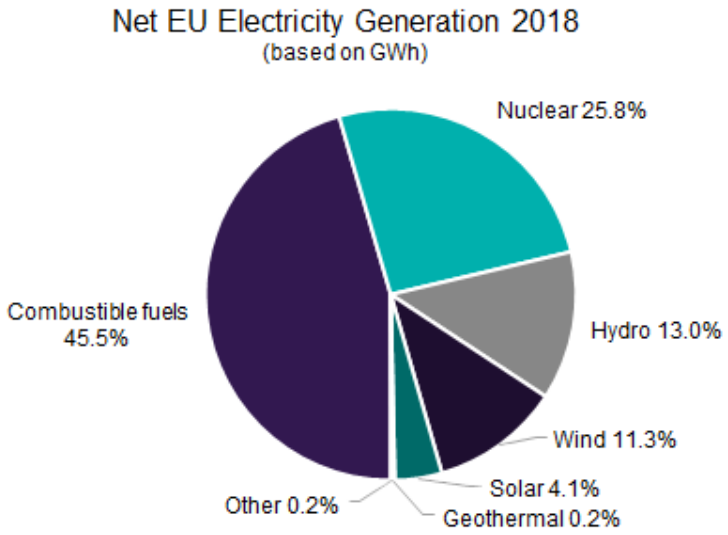

Figure 1.1: Net electricity generation proportions in the EU in 2018, reproduced from [1].

fibre reinforced plastics (FRPs), the first wind turbines produced in the late 1970s had rotor diameters of 16 m [8], but modern turbines feature diameters up to 200 m [9]. In continental Europe, many countries have reached near saturation of on-shore wind farm locations, and subsequently there has been a shift to off-shore wind farm installation [10]. This shift started in the early 2000s, and between 2011 and 2020, the European Wind Energy Association projected a more than 6 fold increase in off-shore wind capacity [2]. The growth of offshore has taken it from 1% of the global wind capacity in 2009 to over 10% in 2019 [11]. The promise of offshore installations is two-fold: larger turbines can be installed and wind speed are higher and more consistent [10]. Both of these factors allow turbines to generate more power, but they also require stronger, more advanced blades.

Blade lengths have continued to grow throughout the development of the industry, with the average diameter of installed rotors in the United States increasing by 141% from 1998 to 2018 [4]. Longer blades allow the turbines to produce more power by capturing a greater wind area [8], but this also creates increased structural and subsequently manufacturing demands. Wind turbine blades have been predominantly manufactured out of composite materials since the 1970s [12], due to composite's higher stiffness per unit weight. Traditionally made with glass fibre composites and sandwich laminates featuring balsa cores, modern wind turbines have also started to integrate carbon fibre and PET (polyethylene terephthalate) foams as blade lengths grow and manufacturing techniques change. The evolution of wind turbine blades has brought about changes and improvements in various parts of the blade, including the leading and trailing edges, web, and root. One of the most structurally critical areas in the blade is the root, where the blade connects to the hub [13]. Increasing blade diameters create unique structural challenges in this area since the presence of fasteners to attach the blade to the hub inherently weakens the laminate.

The large loads at the blade root require thick laminates and large root diameters to achieve the necessary load capacity to support the rest of the blade. For example, a 100 m glass fibre reinforced polymer (GFRP) blade designed by Griffith and Ashwill [14] has a root diameter of 6 m and a thickness of 160 mm. As a direct result of this size, the root accounts for around 7% of the blade's weight and 20% of its cost [15]. Furthermore, the root diameter sets the size of the hub, which is typically cast as a single steel part: an expensive and challenging process [5]. A life cycle analysis by Crawford [6] found it takes 85.3 GJ of energy to process each tonne of steel, and even a medium size blade (113 m rotor diameter) contains 19.2 tonnes of steel. Therefore reducing the size of the hub creates cost savings in manufacturing, and as a result, there is considerable interest in improving the root's structural capacity without increasing the root diameter.

A variety of root joints have been proposed and employed in wind turbine blades, but the majority of modern blades use either T-Bolts or bonded inserts [15]. Typically, these methods are applied similarly, with a single ring of repeating fasteners around the circumference of the blade. As with most modern structures, there are many different geometrical, material, and external factors that influence the design and performance of the root. While this project aims to understand as much root behaviour as possible, the scope must remain manageable. An investigation on T-Bolts can be somewhat informative when designing with root joints that use inserts, but the same cannot be said in reverse. The reasons for this include the shaftbolt and bearing behaviours seen in T-Bolts but not root inserts and inversely, the lack of any adhesive bonding/co-curing in T-Bolt connections. Thus the decision was made to focus solely on the geometrical parameters of T-Bolt root configurations, which ensures the project will be able to fully address the gap in understanding on the effects of bolt spacing.

This MSc Thesis investigates new ways in which T-Bolt connections can be implemented in wind turbine blades: exploring joint design as a method for increasing the load capacity of the root. By repositioning the T-Bolts in the root from a single row to a staggered double row configuration, the stress concentration effects at the edge of the bushings can be reduced. Building upon this simple concept, this project provides a parametric exploration of the staggered design, performed through finite element modelling, which is expanded into a finite element (FE) driven optimization of the T-Bolt root connection. To validate the numerical investigation, an experimental campaign was carried out at the lab- and full-scales, the design and results of which are also presented in this thesis. While the experimental testing in this project did not provide validation to the level required for blade production, the experimental method was designed with future validation and subcomponent testing in mind, contributing a first step in the development of a root subcomponent test (SCT).

The remainder of this chapter provides an overview of the thesis structure, emphasizing the key steps required in realizing the optimized root design that was the main goal of the project. To begin

the investigation and this thesis, a literature review was carried out to understand the state-of-the-art in blade root design, the results of which are presented in Chapter 2. This begins with a general overview of wind turbine blade loading, design, and certification considerations. Fully understanding these design and structural analysis processes requires a more specific discussions of composite failure theories and FE modelling techniques. Furthermore, certification guidelines and other subcomponent tests are discussed and analysed to present a framework for the design of this experimental campaign. The decisions made in designing this project and their subsequent implications are then presented in Chapter 3.

This project can be roughly separated into two phases: the numerical and experimental activities. The results from the preliminary modelling investigation are presented at the beginning Chapter 4. This include explanations of how key spacing parameters such as specimen edge distance and axial spacing effect the behaviour of the model, and by extrapolation, the blade root. These behaviours set the stage for the results of the optimization studies that are found at the end of the chapter. These results were then used to set the dimensions of the specimens used in the experimental tests. Chapter 5 then presents the results from these tests and compares them to the numerical predictions from the previous chapter. This comparison provides a way to validate the numeric modelling approaches and asses their reliability for future use. The conclusions of the work are then presented in Chapter 6, followed by recommendations for future work in the field of root design and subcomponent testing in Chapter 7.

2

Literature Review

This chapter contains a broad overview of some of the topics involved in the structural behaviour of wind turbines. The topics are presented to provide the necessary background information to understand the project and its methods. A general overview of some the design, loading, and certification concerns for the entire blade is given (2.1). This serves to establish the various topics that must be considered in blade design, before focusing on the behaviour of the composite laminates which are used to construct the blade. Various failure theories and structural features of special concern such as holes and delaminations and their implications in composite structures are then discussed (2.2). The blade root represents a composite joint, so the discussion is expanded to consider the failure modes, analysis methods, and design considerations of bolted joints in Section 2.3. Finally, the common elements from each of these topics are discussed in their direct application to the design of wind turbine blade root joints (2.4). As a conclusion of the literature survey, the findings are distilled into focused research questions in Section 2.4.3 to address a key gap in the understanding of wind turbine blade root behaviour.

2.1. Blade Overview

Various configurations of wind turbines have been used for power generation since the 1970s [13]. Modern commercial wind turbines have converged to a three-bladed, horizontal axis design that feature three main components: the tower, the nacelle, and the blades. The blade can be further divided into three regions (the root, the mid-span, and the tip). Each region of the blade has a different function, as shown in Figure 2.1, and subsequently a different design. This section gives a quick overview of the blade components in these regions (2.1.1), a surface level discussion of blade loads (2.1.2) with

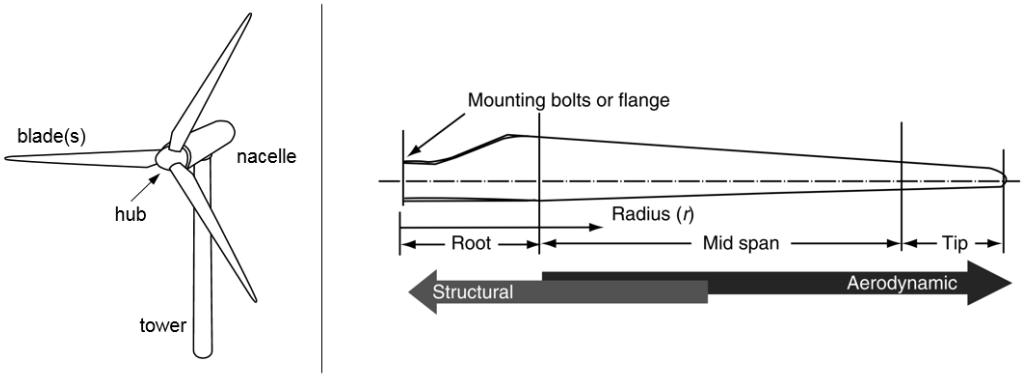

Figure 2.1: Schematic showing the components of a turbine (left) and the regions of a blade (right), adapted from Schubel and Crossley [16].

specific attention to fatigue loads (2.1.3), and lastly some state-of-the-art designs are presented (2.1.4). This serves to introduce the reader the top-level concerns in of blade design.

2.1.1. Design

One of the foremost concerns in blade design is aerodynamic efficiency, or in other words, ensuring that the blades will rotate and generate power. Along the length of the blade, the primary concern shifts from structural to aerodynamic, and subsequently, the cross-sectional shape changes smoothly from a cylinder at the root, to thicker airfoils in the mid-span, to thin airfoils at the tip [17, 13]. State-of-the-art designs employ large root diameters with thick laminates to achieve an adequate number of bolts, and volume of load bearing material, to ensure the root's structural integrity through its lifetime. This is shown visually in Figure 2.1 and can be further seen by inspecting the blade designs of Griffith and Ashwill [14], Griffith [18], and Cox and Echtermeyer [19].

Current state-of-the-art wind turbine blades have reached lengths in excess of 100 m. These large blades can be thought of as cantilevered beams, and in fact, simplified structural analysis of the blade considers it to be a rotating cantilevered beam acting upon by distributed loads [16]. Obviously, these blades are subjected to high loads, and to ensure they have adequate strength, multiple components are combined within the aerodynamic shell of the blade. It is essential that these components are as strong and as light as possible, and thus blades employ composite materials due to their high stiffness to weight ratios.

Traditionally, this has meant glass fibre reinforced polymer (GFRP) structures and an extensive use of sandwich structures. Although carbon fibre reinforced polymer (CFRP) laminates are stiffer and lighter than their GFRP counter parts, they are also more expensive. Mixing glass and carbon fibres has been proposed and studied to increase blade stiffness while limiting the increase in cost. In addition to increased cost, hybrid blades with carbon and glass fibres may present challenges from a lightning protection or strength perspective [20]. Nevertheless, this strategy is seeing increasing use, with carbon being incorporated into blades in the 90+ m range from industry leaders such as LM Wind Power and Siemens Gamesa Renewable Energy (SGRE) [9]. As pointed out by Cox and Echtermeyer [19], this strategy is most effective when replacing the fibres at 0° (aligned with the axis of the blade) with carbon fibre.

Across all the FRP components in wind turbine blades, the fibres primarily used are triaxial, biaxial, and unidirectional fabrics. These are composed of different proportions of fibres in the 0°, $+45^\circ$, and -45° orientations. The numerical prefix indicates how many fibre orientations are included in the fabric. Roughly speaking the 0° fibres predominantly add bending stiffness, and the $\pm 45^\circ$ fibres add buckling and shear resistance while also assisting in load transfer around holes [8]. The layups used vary by component and are chosen from in depth design studies. The main components of a blade are the external shells and the internal web(s), spar caps, root segments, and root inserts.

These components can be seen in Figure 2.2 which shows an exploded view of a butterfly blade

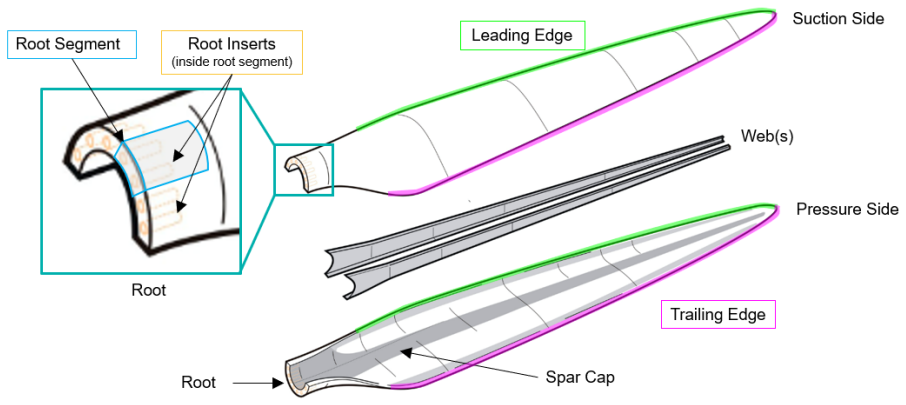

Figure 2.2: Schematic diagram of the major components of a turbine blade manufactured with the butterfly method adapted from Mishnaevsky et al. [12].

that features two shear webs. Additional terminology shown in the diagram include the suction and pressure sides of the blade. These terms refer to the aerodynamic forces on the blade and coincide with the blade halves on a butterfly blade. The redirection of air flow around the blade from the leading to trailing edges, creates a lift force that acts from the pressure side towards the suction side and drives the rotation of the turbine.

A butterfly blade is one where the aerodynamic shell of the blade is fabricated in two halves and joined along the leading and trailing edges as shown in Figure 2.2 [12]. Alternative manufacturing methods include the use of internal mandrels to cast the blade as a single shell and avoid the joining process. Unsurprisingly, the precise aerodynamic cross-section of the blade is not the most structurally efficient shape, which makes the internal spar caps and shear webs essential to the structural integrity of the blade [21]. The former provides high bending stiffness and the latter provides shear stiffness [19]. They can be compared the web and flanges of the traditional I-beam.

Since these parts are situated inside the blade, they are often prefabricated to simplify the manufacturing process. Prefabricating or precasting gives the components structural rigidity that helps keep them in place during the infusion of the entire blade. The prefabrication of these components also improves the quality of the parts [21]. Prefabrication offers a level of quality assurance and reduces the likelihood of production issues, which could require the entire blade to be re-fabricated [15]. This should be avoided due to the large cost (time, money, and materials) associated with blade production [12].

The blade root is one of the most important structural components of the blade and one of the most difficult to infuse, making it a prime candidate for precast components. It must transfer loads from the blades to the hub and tower, and facilitate attachment of the blade to the hub. Furthermore, the presence of fasteners weakens the laminate, and the beginning of the shear web(s) and spar caps (typically occurring a short distance towards the tip) induce high local loads in this region [22]. To facilitate these requirements, laminates well in excess of 100 mm thick are typically used to counteract the reduced laminate area and stress concentrations introduced by the fasteners. Furthermore, to ensure adequate bending stiffness, the bolt-circle-diameter (i.e. the diameter of the circle passing through the center of these fasteners, or in short the BCD) is typically well above 4 m. Infusing a 100+ mm thick laminate around a circumference that is well over 12 m long has necessitated the use of precast root segments.

Root segments are precast blocks of laminate inserted into the root to reduce the about of fabric laid and infused. Their width, and thus the number of root segments included in the blade, varies between manufacturer. Within the root segments, root inserts may or may not be included. A root insert, contains a single fastener, used to connect the blade to the hub and can be cast directly into the root segment or bonded in after casting. Historically, there have been four main attachment methods used in root joints; however, modern blades are rarely seen with designs other than T-Bolts or root inserts [15]. The joint elements, shown in Figure 2.3, are typically installed in a repeating axi-symmetric pattern around the root circumference, much like the root segments.

Both T-Bolts and root inserts rely on a similar mechanism to attach the blade to the hub: they provide

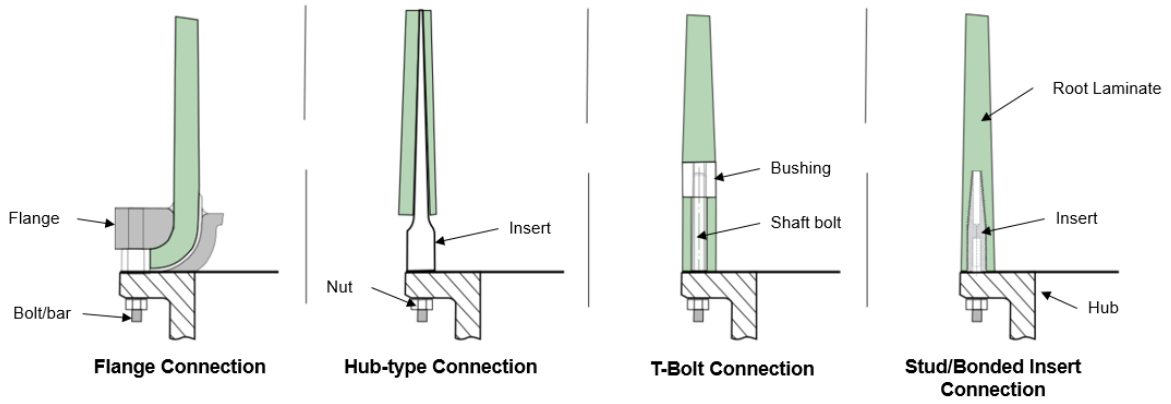

Figure 2.3: Typical types of blade root joints with key parts labeled, adapted from Peeters et al. [15].

an interface in the blade that a threaded bar or shaftbolt can be connected to and then tightened against the hub at the opposite end (via nuts as shown in Figure 2.3). T-bolts transfer the loads from the root laminate into the shaftbolt through bearing forces at the bushing-laminate interface. Root inserts on the other hand, rely upon shear forces at the insert-laminate interface to transfer loads into the shaftbolt. Modern blades feature various designs using both of these connection methods.

2.1.2. Loading and Certification

As their name implies, wind turbine blades are highly loaded by ever changing wind conditions. Consequently, turbines must be designed to withstand a multitude of, site dependent, meteorological conditions, and with each of these comes a different set of loads on the blades and turbine. By the nature of the turbine's rotating motion, these loads are cyclic, generating both static and fatigue loading concerns. It is impossible to predict the weather, so turbines are designed to operate for at least 20 years within their class. These classifications are divided by decreasing average wind speeds from I to III, and decreasing turbulence intensity from A+ to C [23]. The wind is then modelled with as a distribution (Rayleigh or Weibull distributions [23]) obtained from extensive simulations (i.e. 5-10 thousand simulations of 10 minute duration). The shear number of simulations leads to the use of blade element momentum theory as a faster alternative to high fidelity computational fluid dynamics (CFD) simulations to calculate wind and thus load distributions [24]. To reduce the number of structural calculations, these wind load distributions are typically further categorized into worst case scenarios otherwise known as "limit states", that is, the states most likely to induce damage or failure. It is these load states that are then designed for with the assumption that if the turbine can withstand the extreme loads it will also survive the smaller ones.

Even though each site experiences different loads, there is general agreement on what conditions induce the worst case scenarios. These loads come from environmental factors such as wind, storms, and icing; operational factors such starting, stopping, and rotational velocity; and structural considerations such as blade length and size. Typically the three most critical scenarios are: emergency stop, extreme operational loads, and storm loading while not in operation [16]. On the other hand, Griffith and Ashwill [14] consider 7 extreme load cases. There must be a balance in defining these cases such that they encompass all foreseeable conditions without making the structural analysis inhibitively long. To aid in this process, guidelines have been produced for the design of wind turbine blades. The most useful is the *DNVGL-ST-0376* standard from DNV GL [25] – the unified body created after Det Norske Veritas and Germanischer Lloyd merged. The DNV GL [25] guidelines offer detailed specifications on which structural verifications should be performed and which partial safety factors should be applied for each load condition/calculation.

To ensure that the various unknowns in testing, manufacturing, and design are accounted for, the standards include comprehensive guidance on partial safety factors that shall be used for design and certification. They address specific aspects that may be approximated in, or excluded from, analysis and are specified as a geometric sum of: a base factor ($\gamma_{m0} = 1.2$), failure mode criticality factor, long-term degradation factor, temperature effects factor, manufacturing effects factor, analysis method accuracy factor, and a load assumptions accuracy factor [25]. The values of these factors vary between verifications and are multiplied together to yield an overall reduction factor that is applied to the material design value, ensuring conservative calculations. Material design values/allowables are another method used to address unknowns, specifically those from material scatter. It is common practice to perform coupon testing to determine the properties of the materials used for wind turbine blades, providing an element of quality control [21]. There are numerous standards for doing so and statistical methods are used to translate the test results into reliable design values. DNV GL [25] requires these methods to provide 95% confidence and outlines specific procedures and formulas for their calculation in their standards. Combining the material design value with the partial reduction factor sets a limit for the blade's structural response. Incorporating these two methodologies, ensures that the predicted response (typically stress or strain) will not cause failure in the material under any of the critical loading conditions over the turbine's life.

The main loads on a blade are commonly described in terms of (positive and negative) flapwise and edgewise bending moments. These form the main directions as specified by DNV GL [25], and they are defined as $\pm M_{YB}$ and $\pm M_{XB}$ respectively, as shown in Figure 2.4. Despite not including $\pm M_{ZB}$, these two components are accepted as sufficiently representing the loads acting on a blade, as they account for 97% of damage accumulation during service [8]. It should be noted that, an additional partial

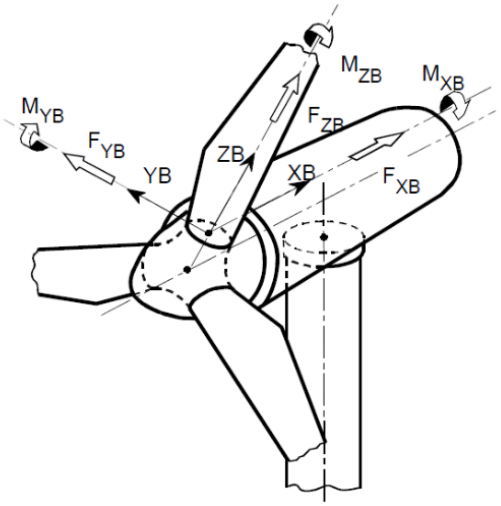

Figure 2.4: Standard blade coordinates as given by DNV GL [25].

reduction factor is required by DNV GL [25] when this reduced form is used for design; the alternative is to discretize moments by splitting the blade into 12 angular sections around the z axis. Flapwise moments are generally aerodynamic in nature, induced by wind loading, and act as a distributed load transverse to the blade. Whereas, the edgewise bending moments are gravitational, initiated by the blade's mass and maximized when the blade is horizontal [16]. Blades are typically modelled as a rotating cantilevered beam, and thus the moments and resulting stresses reach a maximum at the blade's root. The gravitational loads are periodic due to the rotation of the blades, and the aerodynamic loads also vary with time albeit not as uniformly. This means that proper quantification of these load cycles is essential to perform proper fatigue analysis (and thus design a structurally competent blade).

Before further elaborating on fatigue loading, there are a few sections of the DNV GL guidelines that merit discussion as they provide information directly pertaining to T-Bolt joints in the blade root. These sections are *DNVGL-ST-0376* Sections 2.5.8 and 2.5.10 [25]. Some of the specific concerns include: the influence of spar caps in creating a concentrated load introduction point, mismatch in alignment between the positioning of the shaftbolt on the hub and its hole in the root laminate, failure in the threads of the shaftbolts, and loss in pretension of the shaftbolt [25]. Another issue that can arise during service is bolt bending. This can be caused by alignment issues and is of concern because it reduces the strength of the joint by loading the bolt without the blade being loaded externally [26]. This phenomenon can also be envisioned inversely, bolts that experience bending will be loaded more highly than their straight counterparts. Returning to the list of concerns provided by DNV GL, the importance of bolt threads was verified by Kensche and Schultes [27] who found that the forces in the threads of a T-Bolt are proportional to the stress concentrations in the area of contact between the laminate and bushing. Another example of a root specific concern is the pretension in the shaftbolts. The functions of this pretension include avoiding separation between the root and the hub as well as reducing the magnitude of the load oscillations that cause fatigue damage [28]. Consequently, if pretension is lost, the root will face increased fatigue damage, which may be caused by, or lead to, blade-hub separation. This can subsequently lead to catastrophic blade failure. These T-Bolt specific concerns highlight some of the behaviours which must be considered beyond the traditional analysis of bolted joints in both static and fatigue loading.

2.1.3. Fatigue Loading

The many cycles of fatigue loading are analysed through simplified procedures in accordance with the safe life concept. This means using phenomenological models, such as $S-N$ curves and constant life diagrams (CLDs), to describe the gradual reduction of material properties like strength or stiffness [29]. This approach uses the assumption of linear damage accumulation and accounts for the influence of the mean stress effect by using $S-N$ curves for specific R ratios or Goodman diagrams [25]. In fatigue

analysis the R ratio is defined as:

$$R = \frac{\sigma_{min}}{\sigma_{max}} = \frac{\epsilon_{min}}{\epsilon_{max}} \tag{2.1}$$

These relations use previously collected experimental data and are specific to a given material. An example of such a fatigue life calculation can been seen in a study by Marín et al. [30]. Although it references a previous standard, the procedure is the same as in the current DNV GL standard.

To simplify the load series that the blades experience, reduced methods such a rain flow counting (RFC) or Markov matrices are typically used. These methods distill load cycles into blocks of constant amplitude oscillation, and by recording the number of oscillations in each block, but not necessarily the order of the oscillations, the expected loading is simplified and approximated. It should be noted that these fatigue analysis approaches are not directly based on the physical behaviour of the material nor do they include the influence of specific damage inducing events [29], but with the appropriate conservative assumptions and partial load reduction factors, they can still be used for analysis. These methods allow fatigue strength or strain allowables to be predicted, which is advantageous because they can then be applied in the same manner as in static analysis.

In fatigue analysis, particular attention should be paid to delamination failure. This has been identified as the main failure mode during fatigue [31], and it has been documented to induce failure in the blade root [32, 28]. To monitor and study this phenomenon, Salimi-Majd et al. [32] propose the use of cohesive zone modelling (CZM). Meanwhile, Lee et al. [28] point out that the assumptions of FE modelling may not match the conditions of the blade in service, and as a result, it is necessary to incorporate bolt strain measurements into simulations to accurately predict fatigue failure. This latter observation supports the conclusion of Ravikumar et al. [31]: that blade testing is the best way to properly quantify fatigue loads. This further supports the use of full scale testing to ensure blade performance in certification. Fatigue is a significant issue in turbine blades, and represents just one of the potential failure modes that must be considered in root design. The relative criticality of which is dependent of the specific design and loading conditions of the turbine.

2.1.4. Load Profiles

With this discussion of loads, it is informative to consider values from real blades to retain some context. Unfortunately, since the development of off-shore blades is highly proprietary, there are not many published load magnitudes for state-of-the-art wind turbine blades, but some representative values can be found in the Sandia National Laboratories 100 m glass and carbon blade designs by Griffith and Ashwill [14] and Griffith [18], as well as the analysis of a 100 m spar performed by Höyland [33]. Additional estimations can be made by scaling the loads of smaller blades, knowing that the gravitational loads scale roughly cubically with length [16]. In fact, scaling is often used in preliminary estimations of blade loads for novel turbine designs. It should be noted that the value of the scaling exponent is also a function of blade length. Hillmer et al. [34] determined that an exponent of 1.9 was appropriate for blades under 58 m in length whereas one of 2.5 was better for lengths up to 83 m long.

Loads can be scaled from the work of Etemaddar et al. [35] who presented root bending moments due to ice loading for a 60+ m blade, or Lee et al. [28] who calculated bending moments in root bolts during fatigue loading of a 56 m blade. When assuming relationships between the loads on different turbines, or when calculating loads from environmental conditions, it is useful to quantify the reliability of the estimates. Hu et al. [36] developed a method to improve fatigue loading quantification from aerodynamic analysis for this end. The method allows the uncertainty associated with the wind loading inputs to be directly translated to a reliability quantification in fatigue analysis. The presence of assumptions and uncertainties reaffirms the need for load conditions to be individually calculated for each blade and location it may be used.

Due to the differences between blades, the structural design and load calculations must be an iterative process to obtain the most accurate loads possible. To ensure the structural performance of a blade under its anticipated loads, all components of the blade, from root to tip (laminate, bolts, adhesives, add-ons, etc), must be checked against all foreseeable failure modes. As defined in DNV GL [25], this requires checking for fibre failure, inter-fibre failure (IFF), and bolt/insert failure, under the extreme static and fatigue load cases. It is thus essential to have reliable methods to predict these failure modes and corresponding failure loads to guarantee the performance of the wind turbine blade.

2.2. Failure Criteria

This section is devoted to a brief discussion of the some of the many failure theories used in the design and analysis of composite structures, a vast field of study in its own right. Even if the focus of an investigation is specimen behaviour prior to failure, failure theories are elucidatory in describing the way loads develop in a laminate, and one should understand when failure may occur if they want to avoid it, as one would in a SCT. As such, the discussion starts with an introduction before addressing the two largest categories of failure criteria: 2D and 3D criteria in subsections 2.2.1 and 2.2.2 respectively. Lastly, in view of focus of this work, additional discussion is given to the interplay of failure criteria and key features/concerns of the blade root: holes and delaminations (2.2.3).

In order to safely use composite structures, designers must be able to accurately predict their failure. On a component (or macro) scale, a FRP part may be thought of as a homogeneous material, but the distinct phases of the fibres and matrix govern the behaviour of composites up to and beyond failure. The anisotropic nature of composites prevents the application of a simple failure criteria like the von Mises yield criteria commonly used for isotropic metals. There are a variety of failure criteria available for composite materials, however there is not widespread agreement over which are the most accurate and reliable [37]. In some respects, the only agreement is that none of them are truly accurate. The accuracy and effectiveness of different failure criteria have been compared in the World-Wide Failure Exercises (WWFE). The first iteration of which offered a comprehensive comparison of failure criteria for laminates in 2D stress states, and the second and third iterations expanded scope to more complex, 3D stress states [37–39].

These failure theories use the stresses and strains in a structure, as found analytically or computationally, to predict the onset of failure by comparing them to known material properties. The method of this comparison varies greatly between criteria, but the calculation of the stresses and strains is typically done via classical laminated plate theory (CLPT) or FE modelling. CLPT represents the well known analytical approach for calculating stresses and strains based on the ABD matrix of the laminate and the line loads applied to it:

$$\begin{bmatrix} N_x \\ N_y \\ N_{xy} \\ M_x \\ M_y \\ M_{xy} \end{bmatrix} = \begin{bmatrix} A_{11} & A_{12} & A_{16} & B_{11} & B_{12} & B_{16} \\ A_{12} & A_{22} & A_{26} & B_{12} & B_{22} & B_{26} \\ A_{16} & A_{26} & A_{66} & B_{16} & B_{26} & B_{66} \\ B_{11} & B_{12} & B_{16} & D_{11} & D_{12} & D_{16} \\ B_{12} & B_{22} & B_{26} & D_{12} & D_{22} & D_{26} \\ B_{16} & B_{26} & B_{66} & D_{16} & D_{26} & D_{66} \end{bmatrix} \begin{bmatrix} \epsilon_x^\circ \\ \epsilon_y^\circ \\ \gamma_{xy}^\circ \\ \kappa_x \\ \kappa_y \\ \kappa_{xy} \end{bmatrix} \tag{2.2}$$

where the subscripts $x, xy, 26,$ etc represent the direction of the value/property, the superscript $^\circ$ denotes the value at the laminate midline, and the line loads N, M are the forces and moments per unit width of the laminate. This can subsequently be used to obtain the stresses and/or strains in each ply and then assess if the ply will fail under the applied load. It should be noted that this method is limited to predicting the in-plane behaviour of a structure, and it is assumed that the plies are thin enough they do not develop out-of-plane stresses.

In a wind turbine blade the most prevalent load and strain components are the longitudinal ones (along the blade axis) typically denoted as ϵ_x and N_x or ϵ_{11} and N_{11}. Using FE modelling, instead of analytical methods, it is possible to consider 3D stress states, complex 3D geometries, and material non-linearities. This allows for the calculation of out-of-plane shear and normal stresses that are not considered in CLPT. Both of these are found in the root joint, so finite element analysis (FEA) is essential for blade design [26]. Additionally, since FEA calculates the local strains and stresses within a structure, failure criteria can be directly implemented in the program to predict failure for analytically intractable problems.

2.2.1. Two-Dimensional Criteria

Like much of the other initial analysis of composites, the first attempts to determine a yield criteria imitated the approach used for isotropic materials. This spawned the Tsai-Hill criteria, based on an extrapolation of the von Mises criterion to anisotropic materials [40]. From there, a variety of mode independent failure theories were created; of which the most notable is the Tsai-Wu failure criterion,

because despite its short-comings, is still widely used in industry [41]. It is given by:

$$\frac{\sigma_x^2}{X_T X_C} + \frac{\sigma_y^2}{Y_T Y_C} - \sqrt{\frac{1}{X_T X_C Y_T Y_C}}\sigma_x\sigma_y + \left(\frac{1}{X_T} - \frac{1}{X_C}\right)\sigma_x + \left(\frac{1}{Y_T} - \frac{1}{Y_C}\right)\sigma_y + \left(\frac{\tau_{xy}}{S}\right)^2 = e \tag{2.3}$$

where $e \geq 1$ indicates failure. The short-comings of the Tsai-Wu criterion are that it is empirical, does not have a physical basis, and does not distinguish between the different failure modes that can occur in a ply. Nonetheless, the Tsai-Wu method offers a relatively simple criterion that, as Kassapoglou [42] points out, can give excellent predictions in many 2D load states, with the exception of biaxial compression. Other relatively simple criteria include the maximum stress and maximum strain theories, in which the stress or strain in each ply is compared to the stress/strain at failure in principal coordinates. For example, with the maximum strain criterion, the strain in each principal direction is compared to the strain at failure under uniaxial loading:

$$\begin{array}{l|l|l} \dfrac{|\epsilon_x|}{\epsilon_{x,C}^{ult}} = 1, \quad \epsilon_x < 0 & \dfrac{|\epsilon_y|}{\epsilon_{y,C}} = 1, \quad \epsilon_y < 0 & \dfrac{|\gamma_{xy}|}{\gamma_{xy}^{ult}}, \quad \forall\ \gamma_{xy} \\ \dfrac{|\epsilon_x|}{\epsilon_{x,T}^{ult}} = 1, \quad \epsilon_x > 0 & \dfrac{|\epsilon_y|}{\epsilon_{y,T}^{ult}} = 1, \quad \epsilon_y > 0 & \end{array} \tag{2.4}$$

where superscript ult denotes the strain at failure and subscript T, C denotes tension and compression respectively. While the maximum stress/strain criteria do offer some distinction between fibre and matrix dominated properties (the x and y directions respectively), they cannot consider the effects of combined loading like the Tsai-Wu theory does. Despite accuracies within 10% only 40% of the time [38], the max stress/strain methods are still used frequently in industrial applications. The distinct fibre and matrix phases present in composite materials have vastly different mechanical properties, and as a result they fail through distinctly different mechanisms. Much of the investigation into failure theories is not just predicting the onset of failure but progressive damage analysis beyond this point, for which mode dependent failure criteria are required.

The majority of commonly used failure theories are mode dependent, as they offer a more physically grounded explanation of what is happening in the material. One of the first theories developed in this area was developed by Hashin [43], who made distinctions between tensile and compressive failure for both the fibres and the matrix. Naturally, a variety of theories emerged from there with varying degrees of physical basis and complexity. Many of these different theories were compared in the first edition of the WWFE [37]. Comparing many different load cases, this study ultimately found that the failure predictions of five criteria, those of: Puck, Zinoviev, Tsai, Cuntze and Bogetti, gave promising results [37]. The Tsai method is based upon the Tsai-Wu failure criterion, and despite its empirical basis, it was still found to predict in-plane failure fairly well. Puck's criteria is based upon a fracture plane concept that garners weight and validity due to its physical basis in addition to its good predictions. This was as noted by Kaddour et al. [37] and is further supported by its inclusion in the development of LaRC03 failure criterion by Dávila et al. [44]. Not included in the WWFE I, the LaRC03 criterion, built upon the work of Puck along with Hashin, Sun, and others (see [44]). Puck and LaRC03 represent strength based failure criteria, both of which can be integrated into FE modelling, allowing the analysis of the complex stress states found in wind turbine blades. The accuracy and physical basis of these two failure criteria [45], that is the ability to predict, and distinguish between, multiple failure modes including inter-fibre failure (IFF), are why they are recommended for use in wind turbine design by DNV GL [25].

2.2.2. Three-Dimensional Criteria

The criteria discussed so far deal with 2D stress states, but when dealing with thick laminates and holes for T-Bolts or adhesive inserts, like at the blade root, 3D stress states arise. The WWFE I identified this gap and organized a follow up effort, the WWFE II, to investigate failure theories that were expanded to three-dimensional problems under a variety of test cases. Organized by Kaddour and Hinton [46], the WWFE II features theories from many of the same authors. The outcomes of the exercise feature some discussions on the relative merits of relying more or less heavily on empirical constants that must be obtained through physical tests. In short, it was found that the better predictions required separate, physical tests to find non-standard, material constants that in turn increased the accuracy of their numerical predictions.

Ultimately, the WWFE II did find that the better three-dimensional failure theories are capable of making predictions that have good agreement with test results. Due to the complexity of the three-dimensional stress strates, some of the participants in the WWFE II integrated the finite element method (FEM) into their predictions: notably the theories of Puck [47] and Pinho [48]. For the specific details and implementations of these failure theories, the reader is referred to their respective author's work. This is encouraging because as previously mentioned, FEA is frequently used in industry: in fact the DNV GL guidelines specifically recommend Puck's theory for predicting IFF [25]. Subsequently, the accuracy and ease integration of failure theories into FEA is advantageous for blade designers.

2.2.3. Additional Concerns: Holes and Delaminations

Despite the successes of the WWFE II, there are remain a couple of phenomena in the blade root that are not considered: for example delaminations and the stress states around holes. These additional concerns have been shown to display complexities that are not well addressed through 3D failure criteria. Failure predictions for open hole tension (OHT) and delaminations are both included in WWFE-III, although the results of the study are not yet available [39]. The importance of anlaysing structures with holes is self-apparent with T-Bolt root designs, but delamination analysis is also important as bearing loads frequently induce delaminations. Furthermore, as shown by Lee et al. [28], when delaminations occur in the blade root, they can cause failure during fatigue loading. Delaminations are an out-of-plane failure mechanism where plies separate along their interfaces, and they can be predicted by a variety methods. These include the relatively simple maximum stress criteria, the quadratic formulation of Hashin [43] and others: many of which are discussed by Orifici et al. [41]. It has been shown that ply blocking, and the magnitude of change in fibre orientation between layers, both influence the onset of delaminations [49]. These factors are typically not addressed through 3D failure criteria. Delaminations are common in both adhesive and bolted joints, and some of the best methods to predict them are CZM and the extended finite element method (XFEM). For a detailed discussion of these methods, the reader is referred to Section 2.3.3. Prior to that, the analysis of the other key phenomenon, namely holes, is addressed.

When analysing composite laminates with holes, it is necessary to consider the influences of stress concentrations and notch sensitivity. Much like metals, composites display stress concentrations at the edges of holes, but their magnitude is a function not only of geometry, but also layup. Lagace [51] demonstrated that composites behave somewhere in between notch sensitive and insensitive materials. This means that composites have a limited ability to redistribute load around holes. Their resulting behaviour can be explained with the aid of Figure 2.5. This plot compares the failure stress, σ, of OHT

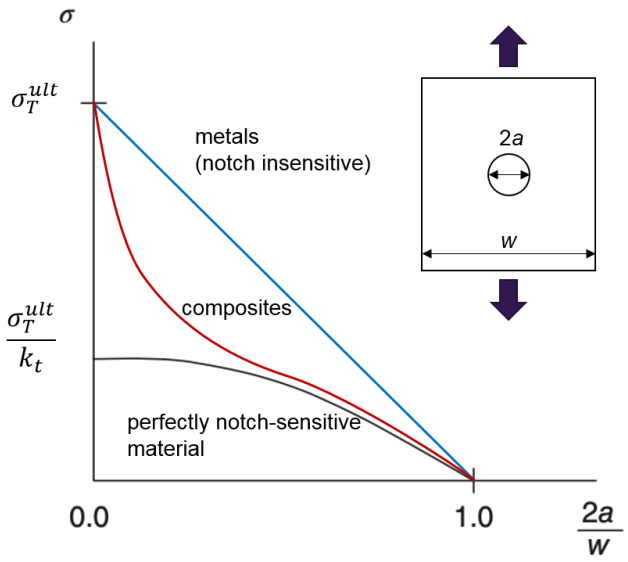

Figure 2.5: Failure stress as a function of hole size for OHT specimens, adapted from Kassapoglou [50].

specimens with varying hole sizes (various $2a/w$ values on the x axis) for different materials. Metals yield and thus can completely redistribute load around the hole in the specimen allowing the specimen to reach a total load of

$$F = \sigma_T^{ult} (w - 2a) t \tag{2.5}$$

where σ_T^{ult} is the ultimate tensile strength of the material without a hole and t is the specimen thickness. In other words, the specimen does not fail until the stress in the net-section (minimum width of material) reaches the pristine strength. This occurs because material at the hole edge deforms transferring load to the adjacent material. This is derived from the ductility of metals.

By contrast, perfectly notch sensitive materials (think glass and ceramics), are entirely incapable of deformation to redistribute load. As a result they fail when the stress concentration factor (SCF) k_t causes the stress at the hole edge to reach the pristine strength of the material. As a result these materials fail suddenly when the local stress $\sigma = \sigma_T^{ult}/k_t$ as shown in Figure 2.5. Since composites have a limited degree of load distribution, their failure stresses lie in between the metals and ceramics. As seen, they initially (at small hole sizes) behave in a somewhat notch insensitive manner, before approaching a more notch sensitive behaviour at larger hole sizes. With some degree of load redistribution, it is unknown at what load, or local stress/strain level, a composite with holes will fail.

To account for this, Whitney and Nuismer [52] proposed the average and point stress criteria for predicting failure around holes: the stress around a hole is either averaged over or calculated at a characteristic distance a_0 or d_0 and then compared to the material failure strength. These distances are shown in Figure 2.6. The Whitney Nuismer method assumes that the material is fully notch sensitive, and that when the stress in the material, at/over the characteristic distance, is equal to the pristine strength, failure occurs. Mathematically, that means failure occurs when

$$\sigma^{ult} = \begin{cases} k_t \overline{\sigma} \, (r = [0, a_0]) & \text{average stress method} \\ k_t \sigma \, (r = d_0) & \text{point stress method} \end{cases} \tag{2.6}$$

Note, r is defined as 0 starting from the hole edge, not the center of the hole. Through material testing the values of a_0 and d_0 can be calculated for further calculations, creating a semi-empirical method much like the previously mentioned failure theories.

The Whitney Nuismer method has been improved and built upon in many subsequent analysis methods. A similar approach was proposed by Garbo and Ogonowski [53], which not only addresses unloaded holes, but bolted joints as well. This is the well known Bolted Joint Stress Field Method (BJSFM): a computational method producing good, semi-analytical results for stress distributions around open and loaded holes [54]. It is worth noting that the BJSFM, unlike modern FEA, does have geometric limitations: namely the width-to-diameter and end distance-to-diameter ratios must be greater than 4 and 3 respectively [54]. The stresses obtained from this method can be analysed using any of the previously mentioned failure criteria. Ultimately, these (semi-) analytical methods for analysing stresses around holes formed the foundation of the analysis of bolted joints, which feature the same geometry but the adding complexity of bearing loads since the holes are now filled.

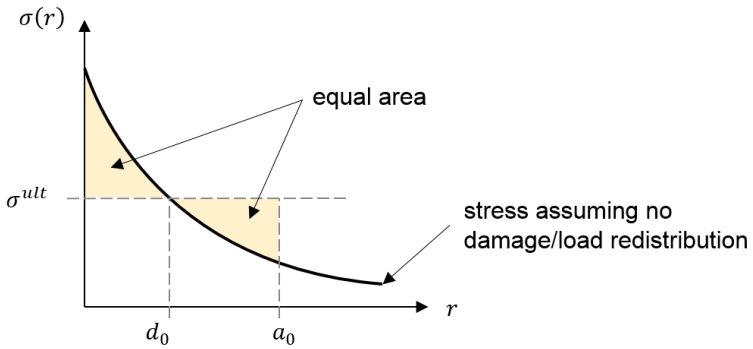

Figure 2.6: Stress as a function of radial distance from hole edge, r, with average and point characteristic distances a_0, d_0.

2.3. Bolted Joints

The crux of blade root design is the incorporation of the fasteners that connect it to the hub. Whether T-Bolts or root inserts are used, discontinuities and their subsequent stress concentrations are introduced into the root laminate. The designer must understand their effect to ensure that the strength of the joint can be accurately predicted. Much like the analysis of composite laminates, predicting the strength of composite joints was initially done with analytical methods. Analytically, adhesive and bolted joints require fundamentally different approaches due to their different geometries and constituents, however as will be shown, when employing FEM many of the same techniques can be used for both joint types. The initial analysis of bolted joints was 2D and the majority of analysis methods for adhesive joints are still two-dimensional [55]. However, as pointed out by Camanho and Matthews [56], 3D analysis is necessary due to the inter-laminar stresses that develop at the edge of holes due to the stress free condition and the mechanics of bearing failure. Furthermore, the blade root has an inherently 3D geometry making 2D analysis fundamentally inaccurate for both T-Bolts and bonded inserts.

This section discusses the design and analysis of bolted joints in five subsections. The presence of holes bolts adds additional failure modes to composite structures, and these are discused in subsection 2.3.1. It is essential to consider all failure modes when analysing joints, and an overview of the different analysis methods used in bolted joints is given in subsection 2.3.2. A brief aside is then given for a description of the extensive capabilities of the advanced FE analysis methods CZM and XFEM (2.3.3). The colloquialism “where there is one, there are many” typically applies to bolts used in large structures, and it certainly applies to the blade root. Therefore, the discussion of analysis methods is expanded to multi-bolt joints and the behaviours of interacting holes (2.3.4). To complete the overview, some additional factors in bolted joint design, such as bolt-hole clearance and laminate stacking effects, are considered in subsection 2.3.5.

The vast majority of work on bolted joints has focused generic types of joints such as lap and strap joints. Examples of detailed reviews of the mechanics and analysis of these joints can be found in the works of Camanho and Matthews [56] and Thoppul et al. [26]. Although T-Bolts have received notably less attention and research, studies do exist, for example those of Kensche and Schultes [27], Martínez et al. [57], and Briggs et al. [17]. These studies demonstrate that the complex geometry of T-Bolts requires some additional consideration beyond those of classical bolted joints. Nonetheless, the cross-nut of T-Bolt takes bearing loads much like a traditional bolt, it just lacks the ability to be tightened through the thickness of the laminate. Subsequently, much can, and must, be gained from the knowledge of traditional joints.

2.3.1. Failure Modes

In a T-Bolt it is important to consider failure in both the shaftbolt and the bushing (also called the axial screw and the cross-nut respectively). In fact, some T-Bolt connections are designed such that the first element that fails is the shaftbolt [57]. In addition to failure in the T-Bolt (the shaftbolt, bushing, and their connection), failure may also occur in the laminate through one of the failure modes illustrated in Figure 2.7: net tension, shear-out, bearing, tear-out, and cleavage. While a bolted joint can also fail through pull-out, this is generally more of an issue with counter-sunk fasteners and thin laminates [56]. Here, pull-out refers to the bolt, including its head and nut, moving completely through the laminate

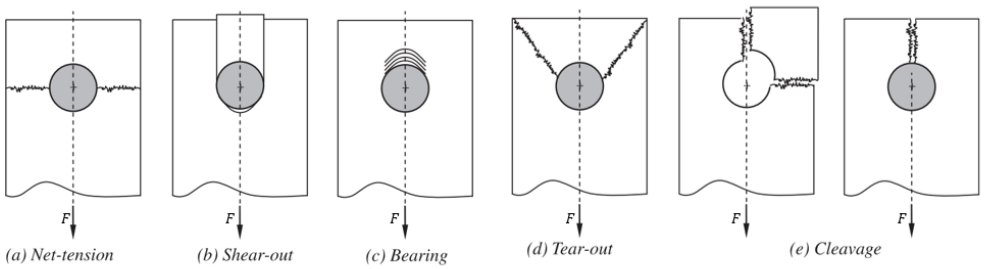

Figure 2.7: Failure modes for pin loaded joints from Pisano and Fuschi [58].

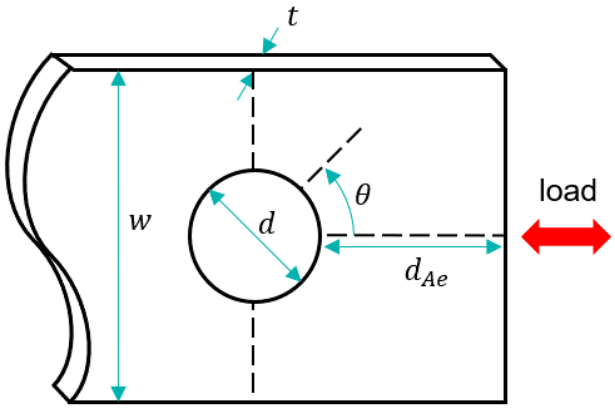

Figure 2.8: Schematic of pin loaded joint with key geometric parameters.

(into or out of the page in Figure 2.7) leading to separation of the joint. Given the presence of the shaftbolt and the thickness of the root laminate, this failure mode is highly unlikely in a blade root using T-Bolts. Of the failure modes presented in Figure 2.7, bearing failure is the only one that does not occur suddenly. Tear-out and cleavage failure do not occur until after bearing failure: they are secondary and mixed failure modes [26]. Of the remaining two failure modes, net-tension and shear-out, the latter is more difficult to predict due to the complex stress state under which it occurs. In many applications, joints are designed to fail in bearing first, as it avoids catastrophic failure and leads to a more efficient joint [57]. Each failure mode has an associated failure plane, in which the critical stresses that lead to failure occur. Through an analysis of these failure planes, the failure mode can be predicted.

Which failure mode is most likely to occur is a function of joint geometry, specifically the hole diameter d, edge distance d_{Ae}, laminate thickness t, and the specimen width w, which are defined in Figure 2.8. There is consensus that net-tension failure occurs at low w/d ratios, bearing failure occurs at high w/d ratios, and shear-out failure occurs at low d_{Ae}/d ratios [56, 58]. Subsequently, design recommendations and analysis methods commonly give minimum w/d and e/d values to avoid net-tension and shear-out failure [54]. The position around the hole where failure occurs (defining the failure plane) is also denoted by θ, where θ is measured counter clockwise from the axis of load application (as shown in Figure 2.8). In addition to visual detection, the failure mode can be determined by location of the failure plane: bearing failure occurs at $0° \leq |\theta| \leq 15°$, shear-out at $30° \leq |\theta| \leq 60°$, and net-tension at $75° \leq |\theta| \leq 90°$ [59]. Values in between these ranges indicate uncertainty or mixed-mode failures.

These geometry ratios, and their recommended values, are based upon traditional single or double bolted lap joints, and cannot be applied to the letter for joints with T-Bolts. For example, the removal of material for the axial screw changes the behaviour of a joint with T-Bolts compared to a standard lap joint. Briggs et al. [17] state that greater d_{Ae}/d ratios are required due to reduced shear area while Martínez et al. [57] states that at a given d_{Ae}/d shear failure is less likely due to the same removal of material. Other differences include the consideration of not just the bushing diameter d_b, but also the diameter of the shaftbolt d_{sb}. A ratio of $d_b/d_{sb} = 2$ is commonly recommended [17]. Finally, in a root joint the parameter w, does not represent the specimen width but instead the spacing between holes. This parameter is very important in root design as it is closely related to the bolt packing density and the root capacity [57]. These topics are elaborated on in Section 2.4, but the packing density is a measure of the number of bolts/inserts around the root circumference, or inversely the spacing between these elements [15]. It is evident that T-Bolts are not as well understood as traditional bolts are, so design guidelines and analysis methods specific to T-Bolts are lacking, and thus they must be adapted from traditional bolts.

2.3.2. Analysis Methods

The analysis of bolted joints is similar to that of laminates with holes. The main components are the determination of the stresses around the joint and then the application of some failure criteria; both of which can be done analytically or via FE modelling. One of the first analytical solutions was presented by de Jong [60], who built upon Lekhnitskii's work on stress concentration factors in anisotropic materials, to solve the stress distribution around a pin loaded hole. In bolted joints, the bolt is often generalized as a pin, allowing the analysis to cover joints with bolts, lugs, or other cylindrical bearing components (like a T-Bolt). There were many factors not considered in this first analysis, but they were added in subsequent investigations. For example, the influence of friction between the pin and the laminate as well as the effects of pin elasticity were investigated by Hyer et al. [61], who found that the inclusion of frictional effects is essential, while pin elasticity only has minor impact on the predicted stresses. To further improve the analysis, and particularly to simulate contact between the bolt and the laminate, it is necessary to use FE modelling [56]. In this manner, Serabian [62] showed the importance of material non-linearity in modelling the shear behaviour of pin loaded joints, especially with low spacing between holes and high load levels. Garbo and Ogonowski [53] developed an analytical method that can calculate the load distributions around bolts for geometries with $w/d \geq 4$ and $d_{Ae}/d \geq 3$. The BJSFM has retained relevance because its approximate results are fairly accurate and can be computed quickly [54]. Regardless of which method is used to obtain the stresses in a joint, the stresses still must be translated in a strength prediction.

From the stresses around a bolted joint, some form of failure criteria must be used to predict the joint's strength. An aside should be made at this point to acknowledge that there is some disagreement over at what point a bolted joint should be considered failed: it is mostly commonly defined by the hole deformation percentage (often 2% or 4%) or by the location of the first non-linearity in the stress strain curve [56, 26]. One of the simplest ways to predict failure would be to apply a failure criteria in the same manner as a laminate without holes or bolts. This approach was taken by Tserpes et al. [63], where it was found that using the 3D Hashin criteria under predicted the strength of joints, so the authors used the maximum stress criteria instead. High shear stresses at the edge of the bolt at $\theta = 45°$ were causing the premature failures with the Hashin criteria, which the authors noted is common [63]. Parallels can be drawn between this and the Whitney Nuismer method: in both cases failure did not occur when the stresses on the hole edge reached the failure strength of the laminate, but instead at a higher load.

To overcome this issue, Chang et al. [64] proposed expanding on the Whitney Nusimer point stress method. It was proposed that characteristic distance depended on the failure mode, specifically that the characteristic distance for net-tension failure was smaller than bearing failure. To account for this they proposed a characteristic curve that varied the characteristic distance around the hole as a function of θ. Then, by applying a failure criteria at each point along the curve, both the failure load and failure mode could be predicted. Although any failure criterion can be used with this method, the authors originally used the Yamada-Sun failure criteria [65], given by

$$\left(\frac{\sigma_x}{X_T}\right)^2 + \left(\frac{\tau_{xy}}{S_c}\right)^2 = e^2 \tag{2.7}$$

where $e \geq 1$ denotes failure, and S_c is the measured shear strength for a symmetric, cross-ply laminate with the same number of plies as the laminate being analysed. The characteristic curve was defined as

$$r_c(\theta) = r + d_{0T} + (d_{0C} - d_{0T})\cos\theta, \quad -90° \leq \theta \leq 90° \tag{2.8}$$

where r is the radius of the hole, and d_{0T}, d_{0C} are the characteristic distances in tension and compression, representing net section and bearing failure respectively [64]. As in the Whitney Nuismer method, these characteristic distances must be determined experimentally. The method is applied by iteratively increasing the load, whereupon the first value of $e \geq 1$ obtained along the curve defines the strength of the joint, and the value of θ at that point defines the failure mode, using the ranges given in Section 2.3.1 and shown in Figure 2.9. This method was found to make good predictions achieving better results (within $\pm$10% of experimental values) then previous methods [64]. The accuracy of this method is further demonstrated by its inclusion in the bolted joint design methodology from Camanho and Lambert [54]: the stresses in the laminate were evaluated using both stresses at the characteristic curve and average stresses and then the LaRC04 failure criteria was used.

Further work on the characteristic concept was performed by Zhang et al. [59] who expanded Chang's characteristic curve to also incorporate a characteristic distance for shear failure to address

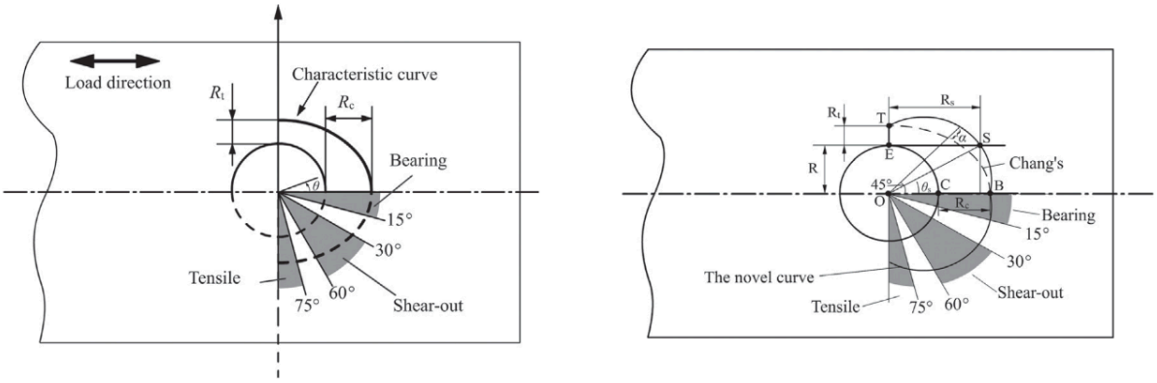

Figure 2.9: Comparison between the characteristic curve proposed by Chang et al. [64] (left) and the improved curve proposed by Zhang et al. [59] (right). Graphics from Zhang et al. [59].

the incorrect failure mode predictions found by Kweon et al. [66]. The revised curve was modified to pass through the shear-out plane, and it is shown in Figure 2.9 alongside the original curve proposed by Chang et al. [64]. Note the variables used in this visualization differ from (2.8), as the latter uses d instead of R for characteristic distances to imitate the notation of Whitney and Nuismer [52]. The novel curve is defined as

$$r_c(\theta) = r + d_{0T} + (d_{0C} - d_{0T})\cos\theta + 2\alpha|\sin\theta|\cos\theta, \quad -90° \leq \theta \leq 90° \tag{2.9}$$

Where α is a non-dimensional parameter that incorporates the characteristic shear distance (for full definition see [59]). It was found that including the characteristic shear distance in this method improved joint strength predictions [59]. It should be noted that other modifications of the characteristic curve method also exist [56]. All of these methods represent stress based approaches, which are the most common, but not the only, approaches used. Alternatives include the fracture mechanics and boundary element methods (BEM).

Fracture mechanics methods are based upon considering the bolt hole as a crack in the material. To prove the joint has adequate strength, it is necessary to show that the energy required to grow the crack is higher than the energy applied by loading [25]. Originating from metals, these methods are also commonly used in fatigue analysis as they deal with crack growth. An example of the application of fracture mechanics to bolted joints can be seen in the work of Schulz et al. [67]. While their predictions were found to be accurate for some laminates, they were not accurate for laminates with a large percentage of $\pm 45°$ plies, which Camanho and Lambert [54] attributed to the inability of linear elastic fracture mechanics (LEFM) to capture non-linear material behaviour. This is important, because a higher percentage of off-axis fibres are required to strengthen laminates around holes, and LEFM cannot accurately predict the strength of these common laminates. Subsequently, fracture mechanics approaches are not commonly used in bolted joint analysis.

A final approach that has seen some attention is the BEM, which can be used as an alternative to the FEM for calculating stresses around bolts. This method discretizes only the interface between the bolt and the laminate which, compared to 3D FEA, reduces the dimensionality of the problem [68]. As a result, Zhang [69] found that this method can reduce the time required for analysis. Additionally, as demonstrated by Lie et al. [70], this approach can also be expanded to multiple bolted joints by use of a one dimensional spring concept. In the application of these methods, the stresses at the edges of the holes may be over-predicted, and consequently the stresses must be evaluated at a distance [69]. The BEM has been shown to account for the effects of friction and clearance around bolt holes, giving good predictions of joint strength [71, 70]. Despite the reported successes of the method, Pan et al. [68] point out that since the interfaces between each ply must be discretized, the method leads to large systems of equations, which may limit its computational advantages. This may be why the FEM is more commonly used.

2.3.3. CZM and XFEM

Many of the complex 3D stress states in bolted joints necessitate the use of FE modelling. Furthermore, advances in this field have introduced new ways to study the contribution of these stress states to failure modes such as delamination and matrix cracking. These are especially important in bonded joints, but are also common in bolted joints since the drilling of composite parts often creates delaminations. As these failure modes initiate and grow, they form separations within the laminate. Accounting for this separation in analysis is very challenging, but two prevalent methods have emerged that can address the issue: CZM and XFEM. As previously mentioned, CZM and XFEM are also commonly used in fatigue analysis to monitor crack growth. Both methods are based upon fracture mechanics, but they do not suffer from the same shortcomings that LEFM typically does. Each method represents an advanced and focused field of study within computational mechanics, which is not the focus of this project. Therefore, they are discussed here only briefly, providing a brief background of their governing concepts and how they can be applied.

Despite being based upon fracture mechanics methods, neither CZM nor XFEM require the presence of an initial crack. The use of CZM is well established in literature, especially for the analysis of adhesive joints [72]. This approach uses zero thickness cohesive zone elements (CZEs) inserted at the interfaces between elements along which the variable stiffness and separation of the adhesive can be modelled. A set traction-separation law (for example a Benzeggagh-Kenane interaction law) is used in combination with a damage parameter allowing for discontinuities such as cracks, delaminations, and dis-bonding to be modelled [29]. Disbonding (previously mentioned as cohesive failure) can be considered a delamination between layers of different materials. CZM does not require re-meshing to predict discontinuity growth, however it does require that CZEs be inserted along the growth path. As a result, CZM cannot predict mixed mode failures, for example when a crack jumps from an interface into the adherend [73]. Consequently, CZM requires that the crack or delamination path be known before hand. While some crack or delamination paths may be assumed in adhesive joints [74], not all possibilities can be known, especially not those in the adherend. This becomes particularly relevant when applying CZM beyond adhesive joints, as CZEs must be inserted along *every potential* crack path that is to be investigated.

An alternative approach, that allows discontinuities to grow in arbitrary directions is XFEM. Through this method, mixed-mode failures can be predicted [73]. XFEM employs phantom nodes and enrichment functions to split any XFEM element into two separate elements along an arbitrary crack path. Consider a four node quadrilateral element: once its material fails, damage can progress through the element and a material softening law is used to model the material behaviour [72]. XFEM and CZM both use fracture mechanics concepts to predict the initiation and growth of cracks, but XFEM uses bulk material properties, such as the mode dependent fracture toughnesses G_{Ic}, G_{IIc}, and G_{IIIc}, whereas CZM uses traction-separation laws [74]. It is noted that both methods allow for specific failure criteria to be defined for damage initiation, for example van Dongen et al. implemented the Puck failure criteria with XFEM [45]. Ahmad et al. [75] used XFEM to predict the experimental bearing strength of bolted joints, over a range of conditions, with an accuracy of between 9.6% and 20%. On the other hand, Ataş and Soutis [76] used CZM to predict the strength of bolted joints to within 21% and 10% for cross-ply and quasi-isotropic laminates respectively. Clearly, these approaches offer accurate design capabilities. Their ability to model and account for complex three dimensional stresses and failure mechanisms make them valuable tools for predicting the strength of a wind turbine blade root.

2.3.4. Multi-bolt Joints and Hole Interactions

It is known that when holes come too close together in a structure, their stress fields can interact leading to amplified local stresses. Obviously this is problematic: it defines the maximum packing density of the blade root. Furthermore, as long as this density is not exceeded, the root can be, and typically is, analysed as a repeating unit of a single bolt in an infinite laminate, and all of the previously discussed methods are applicable [15]. It is with this philosophy that design guidelines – which it should be noted are based on joints that are much more representative of lap joints than T-Bolt connections – converged on a recommended spacing between of 4 and 5 hole diameters between bolts. Experimental work by Soutis et al. [77] and Xu et al. [78] has verified these recommendations. If designers reduce the spacing in multi-bolt joints below these guidelines, they need to understand how the stresses around each bolt will interact.

Since most joints in real world structures contain more than one bolt, there are many studies that

have researched how to optimize multi-bolt joints. Persson and Eriksson [79] performed a parametric study on multi-bolt joints and found that the most important factors, in the joint's load capacity, are the ratios of hole diameter to hole spacing (directly related to packing density) and hole diameter to laminate thickness. This study only varied the spacing in the width direction in a single row of bolts and not the spacing between rows. Other investigations have also found that load distribution varies per bolt across: a single row of bolts [80] and between each row of bolts [81]. Therefore, the work of Persson and Eriksson [79] may not have considered all relevant parameters in multi-bolted joints. Chutima and Blackie [82] found the optimal spacing of bolt rows and edge distances in a double lap joint to be twice the bolt diameter. This study also recommended picking the bolt spacing, then the bolt diameter, to minimize the net-tension stress at the hole boundary, as this stress concentration from one bolt may interact with another. These studies all give recommendations on how to design multi-bolted joints, but they do not specifically describe the stress states around the bolts.

Modelling the stresses around each bolt in a multi-bolted joint is closely related to the presence of stress concentrations. These were solved analytically by de Jong [83], but this solution included many simplifications that limit its use in modern designs. Once again, this emphasizes the need for FE modelling in determining the stress states around the bolt without excessive simplification. McCarthy et al. [84] demonstrated the ability of non-linear 3D FE modelling to accurately predict the behaviour of multi-bolted, single lap joints up to the onset of damage. Furthermore, Zhang et al. [59] showed that in combination with FE modelling, their improved characteristic curve could predict failure in multi-bolt joints. These results imply that some degree of stress interaction may be acceptable, challenging the conservative nature of most design recommendations. This topic warrants further investigation, and FE modelling has been shown to be the ideal method to investigate the interaction of these stresses.

One tool for improving the load capacity of the blade root is to increase the packing density of bolts. In a recent study, Solis et al. [86] found that there is little literature investigating the effects of offsets on hole stress field interactions, a trend that carries over into root packing density. It is suspected that this is due to designer's tendencies of conservatism and the proprietary nature of wind turbine blades. The potential for spacing holes at a $\theta = 45°$ offset to increase packing density in traditional joints was first mentioned by Soutis et al. [77], and a similar concept was proposed for the root joint by Doorenspleet et al. [87]. The logic behind this proposal is that, of the stress components along the circumference of the bolt-hole, τ_{xy} is at a maximum in this region while σ_x and σ_y are near zero, as shown by Pradhan and Ramesh Babu [85] in Figure 2.10. Ubaid et al. [88] also investigated the subject of staggered holes, but the specimens they used were troubled by finite-width effects, and as a result, did not yield useful results. Solis et al. [86] successfully applied a finite element approach to predict interacting stresses between two, side-by-side holes. Unfortunately, this work adds only a limited amount of knowledge to the subject, as it only considered holes placed side by side and with low spacings (1.1 to 1.5 hole diameters). It may be possible to reduce the hole spacing to bolt diameter ratio below the tradition

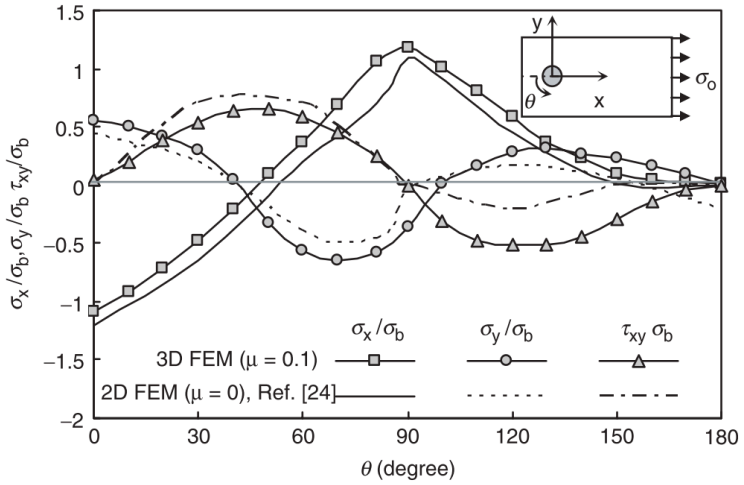

Figure 2.10: Normalized stresses by component as a function of angle around the edge a pin loaded hole, found by [85].

guideline of $w/d \geq 5$; however, the spacing investigated by Solis et al. [86] is probably too small to be feasible in any real structure. Ultimately these investigations show that the interaction of stresses from multiple holes, especially those not side-by-side, has not been fully explored.

2.3.5. Additional Design Considerations

Thus far, many effects of geometrical parameters like the ratios d_{Ae}/d and w/d have been discussed, but additional factors that have been documented to influence the strength of bolted joints, for example the effects of pin clearance/interference fits and bolt clamp force, remain unmentioned. The latter has not been discussed as T-Bolts do not have a head and nut that can be torqued to improve joint strength; however, the shaftbolt of T-Bolts is typically pretensioned, creating similar effects. Lee et al. [28] found that a separation between the blade root and the hub, even as little as 0.77 mm, can lead to the failure of a blade at the root, emphasizing the need for adequate pretension in the joint. Another geometrical parameter effecting the performance of bolted joints is the clearance/interference between the bolt (in a T-Bolt this would be the bushing) and surrounding laminate.

Clearance denotes that the bolt diameter is smaller than the hole diameter, thus leaving empty space between the bolt and laminate, whereas interference describes the opposite: the bolt has a larger diameter than the hole and thus creates compression in the surrounding laminate. McCarthy and McCarthy [89] found that the presence of clearance decreases the stiffness of bolted joints. From these (and further) findings, it is widely agreed that clearance should be avoided. On the other hand, a study by Wei et al. [90] found that interference fits can improve the fatigue life of bolted double-lap joints. They found that as the peak-to-peak amplitude of the fatigue oscillations was increased, the most beneficial interference fit changed from a 3.0% to 1.8% interference where the percentage indicates the relative size of the bolt diameter compared to the hole diameter. This finding was confirmed by Pradhan and Ramesh Babu [85], who found that interference fits improved both static and fatigue strength. While this may improve performance for a traditional joint, no literature was found describing hole the material around the shaftbolt hole would behave under an interference fit. Nonetheless, it is clear that structural performance will be influenced by the tolerance between the bushing and bushing-hole diameters. Furthermore, this behaviour is likely dependent on the composition of the laminate itself.

The behaviour of a composite laminate with a hole is highly dependent on stacking sequence, and thus considerable research has gone into optimizing layups for bolted joints. This can be seen by examining the SCF as a function of layup, as shown in Figure 2.11. This plot shows the theoretical SCF for laminates with varying ratios of $\pm 45°$ to $0°$ fibres. Note, these calculations (performed using formulas from Kassapoglou [50]) do not consider the order in which these fibres are placed through the thickness. From this plot, it can be seen that the addition of $\pm 45°$ fibres around holes reduces the

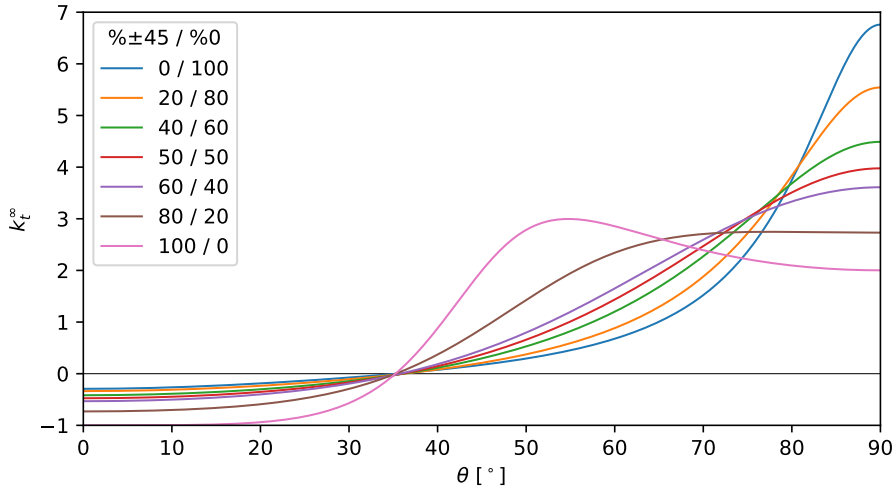

Figure 2.11: Stress concentration factor as a function of position around a hole for various triaxial layups.

maximum SCF, because they are better able to transfer load around the bolt compared to $0°$ or $90°$ fibres. While the presence of $\pm 45°$ fibres reduces the impact of the hole, it also reduces the stiffness of the laminate, so a balance must be achieved.

Another key factor in the layup is the presence of $90°$ fibres at the surface of the laminate, which can significantly improve bearing strength [91, 17]. While other fibre orientations are possible, they have not been found to offer significant benefit for use around holes, thus typical root layups are typically a balance of $0°$ and $\pm 45°$ fibres as seen in the design from Griffith and Ashwill [14]. A final consideration with regards to the stacking sequence is which plies will display the highest stresses. Just as a high percentage of $0°$ plies will increase the stress concentration, Solis et al. [86] showed that the highest stresses between two side by side holes occur in the $0°$ plies. In a T-Bolt, this may become important in the positioning of the shaftbolt hole: for example, it may be beneficial to move these critical plies away from the exposed top of the shaftbolt hole. This may also present a reason to use fabric reinforcement as the $0°$ fibres are not concentrated together but instead distributed amongst the $\pm 45°$ fibres. The exact stresses and stacking sequences of a structure will certainly require some adjustment, but these findings are useful to provide guidelines for the design of bolted joints.

2.4. Applied Root Design

Newly released blades and turbines feature growing blade lengths, often featuring competitions between companies to design and build the longest blades. This requires technical innovations in all areas of the blade including the root. As demonstrated this leads to a relative lack of literature on root design, so those not privy to industry knowledge must draw upon learnings from different applications. This section is dedicated to specifically discuss how the many considerations of wind turbine blade and composite design and analysis apply specifically to the blade root. First, some of the key decisions in root design, and their trade-offs, are presented and discussed in subsection 2.4.1. Considering the role that testing has in certification and design, there is a push to develop and incorporate more testing at the subcomponent level into the design process. Furthermore, this project requires testing to validate its findings, and therefore the philosophy behind SCTs and an overview of existing SCT methods that have been developed is given in subsection 2.4.2. Following these discussions of previous findings, the discussion shifts to the current research project. The main questions that this research endeavours to answer are presented as a conclusion to the chapter in subsection 2.4.3.

2.4.1. Key Design Focuses

Regardless of which fasteners are used, it is in a blade manufacturers best interest to maximize the load capacity of the root joint. The main way of increasing the root capacity is by increasing the packing density of bolts/inserts in the root [92]. Comparing the two fasteners, T-Bolts require drilling two holes in the blade root for the shaftbolt and the bushing, while root inserts may or may not require a hole depending on if they are bonded or cast into the laminate. The bushing of the T-Bolt creates a pin loaded joint, inducing stress concentrations and creating bearing stresses in the laminate. Compared to materials like metals, composite laminates have relatively weak bearing strengths and care must be given to layup design around the pin loaded hole. Despite this, T-Bolts are commonly used as they are lower cost compared to bonded inserts and allow for easy inspection/replacement [15, 49]. In contrast, root inserts rely upon shear for load transfer, and still may induce stress concentrations at their tips [15]. Furthermore, long insert lengths are required to avoid pull-out failure, and there are many challenges in predicting adhesive bond failure, and thus inserts require testing for certification [25].

Governed by structural concerns, the blade root is circular in cross-section and typically features an (initially) uniform thickness. The high, uniform thickness in the region of the T-Bolts or inserts is to maximize bearing or shear transfer area around the fasteners and provide high bending resistance. As previously mentioned, the root laminate is often composed of triaxial fibre reinforcement, which is different from the shell. To aid in curing this region, often precast root segments are used, and to incorporate these, the laminate must transition from the thick triax layup towards thinner shell laminates in the outboard blade. Often this involves covering the root segments with a shell laminate as shown in Figure 2.12. This schematic shows an end view (from the hub looking tip-wards) and a cross section of a representative root design showing both T-Bolt and insert configurations. The end view shows some of the various methods in which the root segments can be designed and installed: some designs propose individual sections for each bolt [93] while others incorporate many bolts into larger section

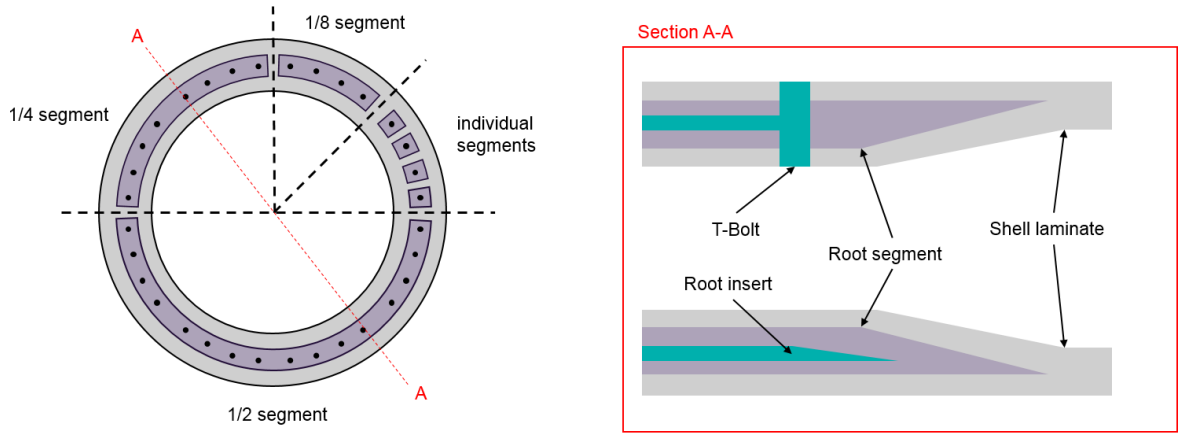

Figure 2.12: Left: end view of a blade root with various root segment widths. Right: root cross section showing a design using T-Bolts (top) and inserts (bottom).

that fills a fraction of the circle (1/2, 1/4, etc) [94, 95]. The feasibility of each design must be thoroughly assessed and verified. With a traditional root design (a single ring of bolts) any of these segment widths are possible and each would have their trade-offs. For example, using a single segment per bolt would result in a small part that would be fast and easy to manufacture potentially creating cost and quality improvements. On the other hand, the placing of each of these segments would be challenging and the resulting structure may be weaker, as there would be no continuous fibres between the segments. Furthermore, it is possible that by separating the segments, the spacing between or size of the segments would need to be increased to avoid failure.

As previously mentioned, designers should try to minimize this spacing, so that they can maximize the number of bolts and thus load capacity of the blade root. One possibility for increasing the packing density is to use staggered bolts as suggested by Doorenspleet et al. [87]. Expanding this concept to staggering in three dimensions, a root configuration with bolts staggered radially could also be envisioned, and for such a configuration it is suspected that a wider root segment containing many bolts would be more structurally efficient. The exact angle that the insert should span (180°, 90°, etc.) would have to be investigated. When using larger root segment widths, the behaviour of the root at the edges of the inserts should be carefully studied, as these discontinuities may occur at the same location as the edges of the blade halves (in a butterfly blade), which are known to be critical to the strength of the blade [15]. The root is a structurally critical part of the blade that also has key implications on blade weight and cost, so in depth analysis and optimization should go into its design.

As a result of this complexity, the structural response of the root is typically predicted through FE modelling. This allows the complex, three-dimensional stress states that govern the behaviour of the root joint to be determined. A key concern in these models is the boundary conditions used. A review by Antoniou et al. [96] found that majority of designers model the blade root by constraining all degrees of freedom. One should note that this strategy would be unable to predict separation between the hub and the blade root, a phenomenon that can directly lead to failure [28], yet it may be necessary due to constraints in computational resources. This potential mismatch between simulated and actual behaviour is the reason for not only the previously discussed partial reduction factors, but also for the incorporation of physical testing into the design process.

2.4.2. Subcomponent Testing

Once a design has been settled upon and analysed, it must be verified/certified before it can be put into service. Some consideration was given to this in 2.1.2, but further discussion is required, specifically on the physical testing of blades. The culminating exercise in certification is a set of full scale blade tests, which are required by DNV GL [25] to be performed in the following order:

1. center of gravity and mass test

2. modal tests
3. static bending tests
4. fatigue bending tests
5. post-fatigue modal tests
6. post-fatigue static bending tests

This is a quite extensive test regime and there are many requirements on how they shall be conducted. These can be found in the *DNVGL-ST-0376* standard [25], but the key point is that they are time consuming and expensive, and as a result they are only performed on one blade. Clearly this has repercussions in testing costs and reliability. Smaller subcomponent and coupon level tests are used counteract this, but there is interest amongst manufacturers and certifying bodies to increase the use of SCTs.

During service, blades experience fully distributed loads from the wind and gravity. In an artificial test setup it is difficult to imitate these distributed loads; instead, loads are typically applied through one or more yoke devices. Generally speaking, the more load introduction points are used, the more closely service loads can be imitated, but the yoked regions show large variations from service conditions [97]. A study on full scale (FS) testing by Antoniou et al. [96] demonstrated that these tests under load the root region, while over loading much of the mid-span of the blade. This can lead to blade damage and require costly repairs, while the under loading requires more cycles to be performed to achieve equivalent fatigue conditions. Rosemeier et al. [97] points out that this extends testing time by weeks to months which has serious monetary implications. Furthermore, Haselbach et al. [98] and Rosemeier et al. [97] (among others) have also found that load conditions introduced during FS testing differ significantly from the critical loads turbines experience in service. All in all, this goes to show that there are many challenges with FS testing, which opens the door for many improvements from the integration of SCTs.

Subcomponent tests are performed on a variety of parts of a wind turbine blade. Material coupon tests do not qualify as SCTs, but some examples found in literature include tests for beam sections, the trailing edge, and spar caps [99–101]. In a comparison between subcomponent and full scale testing, Rosemeier et al. [101] found that subcomponent tests may be able to better represent the loads that a blade section experiences in service than a traditional FS test. This is in addition to the cost and time savings associated with these tests. The value of subcomponent or intermediate level test is also recognized by DNV GL [25] who allow for these tests to supplement FS tests.

The guidelines also specifically mention the utility of these tests in validating T-Bolt designs [25]. In an extensive study on resin transfer moulding (RTM), Cairns and Skramstad [102] tested bonded root inserts, and their procedure can be used as a starting point for blade root subcomponent testing. Unfortunately their study only examined root sections with a single root insert. Additional studies on single T-Bolts have also been performed [17], but no tests involving multiple bolts in a root subsection could be found. In a traditional root design where the stress fields from each bolt do not interact, these testing strategies may be valid, but if staggered bolt configurations and/or the interactions of stress fields are to be studied and verified experimentally, new testing procedures must be devised.

To design a new test, key elements and concerns of other subcomponent tests should be used as guidance. Rosemeier et al. [101] suggest that any load condition can be induced in a subcomponent test, but in their methodology they are testing an entire cross section of a blade. Considering the large diameter of the blade root and subsequent cost of manufacturing, it would be advantageous to instead test an angular subsection of the blade root. When scaling spar cap subcomponents it was found that the test results are highly sensitive to the aspect ratio of the part [103]. Furthermore, Lahuerta et al. [104] studied scaling in the testing of thick laminates, and found that it was essential to scale all aspects of the geometry (as opposed to simply thickness) to obtain a representative distribution of failure modes. Finally, as seen from OHT tests, finite width effects and end distances can change the failure mode seen in the bolted joint. All of these findings emphasize the influence of subcomponent geometry on obtaining useful and representative results in SCTs. Through an examination of past studies on wind turbine subcomponents, one of the key challenges is properly defining a specimen geometry, which is especially relevant for the blade root as there is limited information of root tests beyond a single bolt/insert. Another challenge in testing and validation is that simulations typically

predict first ply failure, which is very difficult to observe in reality, although acoustic emission monitoring can aid in this regard [96]. Ultimately, a well designed test must load the subcomponent to failure such that the displayed failure mode is representative of those seen in service and the failure load is clearly identifiable, all without artificially strengthening or weakening the subcomponent.

2.4.3. Research Questions

From a survey of the current research and industry climate, some gaps in understanding were identified with respect to wind turbine blade root design. Furthermore, relevant research findings and trends were used to design research questions for the specific purpose of improving root technology in this project. Of the many factors impacting root performance, there has not been extensive exploration of staggered or offset bolt patterns. Research in traditional bolted joints has shown that this approach has the potential to reduce stress concentrations between holes. Industry experience indicates similar findings. It remains unseen a) how much benefit can be captured through this technique, and b) which geometries will maximize the benefit of staggered joints.

Recent updates to certification guidelines encourage the incorporation of SCT procedures into the design of blades, and this project offers an excellent opportunity to work towards developing these procedures at the root level. Existing research has very promising findings in other parts of the blade, but there are not yet any SCTs designed for the blade root. If novel stagger patterns are to be incorporated into full length blades, they will require physical testing before implementation, thus SCT methods are a logical secondary focus for this investigation into improving root design.

All of these concerns were distilled into a research question addressing the lack of understanding in T-Bolt stress/strain interactions under staggered spacing, with the goal of improving root design. The subquestions are stated below to provide a skeleton of the knowledge necessary to understand staggered root designs.

How do the geometric parameters of a wind turbine blade root designed with T-Bolts influence its structural response and to what extent can these be utilized to increase the root capacity?

1. How do the strain interactions in the root laminate respond to changes in bushing positions? How can these changes be exploited to increase load capacity through reduced strains?
2. Based upon the individual and combined effects of the different geometric parameters in the 3D root design space on the root laminate's strain response, which parameters are the most influential or offer the greatest benefits in load capacity?
3. How does the strain response change through the thickness of the laminate? Can the difference in strain response at the inner and outer blade surfaces be counteracted as a method to increase load capacity?
4. How well can the behaviour of a simplified 5-bolt root model be replicated in lab-scale experiments? Furthermore, how does this behaviour deviate from that of a full blade root?

3

Methodology

This chapter describes the goals of this project and details the approach designed to achieve them. As touched upon in Chapter 1, overarching goal of the project is to further understand bolted root connections and to use this understanding to design an improved root. These goals are defined more precisely and expanded upon in Section 3.1. Here, some context into the trade-offs and conflicting influences in root behaviour is also provided. The following section (3.2) provides an in-depth account of the experiment designed and performed to answer the research questions defined for this project. Finally, the FE model used to explore root behaviour is unpacked in Section 3.3, describing the key simplifications made in creating the submodel.

3.1. Project Scope

Concisely, this project aims to explore how varying the T-Bolt placement affects the structural response of a wind turbine, and thus uncover to what extent this can increase root capacity. Practically, this means that there are two primary goals: understanding the relationships between the different parameters of the root geometry and determining what measurable improvement they can create in terms of root capacity. As such, it is necessary to define root capacity, as it is the key measuring device for comparing different root configurations. For a given hub geometry (thus a set BCD), the root capacity is then defined as the maximum load that can be transferred from the rest of the blade to the hub. For this project the root capacity will be measured and analysed from a strain perspective: namely, for a constant load, how much does the strain decrease (or increase) between different configurations. With testing in mind, this allows different bolt configurations to be tested under the same loads, and the strongest, or optimal, configuration is thus the one that most efficient transfers load, resulting in the lowest strain. If a configuration has a lower strain at a constant load, inversely it also will be able to withstand a higher load without failure. Therefore, axial strain was selected as the main metric of performance in this study. This also aligns the study well with industry practice. When axial strains are reported in this thesis, they are reported as normalized strains: the measured or extracted strain divided by a blade design strain. The strain values are in [µm/m], so the normalized strains are in [µm/m]/[µm/m], and thus they are reported without units.

To further align the study with the current state-of-the-art and keep the focus of the investigation on the unknown effects of bolt spacing in three dimensions, the external parameters are set to imitate those of real blades. The single-row root designs common in large turbines, and the variety of literature on the subject already presented, make it clear that the influence of material and layup on the bearing and net tension response of a bolt joint, are better understood than the effects of hole spacing. Defaulting to existing blade designs provides a baseline to work from and keeps the project scope manageable.

The spacings that will be varied in this investigation are specifically: the axial spacing along the blade, circumferential spacing around the root, and the radial spacing through the thickness of the root laminate. The impacts of these parameters were investigated through first through FE modelling to determine the specific impacts of these (and other) parameters. Using these conclusions, the secondary project goal was tackled: iterative design modifications were used to maximize the performance improvements of the root joint. Finally the physical testing was performed to verify the FE model and

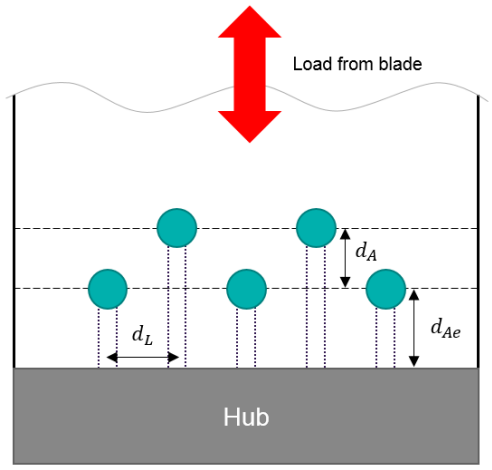

Figure 3.1: Flattened representation of a staggered root design, looking down at the outer surface of the root and showing key parameters.

associated learnings, solidifying the understanding of root behaviour. Before diving into the specifics of the experimental methodology used in this project, it is useful to expand upon some of the trade offs and requirements for a feasible root design.

The discussion of bolt spacing is also the packing density, and there are a many trade-offs that are made when moving bolts closer together or farther apart. Consider the schematic shown in Figure 3.1, here five bolts are shown in a staggered pattern. The packing density is governed by the d_L distance, but the stress interactions between the bolts are also strongly impacted by d_A. As the bolts move closer together, the net-section area between the bolts is reduced, but by shifting the second row away from the hub, this can be counteracted. Regardless of the spacing d_A, the use pretension in the T-Bolts will put the area between the first row of bolts and the hub into compression. It is thus necessary to ensure an adequate bearing distance here, or in other words a large enough d_{Ae}. When the blade is then loaded, this entire section shown in Figure 3.1 then receives an “external” tensile or compressive load. The oscillations from these varying loads is what creates the fatigue cycles, but due to the pretension different regions of the laminate receive loads with different R ratios. This is especially true when a two row design is employed, because the region between first row bolts has a tensile load from the outboard blade combined with a compressive load from the pretension in the second row bolts. Without further investigation it remains unknown what portions of the load are transferred to the hub through the bolts compared to the through the laminate. Load can be transferred to the hub through the laminate due to the pretension in the bolts. Subsequently, this can reduce bearing loads on the bushings, but this also creates bypass loading in the net-tension regions between bolts. For these reasons (among others) the bolt spacing is not simply a trade off between more, closer spaced bolts and higher stress concentrations.

To make matters more complicated, one must look past the two-dimensional sketch of Figure 3.1 and remember that T-Bolts use a shaft-bolt and thus require a second hole in the laminate. This changes the strain distribution through the laminate. Traditionally the shaftbolt is aligned with the centerline of the laminate, but it has also been observed that the inner and outer surfaces of the blades are loaded unequally. As a way to counteract this, different positions of the shaftbolts through the thickness were investigated. FE modelling was essential to this analysis, as it is difficult to measure strain results on the inside of laminate. It was also essential to study the shear number of configurations involved in this investigation: it would be impossible to manufacture and test all of them. Based on a numerical model, the learnings on root behaviour needed to be verified through experimental testing.

While the strain performance of the root prior to failure is the focus of this project, the physical test results would be even more valuable if a representative failure mode could be achieved. The lab scale (LS) testing of this campaign offers a lower cost method for validating the numerical model, and if it achieves representative failure modes, it opens the door for not only demonstrating potential

improvements in root design, but making a first step towards developing a true root subcomponent test. Such a test would be beneficial for many reasons, including reduced test costs and times, and subsequently the experimental campaign serves not only as a verification of root performance. To maximize the likelihood of achieving a representative failure mode, the investigation turned once again to FE modelling: studying secondary geometrical parameters, like edge distances, to determine and tailor the critical regions of the specimen. Ultimately, the dual goals of understanding root geometry and demonstrating a performance increase can only be achieved through the combination of numerical modelling then experimental testing, and this project was structured accordingly.

3.2. Investigation Structure

To investigate the effects of the many different variables in the root geometry, this project utilized numerical modelling (Phase 1) followed by experimental verification (Phase 2). The key advantage of FE modelling is that it allows for the quick comparison of many different geometries. To do this, a reliable and parametric model needed to be created. This model was designed in parallel with the test specimens, and they were both designed to capture the key behaviours found during the numerical investigation. An indepth specification of the model details is provided in Section 3.3. The first phase of investigation, presented in subsection 3.2.1, was used understand general root behaviour, separate the driving and non-driving parameters of the model's strain response, and predict the configurations that would minimize strain response and thus maximize root capacity. The experimental test specimens and test procedure are then outlined in subsection 3.2.2 along with a description of the instrumentation used.

3.2.1. Numerical Modelling

While an entire blade root can be modelled and tested, both the numerical predictions and physical tests are time consuming. Therefore this study focuses on a simplified model that can be scaled down, simulated, and tested at the lab-scale. A parameterized model was created using ANSYS APDL, to allow for quick and easy manipulation of the model geometry while still ensuring reasonable predictions. The ability to change spacing parameters by small or large amounts is essential to determine how sensitive the strain response is to the different parameters. A complete list of the geometric parameters in the model is given in Table 3.1 which provides the definitions to accompany the sketch of the model

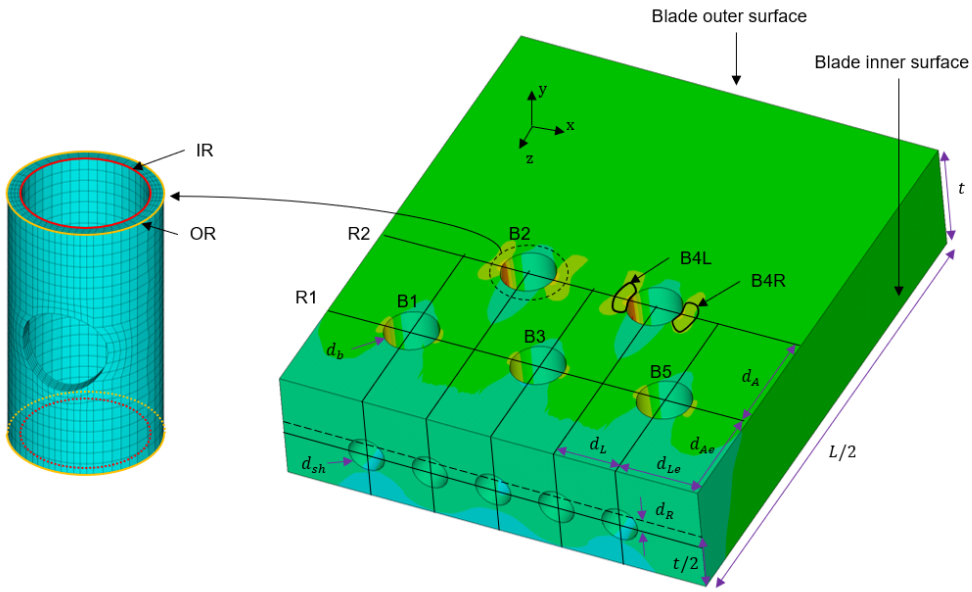

Figure 3.2: Specimen design space with key dimensions and terminologies shown as defined in Table 3.1. Note, only half the specimen is shown because it is symmetric about the midplane ($z = L/2$).

Table 3.1: Parameter definitions used to define specimen geometry as shown in Figure 3.2.

Name	Parameter	Notes
Specimen Length	L	Not scaled from full root, set to accommodate all stagger configurations.
Specimen Thickness	t	Derived from number of plies in laminate.
Axial Spacing	d_A	Distance (z-direction) between the first and second bushing rows (measured center to center).
Axial Edge Distance	d_{Ae}	Distance (z-direction) between the specimen edge and the center of the bushings in the first row.
Lateral Spacing	d_L	Distance (x-direction) between each of the five shaftbolts/bushings (measured center to center). Equivalent to the circumferential spacing at the BCD of a full root.
Lateral Edge Distance	d_{Le}	Distance (x-direction) between the center of the outermost bushings and the specimen edge. Not scaled from full root, set to avoid failure around outer bolts.
Radial Offset	d_R	Through thickness (y-direction) offset of the shaftbolt holes from the laminate centerline ($t/2$).
Bushing Diameter	d_b	
Shaftbolt Hole Diameter	d_{sh}	Derived from shaftbolt diameter, $d_s b$.
Bushing X Left / Right	BXL / BXR	
Inner / Outer Ring	IR / OR	
Bushing Row 1 / 2	R1 / R2	

shown in Figure 3.2.

This figure shows all of the spacing parameters used to define the positions of the bushing and shaftbolt holes through the model. The three most significant dimensions are the axial d_A, lateral d_L, and radial d_R stagger spacings. These correspond to the spacing in the z, x, and y directions respectively, and are the main focus of this investigation. It should be noted that the radial spacing d_R is defined as positive in the $-y$ direction, or in other words $d_R > 0$ moves the bolts towards the bottom of the submodel or inner surface of the root. Also of note are the two edge distances d_{Le} and d_{Ae}. These were investigated individually to determine their interactions with the edges of the specimen, and their dimensions were set independent of the scaling used to size the rest of the model.

Once a working model was created, the first step of the preliminary modelling was to determine the regions of the laminate and the strain components that governed the response of the submodel. This was done by examining the different components of the strain in various locations in the model, for example: around the circumference of the bushings, through the thickness of the laminate, and between the bushings. The model response in these regions is addressed in full in Section 4.1, but in short the axial strain response adjacent to the second row bushings was found to be the critical response. It is the axial strain (ϵ_z) that is used as the primary indicator of hole interactions and root capacity. Accordingly, the next step was to ensure that the loading conditions of the scaled down model were representative of real root behaviour. To accomplish this, a strain matching exercise was carried out to set the loading conditions such that the critical region of the submodel responded equivalently to a full root FE model. An off-center load method was developed to imitate the strain distribution seen in a real blade. For more detail, see 3.3.3. Comparing the loads applied to the simplified submodel between FS and LS geometries provided information on some of the scaling effects that were relevant to both LS testing and future SCT testing.

To round out the preliminary modelling investigation, the impacts of secondary parameters – such as

the edge distances d_{Le}, d_{Ae} and the difference in performance between stagger configurations, that is with three bolts in the first row, two in the second and vice versa (i.e. |*.*.*| vs |.*.*.|) – were investigated. This was done by creating a few series of configurations where for a set stagger pattern (defined by $d_A, d_L, \& d_R$) only the parameter of interest was varied. Each of these configurations was then simulated and the strain response studied. By comparing the different series it could be determined to what degree these parameters influenced the stagger pattern as opposed to creating an edge or scaling effect. From these findings, the secondary parameters were set to minimize non-representative behaviour in the submodel and simplify the design space.

The next major portion of the numerical investigation was to find the optimal hole configuration by varying the lateral, axial, and radial staggering of the T-Bolts (d_L, d_A, d_R). Based on preliminary modelling and existing experience, it was generally known that as the lateral spacing is reduced, the strain around the bushings increases as a result of stress concentration effects, but it was still studied because the local minima with respect to d_A and d_R change with different d_L spacings. All other model parameters were held constant for these simulations, which meant that all specimens had the same overall length and thickness, but their width varied slightly, due to different lateral spacings but a constant lateral edge distance.

When comparing the different configurations, scripts were used to extract the first five layers of nodes radially around each bushing. From these nodes, the axial strains in the adjacent regions were extracted through the thickness of the laminate, and then the peak axial strains were used to compare the different configurations. Configurations were created and simulated in batches, studying first the behaviour of the root first without then with radial staggering ($d_R \neq 0$). Adjusting the position of the shaftbolts affects the strain response, but it also has implications on other parts of the turbine (e.g. the hub) that may be problematic but are ignored in this project. Consequently, it is important to understand root behaviour with and without this geometric feature. Comparing both the local and global responses of the laminate under these spacings ensure that the project could achieve both its goals: understanding the effects of staggering and how these effects can be used for the maximum benefit.

The three lateral spacings studied most extensively were $d_L = 23.7, 25.0, 26.0$ mm, and these were chosen to represent a real root and then the two lateral spacings that can be physically tested at the reduced LS size. The larger two spacings are both included so that the potential improvements of a revised stagger configuration can be demonstrated and validated for different lateral spacings, because when implemented, it will likely be with a different spacing yet again. When fine tuning the different stagger configurations, a minimum interval of $\Delta d_{Le} \geq 0.3$ was used to account for the machining tolerance of a real root (scaled down with the geometry). Further limits on geometry were set to cap the maximum axial spacing at $d_A \leq 80.0$ mm and the maximum radial offset at $d_R \leq 7.0$ mm. These limits were chosen to allow for at least 100 mm of spacing between the second bushing row and the beginning of the tapered section of the root segment. A visualization of this along with the associated axial distances at the lab-scale is shown in Figure 3.3. These boundaries set the stagger ranges for this phase as: $d_L = [23.0, 26.0]$ mm, $d_A = [0.0, 80.0]$ mm, and $d_R = [0, 7.0]$. Also, the optimization simulations focused predominantly on the offset load method but also included some with a centerline

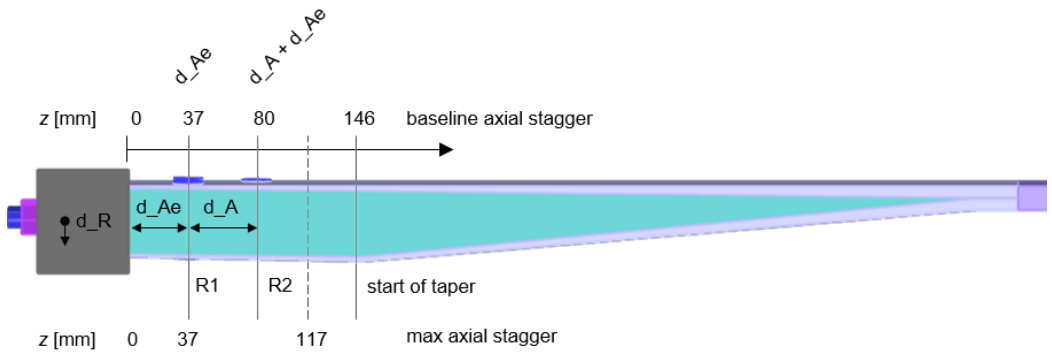

Figure 3.3: Stagger configurations with baseline and maximum axial spacings shown on a real root segment with equivalent lab-scale dimensions.

load to predict the behaviour of these specimens in the physical tests. The results from this phase were used to select the hole patterns used in the test specimens

3.2.2. Physical Testing

To verify the FE studies carried out in the first two phases of this project, 12 specimens were tested in tensile tests. These specimens encompassed 8 different hole configurations with lateral spacings of $d_L = 25.0$ or 26.0 mm, and were used to perform 10 static tests and 2 fatigue tests. Focus was primarily on the static tests, to compare the relative performance of different stagger configurations, whereas the fatigue tests were used as supplementary evidence to support the assumption that these configurations performed the same in static and fatigue loading. The configurations were selected to ensure a wide range of axial, lateral, and radial spacings were represented, including the configurations with the lowest strains, to validate the design space used in the numerical modelling and act as a proof of concept for improved stagger configurations. The edge distances of these specimens were set to minimize the likelihood of non-representative failure modes during testing. Another manner in which the service loading conditions were imitated during testing was through the modification of the test apparatus to allow for a load offset as well as centerline loading.

The off-center loading method is more representative of the strain profiles seen in a real root, so the majority of the specimens (8 of 12) used this method. For further reference, each of the specimen load methods and hole patterns is given in Table 3.2. To introduce an off-center load in a standard tensile test machine, double hinge fixtures were designed. The overall set up used is shown in Figure 3.4, and like the specimens it is symmetric in the z-direction with identical parts on the top and bottom. The main components are the connector lug, shown in teal, and the endplate fixtures, shown in grey. These pieces facilitate rotation about the axis of the machine pin and provide a surface to apply the pretension in the shaftbolts against respectively. Both of these parts, as well as the pin connecting them - the load bearing parts - are made from 8.8 grade steel, to ensure that they are stiffer than the specimens and will not yield.

The key feature of the experimental apparatus is the incorporation of the load offset into the fixture.

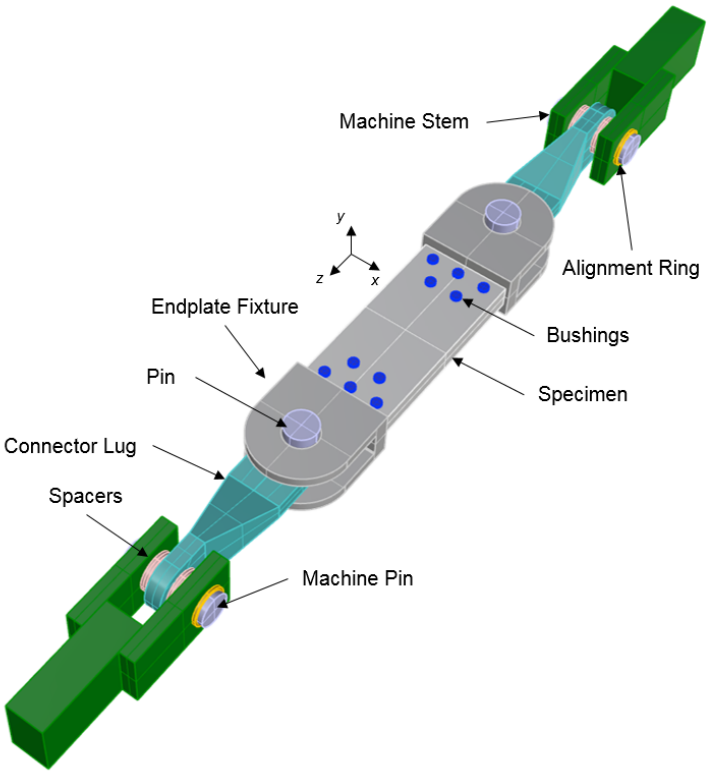

Figure 3.4: CAD model of test setup with components labeled.

Table 3.2: Specimen descriptions with load method and hole pattern dimensions for the 12 specimens tested.

ID	Loading		d_L [mm]	d_A [mm]	d_R [mm]
1A	Static	On-center	25.0	42.9	0.0
1B	Static	Off-center	25.0	42.9	0.0
1C	Static	Off-center	25.0	42.9	1.0
2A	Static	On-center	25.0	80.0	0.0
2B	Static	Off-center	25.0	80.0	0.0
2C	Static	Off-center	25.0	80.0	0.5
3A	Static	Off-center	25.0	62.0	0.8
4A	Static	On-center	26.0	42.9	0.0
4B	Static	Off-center	26.0	42.9	1.0
5A	Static	Off-center	26.0	80.0	0.5
1F	Fatigue	On-center	25.0	42.9	0.0
2F	Fatigue	Off-center	25.0	62.0	0.8

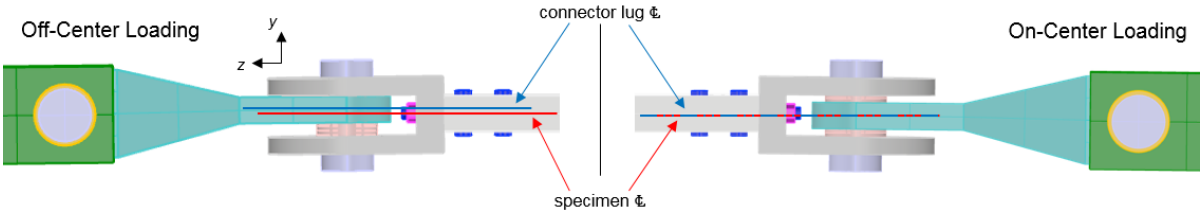

Figure 3.5: Side view of CAD model with complete test setup comparing on-center and off-center loading configurations.

Ultimately the load is applied by the machine stem, but this cannot be moved, so the load offset was achieved by shifting the specimen in the y-direction, away from the machine centerline, which was achieved by using spacers of various thicknesses. This is best seen from the side view show in Figure 3.5 where the off-center method is shown on the left and the on-center method is shown on the right. Here it can be seen that the spacers used around the connector lug have different total heights, and this is what is used to create the offset. From the connector the load is then split between the upper and lower halves of the endplate fixture, but since it must travel through the connector-lug, the line of action of the applied force can be set to the 7.0 mm offset modelled. Overall this setup allows the specimen to rotate in x and y, as required to ensure the machine stiffness does not counteract the load offset.

During the static tests, most of the specimens were not loaded to failure, which when achieved was only seen in the bolts and nuts. As a result, failure of these components inhibited test progress without providing useful information on laminate performance. Each specimen was held at the 260 kN target load used in the FE simulations to ensure adequate data collection for comparison. The static pulls up to 260 kN were used to verify that there was no gap opening between the endplate and the specimens before starting the fatigue tests. For the fatigue tests, the specimens were cycled between 26 kN and 260 kN until failure occurred. To achieve the 53 kN pretension in the 10.9 grade steel bolts, a torque of 150 Nm was applied to each nut in the specimens. An independent bolt stiffness validation found this torque to achieve a pretension of at least 50 kN.

To measure specimen response, a combination of strain gauges (SGs) and digital image correlation (DIC) were used. After manufacturing, the top and bottom surfaces of the specimens were not very flat, so a small circular region was machined down to a smooth surface in the region the strain gauges were attached. Subsequently, SGs were only placed in three key positions, and instead 2D DIC was used on the front and the back of each specimen as the primary measurement technique. DIC was also advantageous because it allowed the strain field to be measured across the specimen as opposed to at distinct points. Both techniques were used to acquire one measurement per second during the static tests. Strain values from the fatigue test were sampled 10 times per decade, where each decade

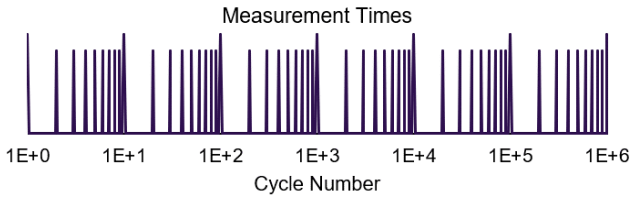

Figure 3.6: Visualization of the cycle numbers at which the strains were sampled during fatigue testing.

is an integer value of n in 10^n. For clarity, a visual representation of the cycles in which the strains would be sampled for a one million cycle test is shown in Figure 3.6.

To see the difference in strain response on the front and back of the specimen (equivalent to inner and outer blade surfaces), the DIC speckling was applied to both sides. On each side, the speckle pattern was only applied to one end (i.e. only the right as shown in Figure 3.7). This was done to take advantage of the specimen symmetry and allow for direct comparison between the DIC and SG strain measurements. The SGs, shown in red, were then placed in three locations. First, at a 2 mm offset from the edge of a R2 bushing, which coincides with a surface node in the OR of the FE model. Secondly, in the net-section (midway) between the two R2 bushings, and thirdly, in the very center of the specimen. In combination, the first and second SGs are used to measure the stress concentration effect in R2: the most highly strained region of the specimen. The final SG is used as to monitor the applied load.

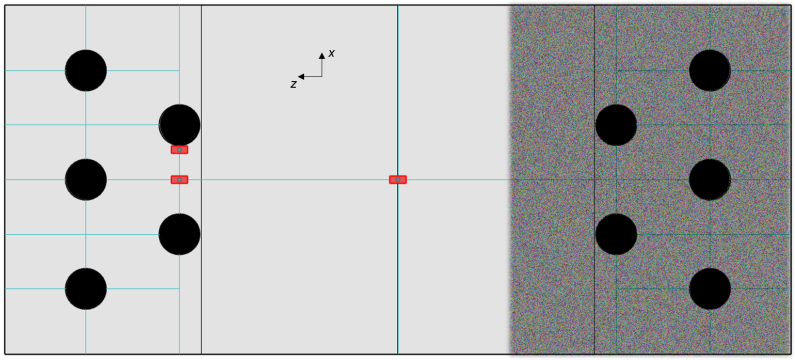

Figure 3.7: Schematic showing region of specimens painted with DIC speckle pattern and the placement of SGs on the specimen. Note the image has been rotated for display purposes.

3.3. Simplified Submodel

This section lays out the decisions made in simplifying the model and their consequences on the sub-model's behaviour. The discussion is separated into four subsections which provide a top down approach. First, the overall geometry is outlined in 3.3.1. Second, the discretization of the solid geometry into a FE model is covered in 3.3.2. While the geometry can be simplified, the same cannot be said of the boundary conditions and loads applied to the specimen. Subsequently, these are presented and discussed in 3.3.3. Lastly, not all behaviours of the blade root could be properly replicated in the simplified model, and these discrepancies and their effects are addressed in 3.3.4.

3.3.1. Geometry

When a full-blade root is modelled, the inherent axi-symmetry of the structure is used to simplified the 3D model. In a traditional, single-row T-Bolt root this means that the model can be reduced to a single bolt. Looking at a double-row staggered root it is immediately clear that symmetry cannot reduce the model to the same extent. Instead the reduced model must include at least two bolts and can use either cyclic or symmetric boundary conditions (BCs) as shown in Figure 3.8. Here different

modelling approaches and their respective boundary conditions are compared, imagining that the blade has been unrolled in cylindrical coordinates. The outboard regions of the blade are not shown here, as they are not typically modelled, but represented through a line load in the z-direction. Comparing the 2-bolt cyclic and 3-bolt symmetric models, they both capture the behaviour of double stagger pattern by modelling a sum of two bolts each. The difference between these models is mainly their computational efficiency. In ANSYS , cyclic conditions are represented internally by copying the behaviour of the left side nodes (light-green boundary) to the right side, effectively doubling the size of the model. On the other hand, the symmetric model can represent the BCs without creating any additional nodes, and thus solves slightly faster. Subsequently, the modelling approach for this project was adapted from the 3-bolt model.

The model shown on the far right, the 5-bolt submodel, is the modelling approach used in this project. It represents a hybrid between modelling a section of the root as it behaves in the blade and as a stand-alone, testable subcomponent. Unlike the FE workspace, were one can apply a symmetric BC, it is very difficult to imitate the constraints from adjacent material in a physical test. In theory the edges of a specimen could be restrained, but to achieve the appropriate stiffness would be challenging. Instead, this model uses 5-bolts to create a symmetric specimen with some lateral constraint from the outer bushings that is modelled in the same way it is tested: with free edges.

When a tensile, axial load is applied to any of the models shown in Figure 3.8 (in the z-direction), it will cause axial deformation and, through the Poisson effect, lateral contraction (in the θ-direction). The cyclic or symmetric boundary conditions represent the adjacent material that would be present in a full root (like the leftmost image of Figure 3.9), and this material prevents lateral (or circumferential) contraction. Without restraint, a free edge sustains a greater amount of lateral contraction, and thus the lateral strain in the edge regions is higher in the 5-bolt submodel, than a standard symmetric or cyclic model. This creates a conservative loading scenario where the model and test specimen experience higher strain than they would in service; however, the edge regions are not fully representative of true root behaviour.

In the 5-bolt submodel, the central region (between the centers of bushings 2 and 4, numbered from left to right in Figure 3.8), is the main region of interest during modelling and testing. The model was designed such that this region encompasses the full behaviour of both first and second row bolts. Overlaying the 3-bolt symmetric model, on this model shows that this inner region is the same in that there is both laminate and at least one bolt on the outside providing lateral constraint. Of course if the model were 7-bolts wide, the behaviour of the central region would be even closer to that of the 3-bolt symmetric model, but it would also be more computationally intensive to model and create a larger specimen, requiring a higher test load. One of the main goals of reducing the test specimen is to reduce the test load, so a compromise was made to use a 5-bolt submodel with free edges.

From the decision to use 5-bolts in the root submodel, the overall specimen geometry was obtained through two major adaptations from the full root. This process is shown in Figure 3.9, and the two steps are first isolating an angular wedge encompassing 5 bolts (blue outline), and then taking the end of the

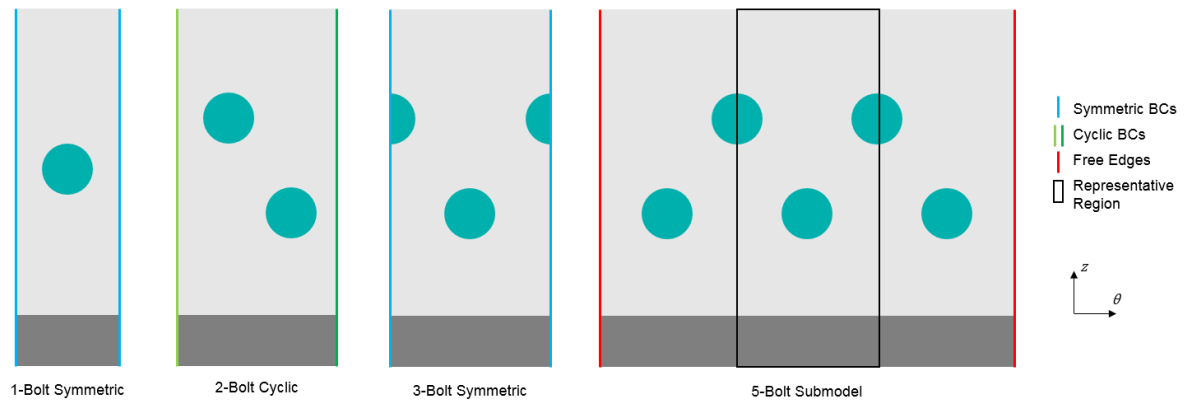

Figure 3.8: Comparison of reduced symmetry models and 5-bolt submodel showing their respective boundary conditions. The root laminate is shown in light grey, hub in dark grey, and T-Bolt bushings shown in teal.

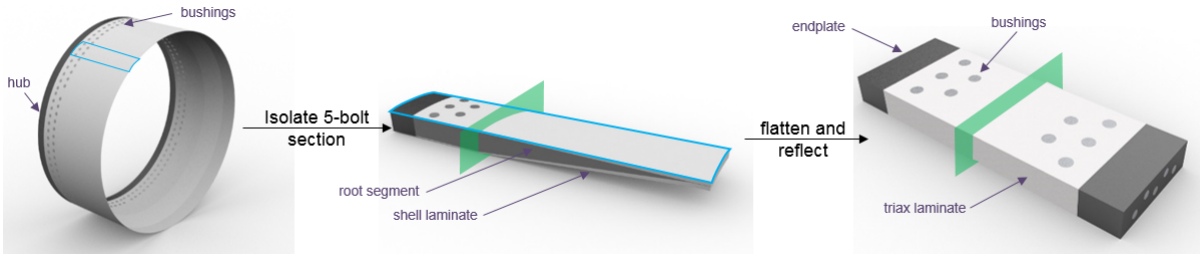

Figure 3.9: Formation of 5-bolt submodel geometry as an extracted and reflected section of a full blade root.

root (section with constant thickness) and both flattening it and reflecting it about the end plane (green plane). These last two simplifications were made to adapt the submodel into a specimen that is easily testable in a standard mechanical testing machine. In the full blade, the curvature of the root provides it with additional area moment of inertia, but with modern BCDs being so large, a 5-bolt section would have only a few centimeters of offset from a flat specimen. Subsequently, flattening the specimen does not significantly change the behaviour, especially when the specimen is tested only in tension. The specimens are tested only in tension because the large BCD and short axial length of the submodel allow the global moment applied to the blade to be distilled to a local line load applied axially to the end of the root submodel. More specifically, the inner and outer surface of the laminate are both a large distance from the neutral axis of the applied moment, and therefore are resolved into axial loads, where the entire laminate thickness is in tension or compression. Additionally, the removal of curvature will reduce out-of-plane loading on the test machine.

The second simplification, that is to model only the constant thickness section and convert it into a symmetric specimen with T-Bolts on both ends, was made to allow for easier mounting of the specimen in a test machine. To test a root specimen, one side needs to have an endplate to apply pretension to the T-Bolts. From preliminary scaling calculations, it was clear that the total specimen load for the LS test specimens would be on the order of 200+ kN, and with a load this large, it would be difficult to clamp the other end of the specimen. The alternative would be to design a bolted connection, and since the goal of the test campaign is to study T-Bolt connections, it made sense to maximize the functionality of the specimen by using testable bolt configurations at both ends of the specimen. Furthermore, since the main region of interest is only the bushing holes, and not the tapered region, the axial distance between the two sets of holes was not critical. In a real root, the constant thickness section extends past the second row of bolts to equalize the strain through the laminate before tapering down to a shell laminate. The equalization of the strain past the second row allows for the reflected specimen design in this 5-bolt submodel, since the hole patterns at either end can be considered independent.

With the 5-bolt symmetric specimen design, the maximum strains occur around the bolt pattern and depend on the relative spacing of the bolts. Unlike the specimen length, the width and thickness have strong bearing on the strain response as they affect strain concentration behaviour. To capture this behaviour at a smaller load, it is necessary to scale the geometry of the specimen uniformly between the LS specimen and a FS root to ensure that failure modes and thick laminate responses are representative [104]. Nearly all of the components in this test, including the T-Bolt bushings, are custom manufactured, except the thickness and shaftbolt thread size, so they can be scaled continuously. On

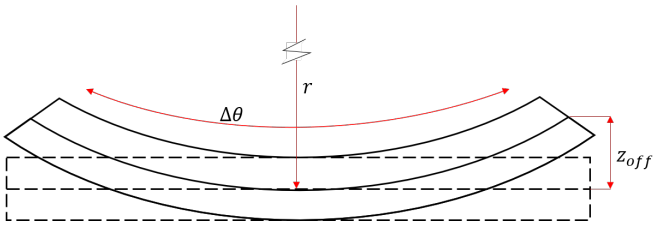

Figure 3.10: End-view (hub to tip) of the difference in geometry, specifically in the out-of-plane height, between a flat specimen and a curved section of a full root.

the contrary, the thickness can only be scaled to a whole number of Triax plies (the layup was monolithic), and to simplify manufacturing, standard metric thread sizes were used for scaling the shaftbolts. Therefore, the scaling factor between the LS and FS was chosen to minimize error in these two dimensions.

3.3.2. Discretization

This subsection discusses the key points of this submodel and how the geometry is discretized into a mesh and elements. The overall model is shown in Figure 3.11. The first key point is that symmetry is used to reduce the model size in half. The split is made at the axial midpoint of the specimen, and is motivated by the BCs of the specimen. Further discussion of these BCs is given in the next subsection.

Some of the geometrical features, like the threads and endplates, have been simplified from their true geometry to reduce the complexity of the FE model. For most part, the 5-bolt submodel has a simple geometry: it is a rectangular block with axial and transverse holes. The shaftbolts and bushings that compose the T-Bolts appear to be similar: two perpendicular cylinders, and they are modelled as such. It is important to recognize that this disregards the threads used to connect the bolt and the bushing. Instead of modelling the many angled contact surfaces that keep the bushing and shaftbolt connected they are simply modelled as one material, perfectly bonded. This may not capture the precise behaviour of the two components, it is a good engineering approximation as it conserves computational power and thread failure is rare.

Further simplifications made to the FE bushing representation include representing the majority of the shaftbolt with beam elements. The shaftbolts have a uniform cross-section, and while they are essential to transfer load from the endplate to the laminate, the precise response of the shaftbolts is not important to this investigation. Therefore, they can be represented with the computationally simpler beam elements. The use of beam elements also greatly simplifies the use of pretension elements in the shaftbolt. Solid elements are used to model the region of the shaftbolt that connects to the bushing (shaftbolt stub), and then these are changed to beam elements a short distance along the bolt. At the interface between the two element types, the nodes are constrained so that it acts as one solid bolt. Pretension elements are then inserted in between the beam elements of the shaftbolt, near the hub end. They are inserted near the hub but not at the end to ensure that they are affected by neither the connection of the shaftbolt to the endplate nor by bolt bending. The resulting FE discretization is shown in Figure 3.12. Here it can be seen that while the threads are not modelled, the chamfer around the thread region is, because this affects the bearing area of the bushing.

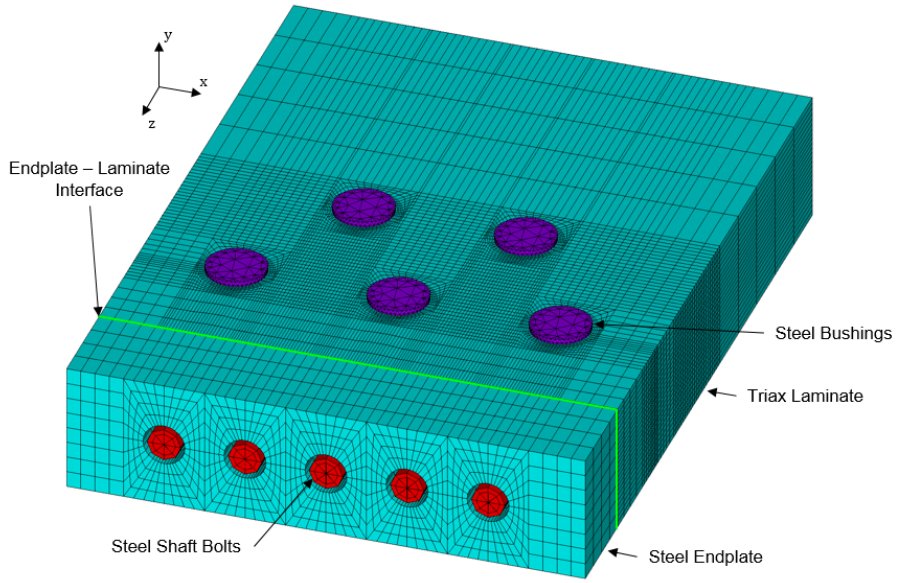

Figure 3.11: Full FE model used for simulations shown without BCs. Elements are coloured by type: beam elements are red, tetrahedral solid elements are purple, and hexahedral solid elements are cyan.

Table 3.3: ANSYS element types and corresponding material definitions used for each component in the 5-bolt submodel.

Region	Material	Element Type	Element Name
GFRP Specimen	Triax (orthotropic)	Solid	SOLID185
Endplate	Steel (isotropic)	Solid	SOLID185
Bushings	Steel (isotropic)	Solid	SOLID187
Shaft Bolts	Steel (isotropic) Steel (isotropic)	Solid Beam Pretension	SOLID187 BEAM 188 PRETS179
Contact Regions		Contact Surface Target Surface	CONTA173 TARGE170

When modelling the T-Bolts, another simplification is that the nuts that secure the bolt to the endplate are omitted, which is why they are not see in Figure 3.12. While nuts could have been modelled, they would have had to be constrained to both the endplate and the shaftbolt somehow. Without modelling threads, the displacement of the nut relative to the shaftbolt would have to be fixed, essentially modelling the two components as a single part. Then to connect to the endplate, either a contact relationship or constrain equation would need to be used. These regions of the model have very little impact on the performance of the hole pattern, so there is no benefit from adding the additional computation time associated with a contact relationship. Furthermore, if a constraint equation is used to constrain the nut to the endplate and the nut to the shaftbolt, then there is no need for modelling the nut at all. Subsequently this model constrains the ends of the shaftbolts directly to the nodes that would fall under the nut (if it were present). This simplification allows for the function of the nuts to be modelled while minimizing the size of the model.

Another consideration when translating the specimen into a FE model, is how to model the fit between the bushing and the laminate. Many studies in literature found the clearance or interference between a bolt and its hole to have a significant effect on the performance of a joint. This study acknowledges the importance of this relationship, but it was not possible to include it in the scope. As such, the outer surface of the bushing and the inner surface of the laminate were modelled as coincident, with the same diameter. This means that the surfaces are initially in contact and stay in contact through the entire simulation. Contact elements were used for this interface as well as the one between the endplate and laminate which is highlighted in Figure 3.11.

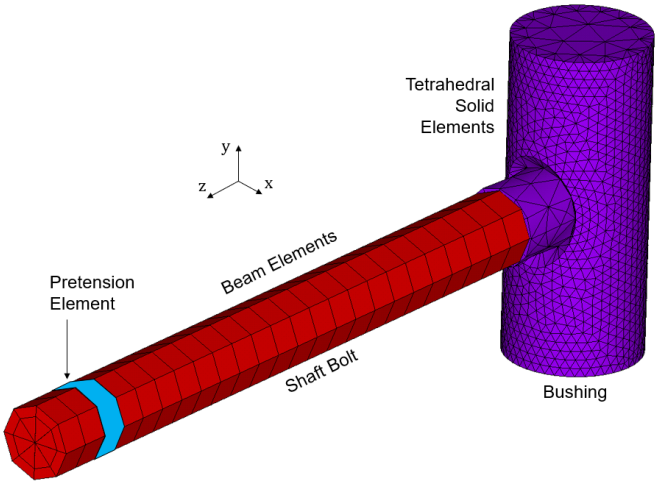

Figure 3.12: Numerical discretization of a single T-Bolt, showing element type by colour.

To model the contact relationships, ANSYS' suite of built in element types were used. These, along with the precise element types used for the rest of the model are given in Table 3.3. The reasoning for using most of these elements has already been discussed, but one more decision work mentioning is the use of hexahedral vs tetrahedral solid elements (SOLID185 vs SOLID187). The advantage of the former is that they give more accurate strain results, however the later is more versatile in terms of discretizing complex geometries. Hexahedral elements can be created using mapped meshes in ANSYS to ensure elements have a uniform shape, whereas the sharp corners of tetrahedral elements often cause distortion in the strain solution. Displacement results, and thus the ability to transfer load, have essentially the same accuracy for each element shape. On the other hand, mapped hexahedral elements require diligently split volumes with a quadrilateral area that can then be swept to form a hexahedral volume. The response in the shaftbolts and bushings is not critical, but their geometry is complex, so tetrahedral elements were used.

The next most complicated geometry in the submodel is the intersection of the shaftbolt and bushing holes, in the laminate. Unlike the shaftbolt stub region, the strain results around the bushing are very important to properly understanding the submodel. For this reason, the 5-bolt submodel is constructed with a modular, bottom-up approach, that is centered around the intersection of these two holes. To create the geometry, a single block is created and then the bushing and shaftbolt holes are added. These blocks are then placed at the centers of each bushing. From this block, divider volumes are added between the blocks to connect the modules. Finally, volumes are added through the thickness of the laminate, axially along the length of the specimen, and then the outer regions are added. These 4 steps are shown in Figure 3.13.

Creating a well structured mesh of hexahedral elements in the laminate requires elements between

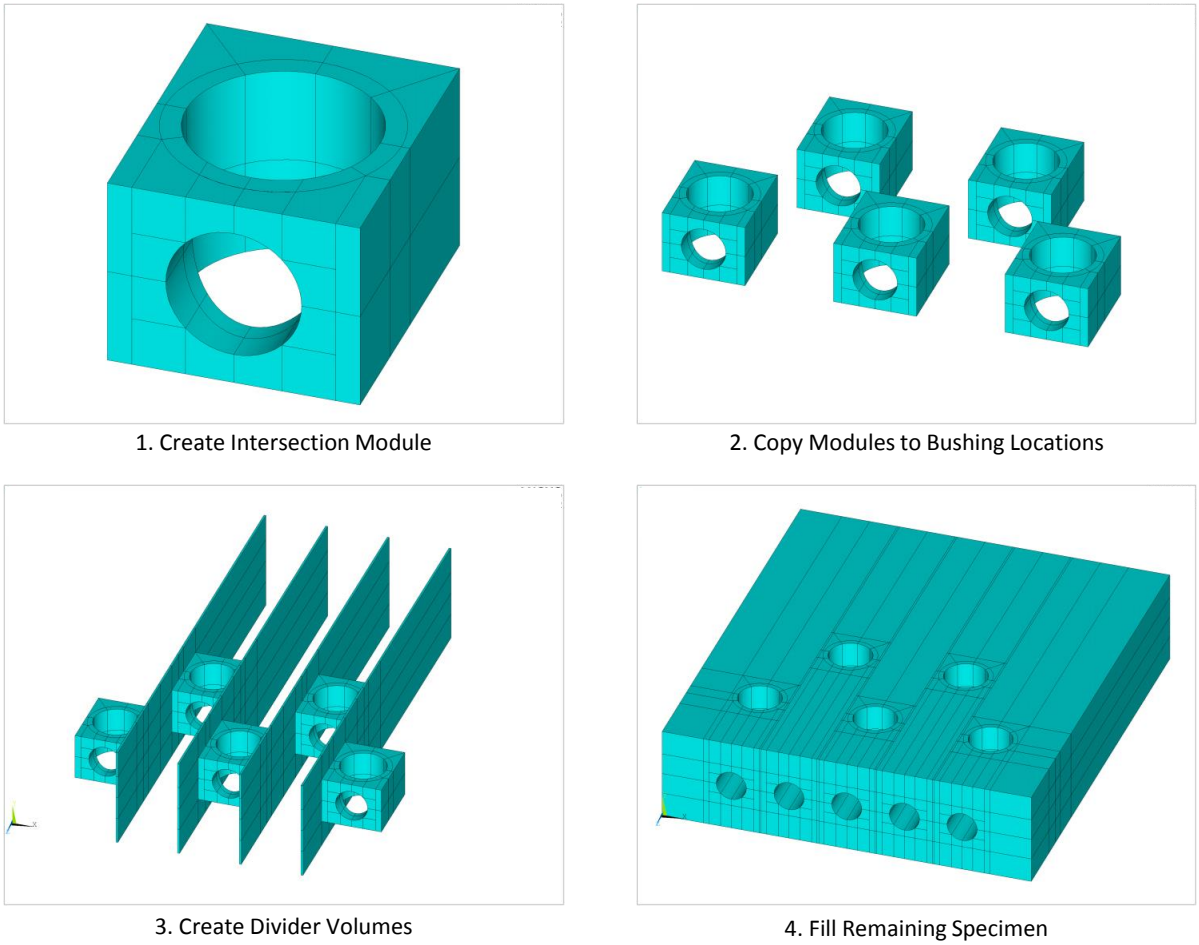

Figure 3.13: Process flow for creating the laminate volumes of the 5-bolt submodel.

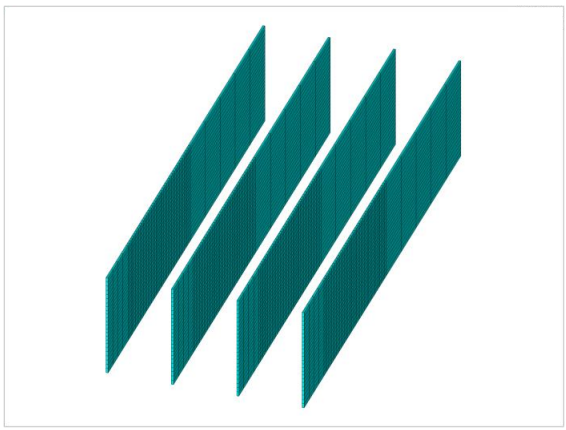

1. Mesh Dividers

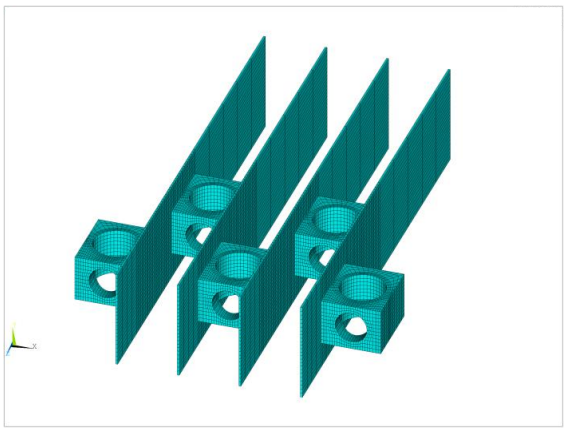

2. Sweep Mesh from Dividers around Modules

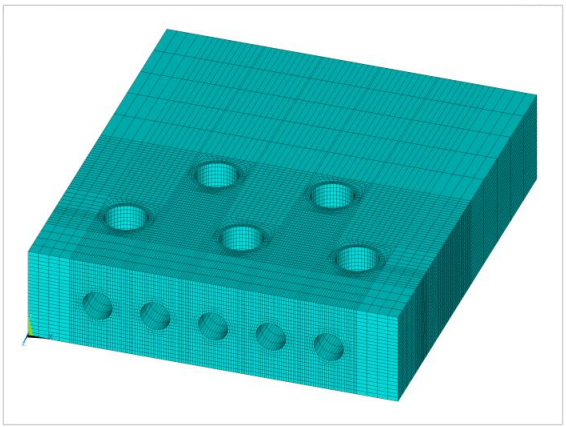

3. Sweep Mesh from Modules to Rest of Specimen

Figure 3.14: Process flow for meshing the laminate volumes of the 5-bolt submodel.

sub-volumes to be continuous. Since different hole configurations have the intersection of the bushing and shaftbolt holes in different locations, it was not guaranteed that the elements in the divider regions would line up if the elements were created by sweeping outward from the bushing hole region. To ensure all hole patterns could be meshed, and to avoid the discretization hindering the model accuracy, these divider regions needed to be meshed first. Then the elements could be swept to the intersection of the bushing and shaftbolt holes. Once this region was meshed, the elements could be swept through the thickness and axially towards either end of the specimen in the same way that the volumes were. This process is shown in Figure 3.14, where it can be compared to the volume creation process from Figure 3.13. Establishing a refined discretization process was essential to creating a model capable of properly comparing different configurations.

To confirm that the model was giving reliable and sensible results, the mesh was refined to check for convergence. A cylindrical division was implemented around each bushing, allowing for programmatic creation of uniform element shaped where the density could be independently refined through the thickness, circumferentially, or radially. Furthermore, these node rings were placed to align with the strain gauges during physical testing. As a metric for convergence, the maximum axial strain (ϵ_z) was compared to the number of nodes around a single bushing (the laminate has approximately the same number of nodes around each bushing), as shown in Figure 3.15. By the sixth iteration (31 thousand nodes), an error of 0.04% was achieved with respect to the finest mesh. This was deemed more than adequate for convergence, so this level of mesh refinement was used for all future investigations.

When discussing the mesh it is important to discuss why the focus is on the nodes adjacent to the bushings. The adjacent nodes are defined as those at any point through the thickness in the region $\theta = \pm 90^\circ \pm 25^\circ = \pm[65^\circ, 115^\circ]$, using the definition of θ presented in Section 2.3, Figure 2.8 for bolted

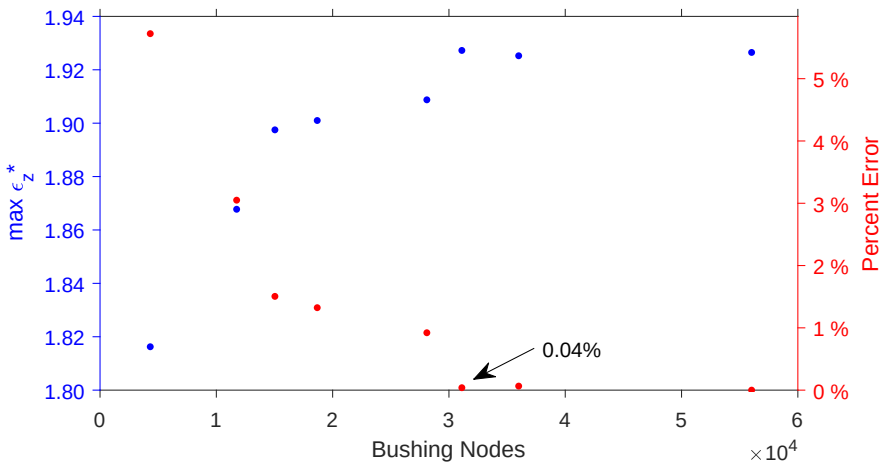

Figure 3.15: Convergence study results showing maximum strains and node count in the cylindrical region around the bushings (region with critical stress concentrations).

joint analysis. This region is the main region of interest in this investigation because it a) contains the maximum axial strains and b) shows the influence of the stress concentrations between bushing that the project aims to investigate. It should also be noted that the elements lying on both the shaft hole and bushing hole are not included in this selection. Element distortion often created high strains in this region, and they were subsequently excluded as non-physical. The strain gradients they displayed were not possible in such a small region that is not even in contact with the bushing. Ultimately decision to focus on the axial strain adjacent to the bushings was based upon the current critical regions of root design. Industry experience has shown that the net-section strain behaviour of the root is design driving, which plays into the gap of knowledge with respect to strain interactions between bolts. Net-section behavior is driven by axial strain, and therefore, axial strain is used as the main metric of analysis in this region and this investigation. In fact, it is used to set the loads applied to the specimen to counteract scaling effects.

3.3.3. Boundary Conditions and Loads

The 5-bolt submodel was designed to imitate the behaviour of a subsection of a wind turbine blade root at the lab scale; however, the loads do not scale uniformly like the geometry. Therefore in the initial modelling investigation, the load magnitudes were set through strain matching between the 5-bolt submodel and a full root FE model. To imitate the strain profile seen in the blade root, there are three main load parameters that are adjusted: the pretension load, the external load, and the pressure gradient. First, the pretension load was set by comparing the axial strain at the front of the bushings ($\theta = 0°$) between a full root model and the 5-bolt submodel: the load was adjusted so that the maximum axial strain (excluding any distorted elements) was equal. This resulted in a LS pretension load of 53 kN.

After the pretension was set, the slope of the pressure gradient and the magnitude of the total applied force were adjusted to match the axial strain response from the full root FE model. Due to the change in thickness between the hub and the tip of a root segment, the outer surface of the root is loaded higher than the inner surface, thus creating a strain bias through the thickness of the laminate. To match the strain response of this 5-bolt submodel to that of a full blade, this load offset must be imitated. In the FE environment, a one dimensional pressure gradient is applied to achieve this effect according to the following formula:

$$P(y) = 2P_0 \frac{y}{t} \tag{3.1}$$

Where P_0 is the total applied force over the total area. This means the pressure is independent of lateral position (x), and goes from 0 at the bottom surface to $2P_0$ at the top surface of the laminate. This means that the net force acts as an axial force through the center of action at $y = 0.67t$, this line of action is a 7 mm offset above the laminate centerline. This positions the load axis at nearly the same

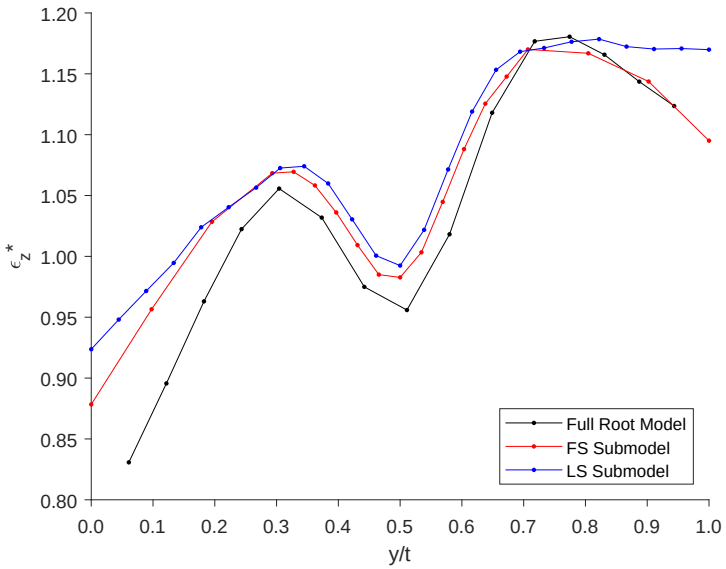

Figure 3.16: Normalized axial strain profiles through laminate thickness at the inside of the second bushing ($\theta = 90°$) used for strain matching between models.

relative position as in a full blade ($y = 0.65t$), and by comparing the strain profiles in the B2R region, as shown in Figure 3.16, the strain profiles in the submodel were matched with the full blade. To achieve this, the gradient given in (3.1) was used with a total external force of 260 kN for the 5-bolt submodel with LS geometry.

It should be mentioned that while this offset loading method (using the pressure gradient) is useful from a FE modelling perspective, off-center loading is often avoided in test specimens. To further study the effects of the load offset, simulations (and tests) were also run with a uniform pressure, simulating a force applied at the specimen centerline. Without the load offset, a higher force is required to reach the same peak axial strain, and at this force the average strain through the thickness of the laminate is also higher. This underlines the importance of the load offset method, as it gives results that are much more representative of a real root.

In this model, the external load is applied directly to the endplate, across the width of the five bolt modules (the semi-transparent blue region shown in Figure 3.17) which does not cover the outside regions of the endplate. It was found that if this load is spread across the entire width of the endplate it overloads the outer bolts, that is they carry a higher axial load than the inner bolts. In a real blade all bolts are equally loaded, so to imitate this behaviour the width of the applied load was reduced, such that the pressure load was applied to the same area around each of the five bolts. Unfortunately, is not possible to simply apply a pressure load to part of the endplate in a physical test. In reality the load was introduced through an expanded fixture that is much stiffer than the GFRP specimen, so it is sufficient to model the fixture as a rectangular endplate in the FE environment. Using the overly stiff, steel, endplate in the model ensures that a uniform contact pressure can be achieved at the interface between the endplate and laminate. This is necessary to properly imitate the hub BC seen in a real blade.

Some compromises had to be made to improve the testability of the specimen. As a result, not all of the BCs used in the model imitate a blade root; they are instead chosen to imitate the behaviour of the test specimen. The test loads on the other hand were chosen to imitate the strain profile found in existing blades. The largest difference in the BCs between a real blade and the 5-bolt model is the presence of free edges on either side of the specimen. On these faces (shown in Figure 3.17) no BCs are applied in to the FE model. The symmetry conditions are applied to the midplane of the model, with additional constraints applied to avoid rigid body motion. The symmetry constraints are applied across the entire width of the specimen to represent the other half of the specimen. These constraints are applied along the midpoint of the laminate to ensure that the centerline does not translate or rotate

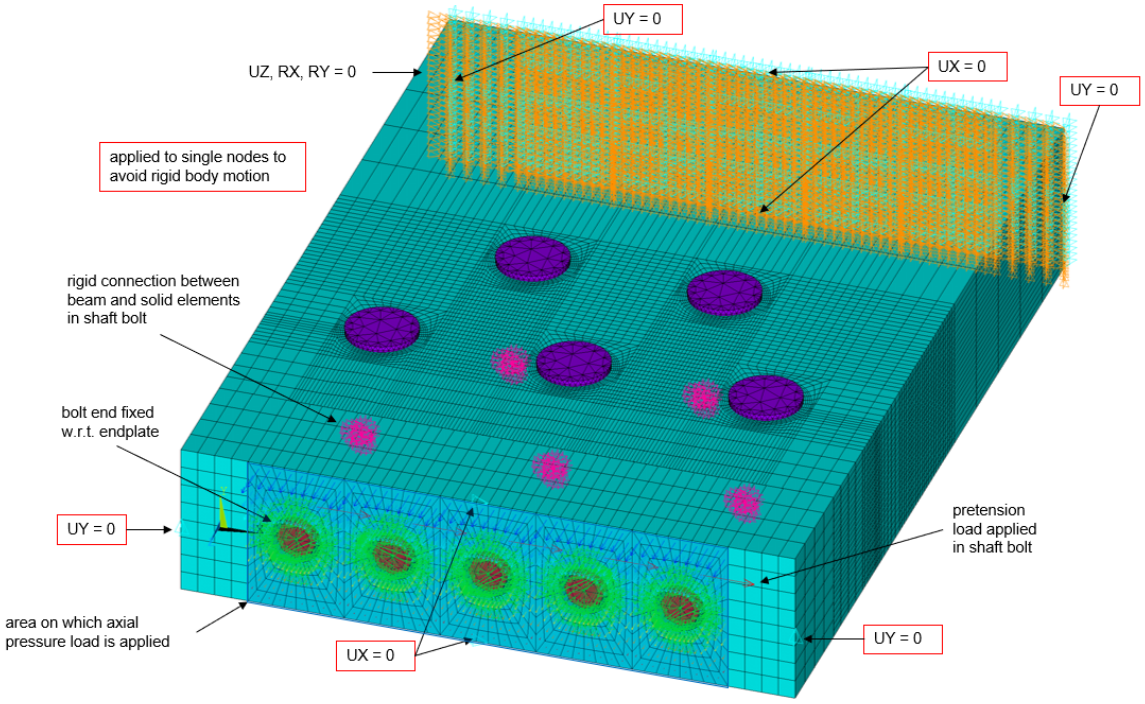

Figure 3.17: Annotated screenshot from ANSYS showing BCs and loads applied to the 5-bolt submodel. Note, pretension loads are shown in x-direction (due to local coordinate systems) but they are applied in the z-direction.

while still allowing for Poisson's contraction. Similar constraints are applied to the endplate to ensure that it translates only in the axial (z) direction, without rotating. These constraints to prevent rigid body motion were applied only on four nodes to limit non-physical constraints.

3.3.4. Model vs Full Blade Discrepancies

The 5-bolt submodel used in this project was derived from a full blade root, making a few simplifications and adjustments to ensure the specimens could be tested and modelled. As a result, there are two main short comings in this model, namely: the nut size barrier and the mismatch between load and geometry scaling.Each of these are acknowledged and discussed here.

For manufacturing purposes, the shaftbolts were scaled to an existing thread size, but the corresponding nuts do not scale at the same 3.5 ratio. More specifically, as the thread size is scaled down, the nut diameter and required clearance do not decrease at the same rate. Subsequently, a lateral hole spacing that is possible on a full-scale root may not be possible on the LS specimens. Furthermore, as the nuts are not included in the FE model, it is possible to simulate configurations that cannot be tested physically. This means the most relevant d_L spacings can only be investigated numerically. Therefore it is important to test multiple lateral spacings to verify the submodel can accurately simulate a range of different hole configurations and thus add confidence to the results.

In some ways, the nut mismatch issue could be classified as a scaling effect. Another scaling effect that needs to be considered when using the results from the submodel is the difference between the scaling factors for the geometry, applied loads, and pretension loads. Preliminary modelling quickly showed that each of these scaled at different rates between the lab- and full-scale. This is not unexpected, considering that scaling factors used in sizing entire blades are a function of the length of the blade itself, as discussed in 2.1.4. This highlights the importance of picking a clear metric for comparison, for this project: axial strain. Nonetheless, it is important to consider what can and cannot be equated in this set up.

As a simplified demonstration of this, consider a 2D cross-section of a single T-Bolt at some point between the bushing and the hub. The cross section of the laminate would be a rectangle with a hole in the center for the shaftbolt (with diameter d_{sh}), and the majority of this hole would be filled by the

shaftbolt (with nominal diameter d_{sb}). The width of this section is taken to be the lateral bolt spacing, d_L. As previously mentioned, the bolt pretension allows for some load to be transferred from the outboard laminate to the hub through the root laminate (prior to separation) in addition to that transferred through the bolt. This is because the pretension load deforms the laminate, so when an external load is applied, it must not only overcome the pretension load in the bolt, but also the deformation the laminate. Subsequently, the total external load required to separate the laminate for the hub is higher than the sum of the pretension load in each bolt. Let the ratio of the separation load to the total pretension load be defined as the overload ratio, R_{OL}. Since both the laminate and the bolt are subjected to the same displacement (up to separation) the ratio of the forces is equivalent to the ratio of stiffnesses, specifically the stiffness of the laminate to the bolt

$$R_{OL} = \frac{F_{separation}}{F_{pretension}} \tag{3.2}$$

The pretension load applies a given displacement, δ to the bolt, and thus considering the bolt as a spring

$$F_{pretension} = \delta k_{bolt} = \delta \left(\frac{E_{11} A_{xc}}{L} \right)_{bolt} \tag{3.3}$$

where A_{xc} is the nominal cross-sectional area of the bolt, and E_{11} is the elastic modulus in the axial direction. The same equation can be used to calculate the force required to apply the same displacement to the laminate

$$F_{laminate} = \delta k_{laminate} = \delta \left(\frac{E_{11} A_{xc}}{L} \right)_{laminate} \tag{3.4}$$

Note that for the laminate, the area is calculated as

$$A_{xc} = d_L t - \frac{\pi}{4} d_{sh} \tag{3.5}$$

The laminate can only transfer load when in compression (it is a contact relationship, not a bonded one), so beyond δ, the all of the load is transferred through the bolts. At the displacement δ, separation will occur, thus $F_{laminate} = F_{separation}$. From here the overload ratio can be calculated as

$$R_{OL} = \frac{k_{laminate}}{k_{bolt}} = \frac{(E_{11} A_{xc})_{laminate}}{(E_{11} A_{xc})_{bolt}} \tag{3.6}$$

Note, since the length and displacement of both the laminate and the bolt are equal, they cancel out. The modulus and geometry of the model is known, so this calculation can be performed for the LS and FS submodels.

Performing this calculation for both scales, then comparing, finds that R_{OL} is estimated to be 7% higher at the LS. Furthermore since the pretension loads are known for both the LS and FS, the scaling factor of LS to FS for both the pretension load and separation load can be calculated. Remember, the pretension load was equated by matching axial strain. Calculating these ratios shows a 6% increase in the load scaling factor at the LS, while the load scaling factor is more than three times higher than the geometry scaling factor. These calculations are only a first approximation, but they show the influence of scaling effects (like thread sizes) and the inability for the submodel to be used to predict precise loads for a full root.

This may seem to limit the utility of the submodel; however considering the other simplifications made to the model, it would not be useful to predict load capacity at the FS even if there were no scaling effects. The focus of this investigation was on the geometry of different hole patterns, and this was monitored primarily via strain response. It was ensured that the load conditions between different configurations were the same to maintain a valid comparison, but the aim was not to imitate the full root exactly. By finding the relative performance of different hole patterns an estimation of the strain reduction achievable in a full root can be estimated, and an optimal hole configuration determined. Any new blade using this improved configuration, would have further changes in geometry or material as well, so there is no use in calculating precise loads at this point.

4

Numerical Modelling

This chapter outlines the findings from the first phase of investigation: the numerical modelling. The primary objective of this phase was to explore the different model parameters to understand how root behaviour changes with different geometries. The key learnings found during this exploratory phase are relayed in the first two sections of the chapter. To begin, Section 4.1 outlines the general behaviours seen in the root laminate. Next, the laminate response is investigated as a function of various individual input parameters in Section 4.2. Here, the key findings used to set the design space of the optimization modelling are explained. This final section of the chapter (4.3) describes the results of the optimization modelling used to achieve the secondary objective of the numerical modelling process: determining the most beneficial stagger configurations. These results were used to set the final dimensions for the specimens used in the physical testing. To conclude the chapter a summary section is included to reinforce the main conclusions of the numerical modelling investigation.

4.1. General Model Behaviour

As alluded to before, the 5-bolt submodel has a few distinct behaviors that were discovered in this first phase of investigation. These behaviours are discussed primarily in terms of axial strain, so before diving into the results, 4.1.1 compares the different stress and strain components to justify this decision. From there, it was found that there are distinct behaviors in the first and second rows of bushings as well as the inner and outer bushings. As such, the general behaviour is compartmentalized and then explained by bushing location in subsection 4.1.2. Here the reasoning for using the inner sides of the second row bushings as a point of comparison between configurations is established. Using the second row as the representative region of comparison has consequences in the strain behaviour in the first row as a result of the load paths through the laminate. A discussion of these consequences and corresponding load paths is thus given in 4.1.3. Following these introductions to the key regions of the strain response, subsection 4.1.4 provides a segue from response for a single configuration towards the changes in response for different root configurations by addressing why some stagger patterns are not beneficial, and how these can be separated from configurations that do reduce strain.

4.1.1. Determining Critical Stress Component

The most important regions of the root laminate are those around the bushings. FE modelling allowed for the stress and strain results to be extracted directly at the edges of the bushing holes in the root laminate, where they were the highest. At these locations it was then necessary to determine which components were most critical. This was done by comparing normalized stress components. All stress values presented have been divided by their respective ultimate strengths. These normalized stresses can then be considered as failure indices from a maximum stress criteria to determine which component would induce failure first.

First, the critical components in different regions of a the baseline configuration were anlaysed ($d_L = 25$ mm, $d_A = 42.9$ mm, $d_R = 0.0$ mm). When examining the results at the bushing edge, it was found that some nodes on the edge of the shaft holes were showing locally distorted stresses and strains. Given that these nodes have two free – and thus unloaded – edges, these local variations were

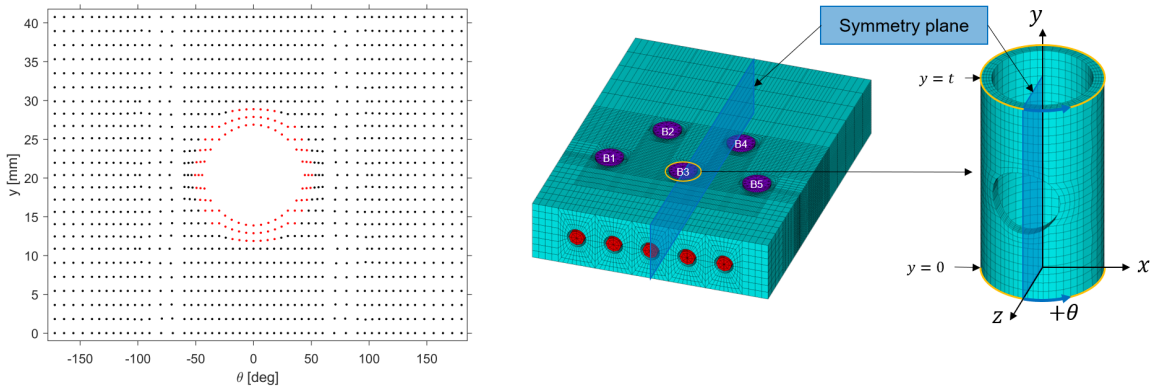

Figure 4.1: Left: flattened representation of the inner ring of nodes around the bushing, where the nodes shown in red were excluded due to element distortion indicated by high aspect ratios. Right: diagram showing how θ and y are defined locally for each bushing (1 to 5) in the model, and how the model is symmetric in the yz plane.

deemed an unrealistic product of element distortion. Subsequently, the nodes attached to any elements with high aspect ratios around the shaft holes where excluded from the analysis. The consequence of this, i.e. the excluded nodes, are shown in red in Figure 4.1. This plot shows a flattened representation of the laminate nodes on the inner surface of the bushing hole, along with the local coordinate system used around each of the bushings. It should be noted that the z direction was chosen to align with the spanwise axis of the blade while retaining a right-handed coordinate system.

The elements and nodes around the bushing holes were created programmatically, so they are in the same location relative to the center of each bushing (B1 through B5, defined as shown in Figure 4.1). The angular position θ was defined as the counterclockwise angle from the front of the bushing, as shown on the right of Figure 4.1. These coordinates make $-180° \leq \theta \leq 0°$ the angular positions on the left side of the bushing and $0° \leq \theta \leq 180°$ those for the right side. More specifically the regions adjacent to B3 where $|\theta| = 90° \pm 25°$ are defined as B3L and B3R for the negative and positive angles respectively. This designation applies to the left and right sides of any of the five bushings holes in the laminate.

Returning to the excluded nodes, it can be seen that there is a small region between $|\theta| \leq 54°$ and $y = [11.8, 28.9]$ mm, where no data was extracted. As a result there is a discontinuity when the laminate behaviour (stress, strain, displacement, etc.) is plotted as a function of y at the front of the bushing. On the other hand, when examining data at the sides of the bushings, this is not seen. The stresses investigated at the remaining nodes around the bushing (shown in black in Figure 4.1) were the axial (σ_z), transverse (σ_x), and shear (τ_{xz}) stresses. Components in the through thickness direction (y), are not shown here because they are out of scope of this project. The laminate used in this submodel contains only root segment fibres which carry axial loads. Out of plane loads, which could arise from root ovalization during transportation for example, are carried by the shell layers used to enclose the root segments, and these layers are not included in this project.

Based upon traditional bolted joints, the maximum stresses were expected to vary in location for each component. To simplify subsequent analyses, the stresses and strains around each bushing were extracted in different planes to isolate the stress trends through the thickness of the laminate and circumferentially around the bushing as a means of finding the region with the highest stresses per component. These were deemed the critical regions and used in subsequent comparisons between different hole configurations.

As expected, the maximum stresses were generally found at $\theta \approx \pm 90°$ for σ_z, $\theta = 0°$ for σ_x, and $35° \lesssim \theta \lesssim 55°$ for τ_{xz}. This can be seen in Figure 4.2, where each stress component is plotted as a function of angular position, θ. Each component is plotted at a constant y location, which corresponds to the through thickness location where the stress component is at a maximum. In other words, many horizontal slices (constant y) were made through the bushing hole, but only the one with the highest stresses is shown, to examine the most critical region. The y locations are listed in Table 4.1. Note the results are only given for B1 to B3, as they are symmetric to those of B3 to B5. The associated

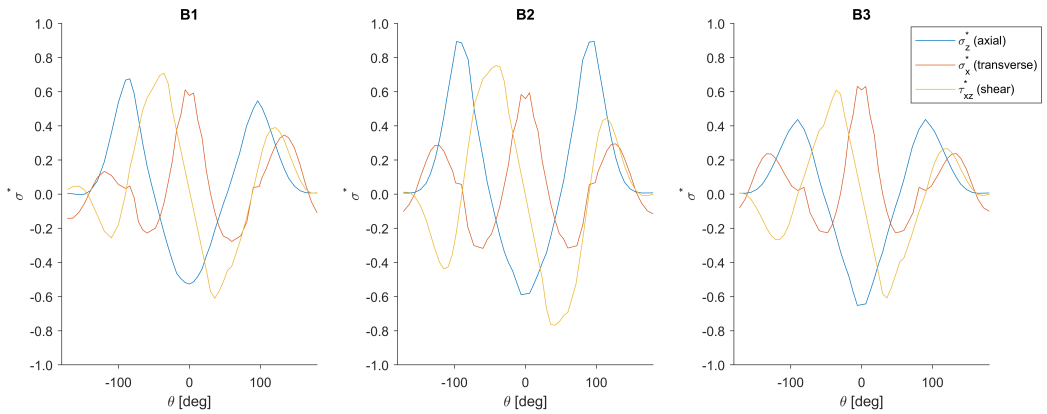

Figure 4.2: Stress response by component around each bushing (B1-B3) as a function of angular position (θ) for the baseline root geometry. Each stress component is shown at a constant through thickness position (y) as given in Table 4.1. This location corresponds to the maximum stress magnitudes, thereby representing the critical y position in the laminate.

symmetry plane and the definition of the local coordinate systems were shown in Figure 4.1.

From these trends, it can be seen that the axial and transverse stress responses were more or less symmetric about the front of the bushing, while the shear stress is antisymmetric about the same plane ($\theta = 0°$). This indicated that even though symmetric constraints were not used on the lateral edges, the response around each bushing was similar to what would be seen if symmetric constraints were used. Comparing the magnitudes of the different components it can be seen that the transverse stresses are of similar magnitude around all the bushings, the axial stresses show the highest values in B2 then successively lower ones in B1 and B3, and lastly, the shear stresses show similar magnitudes at B1 and B2 but lower ones at B3. The conclusions made from these observations are two-fold. Firstly, the most critical stress is the axial stress at B2, and secondly, that the axial stress shows the largest difference between bushings.

It was then necessary to examine the stress behaviour through the thickness of the model, to hone in on the critical regions. This was done using a similar strategy as before, but instead plotting the stress components as a function of y at a constant θ, as shown in Figure 4.3. Once again, only the radial slices with the highest stresses are shown to focus on the critical regions.It should be noted that when these slices occur at $|\theta| \leq 54°$, there is a discontinuity in the center of the laminate due to the excluded nodes around the shaftbolt hole (the red nodes from Figure 4.1). The θ positions at which the slices are made for each bushing and component are also summarized in Table 4.1.

Much like the behaviour as a function of θ, the transverse stress as a function of y shows the same profile at each bushing: a symmetric, near linear decrease in magnitude away from the center of the laminate. This component has the peak magnitudes ≤ 0.6 at each bushing, which gives it the lowest magnitudes at B1 and B2 compared to σ_z, τ_{xz}. The shape of the shear stress response is also quite similar. It shows larger magnitudes at B1 and B2, but the same linear, symmetric shape. At B2 there is a sharp decline at the center of the laminate which is a result of the chamfer in the bushing. This chamfer is to ensure that the threads cut into the bushing do not lie on the contact surface of

Table 4.1: Vertical (y) and angular (θ) locations in cylindrical coordinates of the planes containing the maximum stresses around each bushing. Locations are grouped by stress component and given for bushings 1 through 3 (bushings 3 through 5 are symmetric and their inclusion is redundant). The local coordinate systems used are defined in Figure 4.1.

Bushing	y(max σ_z) [mm]	θ(max σ_z) [deg]	y(max σ_x) [mm]	θ(max σ_x) [deg]	y(max τ_{xz}) [mm]	θ(max τ_{xz}) [deg]
B1	33.5	-90	10.9	0	28.2	-36
B2	31.7	90	10.9	0	28.2	-42
B3	31.7	-90	29.9	0	28.2	-36

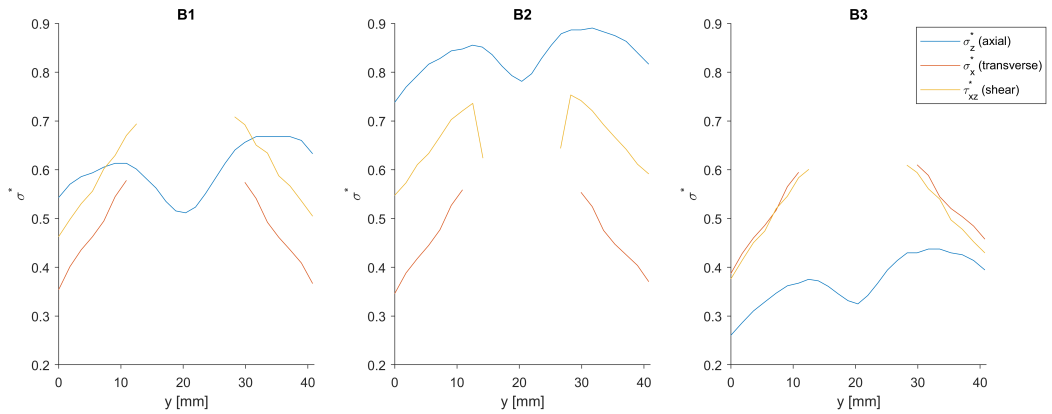

Figure 4.3: Stress response by component around each bushing (B1-B3) as a function of vertical position (y) for the baseline root geometry. Each stress component is shown at a constant angular position (θ) as given in Table 4.1. This location corresponds to the maximum stress magnitudes, thereby representing the critical θ location around the bushing.

the bushing in the blade, and although the threads were not modelled, this chamfer was (as shown in Figure 3.12 from Section 3.3.2). The edge of this chamfer creates a sharp transition in the shear stress where the laminate is no longer in contact with the bushing. The shear stress shows more variation in magnitude between bushing than the transverse, but it is smaller than the variation in the axial stress, which goes from having the lowest magnitudes at B3 to the highest magnitudes at B2. Furthermore, at all y positions adjacent to B2, the axial stress has a higher magnitude than any other component an any other location of the laminate. This was used as the main indication that the axial stress was the most critical component.

Based upon the load conditions and model geometry, it was expected that the axial stress would be the critical response of the laminate, but it was necessary to compare all components as a function of both θ and y to confirm this. The results of this comparison were condensed to the respective θ and y positions that showed the largest magnitudes here. From these plots it was clear that the transverse component could be eliminated as it showed the lowest magnitudes at B1 and B2 (all components are non-critical at B3) and because there are no loads or fibres in this direction. The relative magnitudes of the normalized shear and axial stresses vary per bushing, and even though the shear stresses were shown to be higher around B3, the maximum overall stresses occurred in the axial direction at B2. Furthermore, past experience found the axial component to be the most critical of the components in fatigue loading. The confluence of these factors focused the analysis to a single performance metric: the axial strain. Note, strain was used instead of stress because it can directly be measured from the test specimens.

The previously discussed plots are only for one configuration, but equivalent analyses were also performed for different root geometries to verify that the axial stress remained the critical component. Comparing the results of all the configurations showed that the shapes of the stress trends remained the same as those in Figure 4.2 and Figure 4.3, only with different peak magnitudes. Changes in peak magnitudes were found to change the location of the overall maximum stress, but only by bushing number. In other words, the peak stress continued to be in the axial component and it continued to occur at the same y and θ locations (within a very degrees or millimeters). This indicated that while the geometric stagger pattern influences the magnitude of the stress concentrations, they did not change the global load paths or methods of load transfer. Based upon the geometry of the specimen, this was expected, but necessary to verify before using the axial strain as a method of comparison, in the remainder of the numerical analysis.

4.1.2. Critical Regions in the Laminate

Once the critical strain component was determined, the next step was to determine the critical regions within the laminate. In other words after establishing what to compare, it was necessary to define where to compare it, because not all regions of the laminate are equally loaded. The overall focus for the model is on the structural capacity and thus it is the region of highest axial strain that should be compared

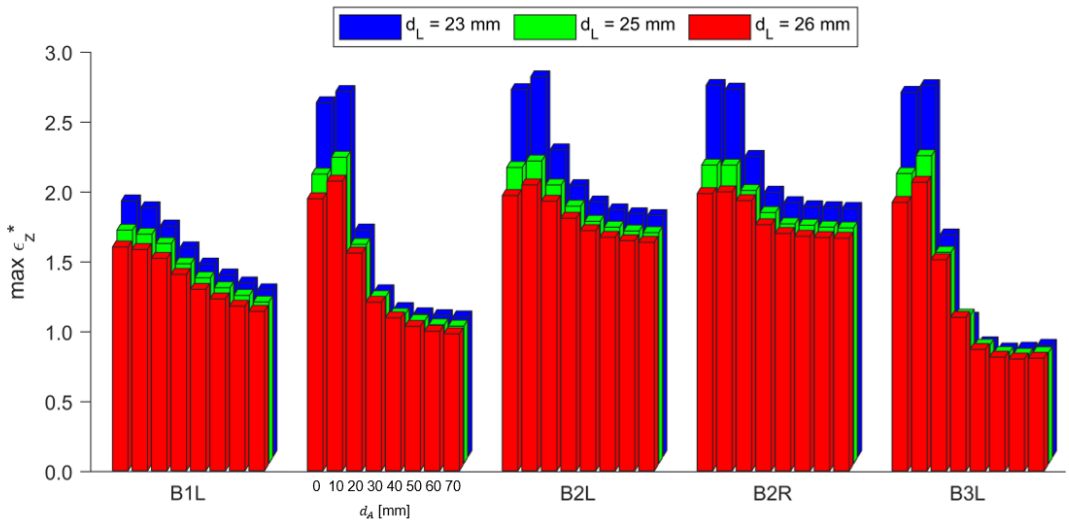

Figure 4.4: Comparison of max strains at five different locations within the model for a variety of stagger geometries. Each of the 5 groups has an array of 24 strain values organized into 3 rows each with 8 columns. Each row and colour represents a d_L spacing while each column represents a d_A spacing. Note the B1R region group title is omitted to define the d_A spacings.

between specimens. Part of the preliminary investigation was to locate this region, and this was done by comparing the ϵ_z response adjacent to each of the bushings. Furthermore, this investigation needed to consider a variety of different stagger patterns to verify if the critical region changed as the placement of the bushing holes changed.

From the symmetric model, five distinct locations were identified: the left and right sides of bushings 1 and 2 (B1L, B1R, B2L, and B2R) and the left side of bushing 3 (B3L). To determine which of these regions was the most critical, the maximum strain through the thickness of the laminate in each region was compared across different lateral and axial spacings, as shown in Figure 4.4. It should be noted that in this plot, and all other numerical results in this chapter, are reported as normalized axial strains, where the axial strain value is divided by the target strain. This plot groups the strain values in each of five locations from left to right, and then within these groups the strains are shown for three lateral spacings (d_L) which are grouped in rows by colour, with the larger d_L values being shown at the back of the graph. In each row within a group, eight multiple axial spacings are shown from left to right, where each bar represents a larger axial spacing, ranging from $d_L = 0$ mm to $d_L = 70$ mm at 10 mm intervals. In other words, there are five groups, each with three rows of eight bars, and the groups distinguish location within the laminate the strain was extracted from, the rows and colours distinguish the d_L spacing of the configuration used, and the lateral position of the bar gives the d_A spacing of the configuration.

Comparing the five locations, it can be seen that the 3x8 groups of B3L and B1R are similar, and the same can be said for B2L and B2R. This allows for the strain response to be classified into three groups: the R1 outer region consisting of B1L, the R1 inner region consisting of B1R and B3L, and the R2 region consisting of B2L and B2R. There are two key geometrical factors that explain this grouping: firstly, if the region is in the first or second row of bushings, and secondly if the region displays edge effects. The first factor is important because the laminate adjacent to the first row of bushings is compressed by the preload in the second row bushings. As evidence of this, compare the strains in the B2R region to the B3L region at $d_A = 0$ mm vs $d_A = 70$mm. This is shown in Figure 4.5.a), and it can be seen that in a single row configuration ($d_A = 0$ mm) the strains are similar, but when there are two rows ($d_A = 60$ mm) the strain response is distinctly different.

The second factor – the influence of edge effects – can be demonstrated in an analogous way: by comparing the strains between B1L, B1R, and B3L at different d_A values, as shown in Figure 4.5.b). Both of these plots show a subset of the data from Figure 4.4 to allow for an easier comparison of their strain values. It can be seen that at both d_A spacings shown, the strain in the B1R region is similar to that of B3L but not of B1L: this is due to the finite width effects which reduce the strain around a

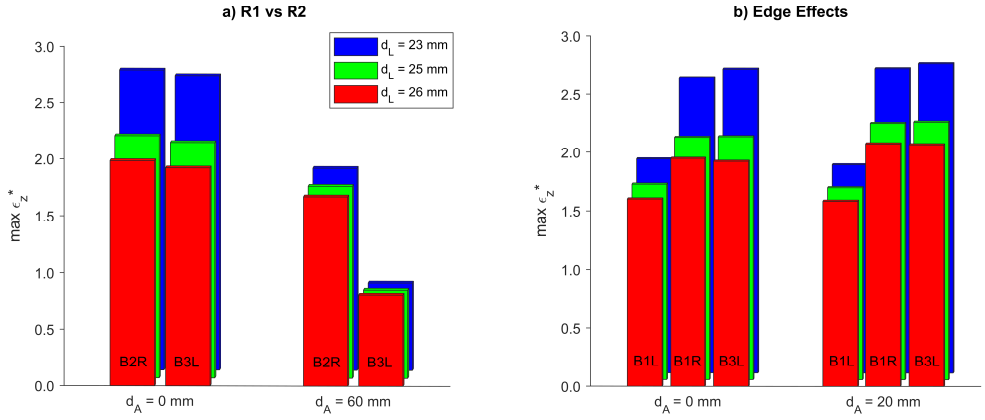

Figure 4.5: Max strains at different locations within the laminate compared to show: a) the difference in first and second row strain response through a comparison of B2R to B3L with and without axial spacing, and b) the influence of edge effects in the B1L region by contrasting the difference between the strains at B1L and B1R with to the similarity of them at B1R and B3L.

hole when it is next to a free edge. In a real root, these edge effects would not be present, but they are unavoidable here and therefore must be recognized. Furthermore, it should be pointed out that at larger d_A values, they influence the strains in B1R as well as B1L. More specifically, the increased strains on either side of B1 (in comparison to B3) are not representative of the root behaviour in a full blade.

It was expected that the submodel behaviour would differ slightly from a full blade, and this comparison confirmed that. This knowledge was then used to focus on the regions of the laminate that were bordered by adjacent bolts. In other words, the regions of the laminate that are most representative of the blade are the B2R and B3L regions, and therefore the remaining regions can be disregarded in the search for the critical region of the laminate.

In addition to the presence of edge effects, the outer region of R1 is distinct because there is no compression from a R2 bolt in this region of the laminate. Without any pretension on the left side of B1, the region is always in tension, whereas the net-section between B1 and B3 is compressed by the preload in B2 and subsequently the strain in the B1R and B3L regions is reduced. It should be noted that this compression in R1 only occurs at large d_A values or when the distance between rows is high enough that the R2 regions show higher strains than the R1 inner regions. For greater understanding of this phenomenon, one must look to the load paths through the root.

4.1.3. Influence of Load Path on Strain Response

Another factor that distinguishes the R2 region is that the R2 bolts carry more load. This is shown in Figure 4.6, where the force in each shaftbolt as a function of external force is shown of the right-hand y-axis (B4 and B5 are not shown due to symmetry). Here it can that the second bolt has a higher load at all external loads above zero for the baseline stagger configuration ($d_L = 25$ mm, $d_A = 42.9$ mm, $d_R = 0.0$ mm). Below this plot, there is a cross-sectional sketch of the root showing the three main load paths that transfer F_{ext} from the endplate into the root. The first two, denoted (1) and (2), are the load paths for the load traveling through the first and second rows of T-Bolts respectively and then into the laminate through contact between the bushing and the laminate. These impose compressive strains at the front of the bushing and high tensile strains adjacent to the bushings in the net-section region. In the case of load path (2), this compressed region in front of the bushing includes the net-section region of the R1 bushings. The final load path, denoted (3), is the transfer of load directly from the endplate into the laminate, bypassing all the T-Bolts.

If one was to plot the cumulative load across the width of the laminate as a function of z, the graph would assume one of two forms depending on if gap opening had been reached or not. Gap opening is when the root is so highly loaded in tension that the laminate begins to separate from the hub or endplate, and this behaviour has been shown to lead to considerable damage and/or risk of failure in the blade. The first form of the graph, prior to gap opening would show an initial load at $z = 0$ from load

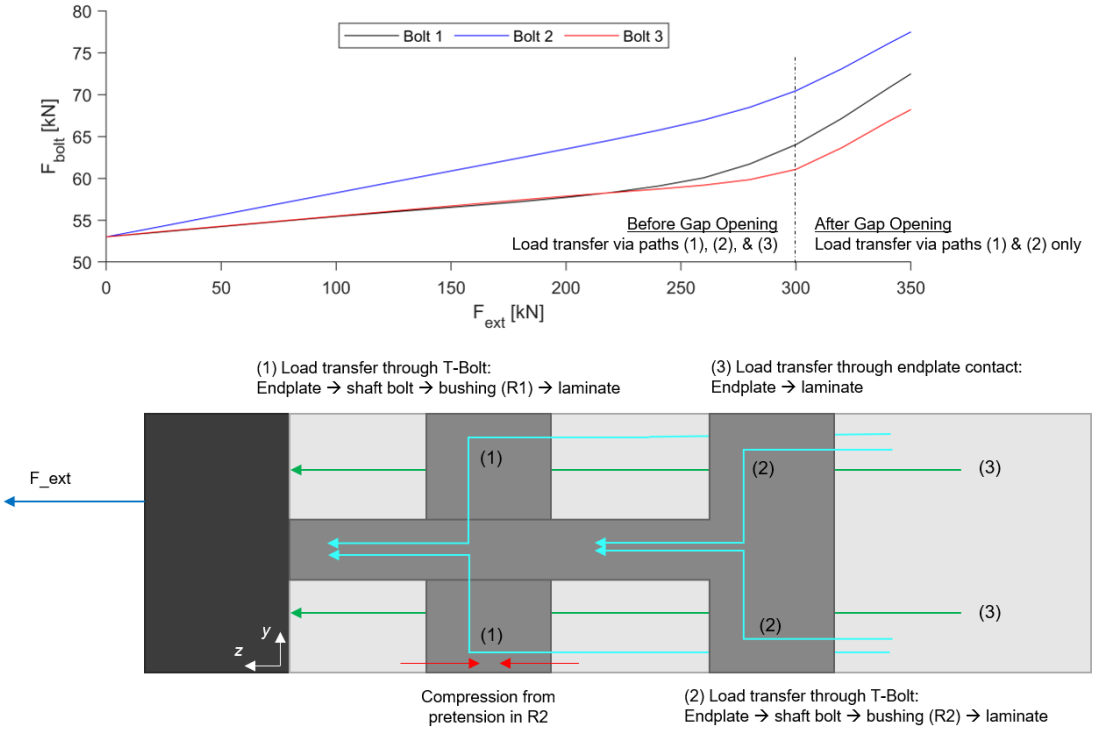

Figure 4.6: Sketch showing load paths through the submodel when an external load is applied to the endplate and pretension is applied to the shaftbolts. The corresponding load in each shaftbolt is also shown to show how the load path changes when contact is lost between the laminate and the endplate (otherwise known as gap opening).

path (3) which would then increase after R1 and R2 as load is transferred through bearing in the T-Bolts. After gap opening, the region between $z = 0$ and R1 would not be transferring any load. Similarly, if the load was plotted as a function of x, it would be seen that the outer regions of the blade do not carry as much load, because there is no R2 bushing, and thus no further load introduction after the first row. In other words, the outer regions are distinct because only load paths (1) and (3) are active. These load introduction points explain why the strain response is different at different locations in the laminate.

Pretension in the shaftbolts enables the direct transfer of load from the endplate into the laminate; however, this is only possible while the endplate and the laminate are in contact. When contact is lost, the endplate begins to separate from the laminate, otherwise known as gap opening. Since path (3) is only active prior to gap opening, increasing F_{ext} beyond this point significantly increased the load in the shaftbolts. This is visible through changes in slope which occur just before 300 kN in Figure 4.6. It should be noted that with the free edges of the submodel, gap opening begins at the outsides of the laminate. First, the corners of the laminate begin to separate from the endplate, and with further loading this gap progresses inwards. As a result, the effects of gap opening can be first seen between $F_{ext} = 240$ kN and 260 kN, with deviations from the initial linear bolt force trends. Full gap opening then occurs at 300 kN, with the separation between the endplate and the laminate at bolt three visible through the change in slope of the red line from Figure 4.6.

Gap opening has been shown to be severely detrimental, to the point of catastrophe [28], and while the behaviour of the root under gap opening is not the focus of this study, it was necessary to find the load at which gap opening occurs, to ensure the specimens where not loaded beyond this point. Therefore the different configurations were subsequently compared at $F_{ext} = 260$ kN. At this load, none of the inner bolts (bolts 2 through 4) show any influence of gap opening, and the model reaches strains representative of the full blade. The onset of gap opening may be visible at the outsides of the laminate here, but this is a result of the free edges, and since these regions are already non-representative, this was not a problem. It should also be noted that while different stagger configurations will experience

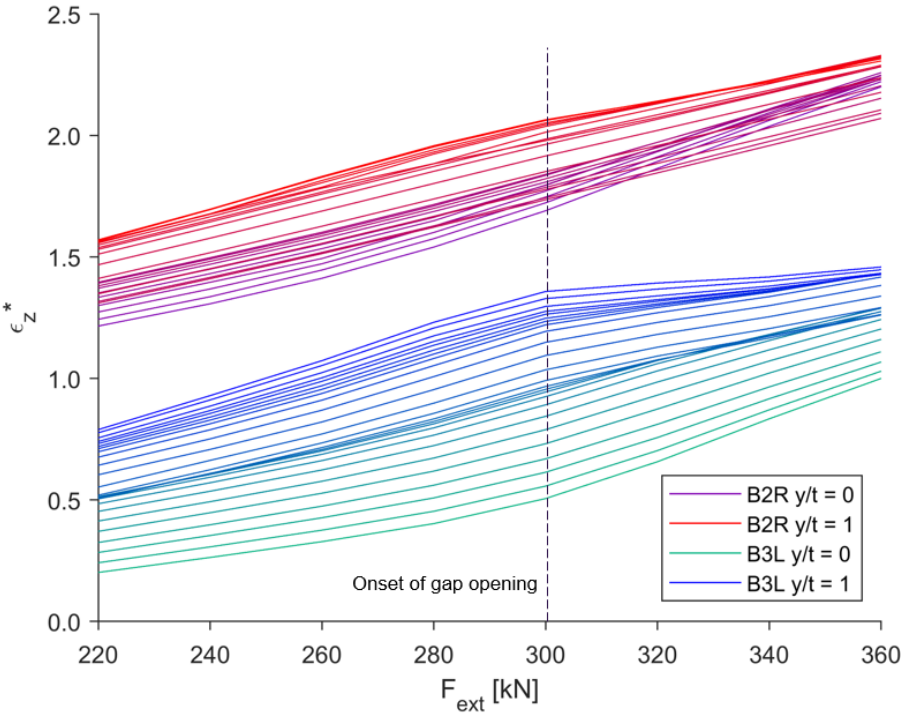

Figure 4.7: Axial strain at multiple locations through the thickness of the laminate adjacent to B2R and B3L as a function of applied external load. The height at which the strain is extracted ranges from the inner surface $y/t = 0$ to the outer surface $y/t = 1$ according to the colour gradient.

gap opening at different loads, the configurations of interest for this study are those that demonstrate increased structural capacity through lower strains. These configurations will subsequently have higher gap opening loads, further supporting to compare and test the configurations at 260 kN.

When the gap opens, the change in load path also changes the strain response. This behaviour is highlighted in Figure 4.7 which shows the response of the B2R and B3L regions specifically around gap opening. The colours of the lines indicate the relative location of their node through the thickness of the laminate with $y/t = 0$ indicating the inner surface of the laminate and $y/t = 1$ indicating the outer surface. Prior to gap opening (to the left of the dashed line), the strain is higher towards the outer surface of the laminate, but after gap-opening the strain profile begins to equalize. This can be seen by the increase in strain vs load slope at nodes towards the inner surface of the blade, visible in B2R and B3L. At the former location, the increase is dramatic enough to load the inner surface of the laminate more than the center region. This shows that the strain bias through the laminate is reliant upon the load transfer along path (3), directly from the laminate to the endplate. It should be noted that while the strain bias decrease, the B2R strains remain higher than those at B3L.

Comparing the strains at B3L and B2R in Figure 4.7 also shows a much broader strain range through the thickness of the laminate around the R1 bushings. This means that there is a large through thickness bias in the first row, which was also noted when setting the load offset method to match the submodel response to the full blade response. The reasoning for this is the manner in which the model bends as a result of the load offset in the 5-bolt submodel compared to a full blade. In this model, the specimens are load subjected to an axially symmetric load, so the midplane of the laminate remains stationary while the endplate deflects out of plane as a result of bending. Conversely, in the full blade, the root is fixed at the hub, and then deflection occurs in the outboard blade through bending. The consequence of this is that the R1 bushings are subject to a larger magnitude of out of plane deflection through bending than the R2 bushings, whereas in a real blade the opposite is true. By match the bending behaviour at the R2 bushings, the R1 bushings in the submodel show more out of plane deflection than in a full blade, and inversely, the tapered region outboard of the R2 bushings would experience less out of plane deflection in the submodel than a full blade. Unfortunately, this cannot be reconciled

with the current set up, which is why the decision was made to match the strain response in the B2R region, so that the most critical region (highest strains) was representative of full blade behaviour.

4.1.4. Beneficial and Detrimental Stagger Patterns

Not all double-row hole configurations are effective at reducing the maximum strain. In fact, starting from a single row pattern, then moving two of the holes outwards (B2 and B4), creates higher strains across the model. This is shown by the yellow peak on the left hand side of in Figure 4.8. This contour plot shows the overall maximum strain in the model for a variety of hole patterns (varied d_A, d_L all with $d_R = 0$). For reference, this plot is accompanied by two screenshots of configurations with bushings spaced relatively close together and far apart. This is useful for visualizing the key distances d_1 and d_2 which are defined as

$$d_1 = \sqrt{d_L^2 + d_A^2}, \qquad d_2 = 2d_L \tag{4.1}$$

These are the distances between a first and second row bushing and between two bushings in the first row respectively. Comparing which distance is longer gives an indication of expected performance of the configuration: when the adjacent bushings in R1 are closer to each other than to those in R2 (exemplified by the upper configuration), the maximum strain in the laminate is lower. These configurations are on the right side of the white line in Figure 4.8, whereas on the left side, some of the stagger patterns show increased strains compared to $d_A = 0$ mm (i.e. a single row configuration).

Across all d_L values, increased strains are seen in configurations with $0 < d_A \lesssim 15$ mm, when compared to a configuration with no staggering ($d_A = 0$ mm). To understand why this occurs, first consider a single, open hole in a monolithic triax laminate. For this laminate, the maximum stress concentration will be at the edge of the hole ($\theta = 90°$, see Section 2.3.5): here the $\pm 0°$ fibres there are carrying extra load that is transferred around the hole by the $\pm 45°$ fibres. Then when two holes are placed close to each other but not side-by-side (with $d_A > 0$), as shown on the right of Figure 4.9, these same $\pm 45°$ fibres are transferring load around the bottom of the bushing in R2 and around the top of the bushing in R1. Furthermore the $\pm 0°$ fibres running over this region must also carry the axial load, and as a result the region will have high axial and shear strains. When the fibres with high shear strains are also carrying axial loads, the axial strains increase, creating the increase in overall axial strain that occurs at small, non-zero axial spacings.

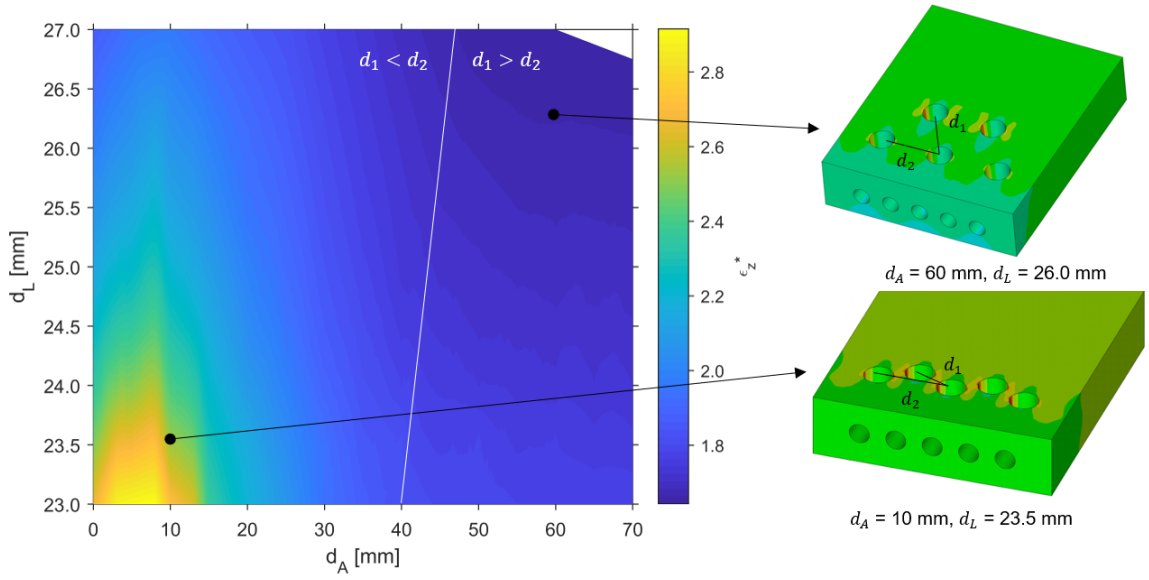

Figure 4.8: Annotated comparison of max strain in the 5-bolt specimen for different lateral and axial spacing configurations, with two example configurations shown on the right. Surface plot produced using code from [105].

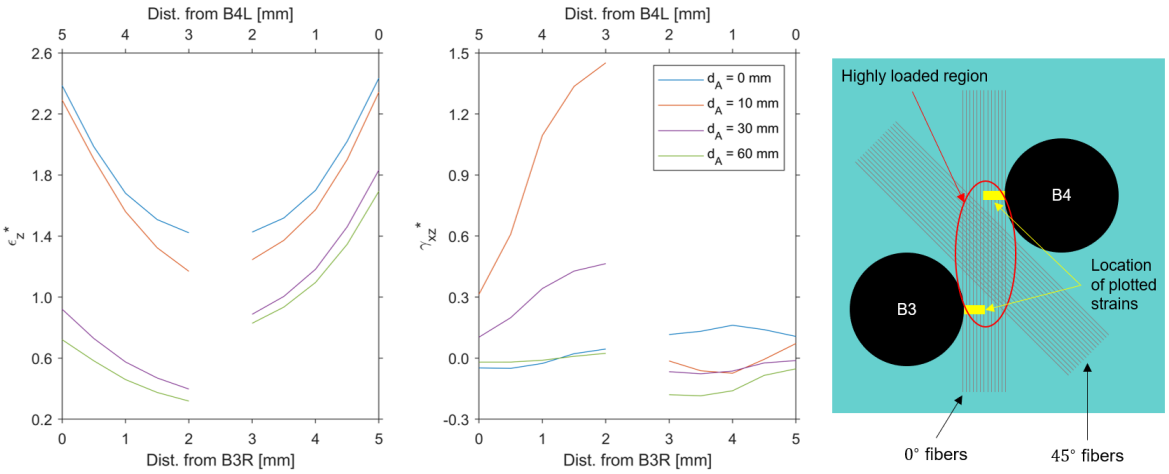

Figure 4.9: Normalized axial and shear strain fields compared under different axial spacings. The plots show the strain values moving radially outward from $\theta = 90°$ and $-90°$ of B3L and B4R respectively, as shown by the region highlighted in yellow on the right-hand sketch.

This phenomenon can be seen by comparing the axial and shear strain fields between B3 and B4 in specimens with different d_A dimensions. Figure 4.9, compares these strain fields for four different axial spacings (all with $d_L = 23.5$ mm). Here it can be seen that the highest shear strains are seen in $d_A = 10, 30$ mm, while the highest axial strains are in $d_A = 0, 10$ mm. The high shear strains in the small stagger configurations demonstrate the overlap in shear transfer regions between the R1 and R2 holes, and when this occurs in region that also contains high axial strains, the compounding effect discussed above is evident. It should be noted that for $d_A = 0$ mm the maximum strains occur at $\theta = \pm 90°$ around each hole, but in $d_A = 10$ mm the compounding effect shifts the location of max strain to $\theta = \pm 96°$ at B3. This explains why the ϵ_z values for $d_A = 10$ mm appear lower than those at $d_A = 0$ mm in Figure 4.9, even though the overall maximum in the laminate is actually higher, as shown in Figure 4.8.

As the axial spacing is increased further, beyond the region of detrimental staggering, the maximum overall strains decrease. Furthermore, at lower axial and lateral spacings, the strain response is more sensitive to changes in geometry. This can be seen by comparing the gradient of ϵ_z^* at different locations across the strain map, as done in Table 4.2. Here the partial gradients with respect to d_L and d_A were calculated at three d_A locations in combination with two d_L locations. Comparing the partial gradients w.r.t d_A, it can be seen that at $d_A = 5$ mm there is a positive gradient, then moving horizontally to $d_A = 20$ mm there is a negative gradient, and finally moving to $d_A = 60$ mm there is again a negative gradient, but this third gradient has a much lower magnitude than either of the first two. This shows that at higher d_A values, the strain response is less sensitive to changes in geometric parameters.

Partial gradients were calculated at high and low d_L values, and from these it can be seen that the

Table 4.2: Maximum strain gradients calculated at six points: low, medium, and high axial spacings (d_A) in combination with low and high lateral spacings (d_L) . The spacing values and normalized axial strain at each location are also provided for context.

d_L [mm]	d_A [mm]	ϵ_z^*	$\partial\epsilon_z^*/\partial d_A$ [mm^{-1}]	$\partial\epsilon_z^*/\partial d_L$ [mm^{-1}]
5.0	23.5	2.675	0.011	-0.405
20.0	23.5	2.166	-0.025	-0.114
60.0	23.5	1.770	-0.001	-0.050
5.0	26.5	2.005	0.009	-0.138
20.0	26.5	1.900	-0.010	-0.071
60.0	26.5	1.652	0.000	-0.028

detrimental staggering is only related to d_A spacings. More specifically, the strain compounding effect increases strains from low d_A values to medium d_A values, then at high d_A values, the gradients level off, and this behaviour occurs at high d_L values as well as low ones. The difference is that at higher d_L values, the magnitudes of the strain gradients are reduced. Increasing d_L always reduces the strain response, because $\partial \epsilon_z^* / \partial d_L$ is negative across all points of the strain map.

To reduce the strain in the laminate, the root configuration must lie in the region of beneficial stagger patterns. From these findings, it is clear that large axial spacings must be used to elicit strain reductions, or specifically: $d_A \gtrsim 50$ mm. Beyond this point, the gradients are reduced, meaning that the stagger patterns are maximizing the potential strain reductions. These configurations occur to the right of the white line shown in Figure 4.8, and in these configurations the bushings are closer to the bushings in their own row than those in the other row. Another way of defining this boundary is:

$$d_A > \sqrt{3} d_L \tag{4.2}$$

In this region, it was also found that the highest strain in the model shifts from occurring around a R1 bushing to a R2 bushing. In other words, the main strain interactions that are causing the high strains shift to the interactions between adjacent bolts in one row, as opposed to interactions between rows. The interactions between rows are the strain compounding effects described above, which were found to be quite detrimental. Although there are also other parameters that contribute to the strain response, these results showed that more in depth studies should focus on large d_A spacings.

4.2. Parameter Specific Behaviour

From the general behaviour of the model, it was more clear which model parameters were linked to strain response overall as opposed to the strain response in a specific region. The findings for these specific parameters are discussed in this section. It was quickly clear that the critical strain response was governed predominantly by the axial, lateral, and radial spacing/offset dimensions (d_A, d_L, d_R). The first two of these have been touched upon already, and they are expanded upon briefly in 4.2.1. The secondary and related later and axial edge spacings d_{Le} and d_{Ae} are given their own discussions in 4.2.2 and 4.2.3 respectively. All five of these parameters are shown in Figure 4.10 for reference. Before returning to the final primary spacing parameter, it is necessary to discuss the findings w.r.t. stagger configurations, for example the impacts of having three bolts in R1 vs three in R2 (4.2.4). This is because preliminary modelling found that in the radial direction, staggering is detrimental to model performance. The reasons for this, and the more beneficial alternative of radial offsets are described in detail in 4.2.5.

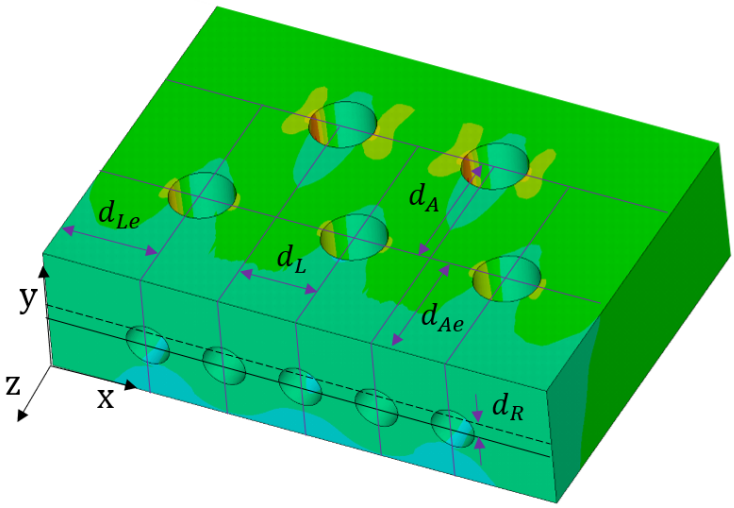

Figure 4.10: Key spacing parameters overlaid onto a screenshot of the 5 bolt submodel used for simulations.

4.2.1. Axial and Lateral Spacing

It is no surprise that moving the bushing holes farther apart decreases the strain in the laminate, but it worth taking a deeper look at the strain response to axial and lateral spacing. One reason for this is to compare the relative importance of each parameter, but another is also to consider the ramifications of only testing at $d_L = 25$ and 26 mm due to geometric constraints. The surface plot presented in Figure 4.8, has been rotated to examine ϵ_z as a function d_L and d_A in Figure 4.11, where one parameter is shown on the x axis and the other is shown through the color map. This allows for easier comparison of the range in strain responses with a specific d_L or d_A configuration.

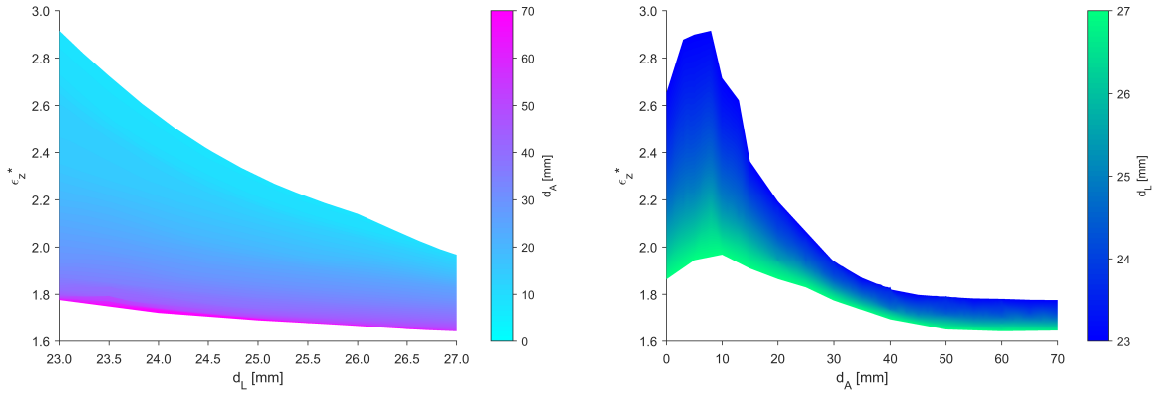

Figure 4.11: Overall max strain in model as a function of lateral (left) and axial (right) spacing shown in two dimensions to isolate normalized strain trends. Two dimensional interpolations were performed using code from [105].

From this representation it is very clear that the strain response to these parameters is coupled. Geometrically this makes sense, the two parameters can be directly correlated to components of the spacing distance. At low $d_A = 0$, changing d_L can reduce the maximum normalized strain from 2.66 at $d_L = 23$ mm to 1.86 at $d_L = 27$ mm, a 30% reduction and a range of 0.80. The difference in strain decreases dramatically at higher axial spacings, with a difference of less than 0.15 between $d_L = 23$ mm and $d_L = 27$ mm at $d_A = 70$ mm. It can also be seen that for all $d_A > 30$ mm, this range remains small (≤ 0.18). Over the range of d_L spacings studied a similar decrease in range can be seen w.r.t. d_A: the range (between $d_A = 0$ mm and $d_A = 70$ mm) goes from 1.14 at $d_L = 23$ mm to 0.33 at $d_L = 27$ mm. When d_L is taken as a constant, the strain range remains larger, whereas when d_A is held constant, the range is remains similar for all $d_A > 30$ mm (reducing only slightly from 0.18 to 0.14). From these observations, it is concluded that the d_A value is more influential on the strain reduction than the d_L value, especially at the large d_A values that show the most beneficial strain reductions.

Another difference between the two spacing parameters is the presence of local maxima and asymptotes, or in other words, the nature of their relationship. Examining the strain response as only a function of the lateral spacing, appears to show a reciprocal relationship: the strains decrease continuously and approach a horizontal asymptote. On the other hand, it can be seen that the axial spacing displays a similar horizontal asymptote as d_A increases, but there is a local maxima under small strain offsets. This behaviour cannot be linked to a common function like that of d_L. Without considering the increased strains at small d_A, an 's'-curve could represent the behaviour. Although this ignores a key region of the behaviour, the region of interest is mainly at those larger d_A values that result in strain reductions. Formal statistical regression was not performed for this data, but it was found that an inverse fit w.r.t. d_L described the trends well. The fits took the form:

$$\epsilon_z\,(d_L) = C_1\,(d_L - C_x)^{-1} + C_2 \tag{4.3}$$

where C_1 and C_2 and fitting parameters, and a horizontal offset of C_x was used as to account for the fact that the lower limit of d_L is set by the spacing at which not material exists between adjacent holes. In a single row configuration this offset would be d_B, but with larger d_A this spacing could (in theory) be further reduced to $d_b/2 + d_s h$. This demonstrates the limitation of such a simple function to fit this behaviour: different d_A would require different C_x constants in addition to different C_1 and C_2 constants. This is a byproduct of the coupling between d_A, d_L, and other parameters, but the general trend of the

reciprocal relationship is valuable. It can be used to estimate relative strain reductions under increased spacings. Considering the coupling between these two parameters, it is clear that the optimization modelling in Phase 2 needs to consider at least two dimensions, specifically in the region of large d_A.

4.2.2. Lateral Edge Spacing

Edge effects, as previously shown in Figure 4.4, were identified as a potential source of a non-representative failure mode. From past research on stress concentrations, it was known that stress concentrations in finite width specimens are influenced by the distance of the hole from the edge. In this model, the region outside the center of B1 and B5 acts essentially like one side of a single hole in a finite width laminate. Thus an investigation was performed to determine the influence of the edge distance on the strain response. Furthermore the results of this investigation were used to set the edge distance of the specimens such that the strain in the B1L region could be reduced. By varying only the edge distance, it was found that that a minimum strain in this outer region could be achieved. This is shown in Figure 4.12, were the relationship between edge distance d_{Le} and the strain in the outer region is shown for a variety of different lateral spacings. Different d_L values were simulated at the LS and FS level to determine how to set the edge distance for the different configurations that were to be tested.

Comparing the three sets of results for the FS model geometry, it can be seen that each of the different d_L spacings achieves a local minimum ϵ_z w.r.t. d_{Le}. What is even more important is that this minimum occurs at a) approximately the same d_{Le} value, and that b) the trend shows a relatively wide minimum. At the FS, the larger lateral spacings ($d_L = 88, 93$ mm) have a minimum at $d_{Le}/d_L = 1.23$ or $d_{Le} = 80$ mm, compared to $d_{Le}/d_L = 1.31$ or $d_{Le} = 85$ mm at $d_L = 83$ mm, but for all configurations, changing the spacing by 5 mm in either direction increases the normalized strain by no more than 0.007. Therefore it was concluded that in the region of the local minimum, the edge distance was not a sensitive parameter and thus different d_L spacings could use the same d_{Le} distance. Even though there were no tests planned at the FS, this distance was selected as 80 mm for any subsequent modelling.

Looking next to the LS data set, only one lateral spacing was investigated because the edge behaviour could be considered independent from d_L with the small range of spacings under investigation. Only 25 and 26 mm spacings are used for the physical testing, so the edge spacing was studied with $d_L = 25$ mm. It was then found that the strain was minimized at an edge distance of $d_{Le} = 30$ mm, which was used in all subsequent tests and simulations. Similar to the FS data, the strain response was not sensitive to small variations in d_{Le}, with the normalized strain not increasing more than 0.003 from the minimum for d_{Le} between 26 and 32 mm. A key difference between the LS and FS behavior is that the optimal d_{Le} value is larger compared to d_b at the LS. Comparing the non-normalized distances, the

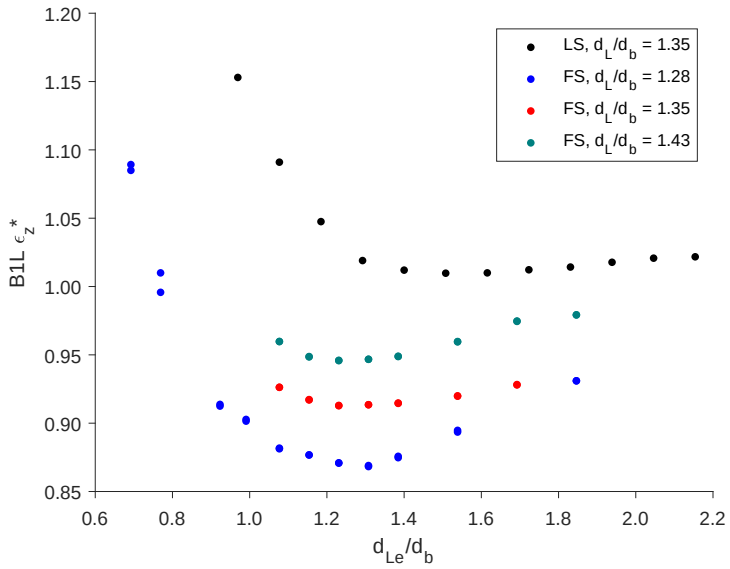

Figure 4.12: Maximum strains adjacent to the outer bushing as a function of lateral edge distance for different configurations.

LS spacing is 2.7 times smaller than the FS, which does not align with the 3.5 times scaling factor used to set the rest of the geometry. This size effect is important to note because it is directly related to the free edge boundary condition: these findings indicate that different specimen scales should investigate these spacings before testing.

4.2.3. Axial Edge Spacing

Given the impact that the lateral edge spacing has on specimen performance, an investigation into the axial edge distance d_{Ae} was also performed. The criticality of this distance is slightly lower because it is related to bearing failure modes, as opposed to net-section or shear-out modes. With the endplate providing a surface against which the laminate is compressed, it is not possible for the bushing to experience bushing failure to the point where it pulls out of the laminate along the loading direction, like in a standard lap joint. Bearing failure can still impact the stiffness of the root and create an interface for the formation/propagation of additional cracks, but it does not cause sudden failure. To investigate the effects of this spacing, d_{Ae} was varied under a couple different lateral and radial spacings. The axial distance between the bushing rows was not varied, because the edge distance only effects the first row of bushings. The results of this investigation are shown in Figure 4.13, where the strain response is shown for the three key regions of the model. The results for each region are grouped together and the line colours are used to distinguish between the different d_L and d_R spacings.

From this comparison, it can be seen that the main effect of increasing d_{Ae} is a reduction in maximum strain around the bushings. This behaviour takes a slightly different form for the B3L region, as there is a kink in the results at $d_{Ae} = 30$ mm. The reason for this kink is unknown as it only appears around B3L, but if it is disregarded, the B3L region shows the same asymptotic decrease as the other regions for increasing d_{Ae}. Comparing the different d_L and d_R configurations it is clear that the influence of d_{Ae} can be considered independent from d_L and d_R as the same trends are seen across each of the configurations in each different region. This makes sense because the d_{Ae} spacing does not change the distances between the bushings, nor their relative positions, it only moves them away from the endplate.

Over the 45 mm range of d_{Ae} spacings simulated, the reduction in strain is most significant in the B1L region. This region is also where separation from the endplate originates due to the free edges. The relatively large change in strains here is attributed to the greater axial distance for the compressive strain field from the bolt pretension to equalize. Further evidence to support this was found by compar-

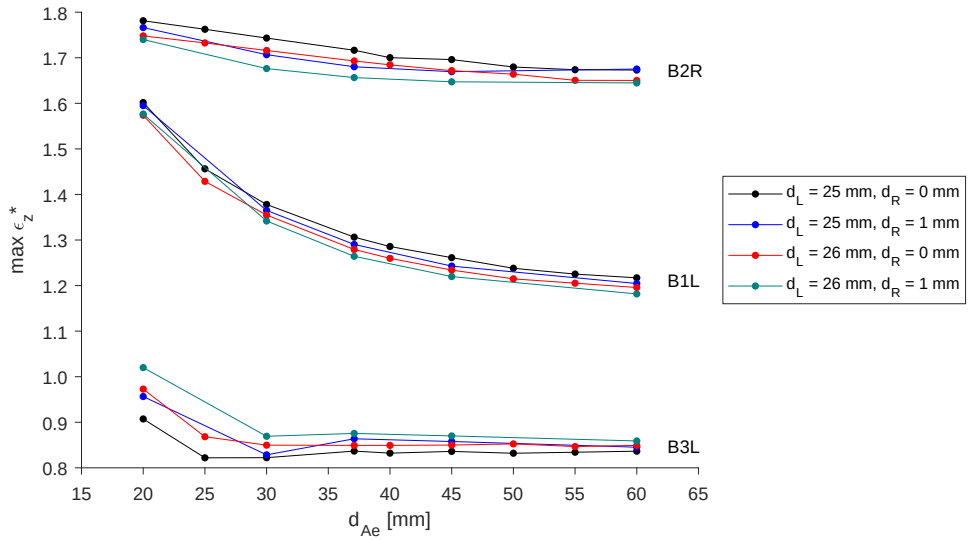

Figure 4.13: Maximum axial strain as a function of axial edge distance. Results are displayed at three locations (from top to bottom: B2R, B1L, and B3L) and colours are used to distinguish four different spacing geometries: combinations of small and large lateral spacings ($d_L = 25$ mm or $d_L = 26$ mm) with small and large radial offsets ($d_R = 0.0$ mm or $d_R = 1.0$ mm). All geometries used an axial spacing of $d_A = 42.9$ mm.

ing the strain and displacement maps across the front of the laminate (between the endplate and R1 bushings across the entire width). Configurations with low axial edge distances show ϵ_z contours that run parallel to the shaftbolts between the R1 bushings and the front of the laminate. Similarly, there are higher axial displacements in front of these bushings, creating a wave pattern with peaks (higher UZ) in front of the R1 bolts and valleys (lower UZ) in front of the R2 bolts and at the edges of the specimen. In the configurations with higher d_{Ae} distances, neither this wave pattern, nor the axial contours are seen. Instead, the ϵ_z contours have a parabolic shape created a closed region in front of the R1 bushings, and the displacement is relatively equal across the width of the specimen, reducing only at the edges. The change from one response to the other can be seen for configurations with d_{Ae} distances over 35 mm. At distances larger than this, the strain field is considered equalized, but there is still a small amount of separation at the outside of the specimens. This explains the asymptotic strain response in the B2R and B3L regions while the B1L region shows a similar response but with a slower approach to the asymptote w.r.t. d_{Ae}.

Due to the asymptotic strain response, the initial value of $d_{Ae} = 37.1$ mm was retained for all further simulations. This has the advantage of being directly compatible with existing FS geometries. It could be pointed out that increasing d_{Ae} to 60 mm would provide an additional strain reduction in the critical B2R region. It would reduce the normalized strains by roughly 0.043 in the configurations without radial offset and by between 0.005 and 0.013 for the configurations with radial offset (compared to $d_{Ae} = 37.1$ mm). There are a few counter points to this. Firstly, a blade root segment only has a finite length, and increasing d_{Ae} thus limits the space available for larger d_A distances. When comparing the strain savings associated with the 20 mm increase in d_{Ae} proposed here, to a decrease in d_A of 20 mm, there may be a net increase in strain. This depends on what d_A was changing between. For example a change from 30 mm to 10 mm would have a very high increase in strain, whereas one from 70 mm to 50 mm would have a lower strain increase.

The second counter point returns to the way that the submodel bends in comparison to a real blade. Since the out of plane bending increases towards the endplate, it is suspected that shifting the entire bolt pattern towards the center of the specimen is reducing the influence of the off-center loading. This artificially lowers the strains, since in a real blade moving the bushings holes away from the hub would increase the bending. Comparing the average strain through the thickness of the laminate (which is less impacted by bending) around B2R between $d_{Ae} = 37.1$ mm and $d_{Ae} = 60$ mm, it can be seen that the strain reduction is lower. It is important to note that bending in the shaftbolts can also be very problematic. The combination of the bending effects and geometric restrictions provided clear motivation not to increase the d_{Ae} distance further.

4.2.4. Stagger Options

In addition to the edge distances, another parameter that was studied and then deemed to be secondary was the stagger configuration of the T-Bolts. When looking at the top of the specimens, or the outside of a blade, this can be visualized as placing more bushings near the endplate, i.e. |∴| , or swapping the first and second rows, i.e. |⁚∴| . In a full blade, there would be more bolts around the entire blade root and the difference between the two configurations would be diminished. During preliminary modelling both configurations were run and the results were compared across different combinations of d_A and d_L. In all cases the trends in strain response were the same, with maximum strain differences of no more than 5% in the IR and 10% in the OR of bushings B2 to B4. The maximum strain at the bushing edge was lower in |⁚∴| configurations, but in the OR nodes (2 mm from the bushing edge) the strains were higher. This indicates that the |⁚∴| may slightly reduce strain concentrations, but it results in higher strain levels in the net-section between the bushings. This makes sense because it has more bushings in the second row, which was identified as the highly loaded area. With more bolts in the second row, the axial displacement of the model also decreased slightly, further supporting that the difference in behaviour could be attributed to average bolt length.

With an odd number of bolts needed for lateral symmetry, it was known that there would be small differences associated with which row has the greater number of bolts, but this difference is magnified in the LS specimens since they only have 5 bolts. This difference would be reduced for a wider specimen, and nearly non-existent for a full blade root which has well over 100 bolts. Given such a small difference ($\leq 5\%$) in the maximum strains, the difference between stagger configurations was deemed inconsequential from an overall performance point of view. However, with the consideration of the edge effects that influence strains around B1 and B5, there are significant consequences. R2 bolts

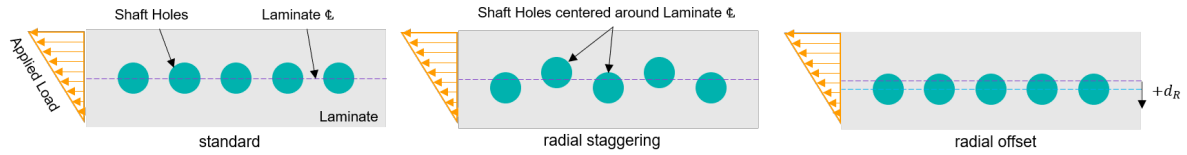

Figure 4.14: Front view sketches of the different options for the positioning of the shaftbolts through the thickness of the laminate.

are more highly loaded, therefore in all future simulations, and in all the physical tests, the |∴.| configuration was used for the axial spacing to minimize the strains around the outer bolts. This decision also has ramifications in full-scale blades, as a design that uses precast root segments will have regions of the root where two root segments are placed beside each other, but have an edge connected only by resin. This could be a critical region, and thus it would be recommended to have the bolts adjacent to this edge positioned in the first row.

The difference between stagger configurations was not only a consideration for the axial staggering, that is the position of the bolts along the length of the blade, but also for the position of the shaftbolts through the thickness of the root laminate. This project explored bolt staggering and positioning in all three dimensions, so it was also investigated if moving the shaftbolts could improve the strain performance of the blade. Typically, the bolts are positioned along the centerline of the laminate, but the could be staggered to alternate one above one below the centerline, or they could all be moved uniformly towards one side of the laminate. These three concepts are contrasted from left to right in Figure 4.14. Through preliminary modelling it was found that no degree of radial staggering (regardless of distance or configuration) reduced strains in the blade. The response of the blade is however sensitive to a uniform offset: moving all the bolts towards one surface of the laminate. It was found that moving the bolts towards the inner surface of the blade could reduce the strains in the laminate. Before presenting and explaining these improvements, it is useful to touch on what they mean.

The premise of axial staggering is to increase the distance between the bushing holes. Introducing radial staggering increases the distance between the shaftbolt holes, but uniformly shifting the holes does not. Finding that the radial staggering does not reduce the strains was taken to indicate that the stress concentrations are not affected by the distance between the shaftbolt holes. The bushing holes are much larger and directly loaded in bearing, whereas the shaftbolt holes are not loaded, they run parallel to the load direction simply offer a channel for the shaftbolts to connect to the endplate. As such, the shaftbolt positioning only influences the load path between the laminate and the endplate. The outer surface of a blade is more highly loaded, so the position of the shaftbolt affects the amount of load carried by the shaftbolt compared to the laminate. Considering the area across the front of the specimen, as shown in Figure 4.14, it can be seen that offsetting the shaftbolt holes changes the fraction of the cross-sectional area of the laminate above and below the laminate centerline. In other words, when the shaft holes move down, there is more laminate above the centerline that can transfer load to the endplate. This is also the region with more load to transfer. An alternative way to consider this is that the shaftbolt being shifted to a position through the thickness that transfers less load. It was found that this can be utilized as a method to reduce strain around the bushings.

4.2.5. Radial Offset

The effects of radial offsets were studied in the region of lowest strains, that is $d_A > 40$ mm for $d_L = 25, 26$ mm, as a way to counteract the strain bias seen through the thickness of the laminate due to the off-center load. As introduced in Section 3.3.3, the strain profile through the thickness of the laminate displays two peaks roughly 20% and 80% through the thickness of the laminate. Without any load offset, these two peaks are equal in magnitude, but as the load offset increases, the magnitude of the peak towards the outer surface ($y/t \approx 0.2$) increases, while the other decreases. It was found that moving the shaftbolt towards the inner surface of the blade (negative global y direction, but positive d_R offset), increases the magnitude of the lower peak, while decreasing the magnitude of the upper peak. A comparison of strain profiles in the B2R region for different d_R offsets, as shown in Figure 4.15 where $d_A = 60$ mm, $d_L = 26$ mm, demonstrates this behaviour.

The light blue line shows the strain profile when there is no radial offset, and as expected the strain is higher towards the outer surface of the blade. By the time the offset has been increased to 1.0 mm

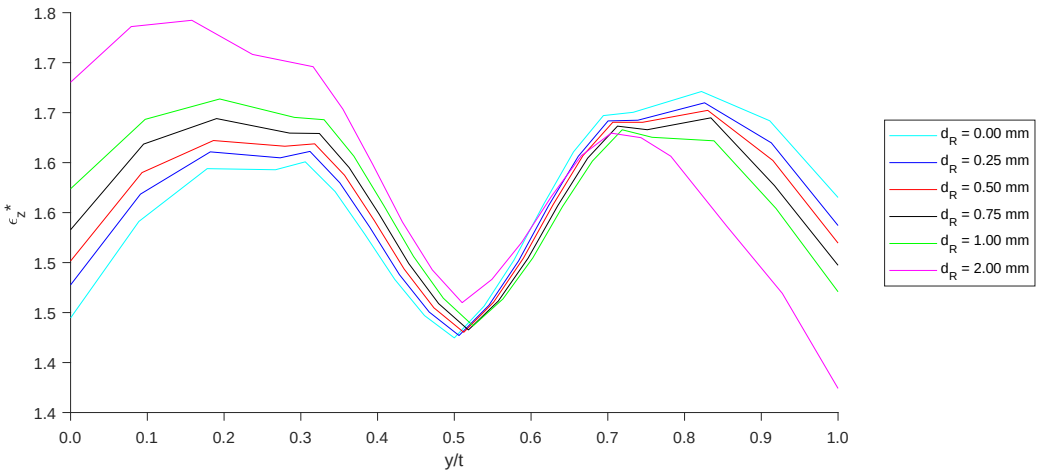

Figure 4.15: Comparison of strain profiles through the thickness of the laminate at the B2R location for different radial offset distances. All configurations have $d_L = 26$ mm and $d_A = 60$ mm

(light green line), the inner peak is already slightly higher, but the overall maximum strain at $d_R = 1.0$ mm is lower than that at $d_R = 0.0$ mm. When d_R is increased to 2.0 mm, that is the shaftbolt centers are 2.0 mm closer to the inner surface of the laminate than the centerline, the peak strain in the lower half of the laminate is higher than the maximum strain without any shaftbolt offset. This shows that the range of d_R that creates a beneficial effect on the load distribution is very small, less than 5% of the thickness

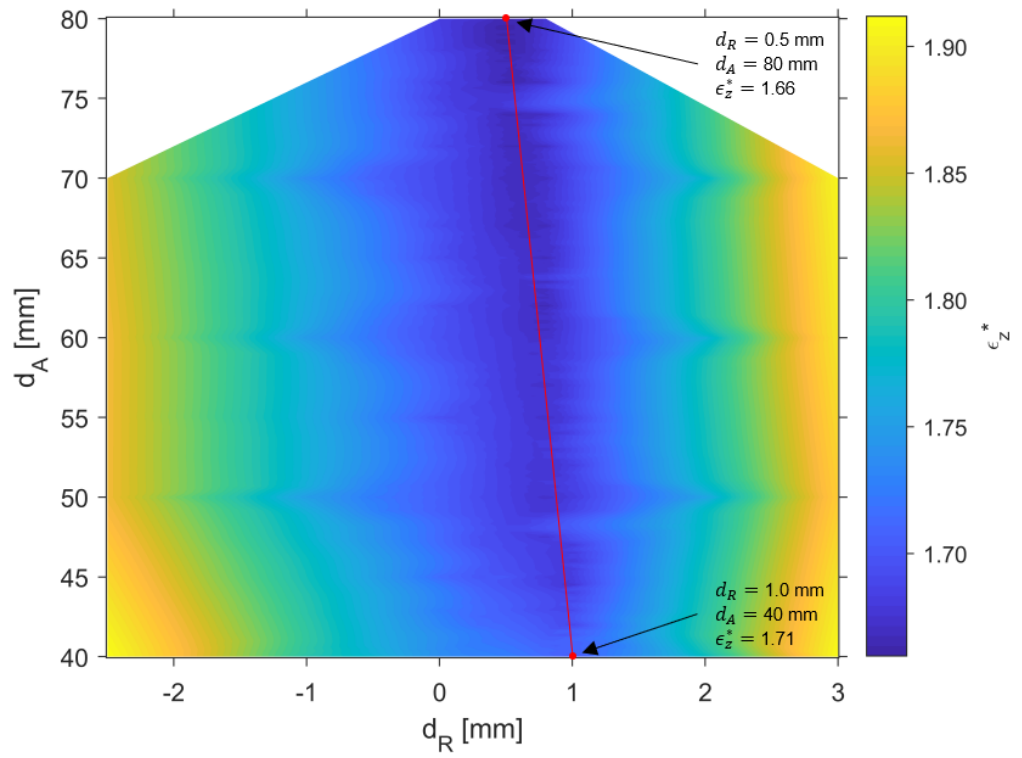

Figure 4.16: Overall max strain in model as a function of radial (x-axis) and axial (y-axis) spacing for $d_L = 25$ mm shown as a surface plot. Two dimensional interpolations were performed using code from [105].

of the laminate. Even with such a small variation, the maximum strain through the thickness of the laminate increase by nearly 5%. This indicates that a fine tolerance will be required for manufacturing at the lab-scale to properly capture the effects of these offsets.

This demonstration is given only for a specific axial and lateral spacing, but the same behaviour (changing the strain distribution by offsetting the shaftbolts) is seen across all configurations to some degree. The most beneficial d_R distance changes with different d_A and d_L configurations, as shown in Figure 4.16. Here the dark blue trough that indicates the lowest overall strain values moves closer to $d_R = 0$ for larger d_A values. This plot shows $d_L = 25$ mm, but the same plot with $d_L = 26$ mm shows very similar results: the minimum strain trough is in the same place (moving from $d_R \approx 1$ towards $d_R = 0$ with increasing d_A) and the magnitude of the normalized strain results are lower by 0.025.

4.3. Optimization Modelling

The final task of the numerical investigation was to address the second main goal of the project: to determine the most beneficial stagger patterns and investigate how much they can decrease the maximum strain in the model. From the exploratory investigations, the general spacing parameters that would lead to the lowest strain response was narrowed down to $d_A \gtrsim 50$ mm and $0 \lesssim d_R \lesssim 2$ mm. It was generally found that the larger the lateral spacing, the lower the strain; however, this corresponds to fewer T-Bolts in the blade as a whole. As with the LS, a full root is also limited by the size of the nuts, or rather the tool required to tighten them. This goes to say, in a full root d_L is often determined by other factors, so it was not varied continuously in these simulations. Instead, three individual values were simulated separately: 23.7 mm, 25.0 mm, and 26.0 mm. The first was obtained by scaling, while the second two represent the closest spacings possible to test at the LS.

The remaining parameters (d_A, d_R) were varied in 0.5 to effectively create three two dimensional optimization exercises. It was known that, at some point, increasing d_A would no longer decrease the axial strain appreciably, but this may not occur before $d_A = 80$ mm which was set as the upper limit for the current geometry. The lower limit was set at $d_A = 40$ mm, because even though this region would have higher strains, it would include the baseline stagger pattern with $d_L = 42.9$ mm. In nearly all of these configurations, the R2 bushings are closer to each other than to the R1 bushings, therefore it was known the critical strain would occur in the B2R region. As the d_R distance changed, it was known that the strain at the inner and outer surfaces would approach the same value, but this is only beneficial

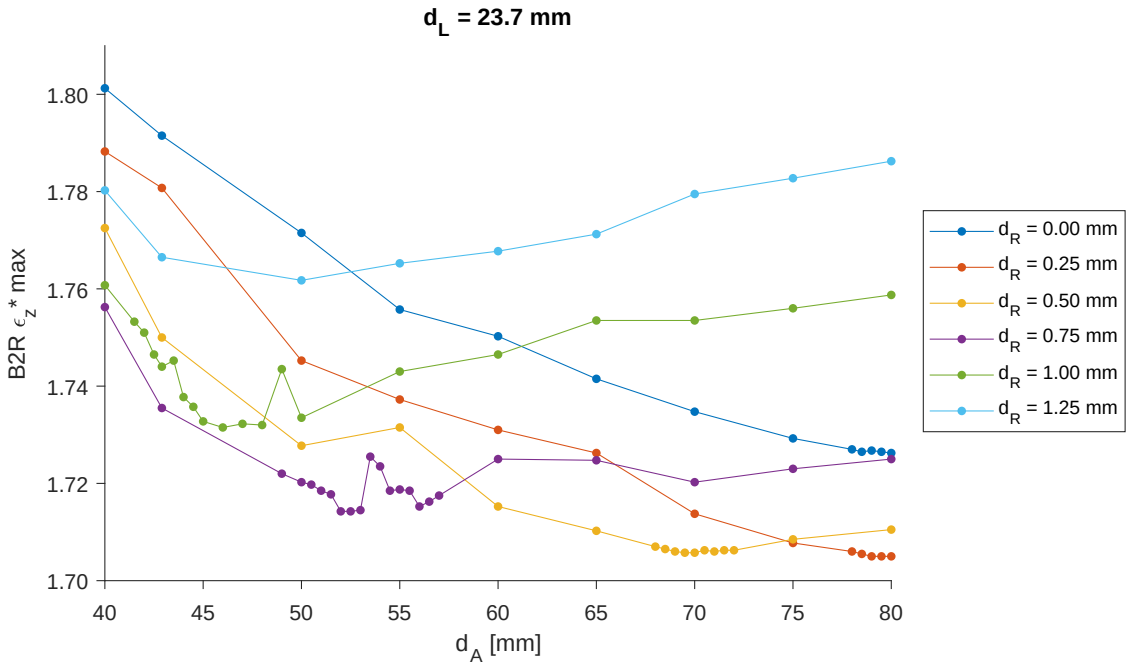

Figure 4.17: Maximum axial strain in the B2R region for different radial offsets as a function of axial spacing for $d_L = 23.7$ mm.

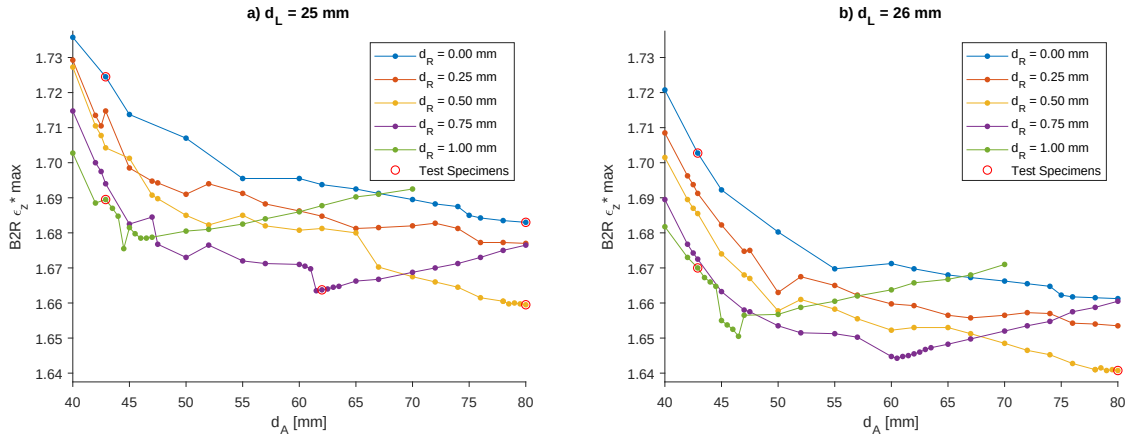

Figure 4.18: Maximum axial strain in the B2R region for different radial offsets as a function of axial spacing. Results are separated by lateral spacing where a) contains data from $d_L = 25.0$ mm and b) from $d_L = 26.0$ mm. Each of the plots also highlights the configurations used for physical testing with red circles.

as long as the overall maximum strain is reduced. Therefore, the different hole configurations were compared on the basis of max ϵ_z through the thickness of the laminate in the B2R region.

The results of these simulations are shown in Figure 4.17 for $d_L = 23.7$ mm and Figure 4.18 $d_L = 25, 26$ mm. In each of these plots, the colors are used to indicate the same radial offsets from $d_R = 0.00$ mm to $d_R = 1.25$; higher offsets result in higher strains and were thus excluded. Additionally, the sudden dip in ϵ_z values around $d_A = 45$ mm seen in the $d_R = 1.00$ mm trends at $d_L = 25, 26$ mm, is suspected to be fictitious but investigating the inputs and outputs of the model did not find any irregularities. From these plots it can be seen that the incorporation of small radial offsets brings a larger strain reduction at smaller d_L spacings (i.e. configurations with higher strains/strain concentrations). While the d_R distance that is most beneficial changes with d_A and d_L, the reduction in ϵ_z stays relatively constant at a normalized strain ≥ 0.021. The maximum benefit is as much as 0.056 at $d_L = 23.7$, the lateral spacing that shows the most benefit from radial staggering. In the larger d_L configurations at $d_A = 42.9$ mm the strain benefit is 0.035 and 0.033 for $d_L = 25, 26$ mm respectively.

To reinforces the observation that d_R is more impactful at smaller d_L spacings, one should look at the d_A values where each d_R trend achieves the minimum strain. Comparing Figure 4.18 to Figure 4.17 shows the three key minimums (in increasing ϵ_z and decreasing d_A) shifting from $d_R = 0.50, 0.75, 1.00$ mm to $d_R = 0.25, 0.50, 0.75$ mm. Subsequently the $d_R = 0.75, 0.50$ mm trends reach their minimum strains at d_A spacings 10 mm lower. On the one hand this is advantageous, because for a given radial offset, the bushing pattern employs a smaller d_A, but on the other this could be problematic in that it shows that the strain is highly sensitive to small radial offsets, offsets on the same order as the manufacturing and alignment tolerances of the blade.

The incorporation of radial offsets creates local minima in the strain response as a function of d_A. As the offset increases, the location of this minima moves to a lower d_A value, but the overall minimum strain increases slightly. It can therefore be concluded that regardless of d_R and d_L, the overall maximum strain in the laminate can be reduced by increasing d_A. As expected, the reduction in strain that is achieved between subsequent minima at different d_R values also decreases with d_A, or in other words the gains plateau. With this in mind, it is suspected that a larger radial offset of $d_R = 0.75$ mm is most advantageous because it offers a reduction of between 0.017 and 0.019 (for $d_L = 25, 26$ mm) in maximum strain while also reducing d_A by 20 mm (or more) compared to the minimum strain without radial offset. At the smaller axial spacing of 23.7 mm, the optimal offset is clearly $d_R = 0.50$ mm because it achieves the minimum strain (normalized strain reduction of 0.021) while reducing d_A by 10 mm.

It should be noted that increasing d_A does not reduce the strain everywhere in the laminate. The R2 regions see roughly double the strain of those in the first row, so the increases in strain seen around B3 do not affect the overall maximum strain. If only the strain around B3 is considered, an axial spacing of $d_A \approx 60$ mm minimizes the strain for all d_R and d_L values. In this region, increasing or decreasing d_A by less than 10 mm changes the maximum normalized strain at B3 by no more than 0.003. Through Figure 4.19, it can be seen that the location of this minima shifts slightly towards higher d_A values (from

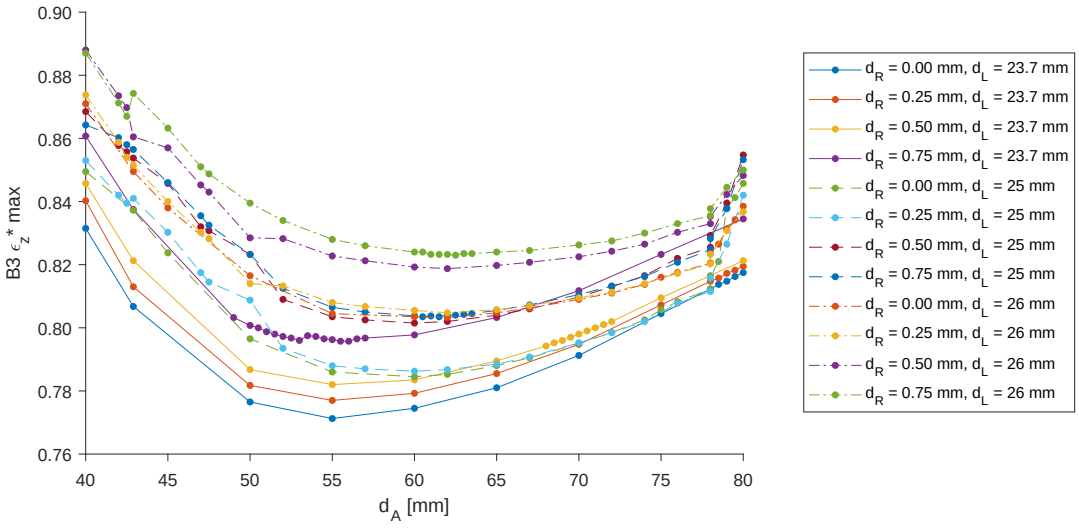

Figure 4.19: Maximum axial strain in the B3 region for different radial offsets and lateral spacings as a function of axial spacing.

60 mm to 62 mm) for larger d_L and d_R values. While the strain response is not very sensitive to d_A around B3, it is more sensitive to changes in d_R. For $d_R > 0.3$ mm there is an increase of over 0.02 in ϵ_z^* at B3 when compared to a configuration with no radial offset. Unlike in R2, the radial offset is detrimental; however, when considering a configuration with $d_A = 60$ mm, the increase in strain at B3 between $d_R = 0.00$ mm and $d_R = 0.75$ mm is smaller than the decrease at B2R that is gained between the same two configurations. Considering this, and the fact that the B2R region remains the critical region of the laminate, the radial offset geometry is still favourable from an overall strain perspective.

Overall from this final phase of numerical investigation, it was predicted that the strain response in the laminate could be subdued through increased axial spacing and the incorporation of radial offsets. To verify these results, the most beneficial configurations for a few different geometries were selected for physical testing. These were pointed out in Figure 4.18 and were selected to coincide (more or less) with the local minima seen. These configurations were listed in Table 3.2, but some context to why they were chosen can now be given. The configurations at $d_A = 42.9$ mm were chosen to show the performance of the baseline staggering with and without radial offset, and these were tested at $d_L = 25.0$ and 26.0 mm to confirm the benefits of radial offsetting at multiple lateral spacings. The extended configurations, those with $d_A = 80.0$ mm were chosen to show the maximum reduction in axial strain possible, and finally a configuration at $d_L = 25.0$ mm, $d_A = 62.0$ mm and $d_R = 0.75$ mm was chosen to test the ability of radial offsetting to reduce strains without increasing d_A as much. It should be noted that for this configuration 62.0 mm was chosen over 61.5 mm because of the jump in strain between 61.0 mm and 61.5 mm.

4.4. Summary of Main Findings

The many different aspects and geometric parameters of root joint design were considered in this chapter. Through the numerical modelling performed, a model was created to imitate full blade behaviour through a reduced, 5-bolt model. This model incorporated an offset load, to imitate the strain bias through the thickness of the laminate. Furthermore, not only did the strain profiles through the thickness align, but the corresponding lines of action for the applied tensile loads are at 67% and 65% of the laminate thickness for the model vs. a typical blade. In this aspect, the physical behaviour of the blade was well imitated; however, it was found that the bending behaviour is slightly different between the simplified model and a real blade.

The difference in bending behaviour was a result of removing the tapered region of the laminate, and meant that the offset load affected the first and second bushing rows slightly differently. It was therefore decided to focus the comparison of different root designs on the strains in the second row and ensure these were the most representative of a real blade. This region contains the highest strains

and thus offers the greatest capacity for root improvement. To focus on this region, less representative behaviours in the first row and specifically the outer bushings was accepted.

One of the key findings from the numerical modelling was how to limit these non-representative behaviours occurring in the outer regions of the laminates. Unlike in a real blade, this model has free edges on either side of the specimen, and it was shown that the lack of adjacent material and the lack of additional, pretensioned bolts changed the laminate behaviour. For configurations with small axial and lateral spacings, these changes result in lower strains in the outer regions, but for beneficial stagger parameters (with larger spacings) these regions showed increased strains. The main handles to reduce these strains are primarily the lateral edge distance d_{Le} and secondarily the axial edge distance d_{Ae}. These parameters were studied and chosen to minimize the strains at the specimen edges and limit the non-representative bending effects for $d_{Le} = 30$ mm and $d_{Ae} = 37.1$ mm respectively.

With the secondary parameters understood, the main investigation into the primary design parameters could be performed. These parameters, in order of decreasing significance, are the axial spacing d_A, the lateral spacing d_L, and the radial offset d_R. For reference they were also shown in Figure 4.10. The strain response was found to very by bushing row, and when the two rows are close together, the higher strains occur in the first row. As d_A is increased the peak strains shift to the second row of bushings, and their peak magnitudes subsequently reduce. Two dimensional stagger studies (d_L and d_A) found that this transition occurs very close to the geometry where the bushings are equal close to their neighbour in the same row as their neighbour in other row. In other words the overall peak strains are lower when distance between B2 and B4 is less than the distance between B2 and B3. In configurations were the opposite is true, the regions beside the first row bushings that show high axial strains also show high shear strains. These strains then compound and increase the peak axial strain, creating configurations with a poorer overall performance and with peak strains in the first row of bushings instead of the second.

The main investigations into the primary spacing parameters focused on the configurations that reduced strain: those with $d_A > \sqrt{3}d_L$ or $d_A \approx [60, 80]$ mm. It was known that stagger patterns could reduce axial strains, and the numerical investigation was then carried out to find how this reduction occurred, how much the strains could be reduced, and which spacings should be used to achieve this maximum reduction. It was found that once the critical strain location shifts to the second row, both 2D spacing parameters (d_A and d_L) shift to an inverse relationship between peak strain and increased spacing. That is increasing either distance will continue to reduce the axial strain, but the strain benefit decreases at large spacings like $d_A = 80$ mm or $d_L = 26$ mm. Changing d_L is not a good handle for reducing strain, because it effects the number of T-Bolts that can be fit around an entire blade, which can subsequently impact the root diameter, but d_A offers a range of stagger possibilities capable of reducing the normalized maximum strain by 28% from a $d_A = 0$ mm or by 4% from $d_A = 42.9$ mm (for $d_L = 23.7$ mm and $d_A = 80$ mm).

The other major finding of this numerical modelling is that by radially offsetting the shaftbolts in the laminate away from the blade's outer surface, the strain bias effect can be counteracted. Shifting the shaftbolts away from the highly loaded surface adjusts the load path through the laminate: the region carrying the most load has a smaller percentage of its cross-sectional area occupied by the shaftbolt hole, and thus it is expected that the laminate transfers load directly into the endplate through contact. The reduction of strains using this technique aligns with the observation that load carried via the bushings and bolts creates a greater stress concentration than the bypass loads that is then transferred directly to the endplate.

A small offset of $d_R \leq 1.0$ mm towards the inner surface will reduce the strain bias through the thickness, but an offset too large towards the inner surface, or towards the outer surface, will increase the peak strains through the laminate. Without any radial offset, the model shows a tilted strain trend with two peaks just above and below the shaftbolt with the magnitude of the outer peak being higher than the inner. Introducing d_R rotates this trend, and with small d_R values come small rotations, and thus the magnitude of the outer peak can be reduced. Further rotation then increases the inner peak to a point that exceeds the initial magnitude of the outer peak. Subsequently, there is a narrow trough of d_R values that reduce the peak axial strains and thus improve root capacity.

To truly understand the benefit that can be gained through these parameters, it was necessary to combine all three primary parameters in an optimization effort. This was the final section presented in the chapter, and from this process the key guidelines for designing a configuration with the minimal axial strain can be distilled. It was found that the axial spacing offers a greater potential for reducing

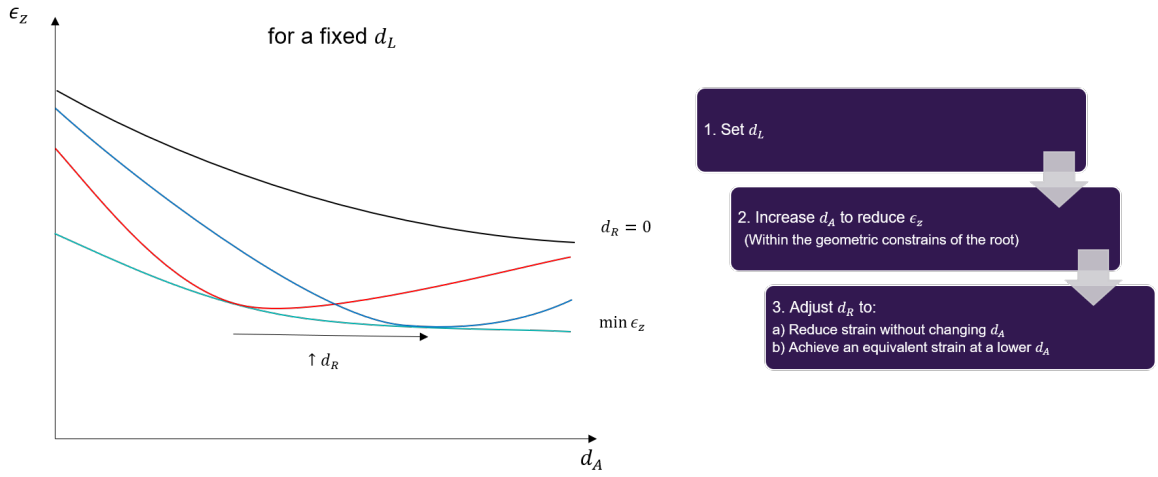

Figure 4.20: Overview of suggested root design process for minimizing axial strain including a sketched graph showing the impact of axial spacing and radial offsets on the maximum strain in the laminate.

strain than the lateral spacing than the lateral spacing or radial offset. Furthermore, minimizing d_L is advantageous from a root diameter perspective, and therefore is typically fixed. As previously mentioned, the largest strain reduction is then achieved by increasing d_A, but this distance can only be increased so much: the second row must be placed before the root laminate begins to taper. Once the maximum d_A has been reached the radial offset can be used as a tool to fine tune the strain. This can take one of two forms: the radial offset can minimize the axial strain for the current geometry by equalizing the strain profile through the thickness, or alternatively, it can be adjusted to achieve an equivalent axial strain at a smaller d_A if the root geometry needs to be condensed. These guidelines are summarized in Figure 4.20, which reiterates these recommended process by showing how the different spacing parameters effect the maximum strain in the laminate.

To provide some numerical context to the strain reductions achievable by fine tuning d_A and d_R, a summary of the key strain minima from the combined optimization of all three parameters has been included in Table 4.3. Here the baseline configuration, a stagger configuration implemented previously is shown first, without any radial offset. Then the successive minima that can be achieved through further axial spacing and/or the incorporation of radial offsets are shown. The strain reduction numbers show how much the strain can be reduced compared to a single row configuration. Each of these minima change in location and magnitude slightly with different d_L values: the magnitudes of the strain minima increase and the d_A values at which each d_R minima occurs increases as well. These results show how d_R can either reduce the minimum strain, like between the baseline and baseline with d_R, or how changing d_R can find an equivalently low strain at a smaller d_A by changing from the absolute minimum to intermediate minima 1 or 2.

Table 4.3: Summary of optimal strain values and associated strain reductions found from the numerical model for different stagger configurations with their associated dimensions. All strain values are the overall maximum in the laminate, and the strain reductions are calculated from a configuration with no staggering ($d_L = 23.7$ mm and $d_A, d_R = 0$ mm). Only one lateral spacing is shown here, because d_L is typically fixed by external factors and is preferred to be as low as possible.

Configuration	d_L [mm]	d_A [mm]	d_R [mm]	ϵ_Z^*	Strain Reduction
Baseline	23.7	42.9	0.00	1.792	25.7%
Baseline with d_R	23.7	42.9	0.75	1.736	28.0%
Intermediate minima 1	23.7	52.0	0.75	1.714	28.9%
Intermediate minima 2	23.7	70.0	0.50	1.706	29.3%
Minimum without d_R	23.7	80.0	0.00	1.726	28.4%
Absolute minimum	23.7	80.0	0.25	1.705	29.3%

5

Experimental Testing

A series of tests were carried out to verify the trends in root response found through numerical modelling. These tests were performed with the double-hinge fixture setup described in Section 3.2.2 using a 500 kN MTS fatigue machine. In this chapter, the results of these tests are presented and compared with numerical predictions from the model used in the previous chapter. The processing of the DIC data was performed using Ncorr, an open-source Matlab software written by Blaber et al. [106]. Harilal and Ramji [107] have demonstrated that this software performs well when compared against commercial post-processing methods.

To fully present the findings from the experimental campaign, the results are broken into sections. First an introduction to the tests performed and he results that will be compared between them is given in Section 5.1. This section also provides an overview of how the 10 different hole and load configurations can be grouped to set up the subsequent presentation of results, the first of which are the center-loaded tests presented in Section 5.2. These results are presented as a direct comparison between numerical predictions and experimental results. The remaining results are broken down by key parameter (d_L, d_A, & d_R) in individual subsections in Section 5.3. Each subsection compares two specimens that differ only by the parameter in question. After all of the static test results have been presented, discussion is given to a few limitations of the experimental process, specifically why they occurred an how they impacted the results in Section 5.4. Lastly, while the static results comprise the majority of the experimental work, two fatigue tests were also performed to verify the assumption that geometric parameters have the same influence in static and fatigue loading. Section 5.5 presents the results from these tests and assesses the accuracy of this assumption. As a conclusion to the chapter, this discussion is the extrapolated to consider the results from all tests and how they can be used to validate the numerical model.

5.1. Overview

The 10 specimens that were tested can be broken into five groups of different d_L and d_A spacing combinations that define the specimen geometry. Within each of these d_L and d_A combinations there are between one and three test specimens (denoted A through C), and each of these have varied d_R spacings and/or use different load mechanisms. An overview of these specimens is given in Figure 5.1. It should be noted that the d_R values given in this table are the measured offsets, not the design dimensions given in Section 3.2.2. As a result of the tolerances around the shaftbolts, the design d_R often differed slightly from the measured values. This overview is useful to visualize what is changing between specimens, for example: moving vertically from the first row to the second row denotes a change in load mechanism (on- to off-center), moving horizontally from column 1 to 2 denotes a change in axial spacing and moving from column 1 to 4 denotes a change in lateral spacing.

Each of the static test specimens were loaded to the target load of 260 kN, at which point strains were measured to compared between configurations. Specimens were then loaded further to verify that the yield point of the laminate was not reached. This can be verified from the test machine load vs displacement data, as shown in Figure 5.2. In this plot, the load vs machine displacement results for each of the specimens are compared. Each of the data sets were shifted so that zero displacement was

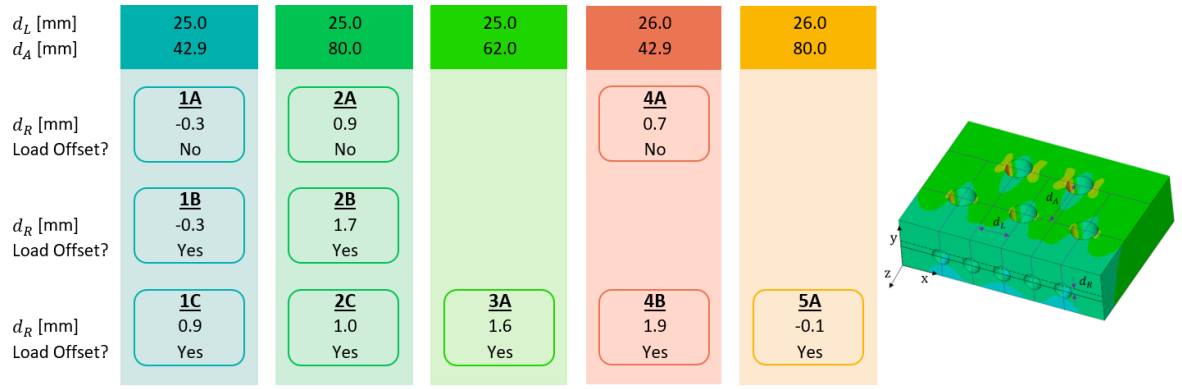

Figure 5.1: Overview of the differences between test specimens: specimen number (1-5) identifying the axial and lateral spacings and specimen letter (A-C) identifying the measured radial offset and load method.

defined as the displacement at 10 kN of external load. With the double hinge fixture, there was some slack between the pin connections, so this shift was necessary to highlight how the stiffness differed between specimens. Specimens 1B, 1C, and 5A are called out to explain their deviation from the linear response shown by the rest of the specimens. In the case of 1B and 1C the 8.8 grade steel nuts side failed at 304 and 342 kN respectively. Specimen 5A was loaded to 436 kN, in an attempt to test to failure, and while the yield point was exceeded, failure was not seen. Inspection of the specimen after removing it from the machine showed bending in all of the bushings and some of the shaftbolts.

The goal of these tests was to validate the strain behaviour before failure, so the results were analysed in the linear response region, specifically at the target load of 260 kN. To collect data at this load, the machine was held with a constant displacement; therefore, small pressure variations in the hydraulic system created the small kink seen in the load displacement curve seen on the right side of Figure 5.2. Examining this region, it can be seen that the displacement between an external load of 10 kN to the target load of 260 kN differed between specimens. This demonstrates that (as expected) the different hole configurations have different stiffness values and thus different behaviours.

To get a closer look at the differences in behaviours between specimens, the strains across the front surface of the laminate as measured through DIC were compared. When extracting and comparing these values, there are two things to consider: the reference state used for the DIC calculations, and

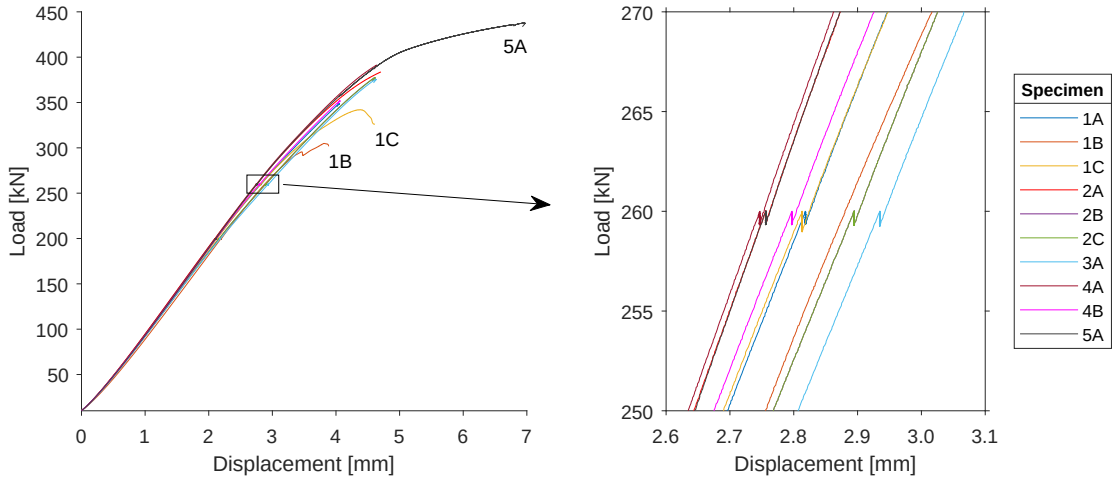

Figure 5.2: Test machine load vs displacement data for all static specimens, with a zoomed in region on the right highlighting the differences in displacement at the target load of 260 kN. The three labelled trends on the left correspond to the two specimens (1B and 1C) that exhibited nut failure and specimen 5A which was loaded past the yield point.

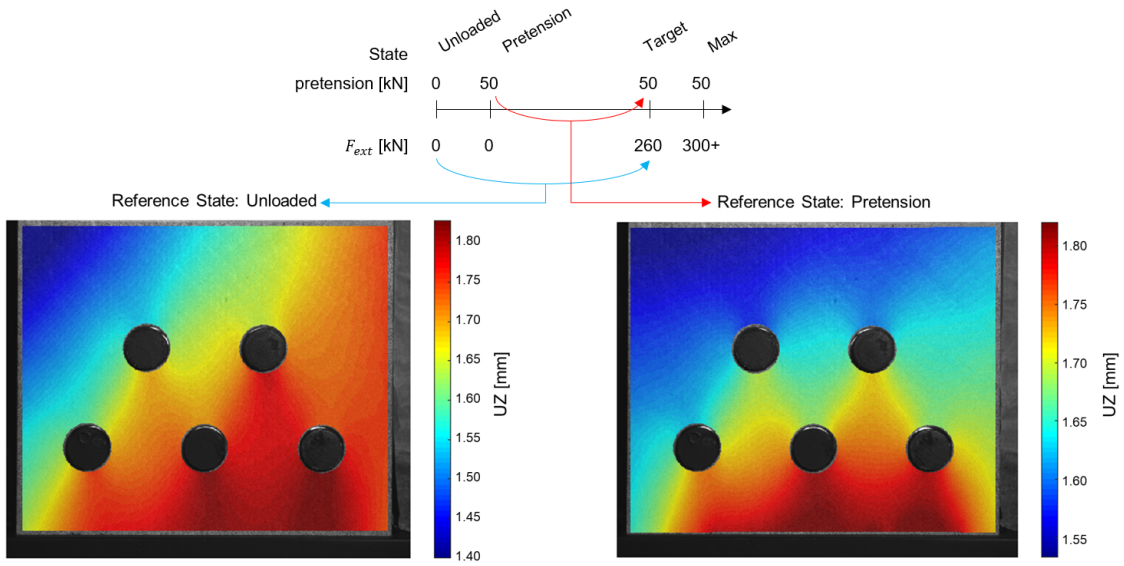

Figure 5.3: Axial displacement plots of the back surface of specimen 1A using the unloaded state as a reference (left) compared to the pretension state (right). Above the displacement fields, the load values of each state are defined.

then where on the specimen specific strains are extracted. To calculate strains through DIC, two images must be compared, and the relative displacements and thus strains between these states are then calculated. As with the numerical model, the loads were applied to the specimen in stages, specifically the pretension load was applied as a step change. As a result, the target load state could be compared to the unloaded state (no pretension and no external load) or the pretension state (full pretension load but no external load). These states are further clarified in Figure 5.3, which also uses the back side of specimen 1A as an example of how the displacement measurements can change when the unloaded state (left) is used as a reference compared to the pretension state (right).

Comparing the two displacement fields from the back of specimen 1A shows a change in displacement trends. More specifically, from the unloaded state, the axial displacement contours running diagonally from the bottom left to the top right of the specimen, but from the pretension state these contours make a conical shape originating from the bushings and spreading towards the front of the laminate. This indicates that for the latter, the largest axial displacements occur just in front of the bushings. Since this is the region with the most bearing load and thus the most local compression, this makes sense. For the unloaded state, there are larger displacements on the right side of the specimen than the left, indicating a rotation within the specimen. Specimen 1A provides one example of how the displacement and strain fields change when different reference states are used. Some (but not all) of the other specimens showed similar behaviour, and this phenomenon is discussed further in Section 5.4. For now it is introduced to explain the different reference states used to analyse the experimental results.

The final matter to discuss before examining the results is the locations across the specimen at which the strain results are extracted. These locations are shown on a test specimen in Figure 5.4. To identify the locations, the same notation was used as in the numerical model: the bolt is defined by BX where X is a number between 1 and 5 indicated the bolts position from left to right across the specimen, then L or R is added to indicate if the strain is extracted from the left or right side of the bushing. It should be noted that the experimental strains cannot be extracted at the interface between the bushing and the laminate, but instead they are extracted at a 2 mm offset from the edge of the bushing hole. The additional extraction locations shown here are the net-section (NSXY) locations. These points are the midpoint between bushings X and Y in the net-section region of the laminate. They are useful to consider to get a broader picture of the predicted vs experimental performance. Furthermore, as previously discussed, the critical region of the specimen is between the second row bushings. Therefore when analysing the experimental results for each specimen, the results across the

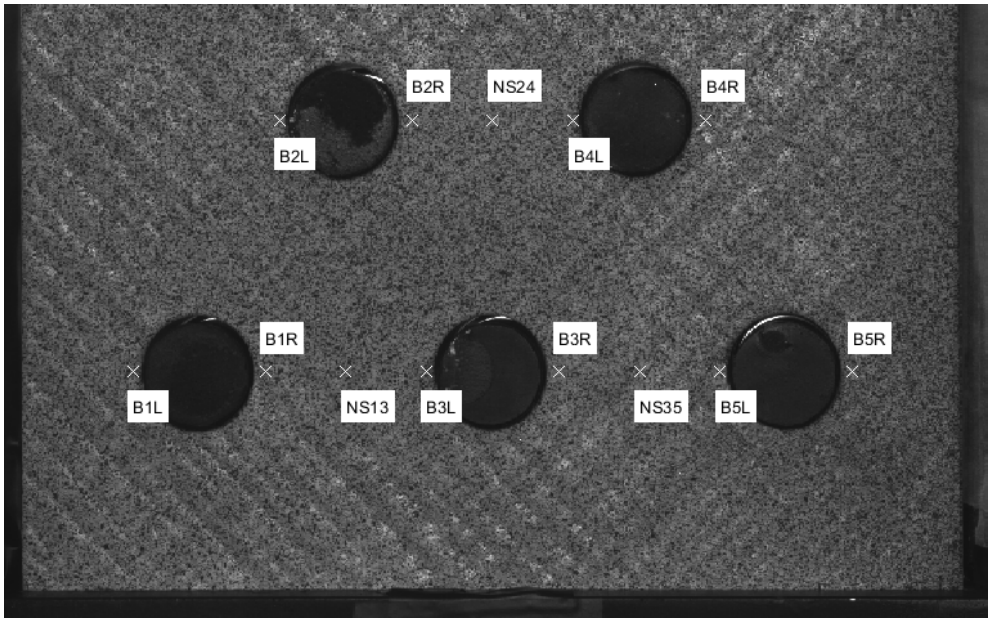

Figure 5.4: Locations across the laminate at which strain values were extracted from the DIC analysis for comparison between the experimental results and numerical predictions.

second row are presented. For the subsequent analysis, the axial strain results from the front surface of the laminate at these five locations (B2L, B2R, NS24, B4L, and B4R) shown in Figure 5.4 are used extensively.

5.2. Center Loaded Tests

Specimens 1A, 2A, and 4A were loaded along the centerline of the laminate, and while these configurations were less representative of true blade root behaviour, they showed the closest agreement to the numerical strain predictions. Subsequently, these are the only specimens for which it is useful to make direct comparisons between the experimental results and the numerical predictions. Quantitatively, the strains in the second row of bushings were extracted and compared using the pretension state as a reference to avoid any rigid translation issues. A summary of the key strains for these three specimens is given in Table 5.1. To provide some context to these values and to offer some qualitative comparison, the strain maps from the front and back of 1A are shown in Figure 5.5. For brevity, only the front and back strain maps for this configuration are shown here; for a complete collection of strain maps refer to Appendix A.

From the tabular results it can be seen that front and back surfaces yield symmetric results for specimens 1A and 4A but not for specimen 2A. Here the symmetry discussed is about the midplane of the laminate (half the thickness), and can also be seen visually by comparing the two right-hand images in Figure 5.5. Specifically, the green butterfly shaped strain contours occur in the same location on both surfaces (just to the left and right of the bushings), and they are of comparable sizes in both plots. Around the second row bushings, the butterfly shape extends axially from $z = -60$ mm to $z = -95$mm on both surfaces. There is also a small amount of connection between the first and second row strain fields in specimen 1A which can also be seen in the ANSYS predictions on the left side.

Examining the tabular strain values, it can be that the measured values are lower than the predicted ones, which is visible through the lack of red contours in the right hand images. This under prediction was common across all center-loaded specimens, on their front and back surfaces. For specimens 1A and 4A, this under prediction is between 20% and 30%, and it suspected that one cause of this is the tendency for numerical models to predict steeper strain gradients than can actually be sustained in the GFRP laminate. Additionally, numerical models are capable of predicting strains right up to the bushing, whereas the DIC method has a small zone adjacent to the bushing that is obscured by its shadow. This means the regions of highest strain cannot be measured with DIC, and this is why the

strains are compared at a 2 mm offset from the edge of the bushings.

Table 5.1: Second row strains for center load specimens on the front and back surfaces. Note all strains are given in [μm/m], and the error values are calculated using the ANSYS predictions as the reference.

Front, PreT

1A	B2L	B2R	NS24	B4L	B4R
ANSYS	3241	3255	1731	3256	3240
DIC	2236	2363	1348	2685	2398
error	-31%	-27%	-22%	-18%	-26%

2A	B2L	B2R	NS24	B4L	B4R
ANSYS	3015	3079	1712	3081	3014
DIC	1491	1582	678	1394	1282
error	-51%	-49%	-60%	-55%	-57%

4A	B2L	B2R	NS24	B4L	B4R
ANSYS	3181	3199	1655	3197	3182
DIC	2423	2315	1187	2467	2266
error	-24%	-28%	-28%	-23%	-29%

Back, PreT

1A	B2L	B2R	NS24	B4L	B4R
ANSYS	3240	3255	1731	3256	3240
DIC	2415	2285	1211	2951	2239
error	-25%	-30%	-30%	-9%	-31%

2A	B2L	B2R	NS24	B4L	B4R
ANSYS	3031	3091	1723	3092	3030
DIC	3216	3141	1968	3116	2978
error	6%	2%	14%	1%	-2%

4A	B2L	B2R	NS24	B4L	B4R
ANSYS	3190	3187	1650	3187	3189
DIC	2597	2376	1482	2868	2548
error	-19%	-25%	-10%	-10%	-20%

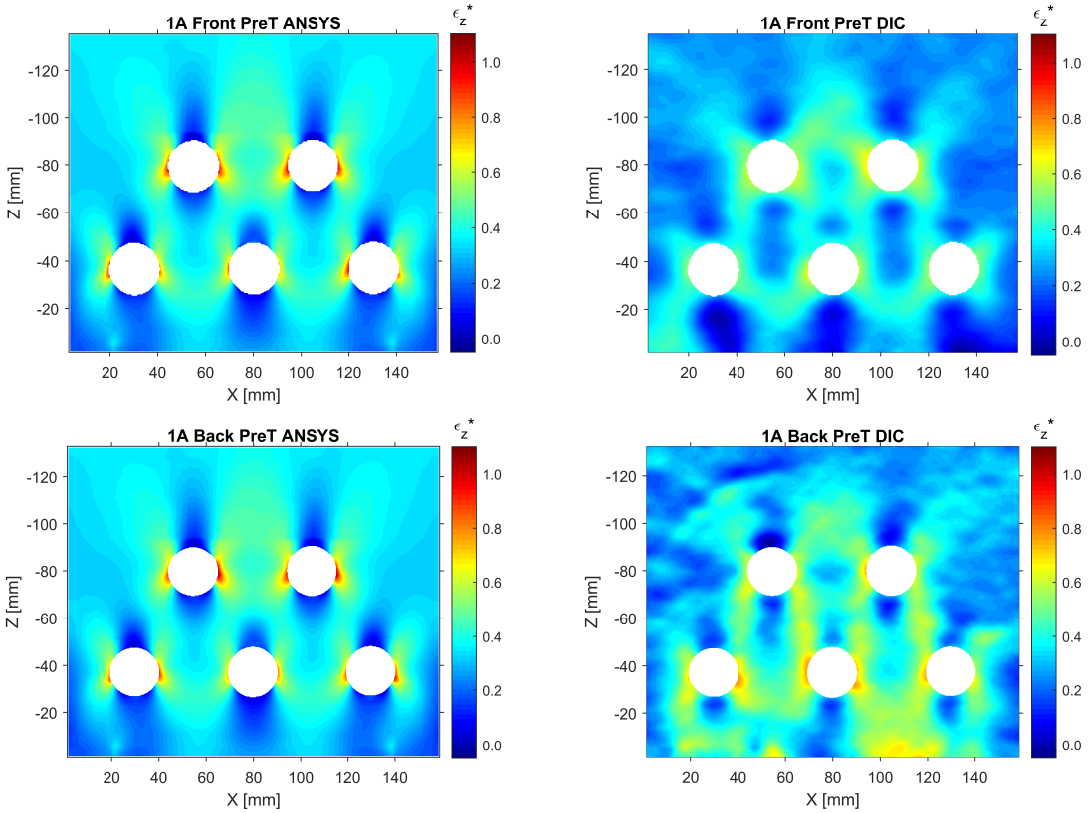

Figure 5.5: Comparison between predicted and measured axial strains for the front (top) and back (bottom) surfaces of specimen 1A. The predictions from ANSYS are shown on the left, while the measured DIC strains are on the right. All strain values were calculated from the pretension state.

Table 5.2: Strain gauge results (SG) compared to the strains from DIC and the numerical model for the center loaded specimens at the row two net-section and inside edge of bushing two.

	NS24				B2R		
[µm/m]	SG	DIC	ANSYS	[µm/m]	SG	DIC	ANSYS
1A	1101	1124	1614	1A	3664	2739	3740
2A	472	903	1614	2A	1874	1898	2570
4A	956	2380	1545	4A	3980	3326	2538

Unlike 1A and 4A, 2A behaved as if the load was offset towards the back surface despite being center loaded with no radial offset: it showed lower strains on the front and higher strains on the back. It is unclear why this occurred, but it coincides with the back surface of 2A having nearly identical strains to the predicted values and the front side having lower strains than either of the other specimens (1A or 4A). To verify the low strain values seen on the front of 2A, the strain gauge values for each of the three center loaded specimens are given in Table 5.2 where they are compared to the DIC measurements and ANSYS predictions for the NS24 and B2R locations. At both gauge locations, the strain gauge readings from specimen 2A were roughly half of the values from the specimens 1A and 4A, demonstrating that the strain bias seen in 2A is not simply the result of measurement error. Furthermore, the endplate to fixture alignment measurements were checked as an explanation for this behaviour: these estimated the real offset in the specimens to be 0.3 mm, -0.9 mm, and -0.7 mm for 1A, 2A, and 4A respectively. Both 2A and 4A show similar offsets but different results, so this does not present a reasonable explanation for the differences either.

Although specimen 2A did not behave as predicted, the results from 1A and 4A do show expected behaviour and good agreement with the predicted values. The strains are consistently lower than predicted, but on both sides of the specimens the relative error is fairly consistent: at most 26% (absolute value, calculated from the predicted results). Additionally, at each location across the second row, the change in strain from specimen 1A and 4A was similar to the predicted value. The numerical results predicted that the central second row strains from 1A and 4A (B2R, NS24, B4L) would be within 70 µm/m of each other, and the measured values were within 170 µm/m of each other. This is may be more than twice the predicted difference, but considering the differences between an idealized model and the imperfections of a physical specimen these values are quite comparable. This shows that while there may be a slight error in the strain magnitude, the response is consistent between specimens and the physical behaviour of the center loaded specimens was captured by the model. Overall, even though the magnitudes of the strains across the specimens were not well predicted, the strain contours and load distribution were similar to the numerical model, and furthermore, when the relative changes of strain between specimens 1A and 4A is considered, the model captures their behaviour well.

5.3. Parameter Based Response

The center-loaded specimens just presented show the closest agreement between predicted and measured strain magnitudes. Direct comparisons between the model and experiment yield significantly worse results for the off-center loaded specimens due to increased strain bias. It was observed that the experimental load offset created a considerably higher bias, that yielded large over predictions of strains on the front surface and under predictions on the back surface. Nonetheless, by comparing the changes in strains on the front surfaces between specimens, the influence of the different geometric parameters could be determined. This change in performance is isolated by comparing pairs of specimens where only one parameter changed. These changes can then be prepared to the changes predicted by the numerical model, which subsequently allows for the evaluation of the model's ability to predict specimen behaviour. The next three subsections evaluate the influence of each of the three key geometric parameters: d_L, d_A, and d_R.

5.3.1. Lateral Spacing

The first parameter to investigate is the lateral spacing d_L. This is investigated through the following specimen pairs: 1A to 4A, 1C to 4B, and 2C to 5A (each of which changes from $d_L = 25$ mm to $d_L = 26$ mm). To compare these configurations the relative change in strain at each of the key locations in

Table 5.3: Percent change in strains from specimen 1C to 4B (left) and 2C to 5A (right) for both measured (DIC) and predicted (ANSYS) values as a result of increased lateral spacing. Strains were calculated from the unloaded state on the front surface.

	1C to 4B					2C to 5A				
	B2L	B2R	NS24	B4L	B4R	B2L	B2R	NS24	B4L	B4R
DIC	3.4%	-6.1%	-5.8%	-2.8%	-3.4%	4.9%	0.2%	-0.7%	-0.2%	-9.0%
ANSYS	-11.8%	-10.8%	-9.4%	-10.7%	-11.8%	2.7%	2.4%	-1.5%	2.4%	2.8%

the second row associated with the increase of d_L was computed. The measured changes were then compared to the predicted changes, as shown in Table 5.3. These results show relative changes within 10% of each other (except at B4R in 2C to 5A). What is especially important is that the relative change is predominantly in the same direction as predicted (increase/decrease). Of the three situations that are not, two are at strains on the outer side of the specimen (B2L in 1C to 4B and B4R in 2C to 5A), and the third arises from a strain difference of 11 µm/m which is well within the uncertainty in the DIC strain measurements. Having the same direction of relative change is important because it confirms that changing d_L creates the same response in reality as predicted.

Comparing at the strain contours of these pairs (see Figure 5.6) shows that they exhibit very similar strains across the front of the specimens. Note specimens 1A and 4A can be seen in the previous section. This similarity is especially visible for specimens 1C and 4B (top row of Figure 5.6). In these specimens, the butterfly contours around the R2 bushings are quite similar, and the largest differences are seen across the bottom of the specimen ($z = 0$ to $z = -10$ mm): each R1 bushing has a conical

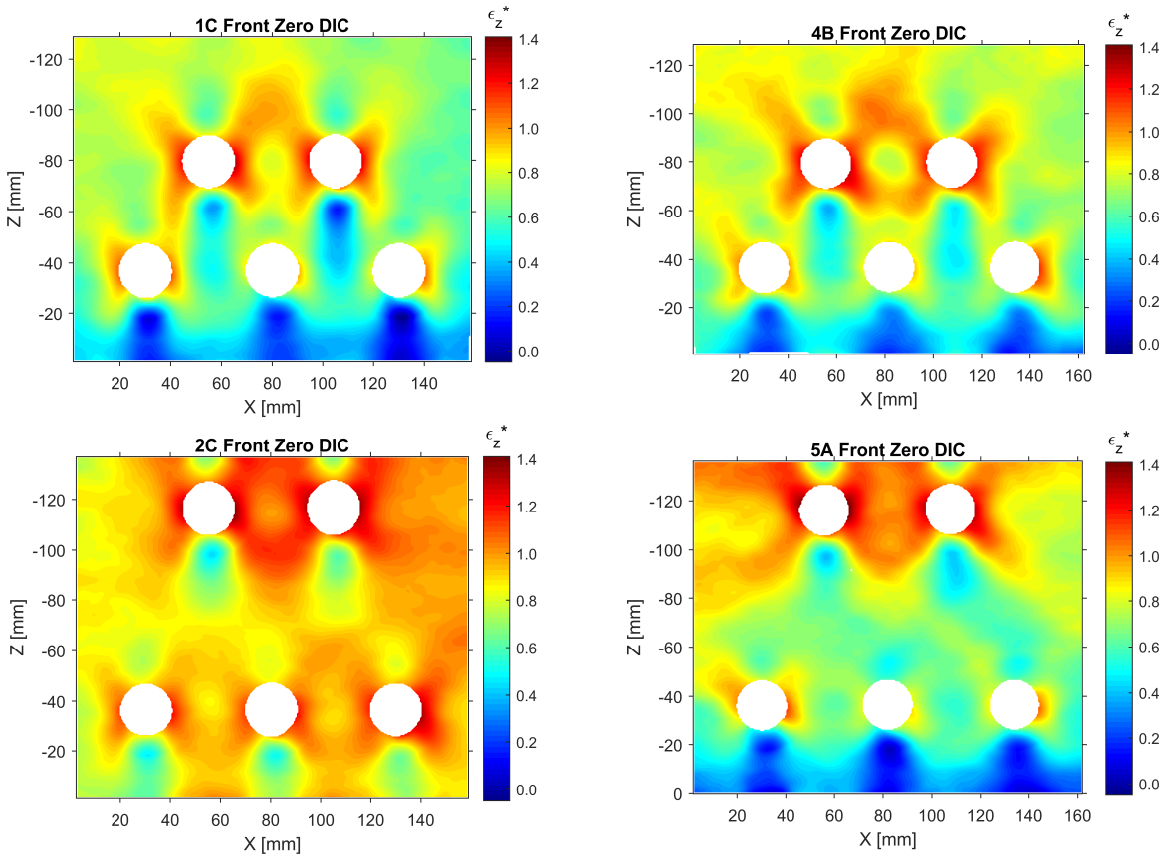

Figure 5.6: Measured strain maps showing the influence of increasing d_L from 25 mm to 26 mm between specimens 1C and 4B (top) and 2C to 5A (bottom) using the unloaded state as a reference.

region of low strain and these cones overlap on 1C but not on 4B. For the other pair of specimens (bottom row of Figure 5.6), the difference is larger: the strains around the R1 bushings are distinctly lower on specimen 5A than 2C. This is clearly visible through the colours of the strain map, much more of specimen 5A is red than 2C. One explanation for this can be derived from the specimen to endplate alignment measurements. These found that specimen 2C had an estimated radial offset of 1.0 mm whereas 5A had an offset of -0.1 mm. It is possible that the large offset in 2C had a negative effect, as the intended offset for both specimens was 0.5 mm. The additional 0.5 mm offset would increase strains at $d_A = 80$ mm, as shown in Section 4.3. Regardless of the difference between the strains in the first row, the maximum strains in the second row appear quite similar between 2C and 5A. The similarities between the contour plots for both of these specimens reinforce the small relative changes in strains that occur from changing d_L, and this in turn presents experimental evidence to reinforce the effects of lateral spacing found through numerical modelling.

5.3.2. Axial Spacing

Unlike the changes in lateral spacing, the axial spacing between bushings could be varied by a much larger distance. The specimens tested had d_A values of 43 mm, 62 mm, and 80 mm, and two pairs of specimens were identified to study the influence of changing this parameter. Firstly, between specimen 1B and 2B the only geometric change is increasing d_A from 43 mm to 80 mm, and from the experimental strains given in Table 5.4, it can be seen that leads directly to a decrease in strain. Secondly comparing specimen 3A to 2C, where d_A increases from 62 mm to 80 mm, shows the same conclusion, but it should be noted that in this case there is also a small change in d_R of 0.3 mm. The strain reductions across these two pairs also show agreement with the predicted change, just with slightly larger reductions in the DIC measurements than the ANSYS predictions.

In Figure 5.7, the strain maps for both pairs are shown, and it can be further seen that increasing d_A

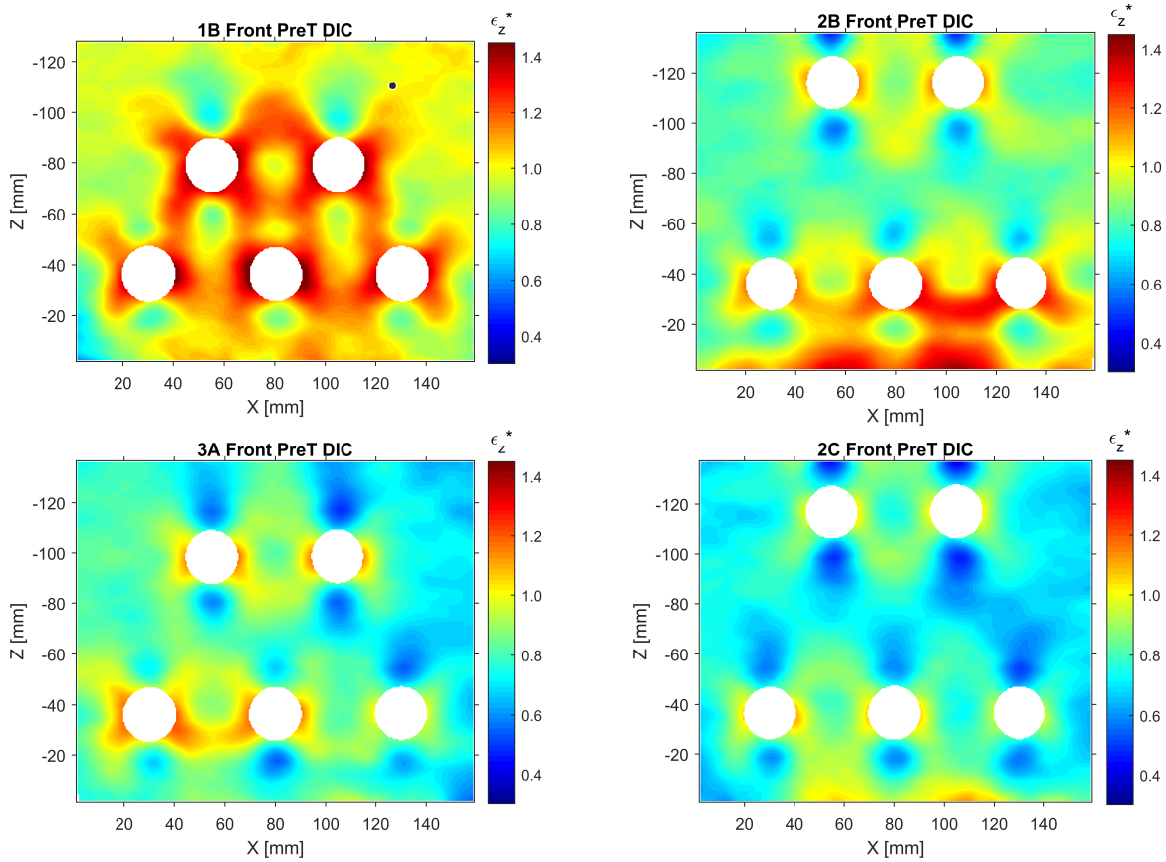

Figure 5.7: Measured strain maps showing the influence of increasing d_A from 43 mm to 80 mm (top) and from 62 mm to 80 mm (bottom) using the pretension state as a reference.

Table 5.4: Percent change in strains from specimen 1B to 2B (left) and 3A to 2C (right) for both measured (DIC) and predicted (ANSYS) values as a result of increased axial spacing. Strains were calculated from the pretension state on the front surface.

	1B to 2B					3A to 2C				
	B2L	B2R	NS24	B4L	B4R	B2L	B2R	NS24	B4L	B4R
DIC	-14%	-20%	-11%	-18%	-23%	-12%	-12%	-9%	-11%	-9%
ANSYS	-8.9%	-7.4%	-3.1%	-7.4%	-8.9%	-3.4%	-4.9%	-5.2%	-4.9%	-3.4%

reduces strains. The butterfly strain contours in the second row of bushings get noticeably smaller for both pairs. Looking at the strain map from specimen 1B the red contours are connected between the first and second rows, by increasing d_A this is eliminated in all of the other specimens. Furthermore, the regions outside B2 and B4 as well as in between R1 and R2 show lower strains in the right hand images (larger d_A). It should be noted that specimen 2B had a slight ridge just below the R1 bushings that is responsible for the increased strains at the base of the specimen. This ridge is a manufacturing anomaly at the lab-scale and can be disregarded.

Additional data on the influence of d_A was found by comparing specimen 1A to 2A and 1C to 3A. In both of these pairs the reduction in R2 strains was consistent with the predicted changes, and like the data just discussed, the measured change was slightly larger than the predicted. Combined with two pairs from Table 5.4, these comparisons encompass specimens tested with and without off-center loading as well as specimens with and without radial offsets. This shows that the influence of d_A is consistent, which in turn reinforces the numerical findings. Furthermore, it points to the impact of d_A as a driving geometric parameter in stagger root response, an observation that is once again consistent with the numerical findings.

5.3.3. Radial Offset

The final key parameter that was investigated was radial offset through the thickness of the laminate. As previously mentioned, the method for setting the position of the specimen with respect to the end-plate was not very reliable. This alignment directly influences the radial offset of the specimen, so the experimental findings for this parameter are limited. There are two sets of specimens where the only change was the radial offset: 1B to 1C and 2B to 2C. The former features an estimated change in radial offset of 1.2 mm and the latter of 0.7 mm. With a larger change in radial offset, the first pair showed a larger reduction in strain, as presented in Table 5.5. Only the strain maps of 1B and 1C are shown in Figure 5.8, because they show a greater difference as a result of the larger strain reduction.

From these results it can be seen that the experimental strain reduction was much larger than

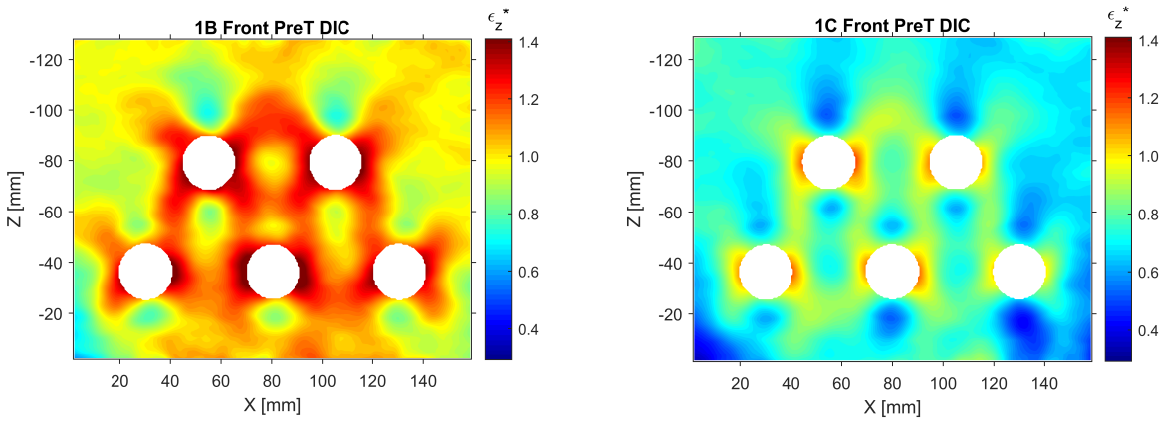

Figure 5.8: Measured strain maps showing the influence of changing the radial offset from $d_R = -0.3$ mm for 1B (left) to $d_R = 0.9$ mm for 1C (right) using the pretension state as a reference.

Table 5.5: Percent change in strains from specimen 1B to 2B (left) and 3A to 2C (right) for both measured (DIC) and predicted (ANSYS) values as a result of offsetting the shaftbolts from the laminate centerline. Strains were calculated from the pretension state on the front surface.

	1B to 1C					2B to 2C				
	B2L	B2R	NS24	B4L	B4R	B2L	B2R	NS24	B4L	B4R
DIC	-12%	-17%	-19%	-20%	-28%	-12%	-10%	-13%	-9.1%	-8.6%
ANSYS	-0.4%	-0.4%	-1.1%	-0.5%	-0.4%	-0.7%	-1.3%	-1.3%	-1.3%	-0.7%

predicted; however, so were the magnitudes of the strains as a result of the greater than expected influence of load offset effects. It appears that the influence of the radial offset was similarly heightened. Nonetheless, both the of the specimen pairs show reductions as predicted. While the exact amount of offset was not well controlled, the alignment measurements offer clear evidence that the offset changed, and the result was reduced strains on the front face of the laminate.

Further evidence of the influence of d_R can be seen from the results presented earlier for changing d_L spacing. The hole positions in 2C and 5A varied only in d_L, but when the specimens were loaded into the machine it was found that they also differed in d_R. It is known that increase d_L should decrease strains (based on experimental results and numerical predictions), but this behaviour was counteracted by a change in d_R. Considering this in combination with the results obtained from changing only d_R, the experimental influence of d_R was found to be consistent with the numerical predictions. More specifically, moving the shaftbolts towards the outer surface increases strains, while the opposite reduces them by countering the strain bias from the off-center load.

5.4. Experimental Limitations

When comparing the numerical predictions to the experimental results, there are a couple of key differences in behaviour and what is being modelled as opposed to tested. These differences can be viewed as limitations of the experiment, as they are systematic issues contributing to the large difference in strain magnitudes between the measurements and predictions. The two largest limitations are the load-offset methods created an “over bias” in the experiment and the issues with endplate and specimen alignment.

In a real blade, the outer surface receives higher strains due to the tapering of the root laminate. The lab-scale specimens used for this experiment did not have this taper region, so they attempted to imitate the strain bias by changing the load application point. In the tests, this bias was seen; however there was a much larger strain bias than was expected. The difference between the strains on the two surfaces was so large that for many specimens the back surface showed compressive strains in the DIC data. This is not representative of real blade loading, so these surfaces did not yield useful results and were not compared. Nonetheless, the measurements from the front surfaces could still be used, and on the front of every off-center loaded specimen, except 2B, the measured strains were higher than the numerical predictions. The SG readings gave similar results, with the gauges at the center of the specimens measuring values that were, on average, 42% higher than predicted.

With the increased strain bias through the specimen, the front surface often showed tensile strains across its entire surface. Initially this seemed to indicate an error in the measurements because the bushings transfer load into the laminate through bearing; however, it is suspected that the bending from the load offset was severe enough to unload the front surface. The back surface shows compressive strains indicative of bearing load transfer, and it is suspected this continues through the thickness of the laminate near the shaftbolt, but towards the front surface, the contact pressure at the front of the bushing appears to reduce significantly. An equivalent explanation can be made considering that before applying external load the pretension in the bolts creates compression through the entire laminate without inducing bending. Then when the external load is applied, it is applied off-center inducing bending with the concave side on the back of the specimen. In turn, the front surface is brought into tension, and thus bearing is reduced around the front of the bushings.

The other, major, non-representative behaviour that was seen in some specimens was a difference in displacement (and thus strain) on the left and right sides of the specimens occurring as a result of

misalignment between the specimen and the endplate. An example of this behaviour was shown in Figure 5.3, where in the left image, noticeably larger axial displacements are seen on the right side of the specimen compared to the left. As noted at the top of Figure 5.3, the left hand plot calculates the displacement of the specimen from the unloaded state to the target load, whereas in the right hand image the displacements are calculated from the pretension load state (no external load, but 50 kN of preload in each bolt).

In the experimental procedure, the specimen was loaded into the machine to take the unloaded measurements, but then it had to be taken back out to apply the pretension. After applying the required torque to each nut, the specimen was re-loaded into the machine. The application of 50 kN of pretension to the bolts compressed the specimens, so to load them back into the test machine, the piston of the machine had to be moved. Subsequently the specimen could exhibit small, rigid deformations between the unloaded and pretension states. It was found that using the pretension state as the reference for DIC measurements reduces this error in displacement readings. This strategy was used for the analysis of many specimens, but the difference in displacement was not the only consequence of this misalignment.

Examining the right-hand image of Figure 5.3 closer, it can be seen that while switching the reference image reduces the difference in displacement across the specimen it does not eliminate it. This is due to the difficulty in perfectly aligning the specimen and the endplate, which in turns arises due to the manufacturing tolerances of the specimens and endplates. The shaft holes in each were between 13.0 and 13.5 mm in diameter, but the shaftbolts have a nominal diameter of 12.00 mm. Subsequently, there is a gap around the shaftbolts that allows the endplate to translate or rotate small amounts with respect to the specimen. This is the reason that the design d_R values given in Section 3.2.2, differ from those in Figure 5.1. Furthermore, even if the specimen and endplates are aligned, the application of the 150 Nm of torque by hand requires a large amount of force which can jar or twist the endplates. As an attempt to monitor this behaviour, the distance from the top of the specimen to the top of the fixture was measured on the left and right side of the specimen before and after applying the pretension to the nuts. These measurements were used to estimate any twist and the effective radial offset of each specimen; these d_R measurements were given in Figure 5.1. The latter was in turn used to update the ANSYS predictions that the experimental results were compared against.

While the alignment and offset issues represented two limitations of the test apparatus, neither of them were catastrophic: that is, not all specimens used the load offset method, nor were all the specimens significantly misaligned. In general, the specimens responded largely as expected when the strains are compared between specimens. The relative changes in performance allow for the impact of the geometric parameters to be validated; however, the test set up does not offer representative strain for real blade loading. Furthermore, while it was demonstrated that moving the load line relative to the laminate centerline can create a strain bias, it was clear that more work is needed to refine how much this load should be offset to create a representative strain bias. If one is to use static lab-scale tests to predict full-scale root behaviour, it is recommended that a more realistic strain bias is achieved, especially for investigating radial offsets. Radial offsets are intended to counteract strain biases in the laminate, and while these experiments demonstrated that d_R can do this, they are unable to point to the best d_R value for the strain bias expected in a real blade.

5.5. Fatigue Tests

The final part of the experimental campaign was the fatigue testing. The aim of these tests was to verify that the strain reductions achieved through different geometries under static loading would be replicated in fatigue loading. It was thus far assumed that the specimens perform in the same manner under both loading conditions, and two fatigue tests were conducted to verify this assumption. The first (1F) was tested using the on-center loading method and featured the same stagger configuration as 1A, while the second (2F) used off-center loading and the stagger configuration of 3A. Failure occurred in the shaftbolts of each specimen at 256,419 and 88,659 cycles for 1F and 2F respectively. As with the static tests, the load offset created an “overbias” which lead to an increased strain bias. This amalgamated in bolt failure after only 35% as many cycles as the on-center loading and inhibited meaningful comparisons directly between specimens 1F and 2F. With the longer test only running for just over 250 thousand cycles, these tests only provide a limited amount information on the fatigue performance of the specimens.

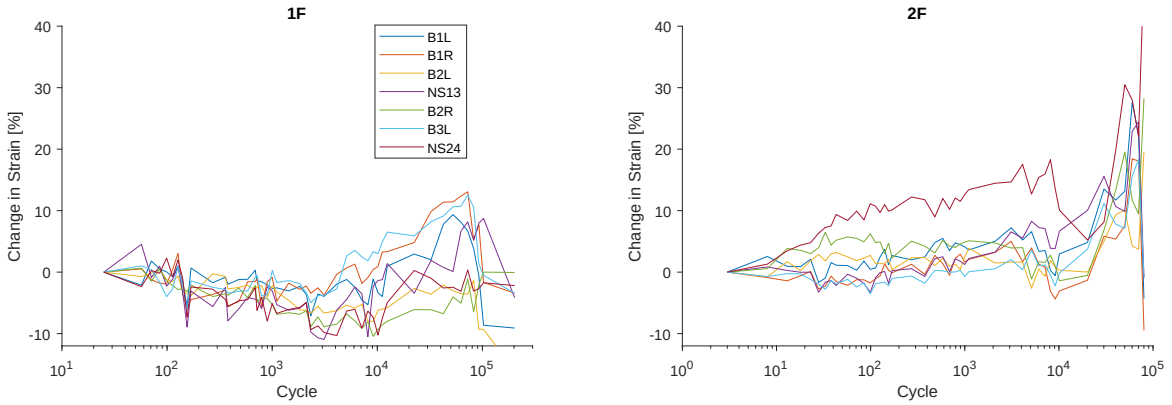

Figure 5.9: Change in axial strain at each location over the duration of the fatigue tests. At each location, strain was calculated as the difference between the strain at the current cycle and the initial cycle divided by the initial strain. Only the locations on the left half of the specimen are shown due to symmetry.

Plotting change in strain as a function of cycle count, as in Figure 5.9, shows that the strains across both specimens change in fatigue. In specimen 1F the strains show a slight decrease and then just before ten thousand cycles, they begin to increase. Specimen 2F also shows an increase at 10 thousand cycles, but the change in strain is much larger. The steeper increase in 2F reaffirms that the off-center loading method created much higher strains than the on-center. In the final measured cycle, there are two distinct behaviours shown: firstly, a decrease in strain to near, or below, the initial strain (cycle 1), and secondly, sharply increasing strains. The former occurs across in the first row locations of both specimens, while the latter occurs in the R2 locations of 2F (B2L, B2R, and NS24).

Decreasing strains short before failure is expected to be a result of gap opening which is accelerated due to shaftbolt fatigue. Fatigue in the bolt will reduce the pretension, and subsequently gap opening will occur at a lower external load. This explains why gap opening occur at the target load at high cycle counts even though it was not observed at the target load in the static tests. The link between lower strains and gap opening and lower strains is then explained by the loss of load transfer between the endplate and the laminate. When the load is transferred exclusively through the shaftbolts, the R2 regions carry more of the load. This similarly explains the increase in strain in R2.

The increase in strains was significantly larger in 2F, the off-center loaded specimen, which can be attributed to the over bias phenomenon. In 2F the load offset created much higher strains on the front surface. This leads directly to a higher increase in strains, but it may also have a second order effect. The greater strain bias is an indicator of more bending in the specimen, and therefore gap opening may occur at the front surface before the back surface. As a result, the R2 regions on the front surface

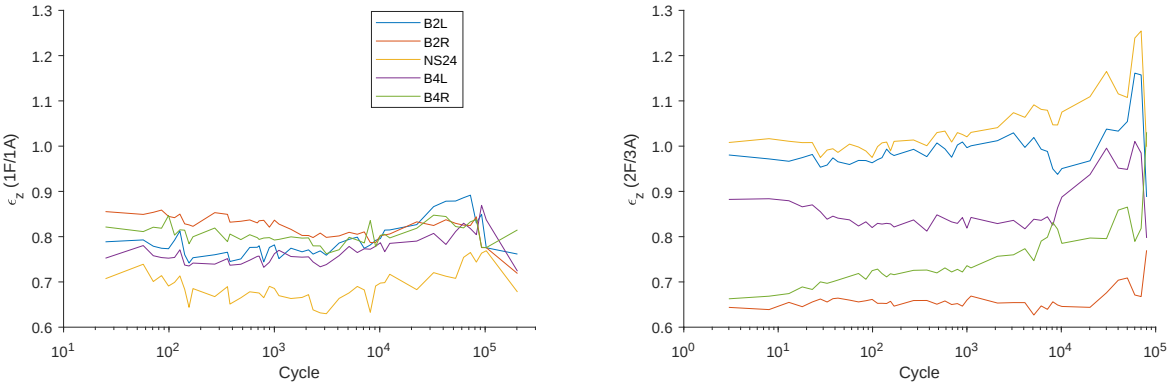

Figure 5.10: Axial strains from the second row over the duration of the fatigue tests normalized by the strain at that location from the static test specimen with the same geometry. For 1F (left) this is specimen 1A, and for 2F (right) this is 3A.

(outside of the blade) are brought into greater tension.

This phenomenon may have implications in the use of d_R, for example: if radial offsets can prevent gap opening from occurring at the outer surface of a blade first, they may be able to extend the fatigue life of the root. On the other hand, if they exacerbate the problem by shifting the pretension away from the outer surface, the opposite effect may happen. Further fatigue testing would need to be done to better investigate this behaviour, as Figure 5.9 only offers a limited and disjointed picture of the fatigue process for two different specimens and load methods. Furthermore, these plots do little to show the influence of the geometric parameters in static vs fatigue because the two specimens are not very comparable.

To get a better picture for the differences between the two loading scenarios, the fatigue strains need to be compared to those from the static tests across all cycles. This was done by normalizing each strain location by the measured strain from the geometrically equivalent static test, as shown in Figure 5.10. Here, the increase in strains at the higher cycle counts is still visible, but behaviour between the different locations of the specimens can be compared. In both specimens the normalized strain trends have the same shapes, that is their peaks occur at the same cycle counts and differ primarily by a vertical offset. This shows that the fatigue loading affects each region of the specimen in the same way, or in other words, there is a change in load path as a result of fatigue loading. A change in load path would increase the strains in some regions while decreasing it in others, and this did not occur. These two tests do not show any glaring differences between static and fatigue behaviour. Returning to the main goal of the fatigue tests, there is nothing to show that geometric parameters impact static and fatigue loading differently, so it is still assumed that different geometries will lead to equivalent strain reductions in static and fatigue loading.

5.6. Summary of Main Findings

To assess the validation of the numerical model, the experimental findings were broken into pairs where only one parameter changed, focusing on the static test results. Static testing was used as the primary source of data because many more configurations could be tested. This relied upon the assumption that the impacts of geometric parameters are the same in static and fatigue. Two brief fatigue tests were performed to check this, and they did not show any change in load distribution or strain response compared to the static tests. The influence of d_L and d_R could then be seen in the on-center and off-center loaded static test, and the different responses to the load offset as a result of d_R could be isolated. For each of these pairs, the relative reduction in strain between the numerical model and experimental specimens was compared. As shown in Section 5.3.2, it was the d_A pairs that showed the clearest strain reductions in the strain contour maps: when mapping the strain from the pretension state, the increase in the second row was roughly 1000 µm/m less than the first row at greater d_A. This is partially because at the pretension state ($F_{ext} = 0$ kN, $F_{pretension} = 50$ kN), the strains around the R2 bushings were higher than the around those in R1, but this behaviour was reinforced by consistent reductions in strain with increasing d_A.

The reductions in strain with d_A and d_R were consistently higher in the experiments than predictions, but they did agree in that they were both reductions. This agreement reinforces that the model captures the physical behaviour of the specimens, and the increased magnitude can be attributed to the increased strain bias. Unlike the numerical model, the strain reduction from d_A and d_R was about equal. It is suspected that this is a combination of the increased strain bias and the fact that the numerical model was comparing maximum strain at any point through the thickness, while the experimental results compared only the surface strains. With respect to the lateral spacing, the change in strain was smaller, and the experimental results showed less change than the predictions. Both changes still generally occurred in the same direction: the exceptions were in the outer, non-representative, regions of the specimen. Compared to the other spacing parameters, the lateral spacing between bushings has received the most extensive investigation in other experiments, and thus the validation of d_L was also accepted. From the experimental results collected across different stagger configurations, it was concluded that the numerical model does indeed capture the physical behaviour of the five bolt specimens and therefore validate the findings obtained from the numerical model.

Testing the 5-bolt specimens at the lab-scale highlighted some scaling effects that hindered the effectiveness of the investigation. These arose primarily from two sources: increased impacts of manufacturing tolerances and the fact that some things, like bolt strength, do not scale linearly with geom-

etry. Both of these can be seen when considering the M12 bolts that were used. This was the closest standard bolt size to the scaling factor used for the rest of the geometry. Firstly, the difference between the shaftbolt holes and shaftbolt diameters allowed for movement of the specimen with respect to the endplate which in turn changes the d_R offset for the specimen. Small changes in d_R manifested in large changes in strain, a phenomenon that was exaggerated by the lab-scale geometry due to the relative offset d_R/t. Secondly, since the load capacity of a bolt scales quadratically with the diameter, the relative load capacity of the bolts was reduced. This was expected and highlighted in Section 3.3.4, but its impact was underlined in the experimental test through the failure in the shaftbolts in both fatigue tests. While these tests did not intend to study failure, this still represents an important consideration when conducting scaled subcomponent tests.

6

Conclusions

The overall goal of this project was to explore and understand how the geometric parameters of a wind turbine root designed with T-Bolts influence its strain response, and then to use this understanding to reduce the strains in the laminate and thus improve the root's structural load capacity. To study these numerous parameters, a finite element model was developed and run through a myriad of simulations. This was chosen as the primary avenue of exploration as it enabled a greater number of parameters to studied than a purely experimental campaign. Physical testing was also included in the project to verify the numerical findings. Subsequently, answering the main questions of this research is done primary with knowledge gained from the numerical explorations, with the experimental findings offering further evidence and learnings for future tests.

Before the influences of varying the root joint's geometric parameters were studied, the numerical model was designed to imitate the strain response in a real blade root. Through tests of full blades, it was known that bending creates an asymmetric response through the thickness of the blade. It was therefore necessary to imitate this behaviour in the 5-bolt submodel used for this study. Different load methods were used and it was found that by offsetting the applied load, an equivalent strain bias could be created. From the load offset method, the through thickness strain bias was matched between the simplified model and that of a real blade at the critical second row bolts. To focus on this region, less representative behaviours in the first row and specifically the outer bushings were accepted.

The various geometric parameters were separated into primary and secondary parameters and addressed on an individual level. The primary parameters are: d_A the axial spacing between bushing rows, d_L the lateral spacing between adjacent bushings and shaftbolts, and d_R the radial offset of the center of the shaftbolts from the center of the laminate (towards the blade's inner surface). The secondary parameters are d_{Ae} and d_{Le}, the edge distances in the axial (from blade hub to blade tip) and lateral (across the lab-scale specimens or equivalent to the circumferential direction around the root) directions respectively. Unlike the primary parameters, these did not significantly affect the axial strain response. Through the preliminary modeling is was also confirmed that the axial strain is the main metric of root capacity, as it is the most critical stress and strain component in the laminate. Of the primary parameters, the first two (d_A & d_L) directly change the distance between the holes in the different stagger patterns: the main focus of a staggered root design. These parameters were known to affect axial strains, and through this project it was determined how to use them most effectively. The final parameter positions the shaftbolts through thickness relative to the centerline of the laminate, and this was found to influence the through thickness strain bias. Each of these parameters can be used to reduce the maximum strain in the laminate and thus increase blade root capacity.

Staggered root designs are not necessarily beneficial. The intention is to reduce the stress concentration effects that occur between adjacent bolts and thereby increase root capacity, and while they have been shown effective in doing so, it was found that adequate axial spacing is required. At the lab-scale this means $d_A \gtrsim 45$ mm, but can be stated more generally as $d_A > \sqrt{3}d_L$. With an adequate spacing between bolts, stagger configurations reduce the peak strains in the laminate from a single row root design. Further increases in the distance between bushings reduces the strains, but it does not change the critical regions or strain interactions in the root. Beyond the transition to beneficial stagger

patterns, the gradient of the axial strain vs d_L and d_A trends decreases and begins to plateau. From this it was found that it was nearly always beneficial to increase the axial spacing from a strain perspective, but at some point the second row of bushings would start interacting with the tapered region of the root. Furthermore, it was found that beyond $d_A = 60$ mm, the strains around the central, first row, bushing (B3) begin to increase. These strains are still lower than the critical response in the second row, but this emphasizes the diminishing returns of the excessive axial spacing.

Compared to the impact d_A, the strain reductions from increasing d_L are smaller. This is especially true at large d_A spacings, where changes in d_L illicit at most a 7% reduction in strain (compared to a 12% reduction from d_A at large d_L). Furthermore, by spacing the bushings farther apart, fewer bushings can fit around the circumference of the blade. The secondary effect of this is that each T-Bolt must then carry more load. From this project it was found that when a greater portion of the load was transferred via contact between the laminate and the endplate (simulating the hub of the turbine), that the stress concentrations, and thus the peak strains adjacent to the second row bushings, are reduced. Therefore, increasing the load transferred via the T-Bolts was found to increase the peak strains. Increasing the lateral spacing between bolts reduces the overall pretension around the root, and subsequently gap opening occurs at lower external loads. Gap opening is separation between the hub and root laminate, a phenomenon that has been found as the root cause of complete blade failure. Considering this, it was clear that not only is d_L less influential on the strain response, but increasing d_L is not necessarily beneficial even if it slightly reduces strains.

The third primary parameter than can be used in staggered bolt patterns is d_R, the position of the shaftbolt through the thickness of the laminate. Unlike the in-plane position of the bushings, it is not advantageous to stagger the shaftbolts. It is only through moving the shaftbolts uniformly towards the inner side of the blade that the strains can be reduced. The back surface of the test specimens represents the inner surface of the blade, and in both cases, this is the face that has lower loads and strains due to the off-center loading of the root. Moving the shaftbolt towards the inside of the blade shifts the load path away from the highly loaded outer surface and subsequently equalizes the strain profile through the thickness of the laminate. By counteracting the strain bias, the end effect of this is a reduction in the maximum strain in the root.

It was found that in configurations with higher overall strains, the load path and strain magnitudes are more sensitive to radial offsets. At different axial and lateral spacings, the most beneficial d_R offset also changes. Looking at any given d_L this means that the local minima of different d_R values have a) different magnitudes and b) occur at different d_A values. Inversely, for a given d_R value, the d_A value at which the axial strain is minimized is lower at lower d_L. Additionally, the value of d_R that yields the absolute lowest strain decreases with d_L. The minima for different d_R values occur at nearly the same strain values, and therefore the radial offset was deemed the least influential parameter. This does assumes that any radial offset used is small, but this is a reasonable assumption (large offsets are detrimental and should thus be avoided).

Combining the findings from each individual parameter, the key findings were the shift between detrimental and beneficial offsets and the nature and relative impact of each of the three staggering parameters. Avoiding large interactions between the bushing holes moves a stagger pattern into the beneficial region, and from here the most influential parameters are d_A, d_L, and d_R in order of decreasing impact. Considering the design freedom associated with each, a root design would likely start by setting d_L, since it has additional considerations with respect to the number of bolts that fit around the root. Correspondingly, the axial spacing is then the parameter with the greatest design freedom: the geometry of a blade root allows for the largest changes in d_A. The radial offset can then be used as a final method to offer a slight reduction in overall strain, or as an enabler to decrease d_A without increasing the maximum strain as much. This would be relevant for designs where the tapering of the root laminate sets a maximum feasible d_A distance. These conclusions were derived from extensive numerical modelling; however, before implementing any of these solutions in a real blade, experimental testing is required. Subsequently, this project carried out experimental tests to validate the model and confirm these findings.

The goal of the experimental portion of this project was to validate the predictions of the numerical model. Ten different static specimens were tested, combining baseline and optimal stagger patterns under both on-center and off-center loading. The latter aimed to reproduce the strain bias seen in real blades, and while a bias was created, it was much more severe than in a real blade with the front and back surfaces of the test specimen (equivalent to the outer and inner blade surfaces) having

consistently higher and lower strains respectively when compared to the predictions. Despite this, the many specimens tested could be broken into pairs where only one parameter changed, allowing for the influence of the geometric parameters to be studied through the changes in strain between tests.

Each of the primary parameters was found to elicit the same response in the experiments as the numerical models. That is increasing lateral or axial spacing reduced the maximum strains at the edges of the bushings, and adding a radial offset was effective in counteracting the through thickness strain bias. The experimental results consistently showed greater reductions in strain than the numerical predictions when comparing percent change between two specimens. This was due to the overbias effect, and highlights the challenges of reproducing root behaviour at the lab-scale, especially without the tapered region of the root segment. On the other hand, the tests did demonstrate that the free edges of the specimen did not cause any non-representative behaviours. Ultimately, the main conclusion of the experimental tests was that the key findings of strain reductions with d_A, d_L, and d_R were confirmed by the experimental tests, thus validating the conclusions from the model.

This project tasked itself with investigating how varying T-Bolt geometry affects the structural response of a wind turbine blade root and to what extent this can increase the root capacity. From a structured series of numerical simulations, that were in turn validated by an experimental test campaign, it was found that the critical strain response of the root is governed by three primary parameters: the axial, lateral, and radial spacings. These can be combined to reduce the overall strain in the root, but as highlighted by scaling effects, a reliable estimate of the magnitude by which the strain can be reduced cannot be made at the current time. This test campaign honed in on the spacing regions of the most benefit: specifically large axial spacings with the incorporation of a small radial offset towards the blade's inner surface. Further testing, likely full-scale subcomponent testing, would be required to demonstrate precisely how much strain reduction can be obtained. Nonetheless, this project has proved that there are further strain reductions possible, and it represents a concrete first step towards realizing a root subcomponent test.

7

Recommendations

Throughout the course of this project the wind industry has continued to grow: multiple new wind farms have been announced and turbine manufacturers have announced new, longer blades. To support longer blades, novel strategies will be required in the root and other areas of the blade. These strategies are not purely structural, they also include improved manufacturing and testing techniques. One particular avenue that has been discussed here and is expected to gain momentum in the industry is subcomponent testing. Root subcomponent tests offer a multiple of opportunities for blade manufacturers, including shorter, cheaper tests that will enable the exploration of new designs and technologies. While the work of this project involved many simplifications and assumptions, it also provides many learnings for future tests. These tests could in turn be used to further check or eliminate some of the simplifications and assumptions from this project.

The recommendations that come out of this project fall into two general categories: learnings that will help design a successful root SCT and unexplored avenues that would yield interesting topics for future work. An example from the first category can be seen in the static specimens where there was a visible gap between the bushings and the laminate. This gap highlights the necessity for reducing manufacturing tolerances as much as possible at smaller scales, because like the endplate alignment issue, these clearances have a proportionally larger impact. Clearance in has been well documented to influence the behaviour of pin loaded holes, so it would be valuable to address this issue in future SCTs. Furthermore, as an example of the second category in relation to clearance effects, it would be valuable to incorporate through thickness strain measurements via fibre optic gauges. This would allow for better observation of the strain bias in the laminate. A precise and physical measurement of this effect could allow for greater precision in root design and subsequently a potential reduction in some of the partial safety factors used. Both of these factors could enable increased root capacity in the eyes of a certifying body.

From a certification perspective, this project plays a role in developing future subcomponent tests. Specifically, one of the questions was if the difference in BCs between a real blade and the test specimen would lead to non-representative behaviour. These tests showed that they would not, but they did show the difficulty in properly reproducing the strain bias through the thickness. To maximize the value of a SCT this behaviour will need to be better replicated. It is suspected that including the tapered region of the root laminate would help here, while also offering the opportunity to study the interactions between the second row of bushings and the transition region. In this experiment a maximum d_A was identified to fit with an existing root geometry, but including the tapered region would allow for a better understanding of how much spacing is needed beyond the second row of bushings. It is suspected that if a tapered region is to be incorporated, it would yield better results at the full-scale as well due to the effect of ply drops that would be necessary to achieve the tapering.

Based upon the findings of this project, it would also be interesting to test the influence of d_R at the full-scale. The sensitivity of strain response to small changes makes this parameter better suited for full-scale testing, because a more precise alignment could be achieved. This would in turn allow for a better verification and demonstration of the potential for radial offsets to reduce axial strains. The findings from this project, and specifically the experimental tests are very much a first step, and thus lack confidence. Before these improvement stagger configurations are implemented, they will need to

be tested and demonstrated with increased confidence. Furthermore, the tests carried out were not able to complete a test to failure nor were they able to complete a full fatigue test. A FS SCT would be an excellent opportunity to realize these goals and further understand the behaviour of the blade root.

A developed SCT would be an excellent enabler for future studies. This project had to exclude many factors to limit its scope, and in the first iterations of a SCT these limitations will likely need to be retained. Once matured, a SCT will allow for root studies comparing vastly different root designs. Currently, there is no test scale between the lab- and full-scale blade tests, which means that technologies are subject to the uncertainties of down scaling, or they must be tested blind in a large and expensive full blade test. It would be advantageous to compare the performance of technologies like adhesive root inserts or carbon based root joints at a low cost without large uncertainties. The value of subcomponent testing has become increasing apparent through the course of this research. It is fully expected to be a next step in root design, and it is hoped that the findings of this project can aid in its realization.

Bibliography

[1] European Commission. EU'S NEXT LONG-TERM BUDGET & NextGenerationEU: KEY FACTS AND FIGURES. Technical report, Publications Office of the European Union, nov 2020.

[2] Justin Wilkes, Jacopo Moccia, Paul Wilczek, Rémi Gruet, Vilma Radvilaitė, Mihaela Dragan, Julian Scola, and Sarah Azau. EU Energy Policy to 2050. Technical report, European Wind Energy Association, Bruxelles, Belgium, 2011.

[3] D. Carvalho, A. Rocha, M. Gómez-Gesteira, C. Silva Santos, M G Omez-Gesteira, and Silva Santos. Potential impacts of climate change on European wind energy resource under the CMIP5 future climate projections. *Renewable Energy*, 101:29–40, feb 2017. ISSN 18790682. doi: 10.1016/j.renene.2016.08.036.

[4] Ryan Wiser, Mark Bolinger, Galen Barbose, Naïm Darghouth, Ben Hoen, Andrew Mills, Joe Rand, Dev Millstein, Seogeun Jeong, Kevin Porter, Nicholas Disanti, and Frank Oteri. 2018 Wind technologies market report. Technical report, U.S. Department of Energy, Alexandria, Virginia, 2018.

[5] Dan Ancona and J McVeigh. Wind turbine-materials and manufacturing fact sheet. *Princeton Energy Resources International, LLC*, pages 1–8, 2001.

[6] R H Crawford. Life cycle energy and greenhouse emissions analysis of wind turbines and the effect of size on energy yield, 2009. ISSN 13640321.

[7] Joyce Lee and Feng Zhao. GWEC Global Wind Report 2019. Technical report, Global Wind Energy Council, Brussels, Belgium, 2020.

[8] Ole Thybo Thomsen. Sandwich materials for wind turbine blades - Present and future. *Journal of Sandwich Structures and Materials*, 11(1):7–26, jan 2009. ISSN 10996362. doi: 10.1177/1099636208099710.

[9] Eize de Vries. Turbines of the year 2019: Rotor blades, jan 2020.

[10] D. Carvalho, A. Rocha, M. Gómez-Gesteira, and C. Silva Santos. Offshore winds and wind energy production estimates derived from ASCAT, OSCAT, numerical weather prediction models and buoys – A comparative study for the Iberian Peninsula Atlantic coast. *Renewable Energy*, 102:433–444, mar 2017. ISSN 18790682. doi: 10.1016/j.renene.2016.10.063.

[11] Lee Joyce and Zhao Feng. Global Offshore Wind Report 2020. Technical report, Global Wind Energy Council, Brussels, Belgium, 2020.

[12] Leon Mishnaevsky, Kim Branner, Helga Nørgaard Petersen, Justine Beauson, Malcolm McGugan, and Bent F. Sørensen. Materials for wind turbine blades: An overview. *Materials*, 10(11): 1285–1309, nov 2017. ISSN 19961944. doi: 10.3390/ma10111285.

[13] J Tangler. The Evolution of Rotor and Blade Design. *American Wind Energy Association WindPower 2000*, (July):11, 2000.

[14] D Todd Griffith and Thomas D Ashwill. The Sandia 100-meter All-glass Baseline Wind Turbine Blade : SNL100-00. *Baseline*, (June):1–67, 2011. doi: ReportNo.SAND2011-3779.

[15] Mathijs Peeters, Gilberto Santo, Joris Degroote, and Wim Van Paepegem. The concept of segmented wind turbine blades: A review. *Energies*, 10(8):1–20, 2017. ISSN 19961073. doi: 10.3390/en10081112.

[16] Peter J Schubel and Richard J Crossley. Wind turbine blade design. In *Wind Turbine Technology: Principles and Design*, volume 36, pages 1–34. 2014. ISBN 9781482244953. doi: 10.1201/b16587.

[17] Alexander J.E.Ashworth Briggs, Zhongyi Y Zhang, and Hom N Dhakal. Study on T-bolt and pin-loaded bearing strengths and damage accumulation in E-glass/epoxy blade applications. *Journal of Composite Materials*, 49(9):1047–1056, apr 2015. ISSN 1530793X. doi: 10.1177/0021998314528825.

[18] D Griffith. The SNL100-01 Blade: Carbon Design Studies for the Sandia 100-meter Blade. Technical Report February, 2013.

[19] Kevin Cox and Andreas Echtermeyer. Structural design and analysis of a 10MW wind turbine blade. In *Energy Procedia*, volume 24, pages 194–201, 2012. doi: 10.1016/j.egypro.2012.06.101.

[20] Leon Mishnaevsky and Gaoming Dai. Hybrid carbon/glass fiber composites: Micromechanical analysis of structure-damage resistance relationships. *Computational Materials Science*, 81: 630–640, 2014. ISSN 09270256. doi: 10.1016/j.commatsci.2013.08.024.

[21] Tomasz Sieradzan and Bente Vestergaard. On certification aspects of wind turbine blade load carrying structure. In *European Wind Energy Association Conference and Exhibition 2014, EWEA 2014*, pages 1–10, 2014.

[22] P. P. Camanho, C. G. Davila, M. F. de Moura, C G Da´vila, Da´ Da´vila, and M. F. de Moura. Numerical Simulation of Mixed-mode Progressive Delamination in Composite Materials. *Journal of Composite Materials*, 37(16):1415–1438, aug 2003. ISSN 0021-9983.

[23] International Electrotechnical Commission. IEC 61400-3-1:2019. Technical report, International Electrotechnical Commission, Geneva, Switzerland, 2019.

[24] Zhenye Sun, Jin Chen, Wen Zhong Shen, and Wei Jun Zhu. Improved blade element momentum theory for wind turbine aerodynamic computations. *Renewable Energy*, 96:824–831, 2016. ISSN 18790682. doi: 10.1016/j.renene.2016.05.035.

[25] DNV GL. *Rotor blades for wind turbines*. Number December. 2015.

[26] Srinivasa D Thoppul, Joana Finegan, and Ronald F Gibson. Mechanics of mechanically fastened joints in polymer-matrix composite structures - A review, 2009. ISSN 02663538.

[27] C.W. Kensche and K. Schultes. Evaluation of T-Bolt Root Attachment. In R M Mayer, editor, *Design of Composite Structures Against Fatigue: Applications to Wind Turbine Blades*, chapter 13, pages 194–208. MEP, 1996. ISBN 0852989571.

[28] Hak Gu Lee, Min Gyu Kang, and Jisang Park. Fatigue failure of a composite wind turbine blade at its root end. *Composite Structures*, 133:878–885, 2015. ISSN 02638223. doi: 10.1016/j.compstruct.2015.08.010.

[29] J A Pascoe, R C Alderliesten, and R Benedictus. Methods for the prediction of fatigue delamination growth in composites and adhesive bonds - A critical review. *Engineering Fracture Mechanics*, 112-113:72–96, 2013. ISSN 00137944. doi: 10.1016/j.engfracmech.2013.10.003.

[30] J. C. Marín, A. Barroso, F. París, and J. Cañas. Study of fatigue damage in wind turbine blades. *Engineering Failure Analysis*, 16(2):656–668, mar 2009. ISSN 13506307. doi: 10.1016/j.engfailanal.2008.02.005.

[31] Karthikeyan Ravikumar, Rajkumar Subbiah, Nalini Ranganathan, Joseph Bensingh, Abdul Kader, and Sanjay K Nayak. A review on fatigue damages in the wind turbines: Challenges in determining and reducing fatigue failures in wind turbine blades, 2019. ISSN 2048402X.

[32] Davood Salimi-Majd, Vahid Azimzadeh, and Bijan Mohammadi. Loading Analysis of Composite Wind Turbine Blade for Fatigue Life Prediction of Adhesively Bonded Root Joint. *Applied Composite Materials*, 22(3):269–287, 2015. ISSN 15734897. doi: 10.1007/s10443-014-9405-4.

[33] Jörg Höyland. *Challenges for large wind turbine blades*. Phd, Norwegian University of Science and Technology, 2010.

[34] B Hillmer, T Borstelmann, P A Schaffarczyk, and L Dannenberg. Aerodynamic and structural design of multiMW wind turbine blades beyond 5MW. In *Journal of Physics: Conference Series*, volume 75, 2007. doi: 10.1088/1742-6596/75/1/012002.

[35] M. Etemaddar, M. O.L. Hansen, and T. Moan. Wind turbine aerodynamic response under atmospheric icing conditions. *Wind Energy*, 17(2):241–265, feb 2014. ISSN 10954244. doi: 10.1002/we.1573.

[36] Weifei Hu, K. K. Choi, Olesya Zhupanska, and James HJ Buchholz. A new fatigue analysis procedure for composite wind turbine blades. In *32nd ASME Wind Energy Symposium*, 2014. doi: 10.2514/6.2014-0173.

[37] A. S. Kaddour, M. J. Hinton, and P. D. Soden. *Failure Criteria in Fibre-Reinforced-Polymer Composites*. Elsevier Science & Technology, 1 edition, 2004. ISBN 9780080531571. doi: 10.1016/B978-008044475-8/50038-X.

[38] A S Kaddour and M J Hinton. Maturity of 3D failure criteria for fibre-reinforced composites: Comparison between theories and experiments: Part B of WWFE-II. *Journal of Composite Materials*, 47(6-7):925–966, 2013. ISSN 00219983. doi: 10.1177/0021998313478710.

[39] A S Kaddour, M J Hinton, P A Smith, and S Li. The background to the third world-wide failure exercise. *Journal of Composite Materials*, 47(20-21):2417–2426, 2013. ISSN 00219983. doi: 10.1177/0021998313499475.

[40] Stephen W Tsai. Strength Characteristics of Composite Materials. Technical report, NATIONAL AERONAUTICS AND SPACE ADMINISTRATION, Washington, DC, 1965.

[41] A. C. Orifici, I. Herszberg, and R. S. Thomson. Review of methodologies for composite material modelling incorporating failure. *Composite Structures*, 86(1-3):194–210, nov 2008. ISSN 02638223. doi: 10.1016/j.compstruct.2008.03.007.

[42] Christos Kassapoglou. Design and Analysis of Composite Structures: With Applications to Aerospace Structures. In *Design and Analysis of Composite Structures: With Applications to Aerospace Structures: Second Edition*, chapter 4, pages 55–64. John Wiley and Sons, 2 edition, may 2013. ISBN 9781118401606. doi: 10.1002/9781118536933.

[43] Z Hashin. Failure criteria for unidirectional fiber composites. *Journal of Applied Mechanics, Transactions ASME*, 47(2):329–334, 1980. ISSN 15289036. doi: 10.1115/1.3153664.

[44] Carlos G. Dávila, Pedro P Camanho, and Cheryl A Rose. Failure criteria for FRP laminates. *Journal of Composite Materials*, 39(4):323–345, 2005. ISSN 00219983. doi: 10.1177/0021998305046452.

[45] Björn van Dongen, Alexander van Oostrum, and Dimitrios Zarouchas. A blended continuum damage and fracture mechanics method for progressive damage analysis of composite structures using XFEM. *Composite Structures*, 184:512–522, 2018. ISSN 02638223. doi: 10.1016/j.compstruct.2017.10.007.

[46] A S Kaddour and M J Hinton. Benchmarking of triaxial failure criteria for composite laminates: Comparison between models of 'Part (A)' of 'WWFE-II'. *Journal of Composite Materials*, 46 (19-20):2595–2634, 2012. ISSN 00219983. doi: 10.1177/0021998312449887.

[47] H Matthias Deuschle and Bernd H. Kröplin. Finite element implementation of Puck's failure theory for fibre-reinforced composites under three-dimensional stress. *Journal of Composite Materials*, 46(19-20):2485–2513, sep 2012. ISSN 00219983. doi: 10.1177/0021998312451480.

[48] S. T. Pinho, R Darvizeh, P Robinson, C Schuecker, and P. P. Camanho. Material and structural response of polymer-matrix fibre-reinforced composites. *Journal of Composite Materials*, 46(19-20):2313–2341, sep 2012. ISSN 00219983. doi: 10.1177/0021998312454478.

[49] A Atas, G F Mohamed, and C Soutis. Modelling delamination onset and growth in pin loaded composite laminates. *Composites Science and Technology*, 72(10):1096–1101, 2012. ISSN 02663538. doi: 10.1016/j.compscitech.2011.07.005.

[50] Christos Kassapoglou. *Modeling the Effect of Damage in Composite Structures: Simplified Approaches*. Wiley, 1 edition, 2015. ISBN 9781119013228. doi: 10.1002/9781119013228.

[51] Paul A Lagace. Notch sensitivity of graphite/epoxy fabric laminates. *Composites Science and Technology*, 26(2):95–117, 1986. ISSN 02663538. doi: 10.1016/0266-3538(86)90079-5.

[52] J M Whitney and R J Nuismer. Stress Fracture Criteria for Laminated Composites Containing Stress Concentrations. *Journal of Composite Materials*, 8(3):253–265, 1974. ISSN 1530793X. doi: 10.1177/002199837400800303.

[53] Samual P. Garbo and J. M. Ogonowski. Effect of Variances and Manufacturing Tolerances on the Design Strength and Life of Mechanically Fastened Composite Joints. Volume 1. Methodology Development and Data Evaluation. Technical report, St. Louis, Missouri, 1981.

[54] P P Camanho and M Lambert. A design methodology for mechanically fastened joints in laminated composite materials. *Composites Science and Technology*, 66(15):3004–3020, 2006. ISSN 02663538. doi: 10.1016/j.compscitech.2006.02.017.

[55] Lucas F.M. da Silva, Paulo J.C. das Neves, R D Adams, and J K Spelt. Analytical models of adhesively bonded joints-Part I: Literature survey. *International Journal of Adhesion and Adhesives*, 29(3):319–330, 2009. ISSN 01437496. doi: 10.1016/j.ijadhadh.2008.06.005.

[56] P P Camanho and F L Matthews. Stress analysis and strength prediction of mechanically fastened joints in FRP: A review. *Composites Part A: Applied Science and Manufacturing*, 28(6): 529–547, 1997. ISSN 1359835X. doi: 10.1016/S1359-835X(97)00004-3.

[57] Víctor Martínez, Alfredo Güemes, Dani Trias, and Norbert Blanco. Numerical and experimental analysis of stresses and failure in T-bolt joints. *Composite Structures*, 93(10):2636–2645, sep 2011. ISSN 02638223. doi: 10.1016/j.compstruct.2011.04.031.

[58] A A Pisano and P Fuschi. Mechanically fastened joints in composite laminates: Evaluation of load bearing capacity. *Composites Part B: Engineering*, 42(4):949–961, 2011. ISSN 13598368. doi: 10.1016/j.compositesb.2010.12.016.

[59] Jianyu Zhang, Fengrui Liu, Libin Zhao, and Binjun Fei. A novel characteristic curve for failure prediction of multi-bolt composite joints. *Composite Structures*, 108(1):129–136, 2014. ISSN 02638223. doi: 10.1016/j.compstruct.2013.09.019.

[60] Theo de Jong. Stresses Around Pin-Loaded Holes in Elastically Orthotropic or Isotropic Plates. *Journal of Composite Materials*, 11(3):313–331, 1977. ISSN 1530793x. doi: 10.1177/002199837701100306.

[61] M W Hyer, E C Klang, and D E Cooper. The Effects of Pin Elasticity, Clearance, and Friction on the Stresses in a Pin-Loaded Orthotropic Plate. *Journal of Composite Materials*, 21(3):190–206, 1987. ISSN 1530793x. doi: 10.1177/002199838702100301.

[62] SM Serabian. An Experimental and Finite Element Investigation into the Nonlinear Material Behavior of Pin-loaded Composite Laminates. Technical report, U.S. Army Materials Technology Laboratory, Watertown, Massachusetts, 1991.

[63] K I Tserpes, G Labeas, P Papanikos, and Th Kermanidis. Strength prediction of bolted joints in graphite/epoxy composite laminates. *Composites Part B: Engineering*, 33(7):521–529, 2002. ISSN 13598368. doi: 10.1016/S1359-8368(02)00033-1.

[64] Fu Kuo Chang, Richard A Scott, and George S Springer. Strength of Mechanically Fastened Composite Joints. *Journal of Composite Materials*, 16(6):470–494, 1982. ISSN 1530793X. doi: 10.1177/002199838201600603.

[65] S E Yamada and C T Sun. Analysis of Laminate Strength and Its Distribution. *Journal of Composite Materials*, 12(3):275–284, 1978. ISSN 1530793x. doi: 10.1177/002199837801200305.

[66] Jin Hwe Kweon, Hyon Su Ahn, and Jin Ho Choi. A new method to determine the characteristic lengths of composite joints without testing. *Composite Structures*, 66(1-4):305–315, oct 2004. ISSN 02638223. doi: 10.1016/j.compstruct.2004.04.053.

[67] Kurt C. Schulz, Paul F. Packman, and James R. Eisenmann. A Tension-Mode Fracture Model for Bolted Joints in Laminated Composites. *Journal of Composite Materials*, 29(1):37–58, jan 1995. ISSN 1530793X. doi: 10.1177/002199839502900103.

[68] E Pan, B Yang, G Cai, and F G Yuan. Stress analyses around holes in composite laminates using boundary element method. *Engineering Analysis with Boundary Elements*, 25(1):31–40, 2001. ISSN 09557997. doi: 10.1016/S0955-7997(00)00066-7.

[69] Jin Min Zhang. Design and analysis of mechanically fastened composite joints and repairs. *Engineering Analysis with Boundary Elements*, 25(6):431–441, 2001. ISSN 09557997. doi: 10.1016/S0955-7997(01)00049-2.

[70] S T Lie, G Yu, and Z Zhao. Analysis of mechanically fastened composite joints by boundary element methods. *Composites Part B: Engineering*, 31(8):693–705, 2000. ISSN 13598368. doi: 10.1016/S1359-8368(00)00039-1.

[71] Chien Chang Lin and Chuen Horng Lin. Stresses around pin-loaded hole in composite laminates using direct boundary element method. *International Journal of Solids and Structures*, 36(5): 763–783, 1999. ISSN 00207683. doi: 10.1016/S0020-7683(98)00045-6.

[72] L. D.C. Ramalho, R. D.S.G. Campilho, J Belinha, and L. F.M. da Silva. Static strength prediction of adhesive joints: A review. *International Journal of Adhesion and Adhesives*, 96, 2020. ISSN 01437496. doi: 10.1016/j.ijadhadh.2019.102451.

[73] S Budhe, M. D. Banea, S de Barros, and L. F.M. da Silva. An updated review of adhesively bonded joints in composite materials. *International Journal of Adhesion and Adhesives*, 72:30–42, 2017. ISSN 01437496. doi: 10.1016/j.ijadhadh.2016.10.010.

[74] R. D.S.G. Campilho, M D Banea, F. J.P. Chaves, and L. F.M.Da Silva. EXtended Finite Element Method for fracture characterization of adhesive joints in pure mode i. In *Computational Materials Science*, volume 50, pages 1543–1549, 2011. doi: 10.1016/j.commatsci.2010.12.012.

[75] H Ahmad, A. D. Crocombe, and P. A. Smith. Strength prediction in CFRP woven laminate bolted double-lap joints under quasi-static loading using XFEM. *Composites Part A: Applied Science and Manufacturing*, 56:192–202, 2014. ISSN 1359835X. doi: 10.1016/j.compositesa.2013.10.012.

[76] A. Ataş and C Soutis. Strength prediction of bolted joints in CFRP composite laminates using cohesive zone elements. *Composites Part B: Engineering*, 58:25–34, 2014. ISSN 13598368. doi: 10.1016/j.compositesb.2013.10.017.

[77] C Soutis, N A Fleck, and P T Curtis. Hole-hole interaction in carbon fibre/epoxy laminates under uniaxial compression. *Composites*, 22(1):31–38, 1991. ISSN 00104361. doi: 10.1016/0010-4361(91)90100-U.

[78] X. W. Xu, T. M. Yue, and H. C. Man. Stress analysis of finite composite laminate with multiple loaded holes. *International Journal of Solids and Structures*, 36(6):919–931, 1999. ISSN 00207683. doi: 10.1016/S0020-7683(97)00343-0.

[79] E Persson and I Eriksson. Fatigue of multiple-row bolted joints in carbon/epoxy laminates: Ranking of factors affecting strength and fatigue life. *International Journal of Fatigue*, 21(4):337–353, 1999. ISSN 01421123. doi: 10.1016/S0142-1123(98)00081-4.

[80] O. H. Griffin, M. W. Hyer, D. Cohenrj, M. J. Shuart, S. R. Yalamanchili, and C. B. Prasad. Analysis of multifastener composite joints. *Journal of Spacecraft and Rockets*, 31(2):278–284, may 1994. ISSN 00224650. doi: 10.2514/3.26434.

[81] Rajiv A. Naik and John H. Rews. Stress analysis method for clearance-fit joints with bearing-bypass loads. *AIAA Journal*, 29(1):89–95, jan 1991. ISSN 00011452. doi: 10.2514/3.10549.

[82] Surachate Chutima and Alvin P. Blackie. Effect of pitch distance, row spacing, end distance and bolt diameter on multi-fastened composite joints. *Composites Part A: Applied Science and Manufacturing*, 27(2):105–110, jan 1996. ISSN 1359835X. doi: 10.1016/1359-835X(95)00020-3.

[83] Theo de Jong. Stresses in pin loaded anisotropic plates. In *AGARD Conference Proceedings*, pages 5.1–5.17, Madrid, Spain, 1987. AGARD.

[84] C. T. McCarthy, M. A. McCarthy, and V P Lawlor. Progressive damage analysis of multi-bolt composite joints with variable bolt-hole clearances. *Composites Part B: Engineering*, 36(4):290–305, 2005. ISSN 13598368. doi: 10.1016/j.compositesb.2004.11.003.

[85] B Pradhan and P. Ramesh Babu. Assessment of beneficial effects of interference-fit in pin-loaded FRP composites. *Journal of Reinforced Plastics and Composites*, 26(8):771–788, 2007. ISSN 07316844. doi: 10.1177/0731684407076713.

[86] A Solis, E Barbero, and S Sánchez-Sáez. Analysis of damage and interlaminar stresses in laminate plates with interacting holes. *International Journal of Mechanical Sciences*, 165:105189, 2020. ISSN 00207403. doi: 10.1016/j.ijmecsci.2019.105189.

[87] Florian Doorenspleet, Rainer Arelt, and Enno Eyb. Blade for a wind turbine rotor, apr 2012.

[88] Jabir Ubaid, Mohammad Kashfuddoja, and Manoharan Ramji. Strength prediction and progressive failure analysis of carbon fiber reinforced polymer laminate with multiple interacting holes involving three dimensional finite element analysis and digital image correlation. *International Journal of Damage Mechanics*, 23(5):609–635, 2014. ISSN 15307921. doi: 10.1177/1056789513504123.

[89] M. A. McCarthy and C. T. McCarthy. Finite element analysis of effects of clearance on single shear composite bolted joints. In *Plastics, Rubber and Composites*, volume 32, pages 65–70, 2003. doi: 10.1179/146580103225001390.

[90] Jingchao Wei, Guiqiong Jiao, Purong Jia, and Tao Huang. The effect of interference fit size on the fatigue life of bolted joints in composite laminates. *Composites Part B: Engineering*, 53:62–68, 2013. ISSN 13598368. doi: 10.1016/j.compositesb.2013.04.048.

[91] Heung Joon Park. Effects of stacking sequence and clamping force on the bearing strengths of mechanically fastened joints in composite laminates. *Composite Structures*, 53(2):213–221, aug 2001. ISSN 02638223. doi: 10.1016/S0263-8223(01)00005-8.

[92] Inc. TPI Composites and Sandia National Laboratories. INNOVATIVE DESIGN APPROACHES FOR LARGE WIND TURBINE BLADES FINAL REPORT. Technical report, Sandia Corporation, Albuquerque, New Mexico, 2004.

[93] Gabriel Mironov. (19) United States (12) Patent Application Publication (10) Pub . No .: US 2012 / 0304577 A1 Patent Application Publication, 2012.

[94] Frederic Bussieres and Mats Goldberg. WINDTURBINE ROTOR BLADE ASSEMBLY WITH A RING INSERT IN THE BLADE ROOT, may 2014.

[95] Srikanth Samudrala, Biju Nanukuttan, Dhanesh Chandrashekar Pathuvoth, and Willem Jan Bakhuis. RING INSERT FOR A WIND TURBINE ROTOR BLADE, 2019.

[96] Alexandros Antoniou, Kim Branner, D.J. Lekou, Iñaki Nuin, and Rogier Nijssen. Methodology for testing subcomponents; background and motivation for subcomponent testing of wind turbine rotor blades. Technical report, 2016.

[97] Malo Rosemeier, Gregor Basters, and Alexandros Antoniou. Benefits of subcomponent over full-scale blade testing elaborated on a trailing-edge bond line design validation. *Wind Energy Science*, 3(1):163–172, 2018. ISSN 23667451. doi: 10.5194/wes-3-163-2018.

[98] Philipp Ulrich Haselbach, Martin Alexander Eder, and Federico Belloni. A comprehensive investigation of trailing edge damage in a wind turbine rotor blade. *Wind Energy*, 19(10):1871–1888, oct 2016. ISSN 10954244. doi: 10.1002/we.1956.

[99] D. S. Zarouchas, A. A. Makris, F. Sayer, D. Van Hemelrijck, and A. M. Van Wingerde. Investigations on the mechanical behavior of a wind rotor blade subcomponent. *Composites Part B: Engineering*, 43(2):647–654, mar 2012. ISSN 13598368. doi: 10.1016/j.compositesb.2011.10.009.

[100] F. Lahuerta, N Koorn, and D Smissaert. Wind turbine blade trailing edge failure assessment with sub-component test on static and fatigue load conditions. *Composite Structures*, 204:755–766, 2018. ISSN 02638223. doi: 10.1016/j.compstruct.2018.07.112.

[101] Malo Rosemeier, Gregor Basters, and Alexandros Antoniou. Benefits of subcomponent over full-scale blade testing elaborated on a trailing-edge bond line design validation. *Wind Energy Science*, 3(1):163–172, 2018. ISSN 2366-7451. doi: 10.5194/wes-3-163-2018.

[102] Douglas S. Cairns and Jon D. Skramstad. Evaluation of Hand Lay-Up and Resin Transfer Molding in Composite Wind Turbine Blade Manufacturing. Technical report, Sandia National Laboratories, Bozeman, MT, 2000.

[103] Mohamad Eydani Asl, Christopher Niezrecki, James Sherwood, and Peter Avitabile. Predicting the vibration response in subcomponent testing of wind turbine blades. In *Conference Proceedings of the Society for Experimental Mechanics Series*, volume 6, pages 115–123, 2015. ISBN 9783319069883. doi: 10.1007/978-3-319-15048-2_11.

[104] F Lahuerta, R. P.L. Nijssen, F. P. van der Meer, and L J Sluys. Thickness scaled compression tests in unidirectional glass fibre reinforced composites in static and fatigue loading. *Composites Science and Technology*, 123:115–124, 2016. ISSN 02663538. doi: 10.1016/j.compscitech.2015.12.008.

[105] Will Roberston. delaunay_surf, 2015.

[106] J Blaber, B. Adair, and A. Antoniou. Ncorr: Open-Source 2D Digital Image Correlation Matlab Software. *Experimental Mechanics*, 55(6):1105–1122, 2015. ISSN 17412765. doi: 10.1007/s11340-015-0009-1.

[107] R. Harilal and M. Ramji. Adaptation of Open Source 2D DIC Software Ncorr for Solid Mechanics Applications. In *9th International Symposium on Advanced Science and Technology in Experimental Mechanics*, number November, pages 1–6, 2014. doi: 10.13140/2.1.4994.1442.

Appendices

A. Static Strain Maps

This appendix shows all of the strain maps comparing the measured DIC strains to the predicted ANSYS strains for the static tests. The plots are shown for the front and back of each specimen using the unloaded ("Zero") and pretension ("PreT") states as the reference, and the "end" state for all the measurements is the lab-scale target load of $F_{ext} = 260$ kN. These states are discussed in Chapter 5, from which the image below has been copied as a reference. The motivation for examining results from different reference states is to avoid the influence of any rigid body motion that may have occurred during the pretensioning of the specimen, and this figure shows how the displacement field (and thus the strain) is affected by movement between the specimen and the endplate during the application of the shaftbolt pretension. The strain maps are shown, beginning with Specimen 1A, on the following page.

Before presenting the plots, a few comments are offered to explain the format in which they are presented. Firstly, the plots are grouped such that each specimen (1A, 1B, etc.) is shown on its own page, and this results in a 4 row by 2 column grid. The top two rows of images are the front (row 1) and back (row 2) surfaces of the specimen using the unloaded or zero state as the reference state. Subsequently, the bottom two rows are the front (row 3) and back (row 4) surfaces of the specimen using the pretension state as the reference state. In each of these two groups, the ANSYS prediction is shown on the left while the DIC measurements are on the right. All of these distinctions are also given in the plot titles which are in the format: [Specimen] [Surface] [Reference state] [Data source].

To improve the clarity of the results, the ANSYS and DIC images are plotted with the same colour scales for the same surfaces. That way, 4 of the 8 images shown on each page will have the same colour scales as each other, and to distinguish the two colour scales, different colour maps are used. The colour maps correspond to reference state used for the data. The limits of the colour scales, and thus the normalized strain represented by each colour, is different from page to page or specimen to specimen. This is necessary to avoid losses in contour resolution, but it is important to note if comparing contour maps between specimens. Furthermore it should be noted that in the experimental results (in Chapter 5) are not necessarily shown with the same contour limits as in this appendix.

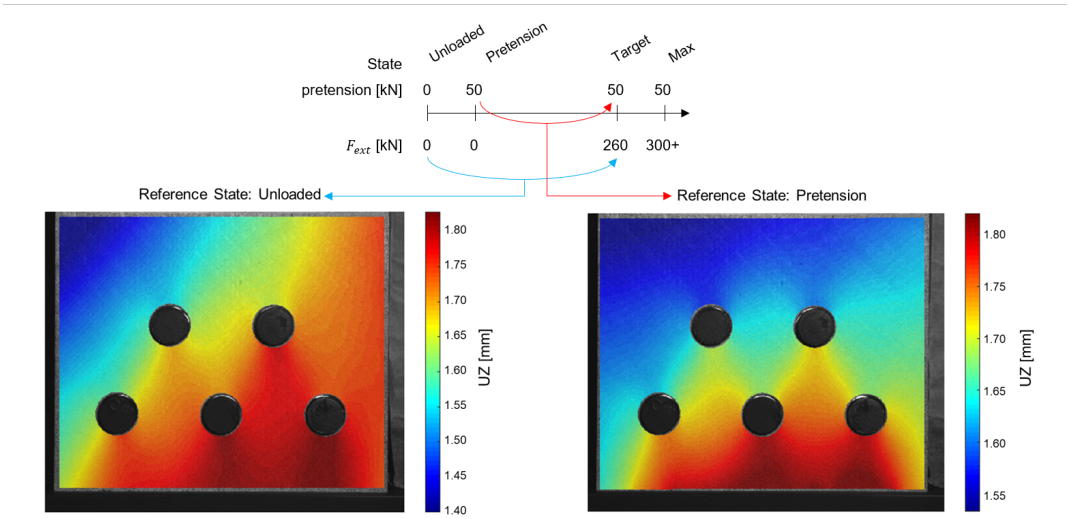

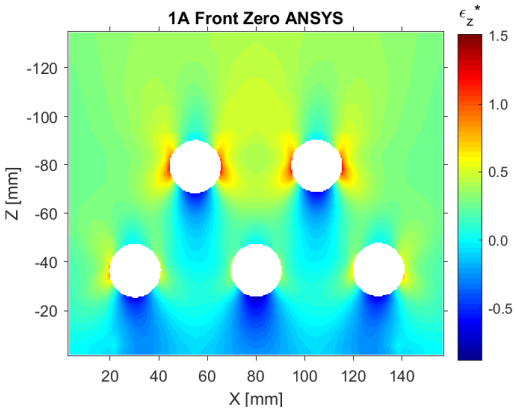
1A Front Zero ANSYS
ϵ_z^*
Z [mm]
X [mm]

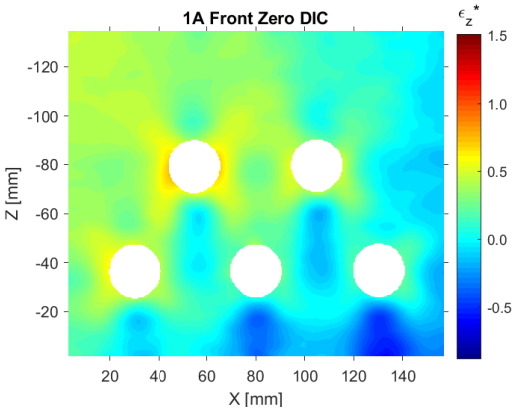
1A Front Zero DIC
ϵ_z^*
Z [mm]
X [mm]

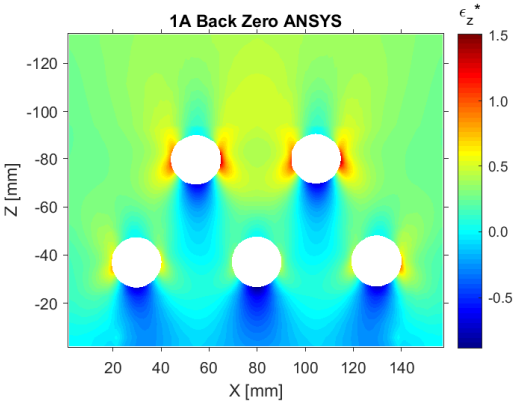
1A Back Zero ANSYS
ϵ_z^*
Z [mm]
X [mm]

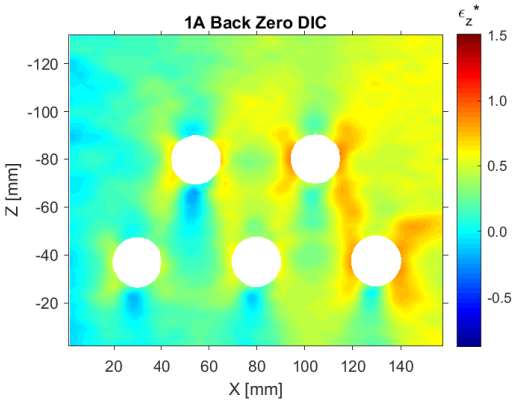
1A Back Zero DIC
ϵ_z^*
Z [mm]
X [mm]

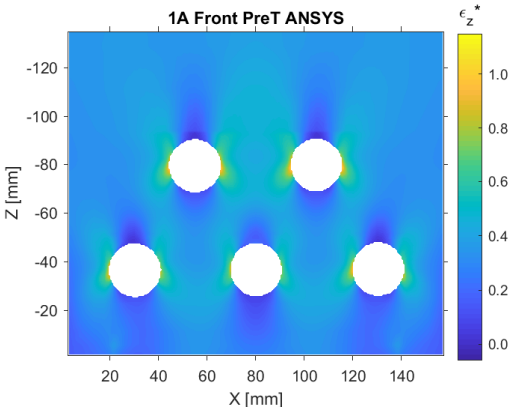
1A Front PreT ANSYS
ϵ_z^*
Z [mm]
X [mm]

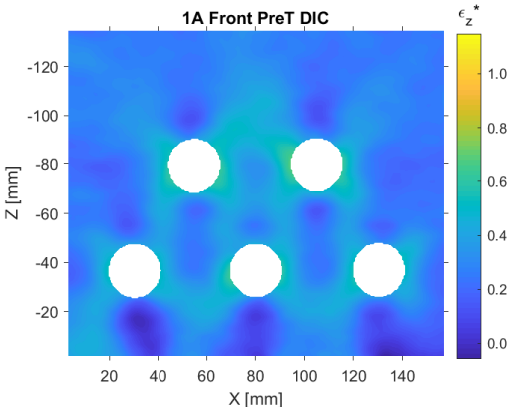
1A Front PreT DIC
ϵ_z^*
Z [mm]
X [mm]

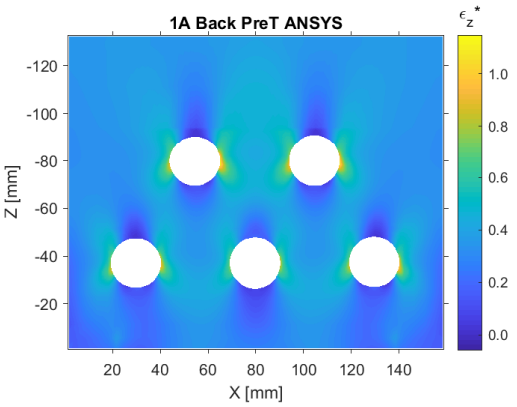
1A Back PreT ANSYS
ϵ_z^*
Z [mm]
X [mm]

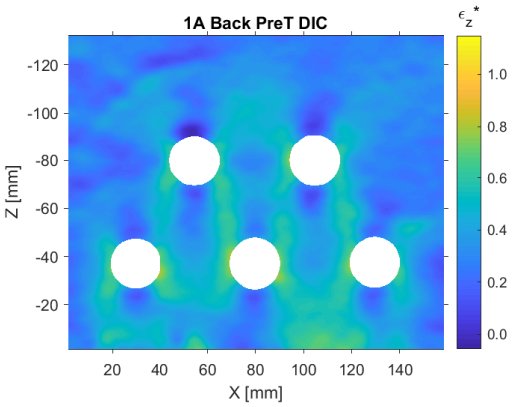
1A Back PreT DIC
ϵ_z^*
Z [mm]
X [mm]

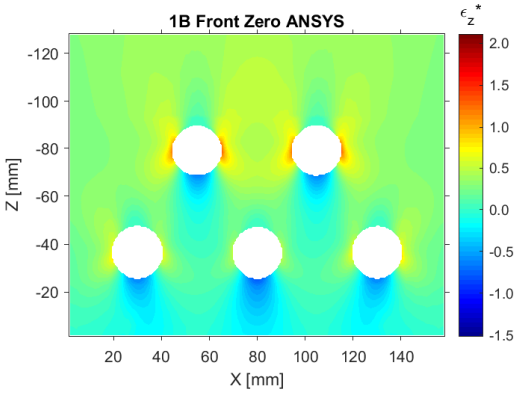
1B Front Zero ANSYS
ϵ_z^*
Z [mm]
X [mm]

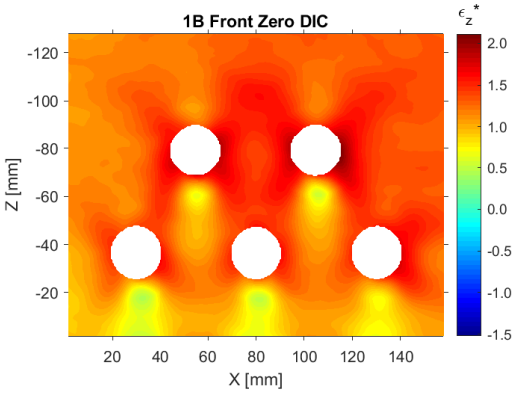
1B Front Zero DIC
ϵ_z^*
Z [mm]
X [mm]

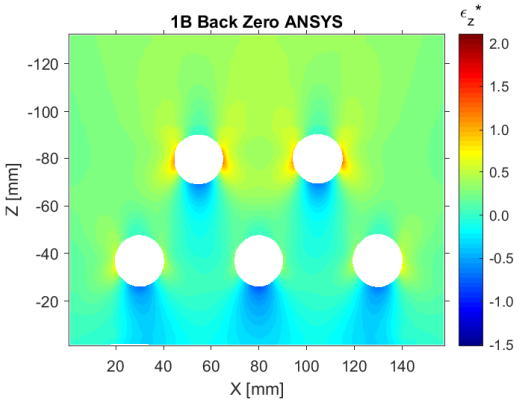
1B Back Zero ANSYS
ϵ_z^*
Z [mm]
X [mm]

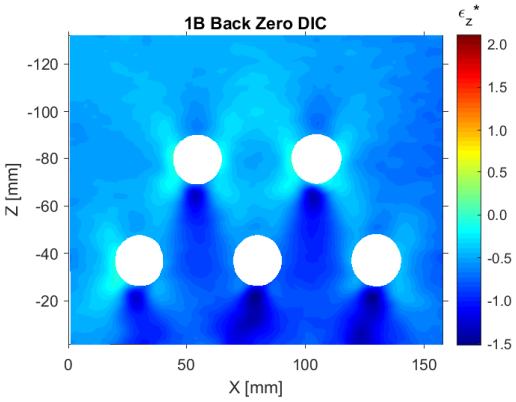
1B Back Zero DIC
ϵ_z^*
Z [mm]
X [mm]

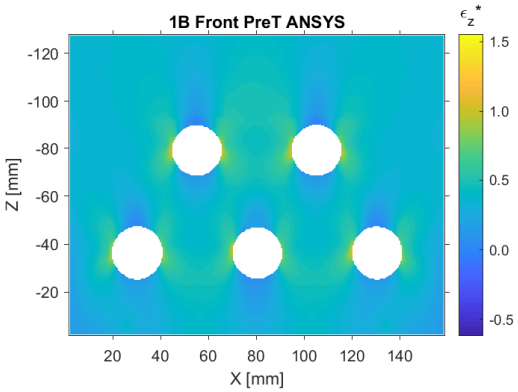
1B Front PreT ANSYS
ϵ_z^*
Z [mm]
X [mm]

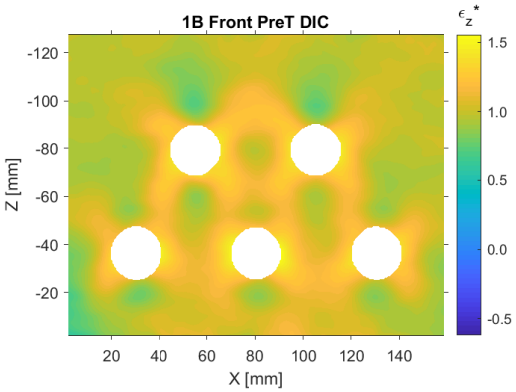
1B Front PreT DIC
ϵ_z^*
Z [mm]
X [mm]

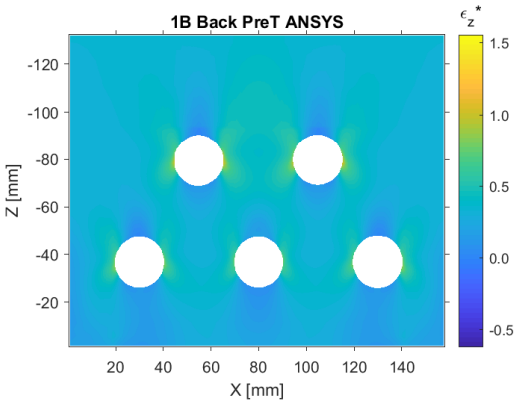
1B Back PreT ANSYS
ϵ_z^*
Z [mm]
X [mm]

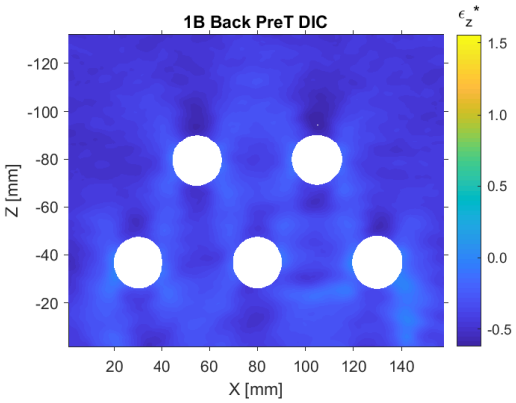
1B Back PreT DIC
ϵ_z^*
Z [mm]
X [mm]

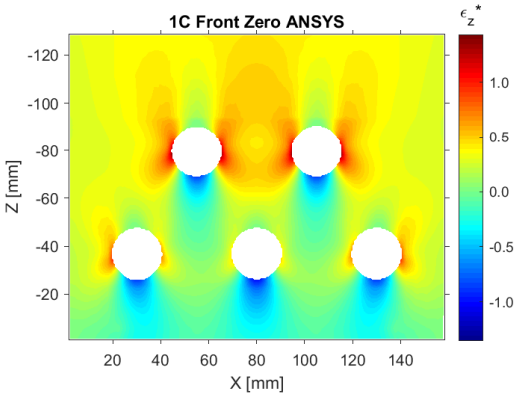
1C Front Zero ANSYS
ϵ_z^*
Z [mm]
X [mm]

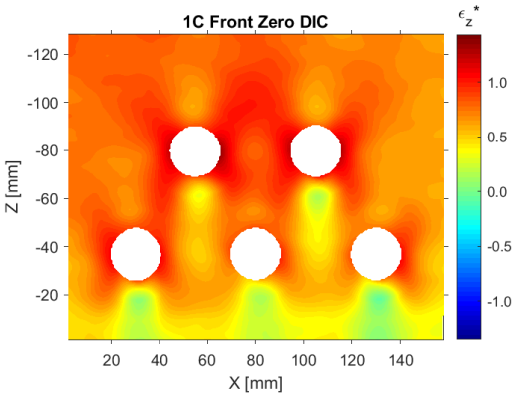
1C Front Zero DIC
ϵ_z^*
Z [mm]
X [mm]

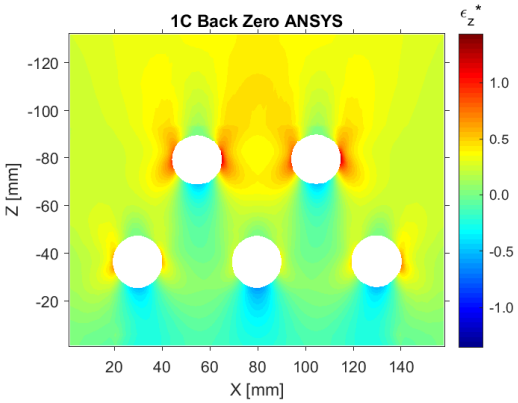
1C Back Zero ANSYS
ϵ_z^*
Z [mm]
X [mm]

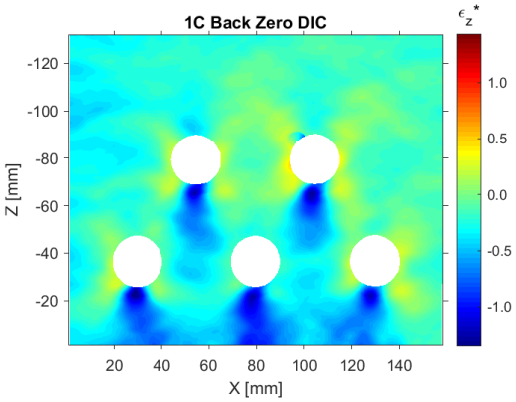
1C Back Zero DIC
ϵ_z^*
Z [mm]
X [mm]

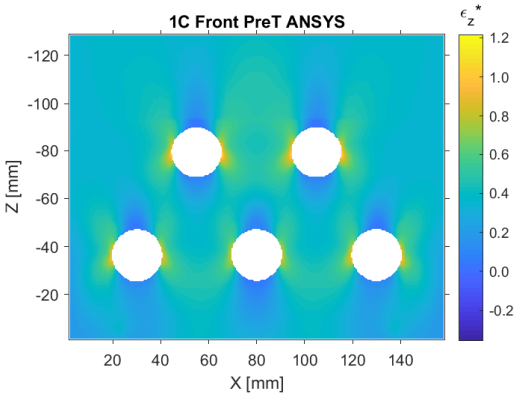
1C Front PreT ANSYS
ϵ_z^*
Z [mm]
X [mm]

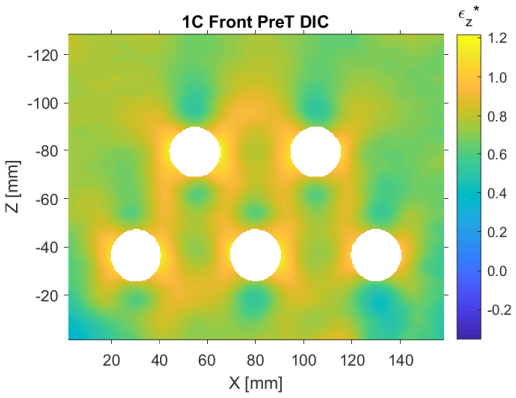
1C Front PreT DIC
ϵ_z^*
Z [mm]
X [mm]

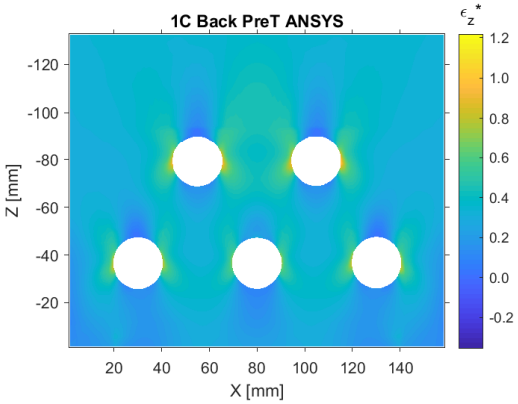
1C Back PreT ANSYS
ϵ_z^*
Z [mm]
X [mm]

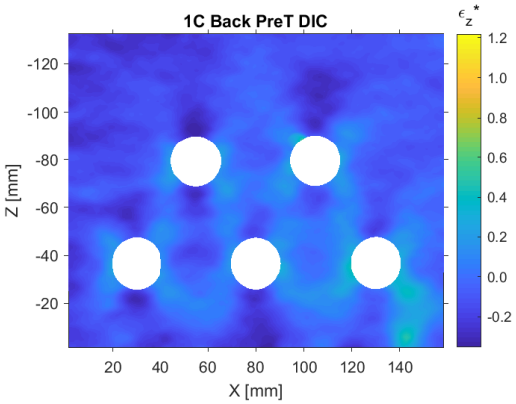
1C Back PreT DIC
ϵ_z^*
Z [mm]
X [mm]

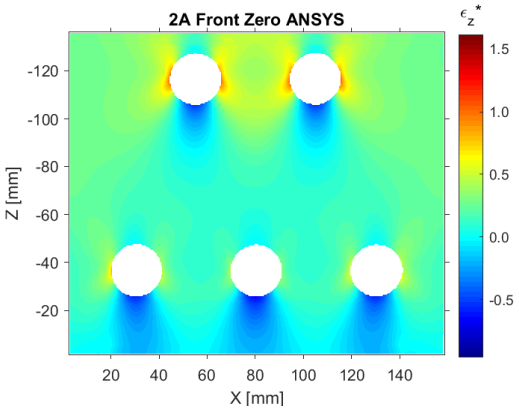
2A Front Zero ANSYS
ϵ_z^*
Z [mm]
X [mm]

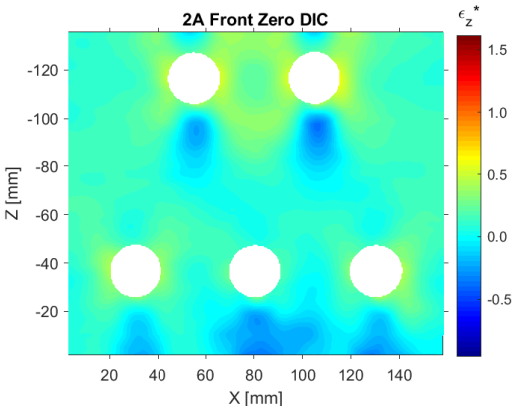
2A Front Zero DIC
ϵ_z^*
Z [mm]
X [mm]

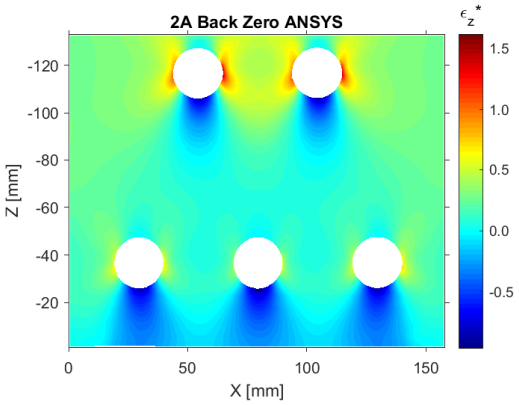
2A Back Zero ANSYS
ϵ_z^*
Z [mm]
X [mm]

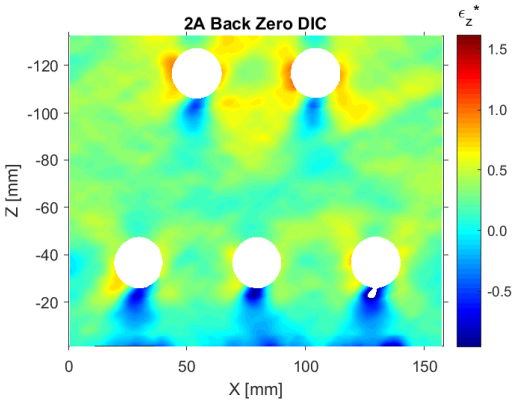
2A Back Zero DIC
ϵ_z^*
Z [mm]
X [mm]

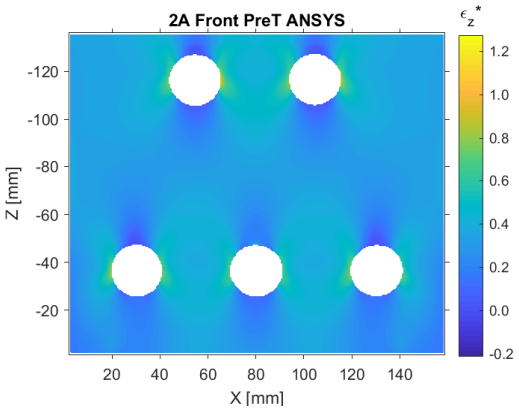
2A Front PreT ANSYS
ϵ_z^*
Z [mm]
X [mm]

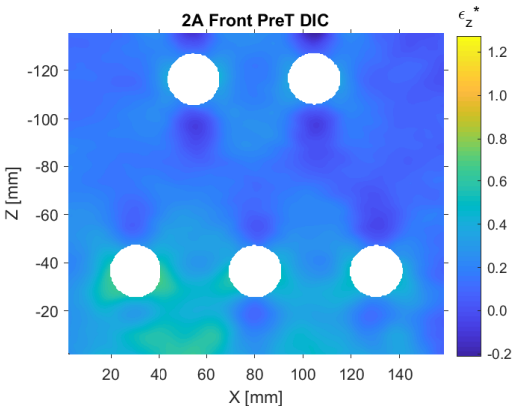
2A Front PreT DIC
ϵ_z^*
Z [mm]
X [mm]

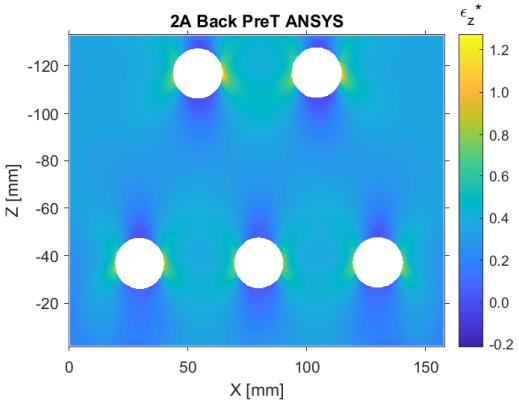
2A Back PreT ANSYS
ϵ_z^*
Z [mm]
X [mm]

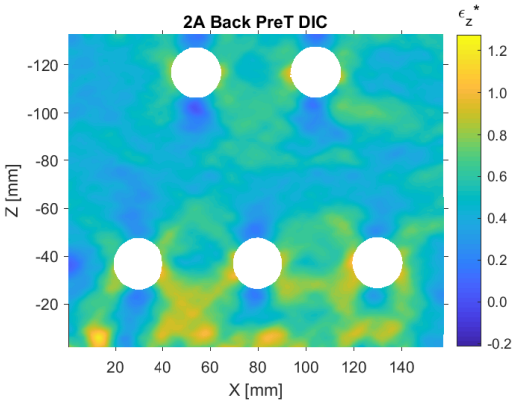
2A Back PreT DIC
ϵ_z^*
Z [mm]
X [mm]

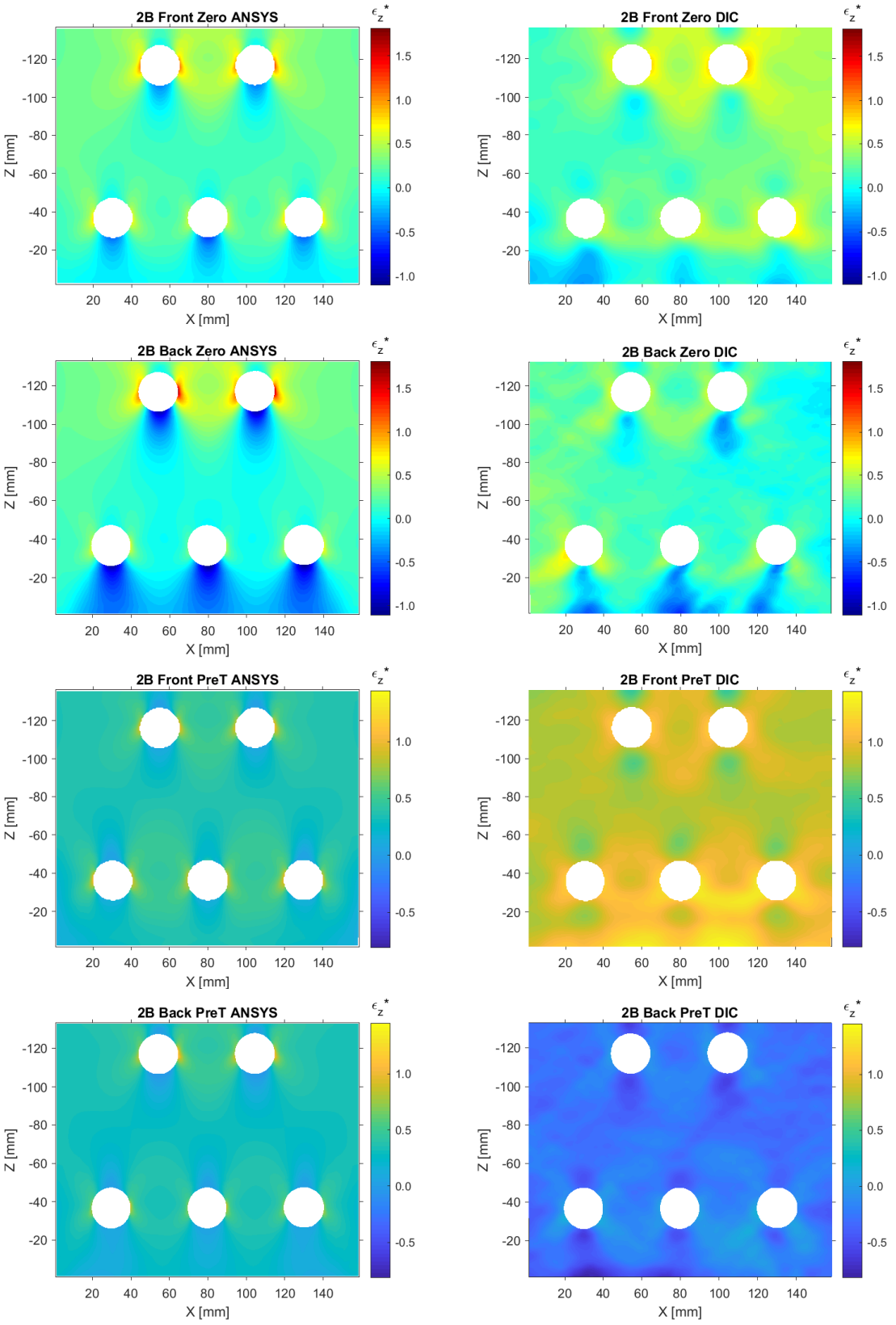
2B Front Zero ANSYS
2B Front Zero DIC
2B Back Zero ANSYS
2B Back Zero DIC
2B Front PreT ANSYS
2B Front PreT DIC
2B Back PreT ANSYS
2B Back PreT DIC
Z [mm]
X [mm]
ϵ_z^*

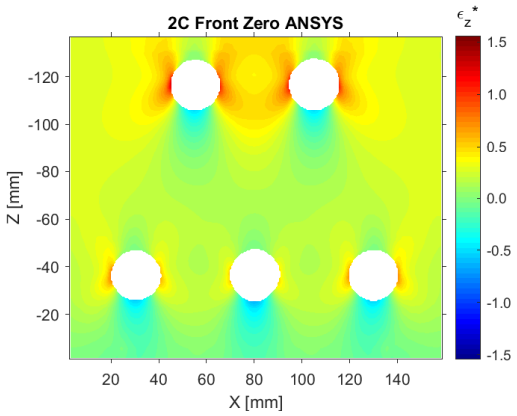
2C Front Zero ANSYS
ϵ_z^*
Z [mm]
X [mm]

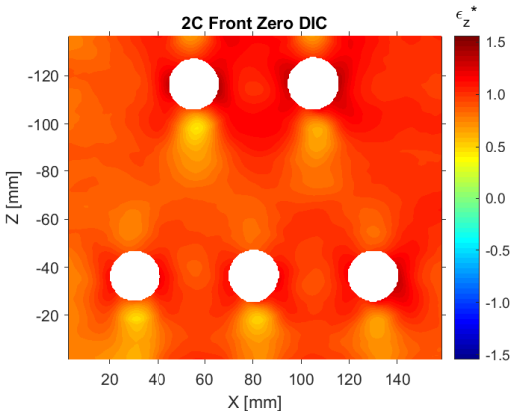
2C Front Zero DIC
ϵ_z^*
Z [mm]
X [mm]

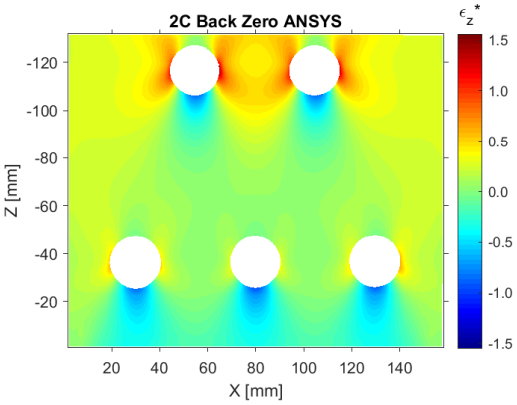
2C Back Zero ANSYS
ϵ_z^*
Z [mm]
X [mm]

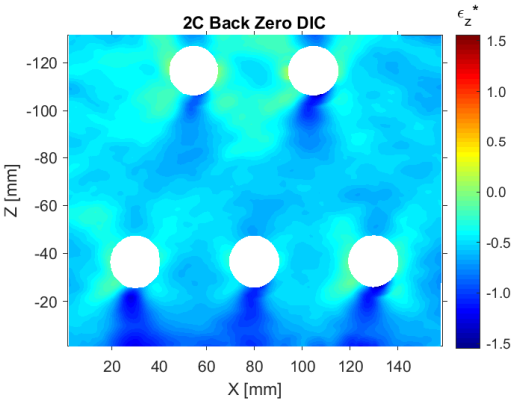
2C Back Zero DIC
ϵ_z^*
Z [mm]
X [mm]

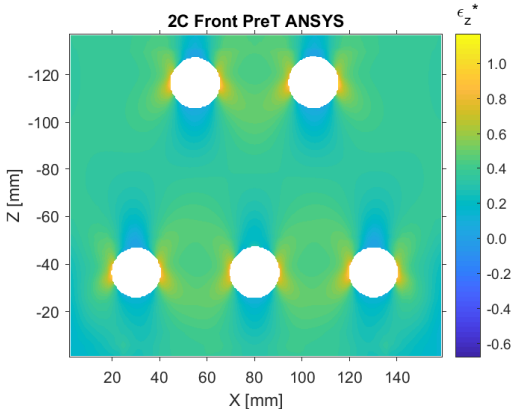
2C Front PreT ANSYS
ϵ_z^*
Z [mm]
X [mm]

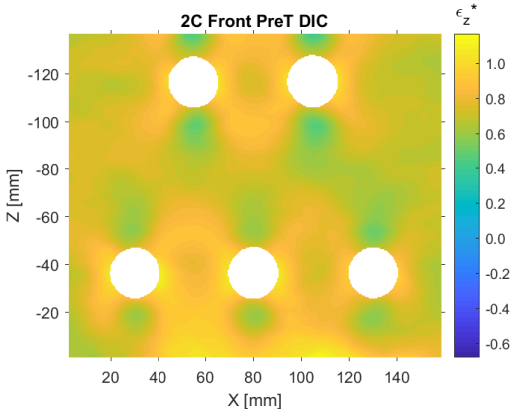
2C Front PreT DIC
ϵ_z^*
Z [mm]
X [mm]

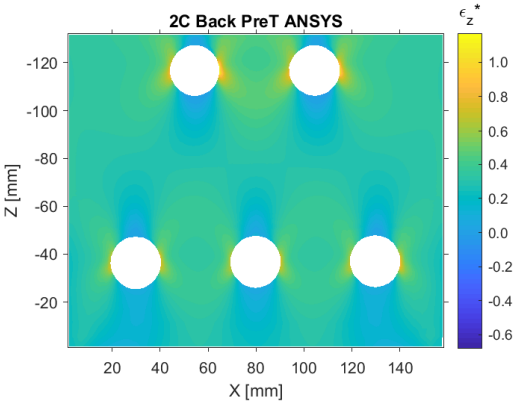
2C Back PreT ANSYS
ϵ_z^*
Z [mm]
X [mm]

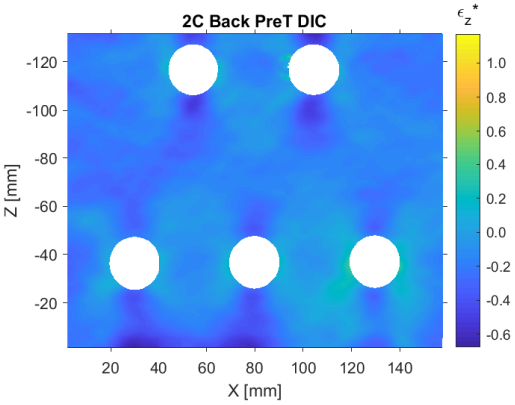
2C Back PreT DIC
ϵ_z^*
Z [mm]
X [mm]

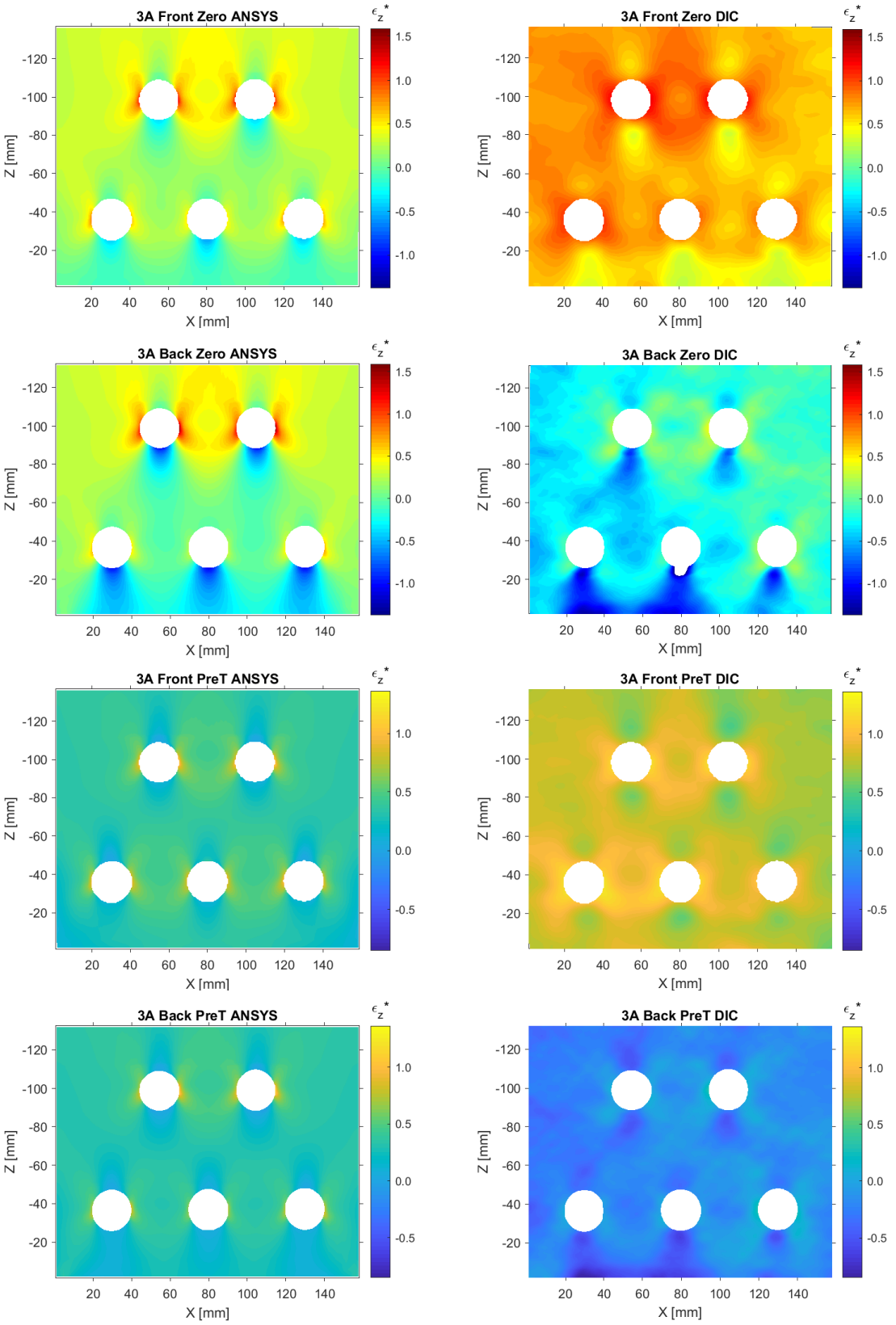
3A Front Zero ANSYS
3A Front Zero DIC
3A Back Zero ANSYS
3A Back Zero DIC
3A Front PreT ANSYS
3A Front PreT DIC
3A Back PreT ANSYS
3A Back PreT DIC
Z [mm]
X [mm]
ϵ_z^*

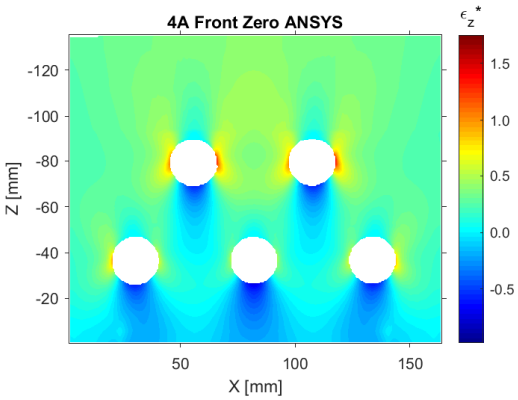
4A Front Zero ANSYS
ϵ_z^*
Z [mm]
X [mm]

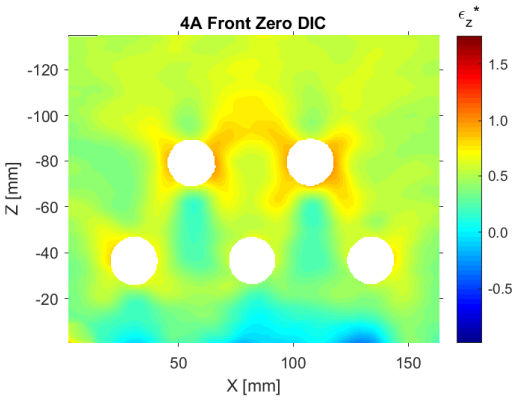
4A Front Zero DIC
ϵ_z^*
Z [mm]
X [mm]

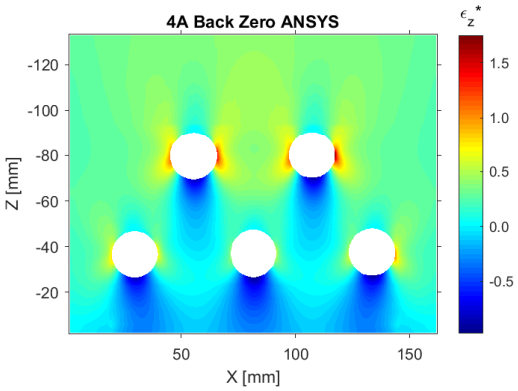
4A Back Zero ANSYS
ϵ_z^*
Z [mm]
X [mm]

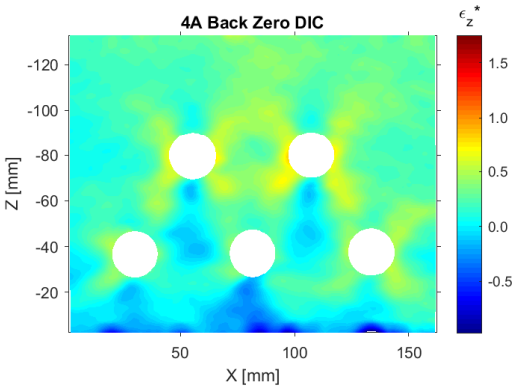
4A Back Zero DIC
ϵ_z^*
Z [mm]
X [mm]

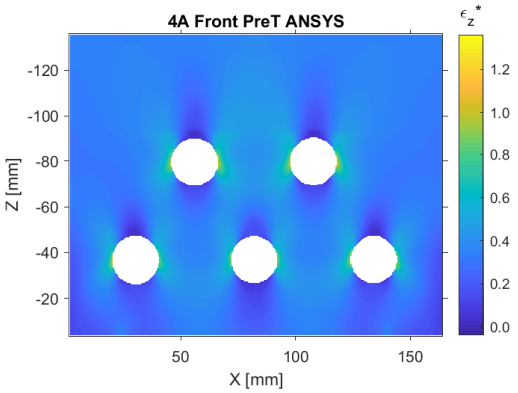
4A Front PreT ANSYS
ϵ_z^*
Z [mm]
X [mm]

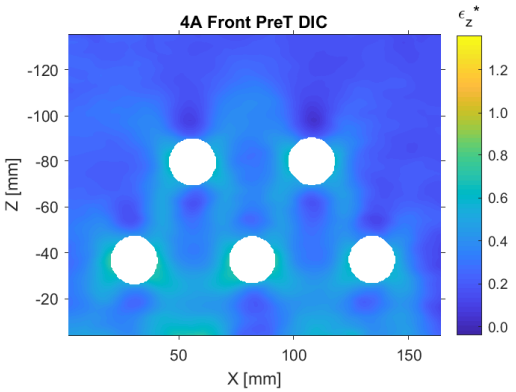
4A Front PreT DIC
ϵ_z^*
Z [mm]
X [mm]

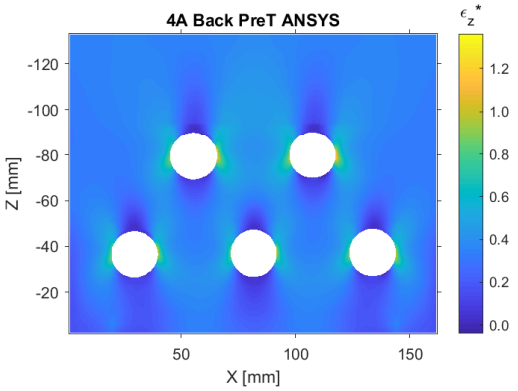
4A Back PreT ANSYS
ϵ_z^*
Z [mm]
X [mm]

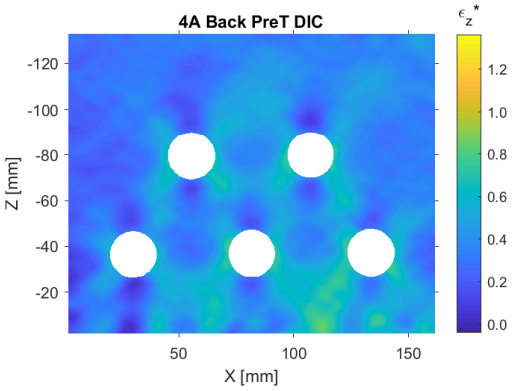
4A Back PreT DIC
ϵ_z^*
Z [mm]
X [mm]

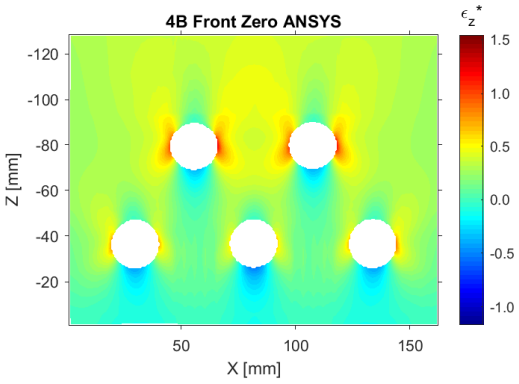
4B Front Zero ANSYS
Z [mm]
X [mm]
ϵ_z^*

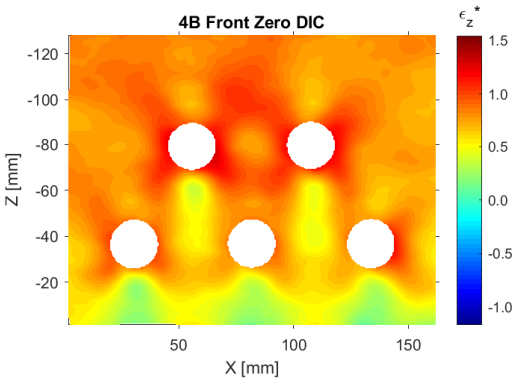
4B Front Zero DIC
Z [mm]
X [mm]
ϵ_z^*

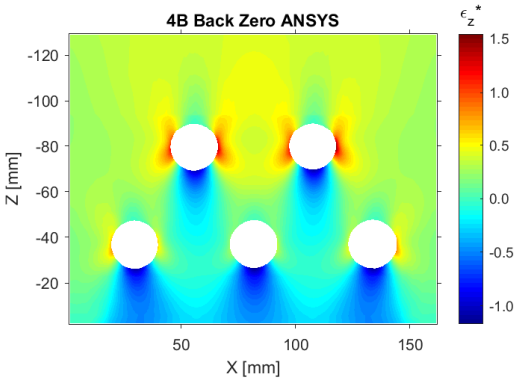
4B Back Zero ANSYS
Z [mm]
X [mm]
ϵ_z^*

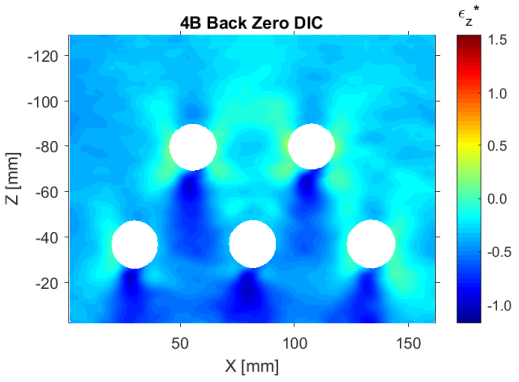
4B Back Zero DIC
Z [mm]
X [mm]
ϵ_z^*

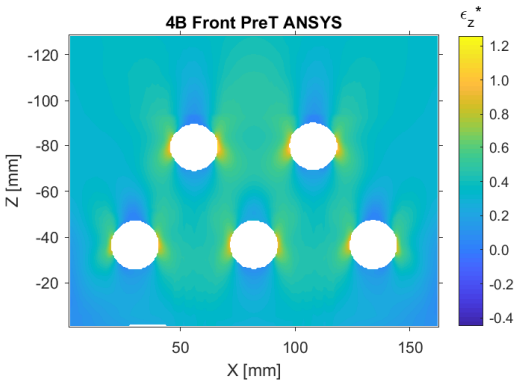
4B Front PreT ANSYS
Z [mm]
X [mm]
ϵ_z^*

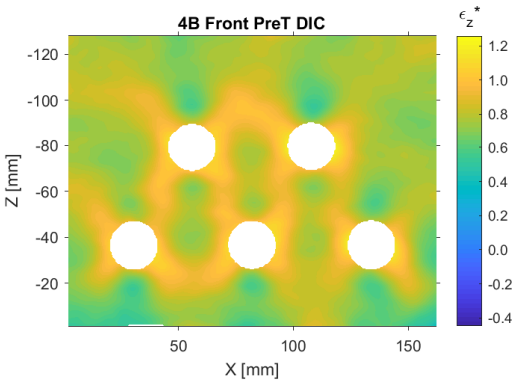
4B Front PreT DIC
Z [mm]
X [mm]
ϵ_z^*

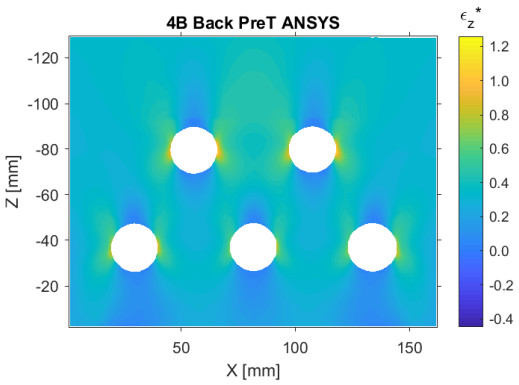
4B Back PreT ANSYS
Z [mm]
X [mm]
ϵ_z^*

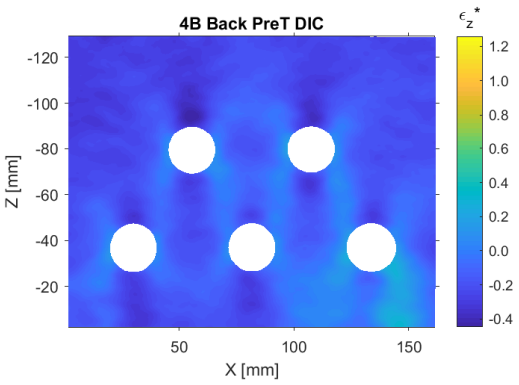
4B Back PreT DIC
Z [mm]
X [mm]
ϵ_z^*

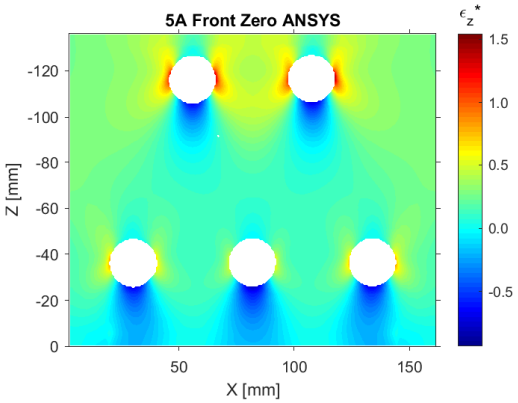
5A Front Zero ANSYS
ϵ_z^*
Z [mm]
X [mm]

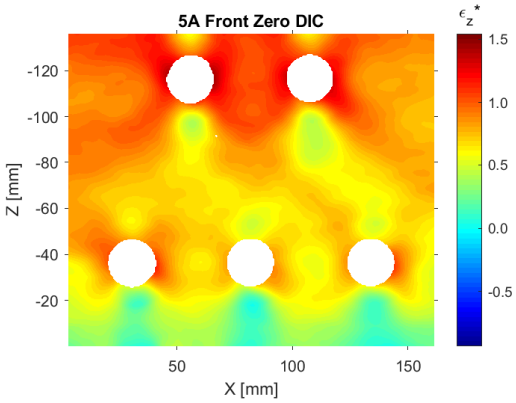
5A Front Zero DIC
ϵ_z^*
Z [mm]
X [mm]

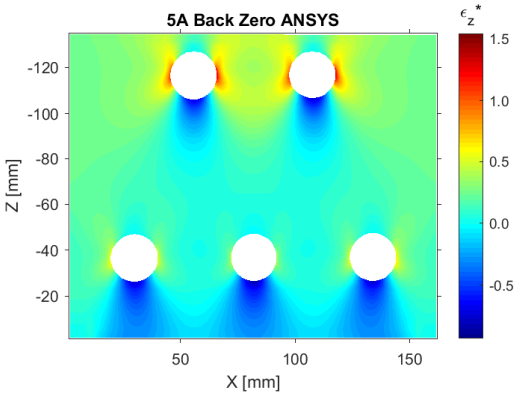
5A Back Zero ANSYS
ϵ_z^*
Z [mm]
X [mm]

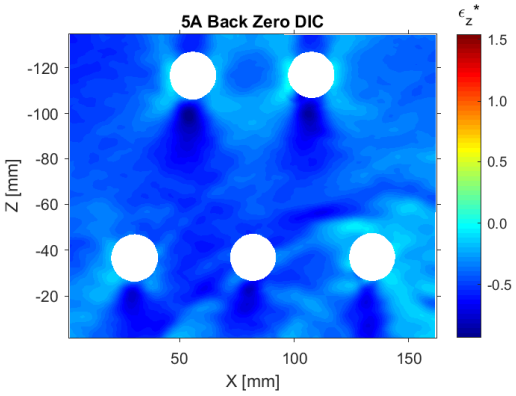
5A Back Zero DIC
ϵ_z^*
Z [mm]
X [mm]

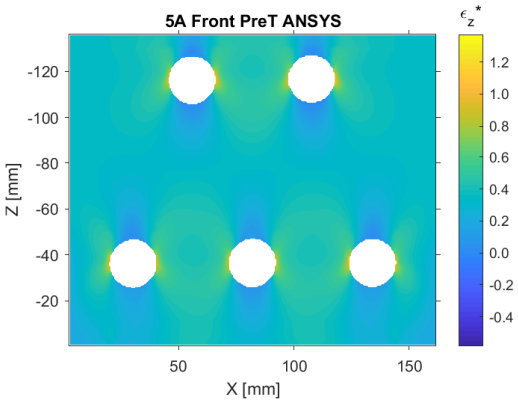
5A Front PreT ANSYS
ϵ_z^*
Z [mm]
X [mm]

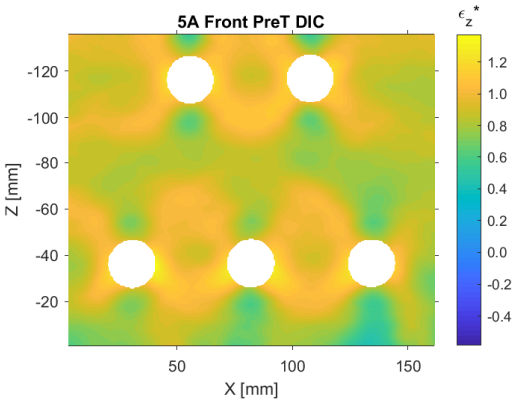
5A Front PreT DIC
ϵ_z^*
Z [mm]
X [mm]

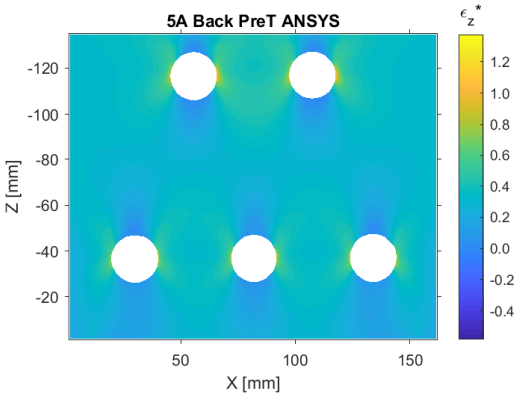
5A Back PreT ANSYS
ϵ_z^*
Z [mm]
X [mm]

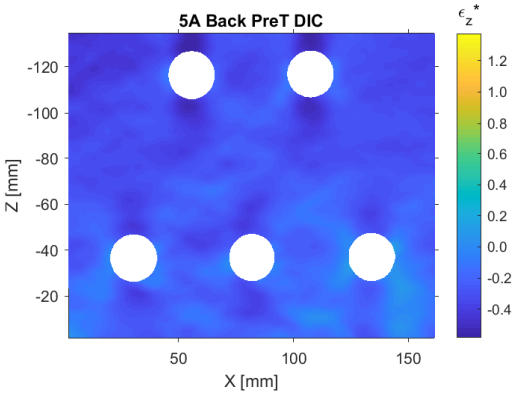
5A Back PreT DIC
ϵ_z^*
Z [mm]
X [mm]